Morphological and intracellular response of the liver to bile acid-mediated toxicity in Cholestasis

Dissertation

zur Erlangung des akademischen Grades des Doktors der Naturwissenschaften
(Dr.rer.nat.)
von der Fakultät Chemie und Chemische Biologie der Technischen Universität Dortmund

vorgelegt von
Amruta Damle-Vartak, **M.Sc.**
Aus Nagpur, Indien

Dortmund 2018

"It doesn't matter how beautiful your theory is, it doesn't matter how smart you are. If it doesn't agree with experiment, its wrong."

 Richard P. Feynman

The work described in this thesis was performed under the supervision of Prof. Dr. Jan Hengstler from April 2015 to April 2018 at the Leibniz-Institut für Arbeitsforschung an der TU Dortmund.

First Examiner:

Prof. Dr. Jan Hengstler   Dept. of Systems Toxicology

Leibniz-Institut für Arbeitsforschung

an der TU Dortmund,

Ardeystraße 67, Dortmund

Second Examiner:

PD Dr. Leif Dehmelt   Dept. of Systemic Cell Biology, Max-Planck-Institute

of Molecular Physiology and

Technical University Dortmund

ZUSAMMENFASSUNG

Die Leber ist das zentrale Organ des Fremdstoffmetabolismus. Wichtige Funktionen dieses Organs sind Synthese und Transport von Gallensalzen. Bei vielen Lebererkrankungen ist die Konzentration von Gallensalzen im Lebergewebe stark erhöht. Dies führt zu morphologischen und funktionellen Veränderungen und letztendlich zum Krankheitsbild `Cholestase´. Allerdings sind die molekularen Mechanismen dieses Phänomens nur unvollständig verstanden, ebenso so wie die Kontrollmechanismen, welche den räumlich-zeitlichen Veränderungen auf Gewebeebene zugrunde liegen.

Um diese Wissenslücke zu schließen, konzentriert sich der erste Teil dieser Arbeit auf die räumlich-zeitliche Antwort des Lebergewebes auf Cholestase. Basierend auf dreidimensionalen Rekonstruktionen und Bildanalysen von konfokalen Laserscans wurde die Veränderung der Leber-Mikroarchitektur bei Cholestase quantifiziert. Dem schloss sich eine Studie an, mit dem Ziel, die molekularen Kontrollmechanismen der Veränderungen auf Gewebeebene zu verstehen. Zur Rekonstruktion der räumlich-zeitlichen morphologischen Veränderungen im Lebergewebe, wurden Lebern von Mäusen bis zu 28 Tagen nach Gallengangsligatur untersucht. Diese Technik stellt eine standardisierte und weit verbreitete Möglichkeit dar, in Mäusen pathophysiologische Veränderungen zu induzieren, welche teilweise denen cholestatischer menschlicher Lebererkrankungen ähneln.

Veränderungen der Mikroarchitektur des Lebergewebes wurden mit einer in dieser Arbeit entwickelten bildgebenden Technik erfasst, basierend auf dreidimensionaler konfokaler Mikroskopie, automatisierter Bildauswertung und Oberflächenrekonstruktion der untersuchten Strukturen. Die Ergebnisse haben gezeigt, dass zwei strukturelle Domänen, die interlobulären Gallengänge und die Gallenkanälchen fundamental unterschiedliche Antworten auf Cholestase zeigen. Die interlobulären Gallengänge zeigen eine exakt reproduzierbare Sequenz der Geweberemodellierung, beginnend mit Proliferation der Cholangiozyten, mit der Folge der Bildung von Runzeln oder kleinen Falten der interlobulären Gallengänge, welche zu einer etwa fünffachen Vergrößerung der Oberfläche führt. Weiterhin kommt es zum Auswachsen neuer Äste der interlobulären Gallengänge. Diese neuen Äste vergrößern ihre Länge und vereinigen sich wieder mit dem Stamm, aus welchem sie hervorgegangen sind. Auf diese Weise kommt es zu neuen Schleifen interlobulärer Gallengänge und führt schließlich dazu, dass sich ein ursprünglich wenig dichtes Netzwerk an Gallengängen um die Portalvene zu einem wesentlich dichteren Netzwerk transformiert. Allerdings nimmt die Zahl der Verbindungsröhren zwischen dem Netzwerk interlobulärer Gallengänge und den Gallenkanalikuli, die sogenannten Hering-Kanäle nach Gallengangsligatur nicht zu. Überraschenderweise zeigten die Gallenkanalikuli bei Cholestase eine bisher noch nicht beschriebene Reaktion auf Gewebeebene. Es kam zu einer deutlichen Zunahme des mittleren kanalikulären Durchmessers. Dies geschah jedoch in einer unregelmäßigen Weise, so dass sich sehr weite mit relativ engen Passagen abwechseln. Diese Veränderungen des Durchmessers wurden von der Ausbildung stachelförmiger kanalikulärer Fortsätze begleitet, welche in das Zytoplasma der Hepatozyten hineinragen.

Zusammenfassend kann festgestellt werden, dass die räumlich-zeitlichen Antworten der Gallenkanalikuli bei Cholestase auf molekulare Veränderungen des apikalen Zellpols der Hepatozyten hinweisen, da die apikale Hepatozytenmembran die Begrenzung der Gallenkanalikuli bildet und daher an der Kontrolle der Mikroarchitektur beteiligt ist. Daher sollten im zweiten Teil der Arbeit die molekularen Mechanismen ergründet werden, welche die räumliche Anordnung der apikalen Hepatozytenmembran kontrollieren und für die oben beschriebenen cholestatischen Reaktionen auf das kanalikuläre Netzwerk verantwortlich sind.

Wie bei allen polarisierten Zellen wird auch die apikale Membran der Hepatozyten durch ein Netzwerk an Aktinfilamenten und Aktin-bindenden Proteinen unterstützt, welche das sogenannte perikanalikulare Aktin-Netzwerk ausbilden. In Hepatozyten stellt die apikale Membran die Begrenzung der

Gallenkanalikuli dar, welche rhythmischen Kontraktionen unterworfen ist. Die funktionelle Untersuchung dieser apikalen Membran zusammen mit dem assoziierten perikanalikulären Aktin erfordert daher eine Methode, welche die Visualisierung der zytoskelettären Komponenten und ihrer Dynamik in Relation zur kanalikulären Membran in lebenden Zellen ermöglicht. Die mikroskopische Darstellung von Proteinen in primären Hepatozyten stellt aus folgenden Gründen eine Herausforderung dar: erstens, erfordern konventionelle Transfektionstechniken zur ektopischen Expression fluoreszierender Fusionsproteine mehr als 24 Stunden, eine Dauer während der kultivierte Hepatozyten dedifferenzieren und ihre kanalikulären Strukturen verlieren. Zweitens erfordert die optimale Ausbildung von Gallenkanalikuli ein Kultursystem im Kollagensandwich, dessen Kollagen den Transfektionsprozess behindert. Weiterhin weist der häufig eingesetzte ektopisch exprimierte Aktin-Marker LifeAct den Nachteil der Bindung an globuläres Aktin auf. Dies resultiert in einer starken Hintergrundfluoreszenz, welche die Eignung der Technik bei Experimenten limitiert, bei welchen eine hohe Spezifität Aktin-assoziierter Signale erforderlich ist. Schließlich kann LifeAct Funktionen des Aktins beeinflussen, zum Beispiel die Bildung von Aktinfilamenten, ihre Zusammensetzung als auch Remodellierung, so dass Artefakte in Bezug auf das Verhalten und die Dynamik des perikanalikulären Aktins nicht ausgeschlossen werden können.

Diese Einschränkungen wurden durch die Entwicklung einer neuen Technik zur Darstellung des Aktin-Zytoskeletts in lebenden Zellen überwunden. Diese neue Technik basiert auf dem Einsatz sub-mikromolarer Konzentrationen von zwei fluoreszierenden kleinen Molekülen, welche wegen ihrer extrem niedrigen Konzentration nicht mit der Funktionalität des Zytoskeletts interferieren. Mit der optimierten neuen Technik basierend auf den fluoreszierenden Vitalfarbstoffen `SiR-actin´ (infrarot) und `Tubulin Tracker´ (grün) können Aktin- und Tubulin-Netzwerke in lebenden Zellen gleichzeitig beobachtet werden. In Suspension gefärbte Zellen wurden dann zwischen zwei Kollagengelen kultiviert. Unter diesen Bedingungen bildeten diese funktionelle Gallenkanalikuli aus. Dieses neue Protokoll bietet auch den Vorteil, dass die Spektraleigenschaften der beiden Fluorophore mit etablierten anderen Färbemethoden kompatibel sind, z.B. Fluorophore zur Darstellung des mitochondrialen Potentials (TMRE) und fluoreszierende Fusionsproteine in Reportermäusen (mcherry/tdTomato). Mit diesem neuen Färbeprotokoll wurden die Effekte von Gallensäuren auf perikanalikuläre Aktin- und Tubulin-Netzwerke untersucht. Die eingesetzten Konzentrationen schlossen den in vivo pathophysiologisch relevanten Bereich bei Cholestase ein. Hierbei wurde beobachtet, dass die Gallensäuren CDCA, DCA, UDCA und TCA zunächst eine Steigerung der Gallenkanalikulären Dynamik verursachten, gefolgt von der Depletion des perikanalikulären Aktins und Tubulins. Während der Gallenkanalikulus weiterhin rhythmische Kontraktionen zeigt, führt die Depletion nach relativ kurzer Zeit unvermeidlich zu einem Kollaps des kanalikulären Lumens und nachfolgendem Zelltod.

Frühere Arbeiten haben gezeigt, dass Myosin-vermittelte Kontraktionen für die Dynamik der Gallenkanalikuli verantwortlich sind. Werden diese inhibiert, führt das zum Verlust der Dynamik und zur Stabilisierung der kanalikulären Struktur. Auf der Basis der gut reproduzierbaren Sequenz perikanalikulärer Aktin-Depletion vor dem Zelltod, wurde in dieser Arbeit ein neues Modell Gallensäuren-vermittelter Toxizität etabliert. Das Schicksal der Gallenkanalikuli folgt zweizügelig aus einem Gleichgewicht zwischen Myosin-vermittelter Dynamik und durch perikanalikuläres Aktin-vermittelter Stabilität. Gallensäuren führen zur Auflösung des perikanalikulären Aktins, verschieben das Gleichgewicht in Richtung von Dynamik, was schließlich zum fatalen kanalikulären Kollaps in Verbindung mit Rupturierung der apikalen Membran und zum Zelltod führt.

Zusammenfassend kann festgestellt werden, dass Cholestase zu den hier erstmals beschriebenen Adaptionen des Gallenkanalikulären-Netzwerks auf Gewebeebene führt. Hierbei konnte die Rolle zytoskelettaler Bestandteile, spezifisch der perikanalikulären Aktin- und Tubulin-Netzwerke aufgeklärt werden. Die Störung dieser zytoskelettalen Netzwerke und die daraus resultierende kanalikuläre Membranruptur stellen frühe intrazelluläre Schlüsselereignisse bei Gallensäuren-vermittelter Toxizität dar. Daher sollte sich Forschung in Zukunft auf den exakten molekularen Mechanismus konzentrieren, mit welchen Gallensäuren das perikanalikuläre Aktin-Netzwerk depletieren. Hieraus könnten pharmakologische Strategien zur Stabilisierung des perikanalikulären Aktins und zur Inhibierung Myosin-vermittelter Dynamik resultieren, welche cholestatische Leberschäden verhindern könnten.

ABSTRACT

The liver is a central organ in xenobiotic metabolism, the primary function of which is synthesis and transport of bile acids. In many liver diseases, the concentration of bile acids in liver tissue is strongly increased, which leads to morphological and functional alterations, summarized as '**cholestasis**'. However, the molecular basis and underlying cellular mechanisms have not been investigated in detail vis-a-vis their relation to spatiotemporal morphological alterations at the tissue level remains to be elucidated.

To bridge this gap, the first part of this work focuses on the spatial remodeling and response of the liver tissue to cholestasis. Based on 3D reconstructions and image analysis of the confocal laser scans we study such architecture-based alterations of the liver in cholestatic liver injury. This was followed by a study of how this tissue-level response is controlled by the underlying intracellular events, forming the second part of this work. To study the spatiotemporal morphological changes in liver tissue, livers of mice were investigated up to a period of 28 days after ligation of the common bile duct (BDL). BDL is a standard interventional model in experimental mouse research, known to induce and display pathophysiology like that seen in human cholestatic liver diseases.

Architectural changes of the liver tissue were investigated with an imaging-based approach involving a custom pipeline of 3D confocal microscopy, automated image quantification, and surface reconstruction developed for this study. The results show that two structural domains, the interlobular bile ducts, and bile canaliculi show fundamentally different tissue-scale responses. The interlobular bile ducts undergo a highly reproducible sequence of remodeling, with a first response being cholangiocytes proliferation, which causes corrugation of the luminal duct surface causing an approximately 5-fold increase in the surface area. Moreover, duct branching, branch elongation, looping, and self-joining are some of the additional architectural adaptations of the liver to cholestasis injury are observed. These adaptations further enhance the surface area. Finally, an initially sparse mesh of the interlobular bile ducts around the portal vein becomes 5-fold denser. However, the number of connections between the interlobular bile ducts and the bile canalicular network known as canals of Hering did not increase per length of the portal vein. Surprisingly, the bile canalicular network showed a completely different hitherto unknown tissue-level response, with massive alterations of the canalicular diameter, alternating with relatively narrow stretches, leading to a high variability of canalicular width. These alterations in diameter of the bile canaliculi were accompanied by spiny canalicular protrusions into the cytoplasm of hepatocytes. Altogether, these changes pointed to alterations of the apical hepatocyte membrane, leading the work into an investigation of the molecular mechanisms that affect the apical membrane and cause the aforementioned morphological or tissue level alterations.

Like all polarized cells, the apical membrane of hepatocytes is known to be supported by a network of actin fibers and actin-binding proteins, forming the 'cortical actin network'. In hepatocytes, the apical membrane is specialized into a dynamic canalicular membrane, and a study of its associated pericanalicular actin network required a method to visualize the cytoskeletal components and their dynamics in relation to bile canalicular membrane alterations in live cells. Microscopic visualization of proteins in hepatocytes is especially challenging for several reasons.: First, conventional transduction or transfection techniques to ectopically express fluorescent fusion proteins require more than 24 hours, a duration in which hepatocytes de-differentiate and lose native canalicular structures. Second, the optimal formation of functional bile canaliculi in culture requires collagen sandwich cultures, and the collagen layers hinder the transfection process. Further, the popular ectopically expressed actin marker LifeAct has been reported to be shown to have a high affinity to bind globular actin. This results in have high background fluorescence, limiting its usefulness in experiments were a high specificity of actin-associated signals is required. Finally, LifeAct has been shown to influence and perturb the actin functions such as the formation of the actin filament, their assembly, and remodeling, increasing the chance of experimental artifacts with regard to the behavior and dynamics of the pericanalicular actin cytoskeleton.

These limitations were overcome by the establishment of a new live cell staining protocol, based on the use of two fluorescent small molecules used at sub micromolar and therefore relatively inert concentrations. With a rapid and straightforward protocol, freshly isolated hepatocytes are incubated under optimized conditions with the far-red fluorescent '**SiR-actin**' dye and the green fluorescent dye '**Tubulin Tracker**' to visualize the actin and tubulin networks in the same living cell. The labeled cells

were then plated between the standardized sandwich culture protocol of two layers of collagen where they form functional bile canaliculi. This novel protocol offers additional advantages because the dyes used remain spectrally compatible with well-established staining methods with visible range fluorophores for mitochondrial potential measurements (TMRE), fluorescent fusion proteins in reporter mice (mcherry/tdTomato) etc.

Equipped with this new live cell imaging protocol, we investigated the effects of bile acids on the pericanalicular actin and tubulin networks, in conditions that mimic cholestasis in vitro. It was found that high, but pathophysiological relevant concentrations of the bile acids CDCA, DCA, UDCA, and TCA caused an increase in bile canalicular dynamics, followed by an eventual depletion of pericanalicular actin and tubulin. While the bile canaliculus continues to display dynamics, this depletion inevitably leads shortly after to a canalicular collapse and subsequent cell death.

Previous work had shown that bile canalicular dynamics are the result of myosin-mediated contractile forces, which when inhibited lead to loss of bile canalicular dynamics and stabilization of the structure. In light of the highly reproducible sequence of pericanalicular actin depletion before cell death, a new model of bile acid toxicity emerged - the fate of bile canaliculi is governed by the balance between myosin-mediated dynamics, and the stability imparted by pericanalicular actin. Bile acids disrupt the pericanalicular actin, shifting the balance towards highly dynamic canaliculi that eventually collapse, rupturing the apical membrane and lead to cell death.

In conclusion, the present doctoral work described unknown spatiotemporal tissue level changes of the bile canalicular network. The role of cytoskeletal components, specifically the peri-canalicular actin and tubulin networks in these changes was elucidated. Their central involvement in bile canalicular dynamics, as well as stabilization of the canalicular structure, was identified. Indeed, the perturbation of these networks and resulting canalicular membrane rupture was shown to be an early intracellular event in bile acid-mediated cytotoxicity. Further ongoing work focuses on the exact molecular nature of the interaction of bile acids with the pericanalicular actin network, as well as pharmacological interventions to stabilize pericanalicular actin and inhibit myosin-mediated dynamics, with the hope of preventing cholestatic liver injury.

CONTENTS

1. INTRODUCTION

The liver is a visceral organ found in all mammals (Elias and Bengelsdorf 1952) and is a part of the gastrointestinal system. This vital organ has various metabolic, exocrine, endocrine, biosynthetic and excretory functions (Si-Tayeb et al. 2010). Metabolic functions include conversion of blood glucose to glycogen and fat, secretion of glucose into the blood, urea metabolism, cholesterol synthesis and transport (Elsevier). Secretion of different hormones like IGF-1, clotting factors such as fibrinogen and production of plasma proteins like albumin are some of its endocrine functions. The liver is also a highly specialized tissue that controls a variety of biosynthetic reactions such as synthesis and breakdown of complex molecules like lipids, proteins. Besides its central function in metabolism, it is also the largest gland in the human body that has a very important exocrine function. One of the exocrine functions is the production and secretion of '**bile**' and its transport (Mitra & Metcalf, 2009). Bile is made up of bilirubin, water, bile acids or bile salts and various electrolytes (Boyer 2013). Bile acids help in the process of digestion by emulsifying lipids (Monte et al. 2009; Mitra and Metcalf 2009). In recent years, it has become clear that bile also contains metabolic products and signaling molecules that mediate essential processes in entero-hepatic cellular communication.

The liver also filters toxins from the blood, detoxifies them, and secretes them into bile, which is eventually ejected through the colonic route (Nathanson and Boyer 1991). These functions of the liver are accomplished through an intricate synergy between the liver anatomy and biochemistry at multiple scales (Duncan and Soto-Gutierrez 2013). Understanding the function of the liver and various mechanisms by which it reacts to any potential toxic insult or disease state as '**cholestasis**' thus requires a detailed architectural information at the cellular level extending to the entire organ.

1.1. Gross anatomy of the Liver

1.1.1. Morphology

The liver is a cuneiform shaped intraperitoneal-organ which is located in the abdomen cavity, upper right quadrant just beneath the diaphragm and is protected by the rib cage (Abdel-Misih & Bloomston, 2010). Morphological anatomy suggests that the liver is incompletely separated

into lobes. These lobes are covered on their external surface by a thin connective tissue layer called the '**Glisson's capsule**' (Elsevier, n.d., p. 2). The human liver consists of two main lobes called the '**right and left liver lobes**' separated from each other with the help of a falciform ligament (1.1.1.F1A) as viewed from the diaphragmatic surface ("Henry Gray. 1918. Anatomy of the Human Body: Bibliographic Record," n.d.). As observed from the visceral side of the liver, the right lobe is further divided into two more lobes '**caudate and quadrate**' (1.1.1.F1B) joined to each other dorsally. In other mammals such as a mouse, the liver is made up of four lobes (Elsevier, n.d.; Maronpot, n.d.) i.e. the median lobe divided into two lobes called the right and the left lobe, left lateral lobe, right lateral lobe attached dorsally to a caudal lobe (1.1.1.F1B).
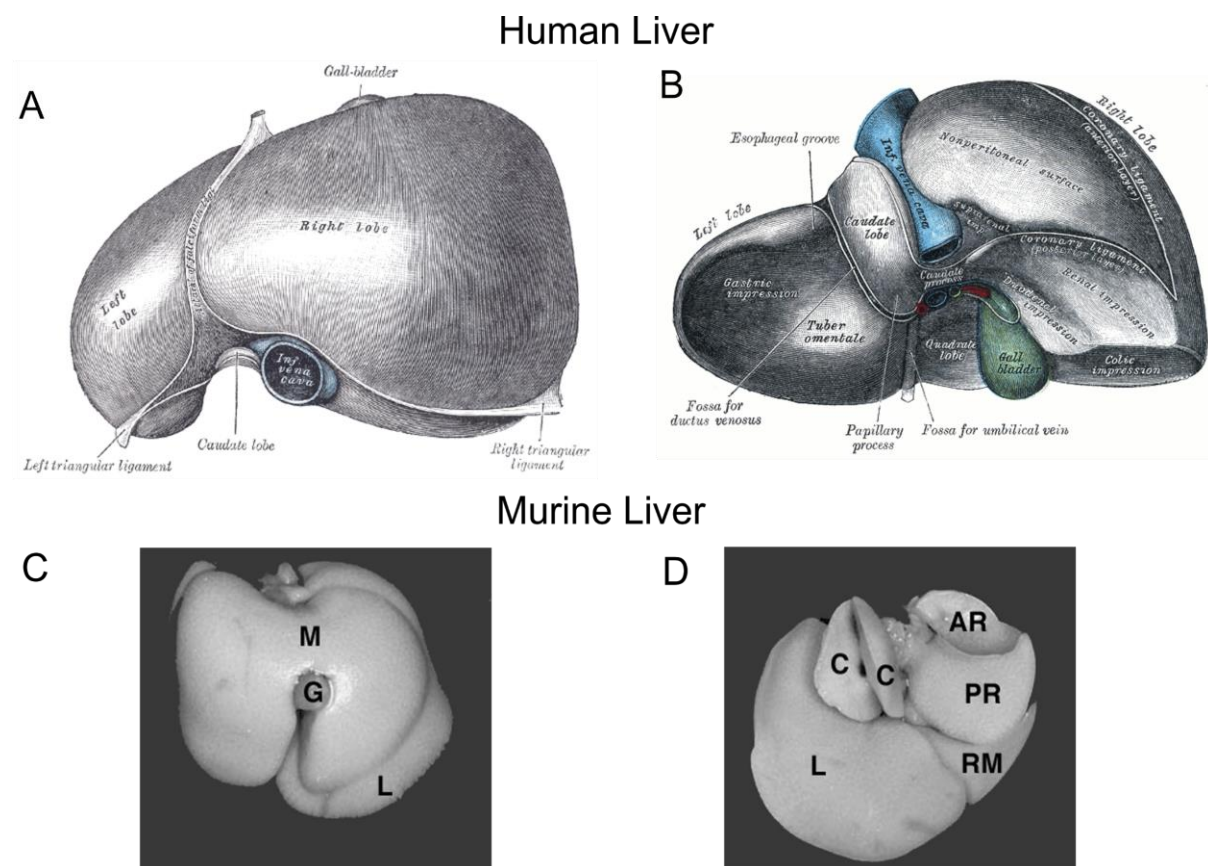
Fig.1.1.1.F1. **Gross anatomy of the human and mouse liver**. A. The superior surface of the human liver showing 2 liver lobes right and left separated by a falciform ligament. B. Visceral surface of the liver shows the presence of two more lobes caudate lobe and quadrate lobe (Image reused and modified from Gray, Henry. Anatomy of the Human Body. Philadelphia: Lea & Febiger, 1918 Bartleby.com, 2000). C. The superior surface of the mouse liver shows at least 2 lobes: Median lobe [**M**], Left lobe [**L**] and gallbladder [**G**] attached to the median lobe. D. Visceral surface of the liver illustrates 4 liver lobes: Caudate lobe [**C**], Left lobe [**L**], right median lobe [**RM**], posterior right lobe [**PR**] and anterior right lobe [**AR**] (Image copyright and reproduced from: The Digitized Atlas of Mouse Liver Lesions, NIH).

1.1.2. Fluid transport in the liver

The liver contains two conduit systems that span through the organ. The biliary system transports the exocrine secretion of the liver called the '**bile**'. The circulatory system transports blood that is detoxified by the liver and supplies nutrients to the liver.

Extrahepatic biliary system

The liver is connected via a hepatic duct to a pear-shaped pale greenish yellow organ called the 'gallbladder' that stores the bile (Fox, 2015; "Wiley: Principles of Anatomy and Physiology, 14th Edition - Gerard J. Tortora, Bryan H. Derrickson," n.d.). The hepatic duct from the liver and the cystic duct from the gallbladder unite to form the common bile duct (1.1.2.F1).

Blood circulation

The liver has a dual blood supply as it is connected by two afferent blood vessels: **the hepatic artery and the portal vein**. Blood from the liver is returned to the heart via the efferent **hepatic vein** which connects to the inferior vena cava (1.1.2.F1). The primary function of the hepatic artery is to carry about 20-25% oxygen-rich blood from the aorta or arterial blood to the liver. The hepatic portal vein carries 70-85% of poorly oxygenated venous blood rich in digestive nutrients from the intestine, pancreas, spleen. The venous blood from the gallbladder can either drain directly into a cystic vein that can empty it to the right branch of the portal vein or drain via the small veins in the gallbladder bed directly into the parenchyma of the liver.
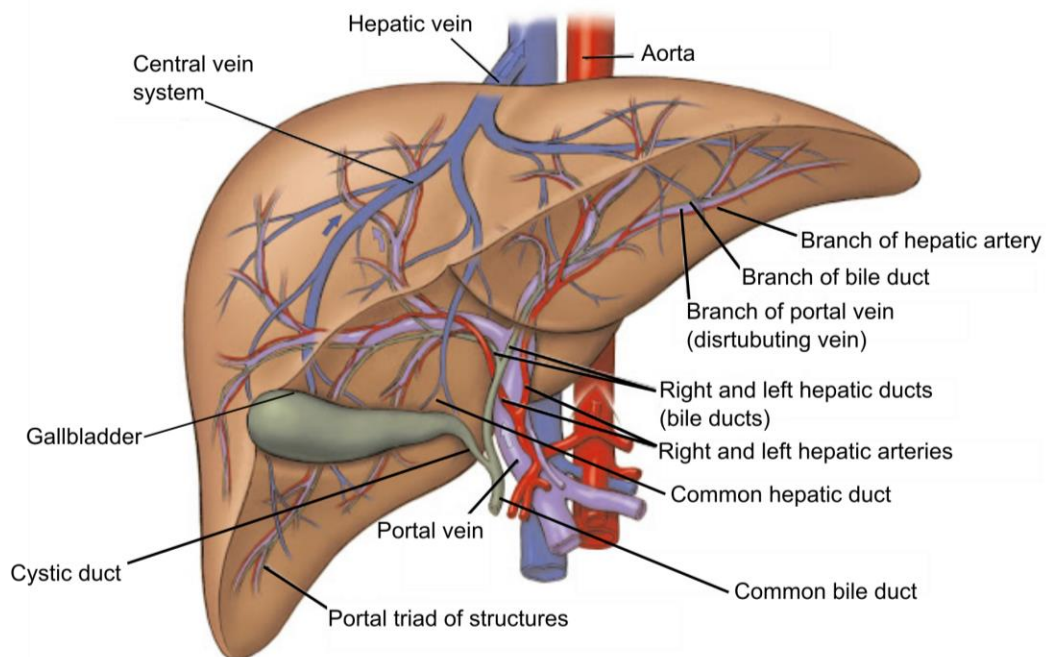
Fig.1.1.2.F1. Extrahepatic biliary system and vasculature of the liver. Figure reproduced from (Vizcarra, n.d.).

1.2. Micro-anatomy of the liver

Conventional histological sections of the liver represent it as a pink-brown tissue with repetitive rows of cells called the '**hepatocytes**' interspersed with the capillary network of sinusoids and the biliary tree (1.2.F1A). Behind this simplistic representation, underlies a highly complex tissue which is composed of different parenchymal and nonparenchymal cell types that are arranged in a small roughly shaped hexagon or the functional units called the '**liver lobules**' (1.2.F1B). The basic unit of a liver lobule consists of a branch of the hepatic vein also known as a '**central vein**' that carries the blood from the liver and is linked to the branch of a portal vein that carries the venous blood rich in all the nutrients and metabolites from gastrointestinal tract (**GI**), a branch of the hepatic artery which carries the arterial blood to the liver and a branch of the bile duct that drains the bile which is secreted and produced in the lobule (1.2.F1B).
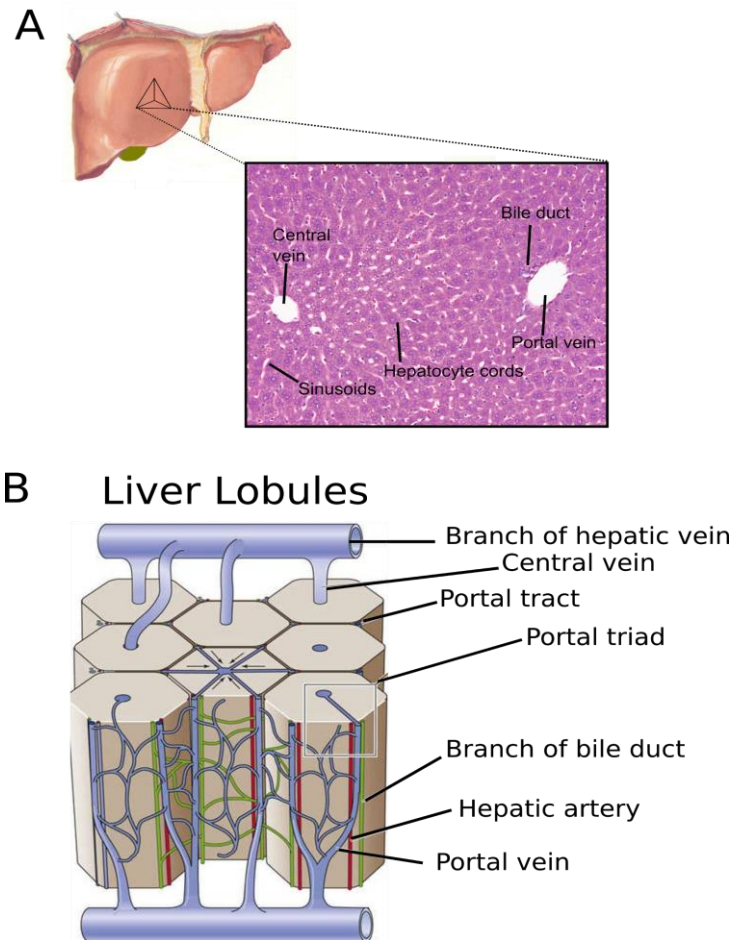
Fig.1.2.F1. A. Graphical representation of the liver with gallbladder (green). An inset shows a representative magnified view of a histological slice of the liver which is made up of hepatocyte rows in cords interspersed between an afferent and an efferent blood supply of the liver i.e. central vein and the portal vein adjacent to a branch of the hepatic artery and bile duct. Image modified from http://livercenter.ucsf.edu/pathology-imaging-core-routine. B. Graphical representation of the functional and structural unit of the liver parenchyma: liver lobules. Each hexagon represents one such hexagonal unit that is made up of a central vein and a portal triad at each edge of the hexagon that consists of a branch of a bile duct, a hepatic artery, and a portal vein. Image adapted and modified from https://doctorlib.info/physiology/medical/253.html.

1.2.1. Functional unit of the liver 'Lobule': classification, organization, microarchitecture and function

Due to a complex structure of the liver, it is difficult to define liver as a single unit like any other organ. The liver is comprised of several liver lobules that are densely packed together. A liver lobule can be classified and organized in at least 3 different ways: '**portal lobule**', '**portal acinus or hepatic acinus**' and a '**classic hepatic lobule**' (1.2.1.F1).
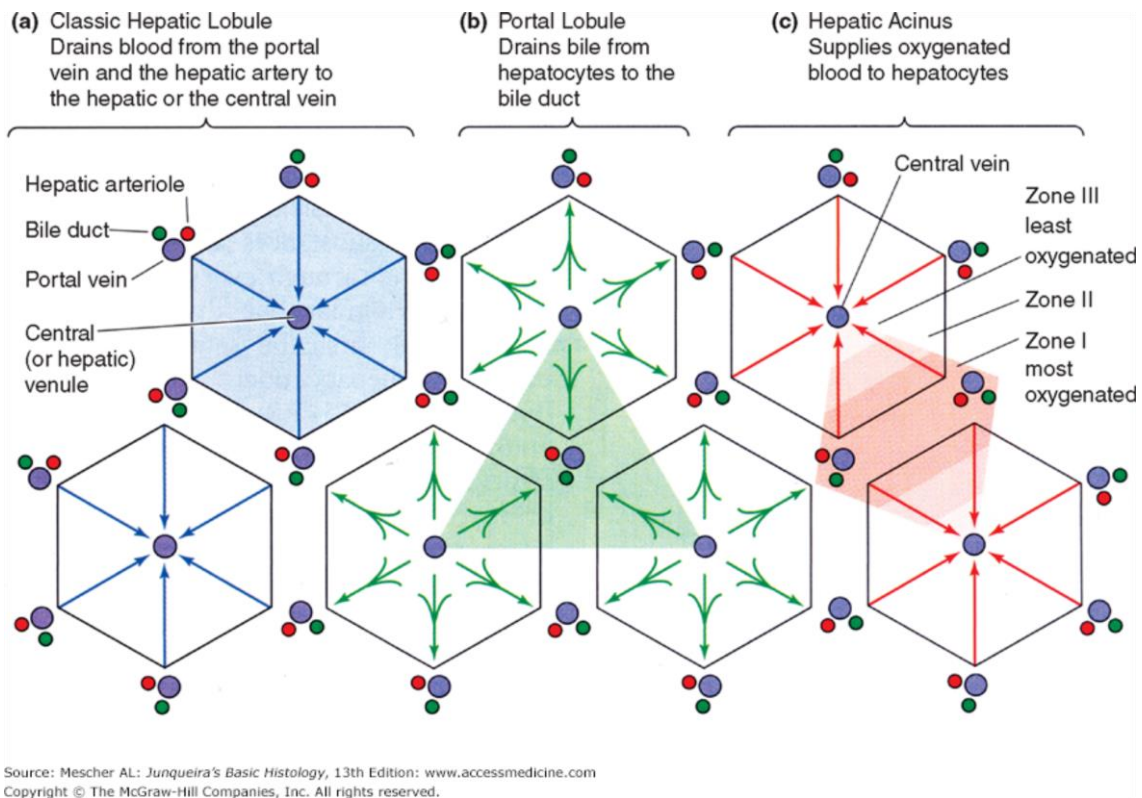
Fig.1.2.1.F1. **Liver organization**. A. Classic hepatic lobule represented as a hexagon with a central vein (purple) in the center demarcated with at least 6 portal triads each made up of a bile duct (green), a portal vein (purple) and a hepatic artery or arteriole (red) at the corner of a lobule. Blue arrows indicate the direction of the flow of blood. B. Portal lobule represented as a triangular block (green) of the liver parenchyma supplied by the circum lobular branches of one interlobular vein i.e portal vein (purple). At the center of the lobule is a portal triad consisting of a portal vein (purple), a bile duct (green) and a hepatic arteriole (red) and at the peripheral angles are located three central veins (purple). Green arrows indicate the direction of the flow of bile secreted that drains into the bile duct of a portal triad located in the center of a portal lobule. C. Hepatic acinus represented as an ellipse or roughly quadrilateral shaped smallest functional unit of the liver parenchyma. The area of an acinus is the region (red quadrilateral) defined by the short axis of acinus i.e connecting line between adjacent portal triads (bile duct, hepatic artery and portal vein) and the long axis is defined by a connecting line between two adjacent central veins (purple circle). The circum lobular vein and artery supply blood to the sinusoids of the hepatic acinus. Depending on the distance between the vein and the artery, distribution of oxygenated blood and nutrients and metabolic activity of the liver, the acinus has 3 defined zones: Zone I (red area), II (light red area) and III (white area). Image reused with copyright and permissions from (Junqueira's Basic Histology, 14e >https://accessmedicine.mhmedical.com/content.aspx?sectionid=109633602&bookid=1687).

The '**portal lobule**' is a triangular triad that is made up of hepatocytes forming the bile canaliculi and draining the bile to a single bile ductule in the center of the triangular portal triad and bound to 2 or more central veins at each corner of the triangular triad (1.2.1.F1B). While a '**portal acinus**' is a smallest unit of the liver roughly quadrilateral shaped or ellipse (1.2.1.F1C)

that is arranged in small three-dimensional mass of hepatocytes (irregular in size and shape) occupying an area that is between 1 axis formed by a line between 2 portal triads and another axis formed by line between 2 central veins. The portal acini have three zones: zone I, II, and III. The cells of the portal acini have a zonal relationship with their blood supply (Rappaport & Wilson, 1958). Zone I cells are hepatocytes that are close or in proximity to the portal triad or periportal fields. These cells are the first to be perfused with blood and receive the highest concentration of oxygen and solutes. The cells are more resistant to the effects of nutritional deficiency, cellular injury and are first to regenerate. Zone II hepatocytes are intermediate hepatocytes immediately located after zone I and before zone III hepatocytes that reside close to the central vein of the portal acinus (1.2.1.F1C). The hepatocytes of zone 2 and zone 3 are sequentially perfused with blood that is modified by zone 1 hepatocytes. These hepatocytes are also exposed to low concentrations of nutrients and oxygen. Exact boundaries of these zones are difficult to define and hence the zones can be classified based on different types of functions mainly metabolic carried by hepatocytes in these zones (Lee-Montiel et al., 2017; Wilton, Chipman, Lawson, Strain, & Coleman, 1993).

1.2.1.1 Organization of a 'Classic hepatic lobule'

The liver tissue is organized into several such approximately hexagonal classical units or lobules (1.2.1. F2.A). It is the functional unit of the liver that is responsible to carry out all the important hepatic functions. The center of this rough hexagon shaped lobule is demarcated by a branch of the hepatic vein called the central vein (CV). The central vein of different lobules converges to form the hepatic vein that carries blood from liver to inferior vena cava. The vertices of the hexagon are demarcated by a trio of vessels called the 'portal triad'. The portal triad consists of branches of the hepatic artery (HA), portal vein (PV) and the interlobular bile duct (IBD). The portal vein and the hepatic vein branches into a capillary-like network called the 'sinusoidal network' lined by liver sinusoidal endothelial cells (LSECs). This network spans the interspersing area of the hexagon and eventually connects to the central vein (1.2.1. F2.B). The blood from the hepatic artery and the portal vein contains nutrients from the intestine and substances secreted by the pancreas mixed together and this blood flows from periphery of the lobule to the central vein through the sinusoidal vessel network (Hoehme et al. 2010). The sinusoidal network is intricated with striations of parenchymal epithelial cells called 'hepatocytes'. Hepatocytes interface with sinusoidal endothelial cells through their basolateral membrane (Treyer and Müsch 2013). The apical membrane of the hepatocytes

interfaces with another hepatocyte to form a vessel like structure called a 'canaliculus'. The canaliculi of adjoining hepatocytes link together to form a second network of vessels that spans the intervening area of the hexagon to connect to a branch of the bile duct in the portal triad. This branch is called the *'canals of Hering or CoH'* (Strazzabosco and Fabris 2008). The CoH connects the bile canaliculi with the peripheral interlobular bile ducts which drain the bile produced by the hepatocytes into the hepatic ducts. The hepatic ducts finally carry the bile away from the liver. It is hard to separate structurally each such single unit from each other in mouse, except the presence of thin connective tissue septa around the portal triad demarcating each such lobular units as present in other species like the pig. Several such liver lobules together form one such lobe of the liver and held together by the Glisson's capsule. The capsule follows and covers the path of branches of blood vessels originating from the hepatic artery and portal vein called the '*sinusoids*' that enter the lobule and the hepatic duct that lead to several branches of the bile ducts. Blood draining from the parenchymal lobular units is collected via these sinusoids and bile produced by the liver is drained out of the liver via the bile ducts.
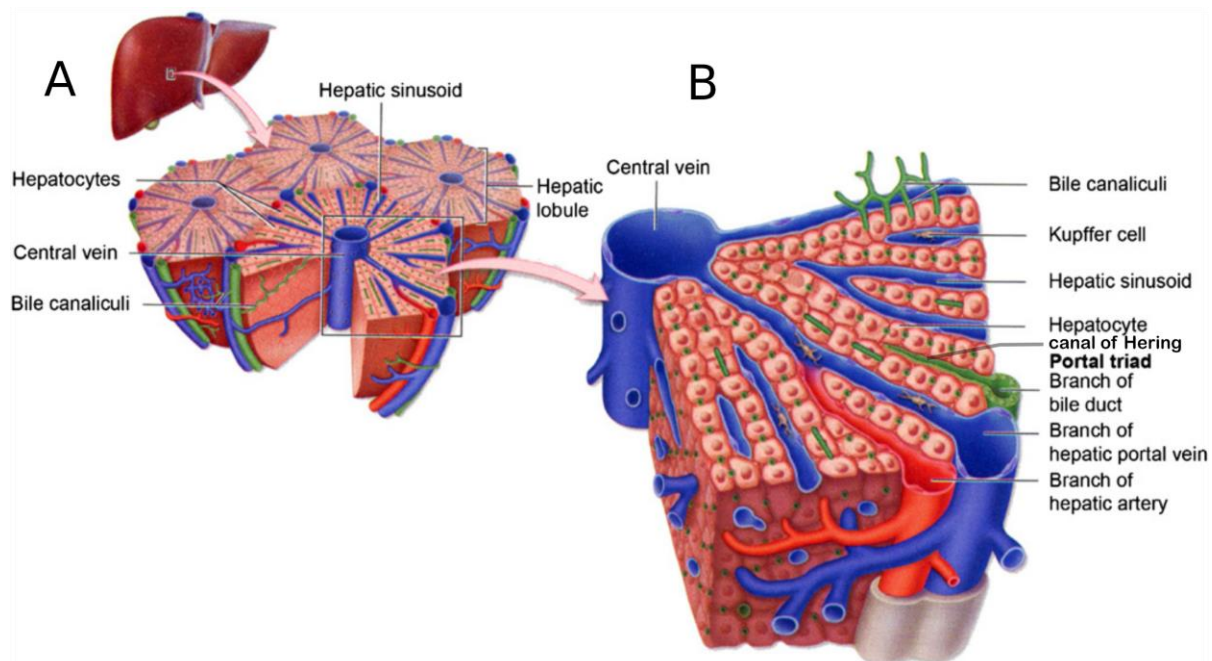
Fig.1.2.1.F2. The microscopic architecture of the liver lobules. A. A cross-sectional view of several lobular units of the liver with the central vein (blue) in the middle and interspersed hepatic sinusoids (blue)and hepatocyte network (light red) forming bile canaliculi (green). B. The detailed microarchitecture of one such lobular unit consisting of a central vein (blue), portal triad made up of a branch of a bile duct (green), branching hepatic portal vein (blue) and adjacent hepatic artery (red) connecting to the central vein. The lobule is intricated with repetitive

rows of hepatocytes (light red) forming bile canalicular network (green) connected to a branch of the bile duct with the canal of Hering (green). Image copyright modified and reused from (Stenvall et al. 2014).

1.2.2. Cellular components of the liver lobule

The liver tissue comprises of at least 6 distinct cell types (Kang, Mars, & Michalopoulos, 2012; Malarkey, Johnson, Ryan, Boorman, & Maronpot, 2005; Si-Tayeb, Lemaigre, & Duncan, 2010). The liver is composed of both parenchymal cells i.e. hepatocytes and nonparenchymal cells like Kupffer cells, endothelial cells, stellate cells. These different cell types are located in specific areas of the liver lobule (1.2.2.F1.A) and they have numerous hepatic functions (1.2.2.T1).
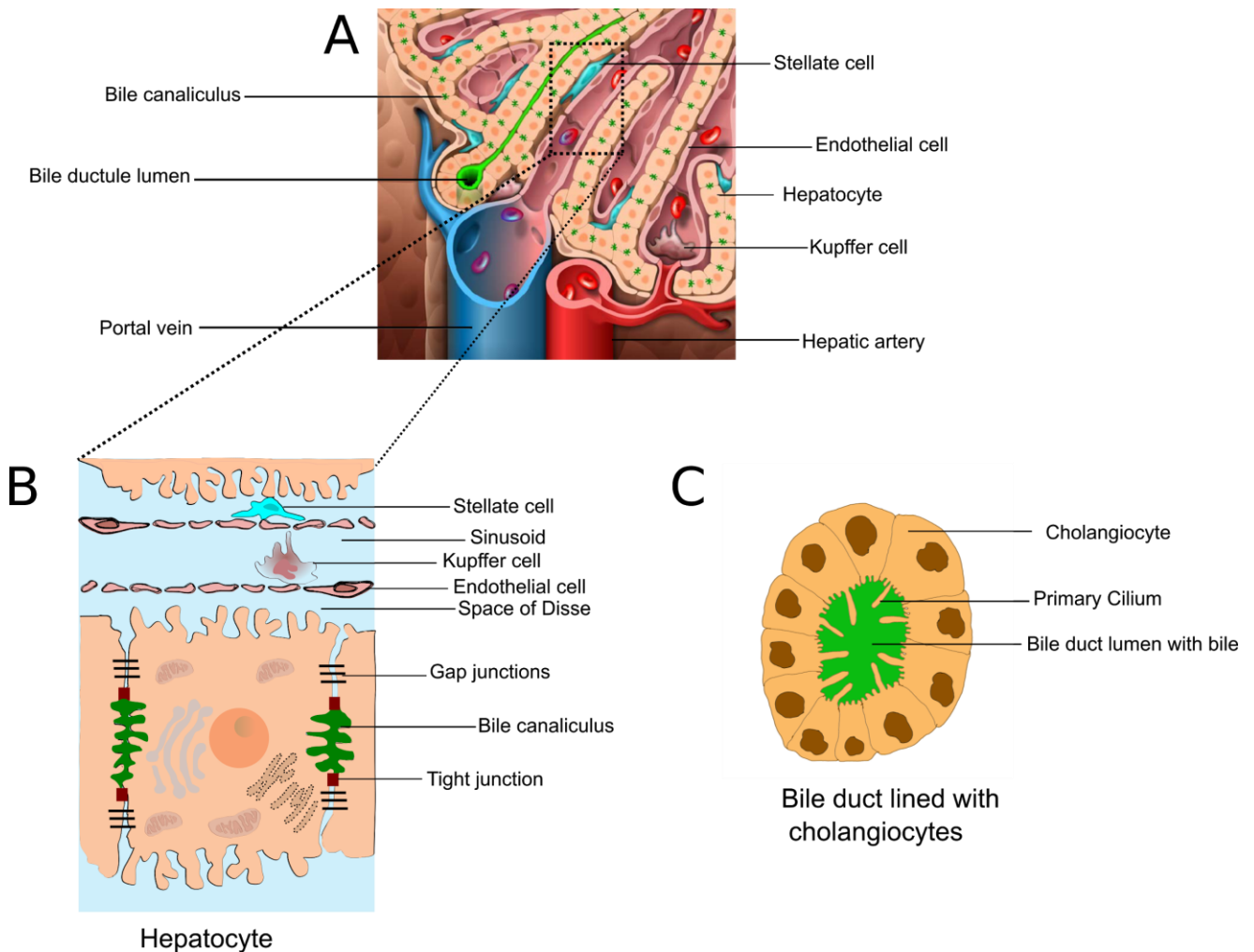
Fig.1.2.2. F1.A. Organization of different cell types of the liver in a liver lobule (Image modified and reused from (Jonker, Stedman, Liddle, & Downes, 2009). B. Liver parenchymal cell: Hepatocyte with the apical membrane

forming bile canaliculus (green) and basement membrane lining the sinusoid (light blue area). C. Bile duct forming cells: Cholangiocytes with primary cilium facing the lumen containing bile (green).

Table.1.2.2.T1. Cell types and their functions in the liver

Cell Type	Position in the liver	Function	Immuno-histochemical markers
Hepatocytes	Parenchyma	Bile secretion Detoxification Cholesterol metabolism Protein secretion	CK18, Albumin
Cholangiocyte/ bile duct cells	Duct epithelium	Control rate of bile flow Secrete water and bicarbonate Control pH of the bile	CK 19
Endothelial cell	Vasculature	Controls blood flow Contribute towards parenchyma zonation Forms veins, arteries, venioles and arterioles	Factor VIII, CD31
Liver sinusoidal endothelial cell	Sinusoids	Forms sinusoidal plexus to facilitate blood circulation Allow transfer of molecules and proteins between serum and hepatocytes Scavenger of macromolecular waste Antigen presentation	Factor VIII, CD31
Kupffer cell	Sinusoids	Secrete cytokines and proteases Scavengers of foreign material	F4/80, CD 68
Hepatic stellate cell (activated)	Perisinusoidal	Maintenance of extracellular matrix, storage and production of vitamin A, retinoic acid Controls microvascular tone Upon activation they become myofibroblasts Contributes towards regenerative response to injury	α-SMA
Pit cell	Liver natural killer cells	Rare Produce perforin and TNF-α Cytotoxic activity Kill tumor cells	CD56 (Humans)

Table modified and adapted from (Kang et al., 2012; Maronpot, 2010; Si-Tayeb et al., 2010).

Hepatocytes

Hepatocytes are the main parenchymal cells which comprise 60-70% of the total liver cell population (Malarkey et al. 2005; Kang et al. 2012; Maronpot). They originate from hepatoblasts during development (Si-Tayeb et al. 2010; Zorn 2008). They are polyhedral in shape and roughly 20-30 µm in diameter (Krishna 2013). Adult hepatocytes are quiescent but upon liver infection, toxic insult or during partial hepatectomy they undergo proliferation thus contributing to the liver regeneration process (Conigliaro et al. 2010; Fausto 2004; Michalopoulos 2007).

Hepatocytes express several specific marker proteins like keratin, type I cytoskeletal 18 (KRT18) [UniProtKB - P05783 (K1C18_HUMAN], transcription factor-like hepatocyte nuclear factor 4-alpha (HNF4-) and albumin (ALB), which are utilized for immunohistological detection (Yanger et al. 2014; Jörs et al. 2015; Shiojiri 1997). They are polarized epithelial cells with 2 distinct surfaces: a basolateral surface and an apical surface. These surfaces in relation to their structure, physiology and biochemical characteristics are distinct from each other. The basal surface of hepatocytes interacts with the underlying extracellular matrix (ECM) and faces the space of Disse while the apical surface forms bile canaliculi (Treyer and Müsch 2013). The lateral surface helps in cell-cell contact. The apical space is lined with several tight junctions like claudins which act as a seal that joins the apical membrane of two hepatocytes and gap junctions, which allow communication between adjacent hepatocytes (1.2.2.F1.B). These junctions also control bile flow and metabolite entry-exit (Lee 2012). Hepatocytes are responsible for most of the metabolic, biosynthetic and detoxification functions of the liver. Major products of hepatocytes include plasma proteins like albumin and clotting factors that are secreted to the blood, as well as bile salts that are secreted as bile into the bile canaliculi. Hepatocytes can also absorb toxins from the blood, detoxify them through metabolic modifications and excrete them via bile. To perform these myriad functions, hepatocytes express a wide variety of transporter proteins to allow the uptake and secretion of biliary and blood metabolites (Baier et al. 2006).

Cholangiocytes

Cholangiocytes are biliary epithelial cells (BECs) that line the bile ducts (1.2.2.F1.C). They form about 2-4% of the liver cell population. They have the same precursor cell as hepatocytes called the hepatoblasts derived from embryonic endoderm (Kang et al., 2012; Zorn, 2008). Cholangiocytes are cuboidal shaped and have two populations i.e. the small and large cholangiocytes based on their location in the biliary tree (Glaser, Gaudio, Rao, et al., 2009; Mario Strazzabosco & Fabris, 2008). In mice, the small bile ducts are lined by small cholangiocytes about 8 µm in diameter while the large ducts are lined by large cholangiocytes about ≥15 µm diameter (Glaser et al., 2000). Small cholangiocytes are mitotically inactive in normal liver but under trauma, they can proliferate to compensate for the loss of large cholangiocytes (G. Alpini et al., 1998; Lesage et al., 1996; LeSage et al., 1999). Cholangiocytes are also polarized with a basal surface facing the basement membrane and apical surface forming lumens also called bile ductules (Tanimizu, Miyajima, & Mostov, 2007).

Cholangiocytes are distinguished from other epithelial cells by their expression of specific marker proteins KRT19, KRT7 and SRY-related HMG box transcription factor [Sox 9] (Cardinale et al., 2012; Carpentier et al., 2011; van Eyken, Sciot, van Damme, de Wolf-Peeters, & Desmet, 1987). Cholangiocytes carry out several secretory and resorptive functions like the modification of the canalicular bile by controlling its pH and rate of flow (Fitz, 2002; Kanno, LeSage, Glaser, & Alpini, 2001). The apical surface of cholangiocytes contains primary cilia that have mechano-sensing properties and regulate bile secretion (A. I. Masyuk et al., 2006). Cholangiocytes also have an immunological role as they are the first line of defense against microbial infections of the biliary system (Chen, O'Hara, & LaRusso, 2008). They are the primary target of injury in cholestatic liver diseases (Gianfranco Alpini, McGill, & Larusso, 2002; Chen et al., 2008; Fava, Glaser, Francis, & Alpini, 2005; McGill et al., 2001).

Sinusoidal endothelial cells

In the liver, the sinusoids i.e. capillary branches of the portal vein and central veins are mainly lined by a continuous layer of fenestrated endothelial cells (De Leeuw et al. 1990; Malarkey et al. 2005) called sinusoidal endothelial cells. These cells approximately cover 2.5% of the lobular parenchyma (Si-Tayeb et al. 2010). These cells express membrane glycoproteins such as CD31 or PECAM-1 (Lalor et al. 2006), VEGF (Sato et al. 2001; Teagan J. Walter, Ashley E. Cast, Kar...). Liver sinusoidal endothelial cells contain fenestrations that have contractile and metabolic functions (Malarkey et al. 2005; Maronpot). The fenestrated capillaries of the liver 'sinusoids' lack a basement membrane and are more permeable for entry of plasma proteins and protein-bound molecules like cholesterol. Fenestrae act as a 'sieve' as they can filter fluids, solutes, and particles that are exchanged between sinusoidal lumen and space of Disse and endocytosis to filter these solutes and particles passing from blood and the space of Disse to parenchyma (Smedsrød 2004; Braet and Wisse 2002). Fenestrae can also remove particles like triglycerides, cholesterol which may accumulate in the blood and in excess lead to conditions like atherosclerosis (Braet and Wisse 2002). Fenestrae of the elongated sinusoidal endothelial cells establish as a filter between hepatocyte and sinusoidal membrane and are functional barriers between blood and hepatocytes that control entry of any pathogenic agents. The space of Disse is the perisinusoidal space between hepatocytes and the wall of the sinusoids. LSECs lack a basement membrane and prevent direct contact between the hepatocytes, fat-storing Ito or Stellate cells with blood cells thus carrying out their clearance of endotoxins, bacteria, and toxic compounds efficiently.

LSECs can synthesize prostaglandins, have numerous vesicles having endocytic capacity and also contribute to the production of collagen in normal and fibrotic liver (Maronpot; Smedsrød et al. 1994).

Kupffer cells

Kupffer cells line the walls of sinusoids in the liver attached to endothelial cells and contribute approximately 2% of the liver cell population (Si-Tayeb et al., 2010). They are derived from circulating monocytes (Bykov, Ylipaasto, Eerola, & Lindros, 2004; Malarkey et al., 2005). They have phagocytic and endocytic properties and are a part of mononuclear phagocyte system (Decker, 1990) thus being involved in the process of innate immunity in liver (Bykov et al., 2004; Fox, 2015; Itoh et al., 1992). These cells have receptors like TLR4 and CD14 on their surface which get activated and activate transcription of different cytokines to stimulate internalization of endotoxins during liver injury such as alcoholic liver disease (Cubero & Nieto, 2006). Kupffer cells secrete mediators of inflammation, detoxify endotoxins, process antigens and catabolize lipids and glycoproteins (Malarkey et al., 2005; Maronpot, n.d.).

Stellate cells

Hepatic Stellate cells are also called 'Ito cells' or 'fat storing cells'. They make up roughly 1.4-5% of the liver cells (Yin et al. 2013). They are found in the perisinusoidal space of the liver called the 'space of Disse', thus in cell-cell contact with LSECs and hepatocytes. The Stellate cells produce extracellular matrix, store and metabolize vitamin A and lipids and control the vascular muscle tone. In the healthy liver, the Stellate cells are dormant but upon damage, they transdifferentiate into myofibroblasts and generate a temporary scar tissue at the site of injury to protect the liver tissue from damage. Their major role is in regeneration and hepatic fibrogenesis and cirrhosis. Activated stellate cells express desmin and smooth muscle actin filaments like -SMA (Carpino et al. 2005).

NK cells

The Natural killer cells or pit cells are large granular leukocytes as they contain azurophilic cytoplasmic granules. They are attached to LSECs and Kupffer cells (Bouwens and Wisse 1992). These cells are distributed in the periportal area (Maronpot). Circulating NK cells migrate to the liver and are attached to the sinusoidal walls were they mature into liver-specific NK cells (Parker and Picut 2012; Gao et al. 2009). These cells have functions like resistance to tumor invasion, control of viral infections by releasing perforin and granzyme that attack the cell membrane and kill targeted cells by apoptosis (Parker and Picut 2005).

Extracellular matrix

5-10% of the liver is made up of collagen that provides structural support, rigidity, strength, and elasticity of the tissue architecture. The extracellular matrix (ECM) is a complex environment made up of water, matrix metalloproteinase, glycoproteins, laminin, fibronectin and collagen (Arriazu et al. 2014; Malarkey et al. 2005). The extracellular matrix is involved in regulation and modulation of hepatic functions. It can interact with cell-surface receptors and regulate cell differentiation, proliferation, migration and survival (Rozario and DeSimone 2010). The ECM undergoes remodeling during development and liver damage such as in fibrosis to maintain homeostasis and repress progression of the disease (Baiocchini et al. 2016). ECM can bind and secrete several growth factors and cytokines that help in remodeling, morphogenesis, and metabolism.

1.3. Bile: Formation, storage, composition and function

'Bile' is a yellow-greenish fluid secreted and produced in the liver (Anwer 2004; Coleman 1987). Bile is primarily composed of water (97.5%), osmotically active ions and various solutes which are secreted by the hepatocytes and released into their apical surface which forms a lumen, or a channel called the 'bile canaliculus' (Boyer 2013; Anwer 2004; Treyer and Müsch 2013). The bile canaliculi form a network of interlinked channels which collect secreted bile and drain it further to the bile ducts of a portal triad via a link called the 'canal of Hering' that is lined by the cholangiocytes (Boyer 2013). The bile ducts finally collect all the bile from the biliary network and empty it to the common hepatic duct. The common hepatic duct is joined to the cystic duct of the gallbladder to form the common bile duct where all the hepatic bile

gets collected. In the gallbladder, water and electrolytes are removed from the bile and the bile is acidified thus increasing its concentration about 10-fold before it is delivered to the intestinal lumen (Trauner and Boyer 2003). Only half of the hepatic bile enters the gallbladder for concentration and storage. The rest of the bile bypasses the gallbladder and enters into the duodenum at a junction that is regulated by the sphincter of Oddi. This then undergoes continuous enterohepatic cycling and bile acids from the bile enter back into the liver through the portal vein for recycling (Begley et al. 2005). The bile secreted in the canalicular network is known as 'canalicular bile' and it accounts for approximately 75% of daily bile production in humans while the bile collected in the ducts is called the 'ductular bile'. Bile formation is regulated by the heterogeneity of hepatocytes and cellular permeability of the solutes.

Bile is complex and mainly composed of water in which several organic solutes like bile salts, bilirubin and inorganic substances like bicarbonate ions exist in dissolved, partially dissolved and undissolved state (Coleman 1987; Boyer 2013; Anwer 2004). Some of the other constituents include proteins, enzymes, porphyrins, peptides like glutathione, small amounts of endogenous substances like thyroid and steroid hormones (Boyer 2013). In humans, some of the major components of bile are bile pigment or bilirubin (50-200 mg/100 ml in the common bile duct bile), bile salts and bile acids (concentration range of 2 to 45 mmol/L), phospholipids (25-810 mg/100 ml) like lecithin, cholesterol (60-320 mg/100 ml), inorganic ions (Na^+, Ca^{2+}, K^+) and bicarbonate (HCO_3^-) (Esteller 2008; Begley et al. 2005) (1.2.3.F1).
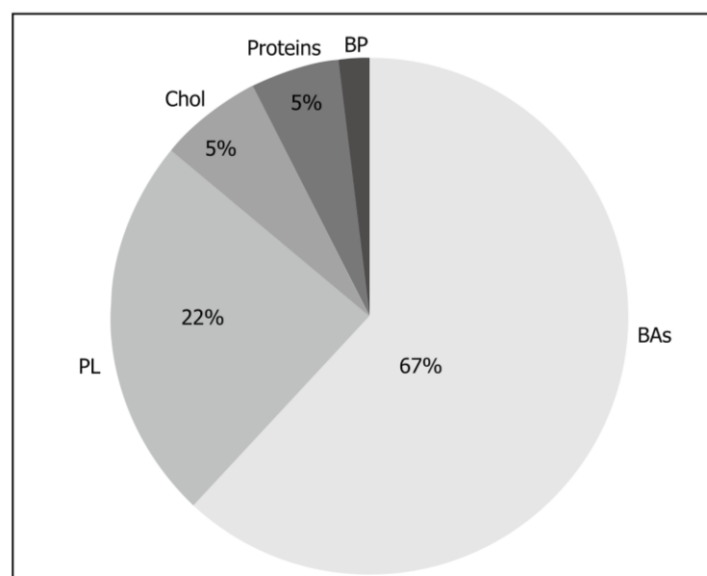
Fig.1.2.3.F1. Percent composition of different constituents of bile consisting of bile acids (**BAs**), bile pigments (**BP**), phospholipids (**PL**), cholesterol (**Chol**) and proteins. Chart reused and modified from (Esteller, 2008).

Bile is a very important exocrine product of the liver that has several functions like elimination of several exogenous materials like environmental toxins, drugs, xenobiotics, lipophilic substances, excretion of liver-derived metabolites or metabolic products such as steroid hormones, bilirubin, cholesterol (Nathanson and Boyer 1991; Boyer 2013; Trauner and Boyer 2003). The secretory function of the bile is delivery or transport of bile salts and associated lipids that help fat absorption and digestion. Bile also acts as a surfactant to emulsify lipids thus increasing their intestinal absorption. Bile has a bacteriostatic function to protect some species from any biliary or intestinal infections by excreting polymeric IgA (pIgA), inflammatory cytokines and stimulates the innate immune system in the intestine (Coleman 1987; Boyer 2013).

1.3.1. Bile acids: Structure, synthesis, transport, regulation, function

Bile acids (BAs) are predominantly found in the bile and structurally they have 2 to 4 polar groups (Chiang 2013). The main backbone of BA is a steroid nucleus which consists of 3 six-membered rings fused to a fourth five-membered ring. In humans, the simplest and most abundant bile acids found are (C24-CDCA) chenodeoxycholic acid and (CA) cholic acid (1.3.1.F1A). Bile acids are amphipathic in nature i.e. each molecule contains a hydrophobic side and a hydrophilic side (1.3.1.F1B). Therefore, in aqueous solution bile acid molecules aggregate to form clusters called 'micelles'. Structurally these micelles have a 'nonpolar or hydrophobic' group in the center covered by 'hydrophilic or polar' groups around it (1.3.1.F1C). Bile acids have a role in lipid absorption and cholesterol homeostasis (Jones et al. 2015).

*Bile acids (BA) or Bile salts (BS)

Note: The ionization state of BA or BS depends on the pH of the environment and pKa of the relevant BA/ BS. Therefore, in this work, the terms bile salts and bile acids are used interchangeably.
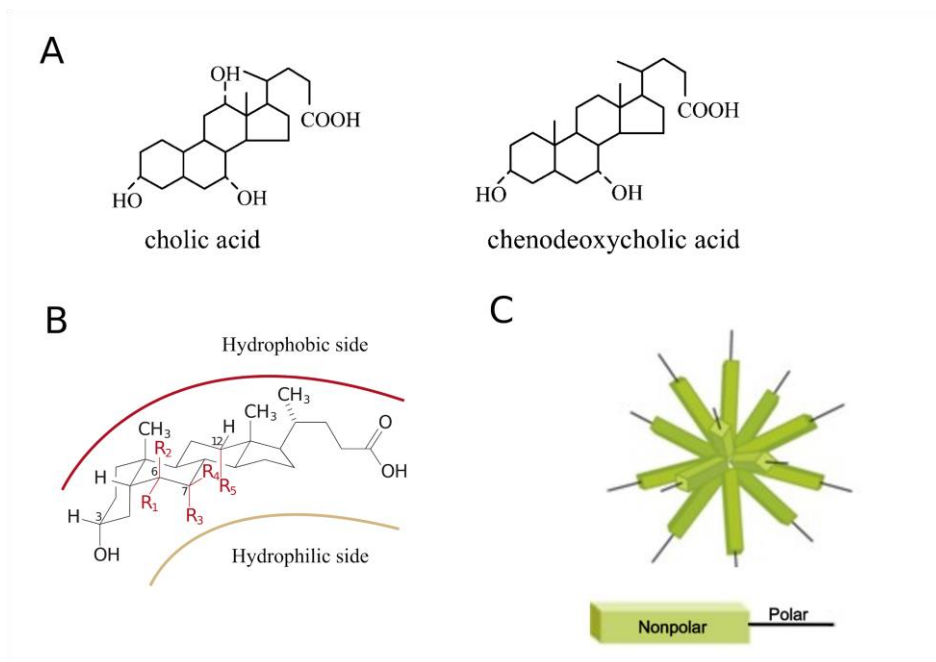
Fig.1.3.1.F1A. Chemical structure of principal primary bile acids of human: cholic acid (CA) and chenodeoxycholic acid (right). B. Hydrophobic (red line) and hydrophilic (yellow line) faces of bile acids. C. The micelle of a bile acid with a non-polar hydrophobic group (center) surrounded by polar hydrophilic groups. Image adapted and reused from (Fox 2015; Begley et al. 2005; Thomas et al. 2008).

Normally when bile is synthesized in the liver by hepatocytes, the bile acids present in the bile are in unconjugated form. They are linked with an amino acid like glycine or taurine to form conjugated bile acids which are then secreted into the bile canaliculi. The conjugation increases the solubility of bile acids and decreases bile acid toxicity (Begley et al. 2005; Reshetnyak 2013). The sodium salts of these conjugated bile acids are known as 'bile salts'. In the gallbladder, these bile salts can form mixed micelles with other lipids like phospholipids and cholesterol and help in their solubilization, reduce their cytotoxicity to the cells (Begley et al. 2005). Bile salts also play an important role in the induction of bile flow. These then are secreted into the intestinal tract to participate in the emulsification of fats, digestion of dietary lipids and absorption of nutrients (Monte et al. 2009).

There are two different types of bile acids primary bile acids that are synthesized in the liver such as chenodeoxycholic acid (CDCA) and cholic acid (CA), while secondary bile acids such as the lithocholic acid (LCA) and deoxycholic acid (DCA) that are deconjugated forms of CDCA and CA are generated from bacterial actions in the colon. Bile acids are '**hydrophilic**' or '**hydrophobic**' in nature. The hydrophobicity mainly depends on the presence and absence of the hydroxyl group at 3,6,7,12 on the steroid backbone and their orientation i.e. α or β

28

(Thomas et al. 2008). This property of bile acids being hydrophobic or hydrophilic affects their solubility. Thus, hydrophobic bile acids are more cytotoxic and less soluble (Araki et al. 2001). Bile acids can be ranked in the following order of their solubility and hydrophobicity, e.g. from hydrophobic to hydrophilic bile acids: LCA > DCA >CDCA > CA > UDCA > MCA (Thomas et al. 2008; Modica et al. 2010).

1.3.1.1. Synthesis of bile acids

Production and synthesis of bile acids from cholesterol begin in the hepatocytes. Approximately half a gram of cholesterol is converted into bile acid per day in an adult human liver (C. Thomas, Pellicciari, Pruzanski, Auwerx, & Schoonjans, 2008). The synthesis is a multi-step enzyme process which involves at least 17 distinct enzymes each having different subcellular localization such as cytosol, endoplasmic reticulum, and mitochondria (J. Y. L. Chiang, 2013). It is also a major process for cholesterol catabolism in the body (J. Y. Chiang, 1998). Some of the major steps involved in synthesis are structural changes in the cholesterol steroid ring such as hydroxylation at position C7 or C24, C25, C27 of the side chain / cleavage of the side chain, oxidation and shortening of the side chain and at last conjugation of bile acid with glycine or taurine amino groups to result in a 24-carbon bile acid (J. Y. L. Chiang, 2013; C. Thomas et al., 2008). Two different pathways are involved in the biosynthesis of bile acids. The '**classical or neutral**' pathway initiated by a microsomal enzyme cholesterol 7α-hydroxylase (**CYP7A1**) or the '**alternate or acidic**' pathway initiated by mitochondrial sterol 27-hydroxylase (**CYP27A1**) (J. Y. Chiang, 1998).

In humans, under normal conditions the primary bile acids CA and CDCA are synthesized in the liver by the classic bile acid synthesis pathway (Monte, Marin, Antelo, & Vazquez-Tato, 2009). **CYP7A1** modifies the sterol nucleus of the cholesterol followed by the oxidative cleavage of the side chain. Cholesterol is hydroxylated at the C-7 position resulting into 7α-hydroxycholesterol (1.3.1. F2). This step is the also the rate limiting step in the biosynthesis of bile acids. 7α-hydroxycholesterol is then converted to 7α-hydroxy-4 cholesten-3-one with the help of a microsomal enzyme 3β-hydroxy-Δ5-C27-steroid dehydrogenase/isomerase (**HSD3B7**).

7α-hydroxy-4 cholesten-3-one is an intermediate that can be further converted either into 7α-hydroxy-5β-cholesten-3-one with the help of 3-oxo-5β-steroid 4 dehydrogenase (**AKR1D1**) or hydroxylated to give rise to 4-cholesten- 7α,12α-diol 3-one by sterol 12-alpha hydroxylase (**CYP8B1**), which further participates in the synthesis of precursors of CDCA or CA (1.3.1.F2).

CYP8B1 also plays an important role in the determination of the ratio of CA and CDCA to be synthesized thus controlling biliary BA hydrophobicity index. A cascade of reactions followed after hydroxylation involves reduction of the oxo-group with oxidoreductases, modifications in sterol nucleus of cholesterol, side-chain oxidation and cleavage with the involvement of several other enzymes like AKR1C4, CYP27A1, SLC27A5, ACOX2 and many others (1.3.1. F2) finally results in chenodeoycholoyl-CoA and choloyl-CoA. About 75% of the bile acids are synthesized with the help of the classic pathway (de Aguiar Vallim, Tarling, & Edwards, 2013), while the acidic pathway contributes about 25% of the total bile acid synthesis. In conditions like liver disorders, when the CYP7A1 activity is low, bile acids are synthesized with the help of the '**acidic pathway**' or the '**alternative pathway'.** This pathway is initiated by the cleavage of the side chain followed by modifications of the steroid ring with the help of the mitochondrial enzyme sterol 27-hydroxylase (**CYP27A1**) (1.3.1. F2). This is the rate-limiting step in bile acid synthesis via the acidic pathway. The end product of the alternative pathway is dominantly chenodeoxycholic acid. The final step of both the classic pathway and alternate pathway is the conjugation of the chenodeoycholoyl-CoA and choloyl-CoA with amino groups glycine or taurine with the help of enzyme bile acid CoA (BAAT) to give rise to primary bile acids chenodeoxycholic acid (**CDCA**) and cholic acid (**CA**). Conjugation decreases the toxicity of bile and increases the solubility of bile acids before they are transported out of the hepatocytes (Reshetnyak, 2013). Normally bile acids are stored in the gallbladder in primary and upon specific triggers such as after a meal, the primary bile acids are absorbed by the intestine where they undergo deconjugation to give rise to secondary bile acids such as the lithocholic acid (LCA) and deoxycholic acid (DCA).The most abundant primary and secondary bile acids synthesized in humans are CDCA, CA and LCA, DCA (25% of total bile acid pool). While in species like mice and rats, the most dominant bile acid synthesized is muricholic acid, predominantly βMCA.

Secondary BAs are more cytotoxic than primary BAs and lipophilic in nature.
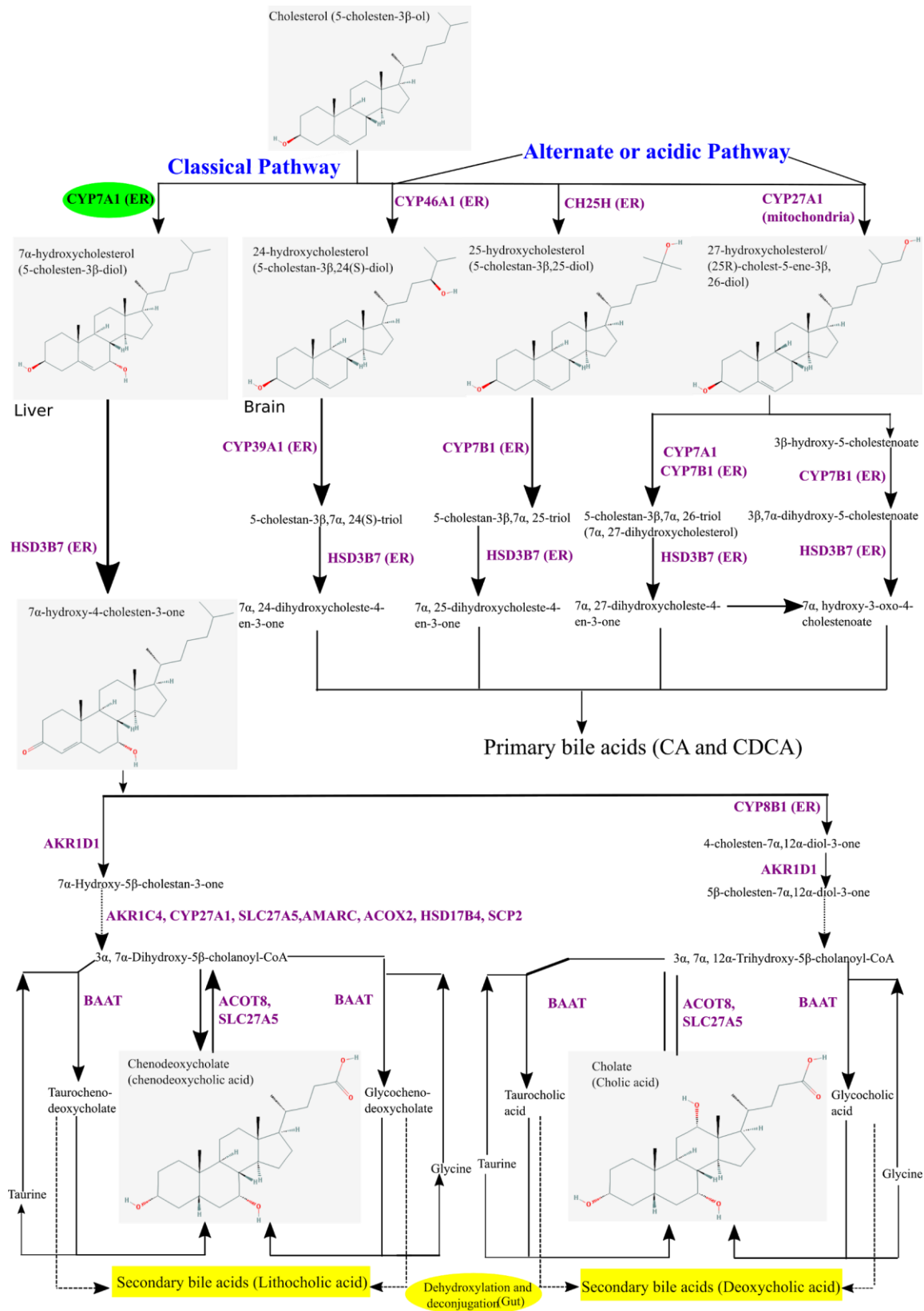
Fig.1.3.1.F2. Pathway of bile acid biosynthesis in humans: Cholesterol is converted to bile acids (BAs) with the help of two pathways: 'classical' and 'alternative' pathway. The classical pathway accounts for 75% of the total bile acid pool. The steps involved in synthesis of primary BAs cholic acid (CA) and chenodeoxycholic acid

(CDCA) which are end products of the classic pathway, include hydroxylation at position 7 of cholesterol with the help of cholesterol 7α-hydroxylase (CYP7A1), modification of the sterol ring via sterol 12α-hydroxylase (CYP8B1) that introduces a hydroxyl group into the steroid nucleus at position 12, oxidation and shortening of the side chain, cleavage of side chain and lastly conjugation with amino groups. CYP7A1 (green) is the rate-limiting enzyme in the classical pathway which regulates the synthesis of bile acids and is inhibited when bile acids are present in excess. CYP8B1 controls the ratio of CA to CDCA thus playing a role in BA pool composition. Sterol-27 hydroxylase (CYP27A1) is the first enzyme required to initiate the alternative pathway of bile acid synthesis and this step is also a rate-limiting step in the alternative synthesis of bile acid that mainly synthesizes CDCA. The end step of both pathways is the conjugation of free bile acids either with glycine (humans) or taurine (mice) with the help of BA-CoA: amino acid N-acyltransferase (BAAT). The conjugated primary bile acids are then further carried to the intestine where they are deconjugated to give rise to secondary bile acids lithocholic acid (LCA) and deoxycholic acid (DCA). Bile acid synthesis by these two pathways leads to more than 18 different BAs with different solubility index and ability to absorb lipophilic substances in the intestine and activate different signaling molecules. **Abbreviations:** ACOT8, acyl-CoA thioesterase 8; ACOX2, acyl-CoA oxidase 2; AMARC, alpha-methylacyl-CoA racemase; AKR1D1, aldo-keto reductase family member 1, member D1; AKR1C4, aldo-keto reductase family member 1, member C4; HSD3B7, hydroxy-δ-5-steroid dehydrogenase, 3β- and steroid δ-isomerase-7, HSD17B4, hydroxysteroid 17-beta dehydrogenase 4; SCP2, sterol carrier protein 2; SLC27A5, solute carrier family 27 member 5. Pathway cited from KEGG primary bile acid biosynthesis - Homo sapiens (human).

1.3.1.2. Transport of bile acids

Homoeostatic maintenance of the bile acid-pool is accomplished by recycling and re-absorption of newly synthesized bile acids. Different classes of transporter proteins are involved in the process of reabsorption and recycling of bile acids or bile salts post secretion by the liver. These transporters have important functions and they are expressed by different cell types such as hepatocytes, cholangiocytes, enterocytes and proximal tubule cells of the kidney. They participate in well-coordinated actions in order to uptake and transport of various bile acids, phospholipids, bile (1.3.1.T1).

Table.1.3.1.T1. Hepatobiliary bile acid transporters in the liver, kidney and intestine

Table.1.2.3.1.2. Hepatobiliary bile salt transporters in the liver and extrahepatic tissues		
Transporter/ gene nomenclature	**Location**	**Function**
NTCP (SLC10A1)	Hepatocyte basolateral membrane	NTCP is the primary carrier for Na^+- dependent conjugated BAs or BS uptake from portal blood or sinusoids.
OATPs (SLC21A)	Hepatocyte basolateral membrane	OATPs i.e OATPB1 and OATPB3. They are multispecific organic anion transporters for sodium- independent uptake of BS or unconjugated BA, range of cations and anions
MRP3 (ABCC3)*	Upregulated expression on basolateral membrane of hepatocytes	MRP3 is an organic solute transporter, normally weakly expressed in the liver and upregulated helps in extruding BS conjugates from the liver
MDR1 (ABCB1)*	Hepatocyte apical or canalicular membrane	ATP-dependent excretion of various organic cations, xenobiotics, cytotoxins into the bile
MDR3 (ABCB4)*	Hepatocyte apical or canalicular membrane	ATP-dependent translocation of phosphatidylcholine from inner to outer leaflet of membrane bilayer; the phospholipid export pump
MRP2 (ABCC2)*	Hepatocyte apical or canalicular membrane	Mediates ATP-dependent multispecific organic-anion transport e.g.bilirubin diglucuronide,sulfates,glutathione conjugates into the bile; major determinant of BS-independent bile flow by GSH transport
BSEP (SPGP) (ABCB11)	Hepatocyte apical or canalicular membrane	ATP-dependent transport of monovalent BS into bile; stimulates BS dependent bile flow
F1C1 (ATP8B1)	Hepatocyte apical or canalicular membrane	Potential aminophospholipid translocating ATPase (unknown role) gene defect in Byler's disease
AE2 (SLC4A2)	Hepatocyte apical or canalicular membrane	Acid loader, excretes bicarbonate into bile and stimulates BS-indenpendent bile flow
ISBT (ABST) (SLC10A2)	Cholangiocyte apical membrane	To remove BS from the bile;facilitate bile salt removal during cholestasis; identical gene product to ileal transporter
CFTR (ABCC7)	Cholangiocyte apical membrane	Chloride channel which facilitates chloride entry into the bile and its exchange with HCO_3^-, anions; mutations in CFTR result in cholestasis
AE2 (SLC4A2)	Cholangiocyte apical membrane	Facilitates bicarbonate secretion into bile and contributes to bile flow independent of BS
MRP3 (ABCC3)*	Cholangiocyte baso-lateral membrane	May be a major transporter for returning or efflux of BS to portal ciruclation from bile during obstructive cholestasis
OATP 3 (slc21a7)	Ileal enterocyte apical membrane	Sodium-independent uptake of bile salts from the intestinal lumen
ISBT (ABST) (SLC10A2)	Ileal enterocyte apical membrane	Primary carrier for sodium-dependent BS uptake from intestine by ileum; critical determinant of enterohepatic circulation of BS
MRP3 (ABCC3)*	Ileal enterocyte baso-lateral membrane and colon	May be a a major transporter for returning BS to portal circulation
ISBT (ABST) (SLC10A2)	Apical membrane of the proximal tubule cells of the kidney	Influx of BS from the glomerular filtrate; downregulated in choelstasis to facilitate BS excretion in urine; identical gene product to the ileal transporter
MRP2 (ABCC2)*	Apical membrane of the proximal tubule cells of the kidney	ATP-dependent multispecific organic anion transporter for divalent organic anion conjugates into urine like sulfates,glutathione conjugates; facilitate renal excretion of BS conjugates in cholestasis
OST α/β	Basolateral membrane of the proximal tubule cells of the kidney	Exports BAs

Abbreviations: ABC, ATP-binding cassette; ABST, apical Na^+-dependent bile salt transporter; AE2, chloride-bicarbonate anion exchanger; BSEP, bile salt export pump or canalicular bile salt export pump/sister of P-glycoprotein; CFTR, cystic fibrosis transmembrane regulator; F1C1, familial intrahepatic cholestasis-1; ISBT, ileal sodium dependent bile salt transporter; MDR, multidrug resistance-1,3 P-glycoprotein/ phospholipid transporter; MRP2, multidrug resistance-associated protein-2/ canalicular conjugate export pump; MRP3,

Bile acids are then transported and recirculated further with the help of two pathways. Firstly, the bile acids that are secreted into the bile canaliculus are transported and get accumulated in the bile ducts that are lined by cholangiocytes that can modify bile. Bile acids are then stored in the gallbladder and are secreted to the intestine, where they undergo further modifications by intestinal bacterial flora. Almost 90-95% of bile acids are reabsorbed by the terminal ileum (de Aguiar Vallim et al. 2013), recycled and transported back to the liver via the hepatic portal vein establishing the 'enterohepatic circulation'. Secondly, BAs secreted in the bile ducts are reabsorbed in the cholangiocytes and recycled back to the hepatocytes via blood or interstitial fluid, thereby establishing a **'cholehepatic shunt'** (1.3.1.F3).
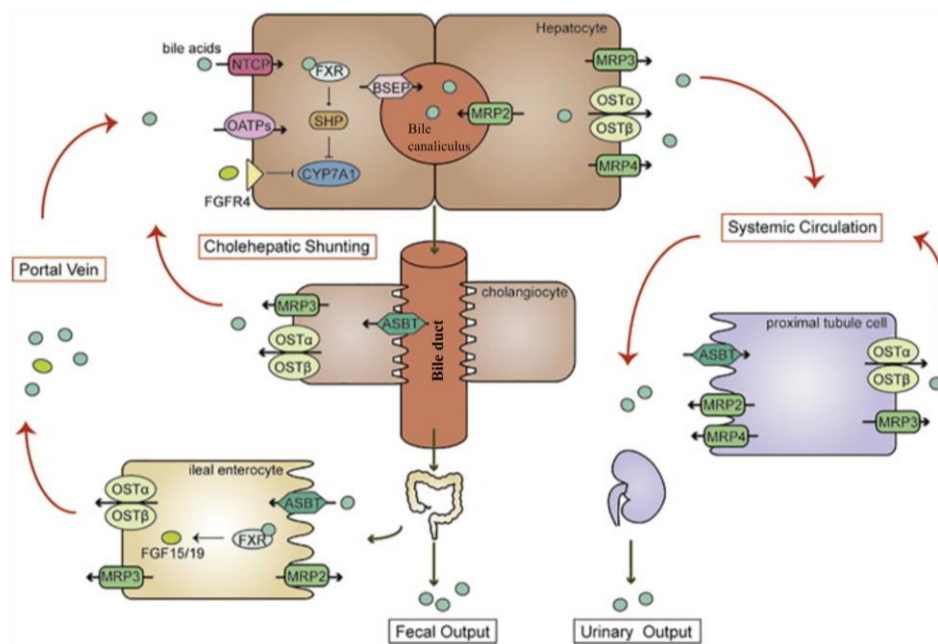
Fig.1.3.1.F3. **Overview of bile acid circulation and transport in the liver, gut and the kidney.** Primary bile acids (green circles) are synthesized and conjugated in the liver by the hepatocytes. Hepatocytes transfer these bile acids (BAs) into the bile canaliculi linked to the bile duct with help the of 2 transporter proteins BSEP (bile salt export pump) and MRP2 (multidrug resistance-associated protein 2). Transport proteins like MRP3 (multidrug resistance-associated protein 3), MRP4 (multidrug resistance-associated protein 4) and OST α/β (organic solute transporter α/β) are involved in transporting BAs by an alternative exit route into the systemic circulation. BAs in the bile duct and the gut are transported back to the liver with the help of cholehepatic shunting and enterohepatic circulation controlled by transporter protein ASBT (apical sodium dependent bile acid transporter), OST α/β, MRP3, NTCP (Na+-taurocholate cotransporting polypeptide) and OATP (organic anion-transporting

polypeptides) located on the membrane of enterocytes and cholangiocytes. The same transporter families are also located on the proximal tubule cells. MRP2 and MRP4 are involved in the secretion of BAs into the intestine and urine. FXR and FGF15/19 play a central role in negative feedback regulation of bile acids and their synthesis (see 1.3.1.3. Regulation of bile acids). Image adapted and modified from (Y. Li, Tang, Leung, Gershwin, & Ma, 2017)**.**

Bile acids entering the hepatocytes via enterohepatic circulation are conjugated in the hepatocytes and are then secreted into the bile canaliculi with the help of the bile salt export pump (BSEP) and multidrug resistance-associated protein 2 (MRP2) located on the apical membrane of the hepatocytes. These conjugated bile acids also are known as bile salts exiting the liver are stored in the gallbladder. Upon contractions, in the gallbladder, they are released into the intestine. In the intestine, these bile salts are both passively and actively reabsorbed (Reshetnyak 2013).

Some of the unconjugated bile acids get absorbed by the upper intestine by passive diffusion, while the conjugated bile acids or bile salts require special membrane transporters an apical sodium-dependent bile acid transporter (ASBT) located on the brush border apical membrane. ASBT influxes the bile acids or reabsorbed them actively into the enterocytes of the distal ileum (Jones et al. 2015; Wahlström et al. 2016; Schadt et al. 2016). Intestinal bile acids trans diffuse across the enterocytes and reach to the basolateral membrane. From here they are transported into the portal blood circulation with the help of a basolateral organic solute transporter α and β heterodimer (OSTα/β). The portal blood flows through the sinusoids which carry these bile acids. Bile acids are finally taken up by hepatocytes with the help of Na+-dependent taurocholate cotransport peptide (NTCP) or via Na+-independent organic anion-transporting polypeptides (OATP) located on the basolateral surface of the hepatocytes (1.3.1.F3). Thus, the bile acids finally reach the hepatocytes and are ready to be excreted into the bile again and initiate another enterohepatic circulation cycle. This cycle occurs at least 4-12 times a day in humans and recovers about 2-4 gm of the bile acids pool synthesized in the liver.

Some of the unabsorbed unconjugated bile acids in the bile canaliculi or ductular bile are recirculated and are taken up immediately by the cholangiocytes lining the bile ducts with the help of apical membrane transporter (ASBT) before they reach the gallbladder (Trauner and Boyer 2003). These BAs are conjugated, modified and then returned to the hepatocytes via the

peribiliary plexus by a 'cholehepatic shunt pathway' (Schadt et al. 2016) by transporters such as MRP3 and OSTα/β located on the basolateral membrane (1.3.1.F3). When in excess, such as in cholestasis, the BAs in the hepatocytes spill over into the sinusoidal blood and are reabsorbed while passing through the renal tubules of the kidney, circulated back to the liver by the third type of cycling called 'systemic circulation'. Any further bile acids discarded such as lost via feces (0.5gm/day) are recovered by the de novo synthesis of bile acids in the liver.

1.3.1.3. Regulation of bile acid synthesis and transport

The accumulation of bile acids in the liver due to any interruption in their transport or enterohepatic cycling causes deleterious effects that lead to a complex pathological condition described as cholestasis (Anwer 2004). To prevent this, the bile acid pool generated in the liver is constantly under regulation such that normal intracellular toxicity thresholds are never exceeded. In tissues that participate in enterohepatic circulation (section.1.3.1.2. Transport of bile acids), the amount of bile acids produced, and transport of bile acids is tightly controlled through the orchestrated activity of several transcription factors, membrane receptors that have high specificity to bile acids and oxysterols, and finally enzymes that are involved in their synthesis.

Bile acid synthesis is dominantly regulated by themselves. This is a negative feedback mechanism by which bile acids returning to the liver via the portal vein during enterohepatic recycling can regulate CY7A1 activity and up or down regulate BA synthesis. CDCA and CA can down-regulate BA synthesis while UDCA can increase BA synthesis. Thus, any interruption in the enterohepatic recycling such as biliary diversion by fistula or feeding of anion exchange resins that can bind the intestinal bile acids can cause up-regulation of CYP7A1 activity. Increase in CYP7A1 activity affects the activity of HMG-CoA reductase (the enzyme that is involved in the conversion of acetyl-CoA to cholesterol).

One level of control on the synthesis of bile acids is imposed by the availability of cholesterol and its effect on CYP7A1 activity. Cholesterol is the precursor of bile acids and its levels are influenced by the availability of nutrients. High cholesterol levels stimulate bile acid synthesis by activating the nuclear receptor LXRα that requires oxysterol binding for its activation (Chiang 2013). LXRα induces transcription of Cyp7a1, the rate-limiting enzyme for bile acid synthesis. Similarly, insulin-regulated bile acid synthesis involves regulation of de novo

synthesis of cholesterol in the liver, which is controlled by genes such as steroid response element binding proteins i.e. SREBP-1c and SREBP-2 (1.3.1.3. F1). SREBP-2 is dissociated from insulin-induced gene-1 (Insig-1) and (Insig-2) in the endoplasmic reticulum when the intracellular cholesterol or oxysterol levels are decreased. Insulin may also inhibit bile acid synthesis through SREBP-mediated downregulation of CYP7A1. Finally, CYP7A1 activity shows circadian patterns, and therefore bile acid synthesis is also subject to circadian regulation.
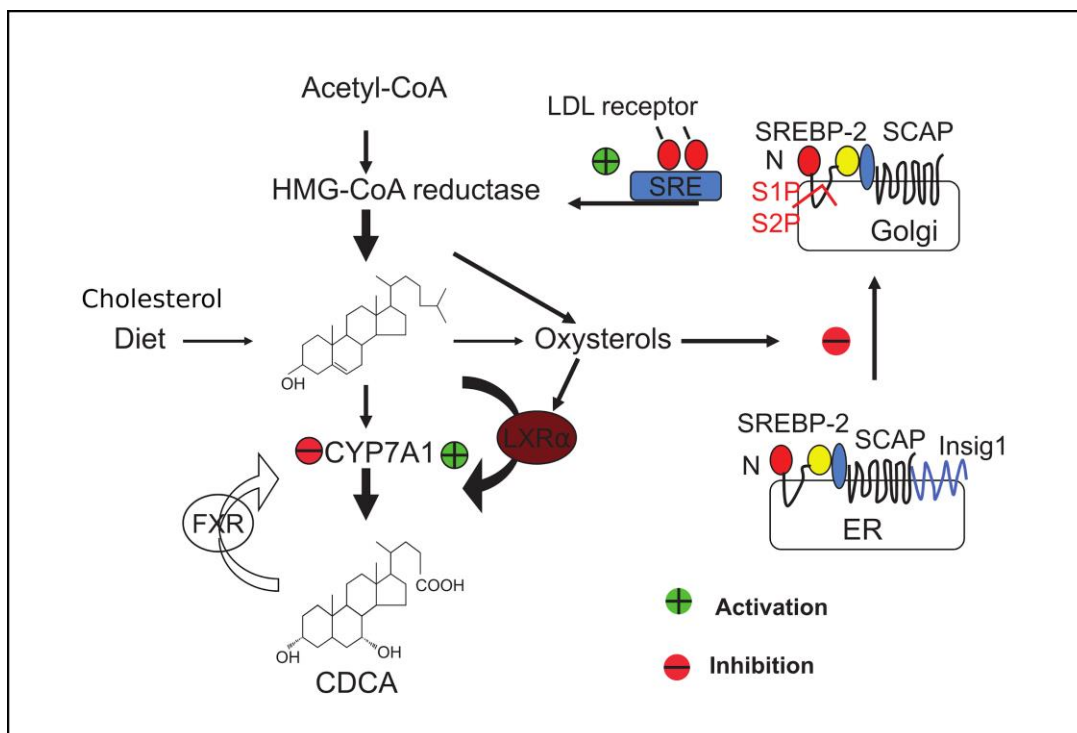
Fig.1.3.1.3.F1. Regulation of cholesterol homeostasis in hepatocytes via bile acid synthesis. Cholesterol homeostasis is maintained by dietary intake of cholesterol, de novo synthesis from acetyl-CoA and conversion of cholesterol to bile acids. When intracellular cholesterol/oxysterol levels are high, LXRα in mice (or HNF4α, PPARα in humans) induces CYP7A1 gene transcription to stimulate bile acid synthesis. Simultaneously, HMG-CoA reductase activity is repressed via retention of SREBP-2 in the ER. When intracellular levels of cholesterol/oxysterol are low, SREBP-2 cleavage allows its transport to the Golgi apparatus eventually allowing its interaction with SRE. This enhances HMG-CoA reductase (and all cholesterogenic gene) expression, thus stimulating cholesterol biosynthesis.

While the above mechanisms influence the bile acid pool in an organism indirectly, a far more potent and direct regulatory mechanism is mediated by the nuclear hormone receptor FXR and the cytokines FGF15/19. These factors are the central players in two distinct, but linked,

negative feedback loops that control the intracellular and systemic bile acid levels respectively. The FXR/SHP signaling pathway exerts intracellular transcriptional control on the bile acid biosynthetic machinery in the liver. On the other hand, the FGF15/19 signaling pathway establishes inter-organ communication between the intestine and liver, serving to regulate total bile acid pools in the intestinal lumen and serum and determine if intracellular bile acid biosynthetic pathways should be active or suppressed.

Dysregulation of these feedback loops is a prominent cause of the pathological manifestations of the cholestatic disease.

1.3.1.3.1. Nuclear receptors and their role in bile acid synthesis: FXR Intracellular control axis

Bile acids are known to be able to enter hepatocytes nucleus and accumulate as observed in bile acid-fed mice (Kulkarni, Soroka, Hagey, & Boyer, 2016). Thus, it is very important to have intracellular checks for controlling and regulating the bile acids and in turn their cytotoxicity. Different types of nuclear receptors such as farnesoid X receptor (FXR); short heterodimer partner (SHP, NR0B2); liver receptor homolog-1 (LRH-1, NR5A2) ; G protein-coupled receptor (TGR5); fibroblast growth factor-19 and its receptor FGFR4 are involved in the regulation of bile acid synthesis, CYP7A1 activity and cholesterol homeostasis via several complex mechanisms.

Farnesoid X-Receptor

Farnesoid X receptor (FXR, NR1H4) is a ligand-activated nuclear receptor which belongs to the adopted member of the nuclear receptors superfamily (NRs) (Pellicciari, Costantino, & Fiorucci, 2005). It was originally isolated from rat cDNA library and named after its ability to interact very weakly with farnesol (Sinal et al., 2000). It is a bile acid sensor located on chromosome 12q23.1 in humans and is highly expressed in the liver, intestine, kidney and adrenal glands (A. M. Thomas et al., 2010). FXR gene is highly conserved from organisms like fish to mammals (mice, rodents, humans) and the exists in two forms i.e. FXRα and FXRβ (Fiorucci & Baldelli, 2009; Lee, Lee, Hubbert, Edwards, & Zhang, 2006).

FXR possesses the basic molecular structure that is common to the all nuclear receptors. The basic structure of nuclear receptors can be characterized into 5 domains A/B, C, D, E, F (1.3.1.3.1.F1.A).
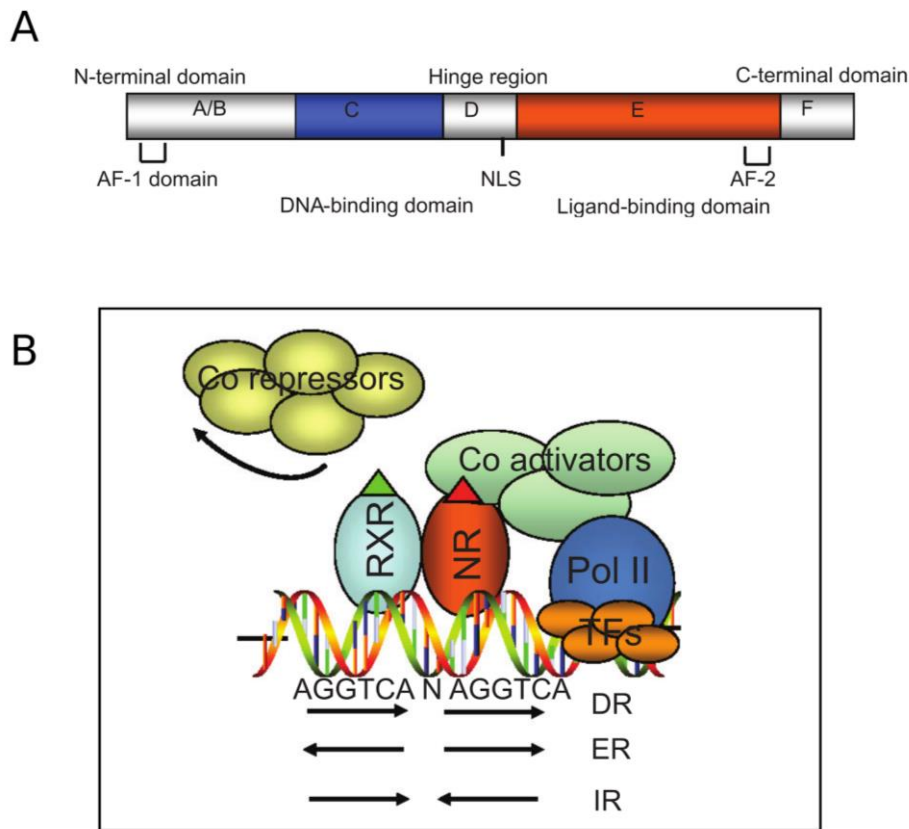
Fig.1.3.1.3.1. F1. **Nuclear receptors**. A. Domain structure of the basic nuclear receptor with 5 domains A/B, C, D, E, F. The N-terminal domain is A/B while the C-terminal domain includes domains E/F. The DNA-binding domain 'C' links the domain is A/B to 'D' which is the hinge region. B. The putative nuclear receptor response element binding sequences, arranged in direct repeat, everted repeat, and an inverted repeat, are shown. Ligand-activated receptors recruit coactivators to replace corepressors, which results in transactivation of target gene expression. Abbreviations: AF-1, activation function-1. AF-2, activation function-2; NLS, nuclear localization sequence. Image adapted and reused from (T. Li & Chiang, 2014).

On the N-terminal of the nuclear receptors, domains A and B are located. These domains are regulatory domains of the nuclear receptors that contain activation function-1 domain (AF-1) that is ligand-independent, and these domains are the most variable region in the receptors. The central domain C is the DNA-binding domain (DBD), composed of a conserved region with two Zn^{2+} fingers. The DBD is responsible for binding to unique hormone response elements (HREs) with two tandem AGGTCA repeating sequences spaced by 1-5 nucleotides arranged in direct, everted and inverted repeat. The D or hinge domain is a flexible domain and has a nuclear localization sequence (NLS). These regions connect the domain C i.e. (DBD) to the

domain E which is the ligand-binding domain (LBD) and controls intracellular trafficking. Domain E is conserved in nuclear receptors within the same subfamily. This domain also consists of coactivator interaction motifs LXXLs and plays a role in transactivation (AF-2) that regulates gene expression. The C-terminal part of the nuclear receptor is highly variable in sequence between different nuclear receptors and encloses the LBD, that has a property of hormone or ligand recognition.

A single gene of FXR in humans, primates, and mice encodes for 4 isoforms (FXRα1, FXRα2, FXRα3, FXRα4) that result from the use of different promoters and alternative splicing of the gene (1.3.1.3.1.F1.A) (Fiorucci, Mencarelli, Distrutti, & Zampella, 2012; Sinal et al., 2000). FXR binds its HRE IR-1 as a heterodimer with another nuclear receptor, retinoid X receptor (RXR) and in the absence of a ligand (Fig.1.3.1.3.1.F2.C), remains inactive due to binding with the corepressors such as Ku, GPS2, and NCoR (Loinder & Söderström, 2003). The confluence of nuclear localization, DNA-binding and the ability to recruit RNA polymerase complexes confers transcriptional regulator activity onto FXR (Fig.1.3.1.3.1.F2.C).
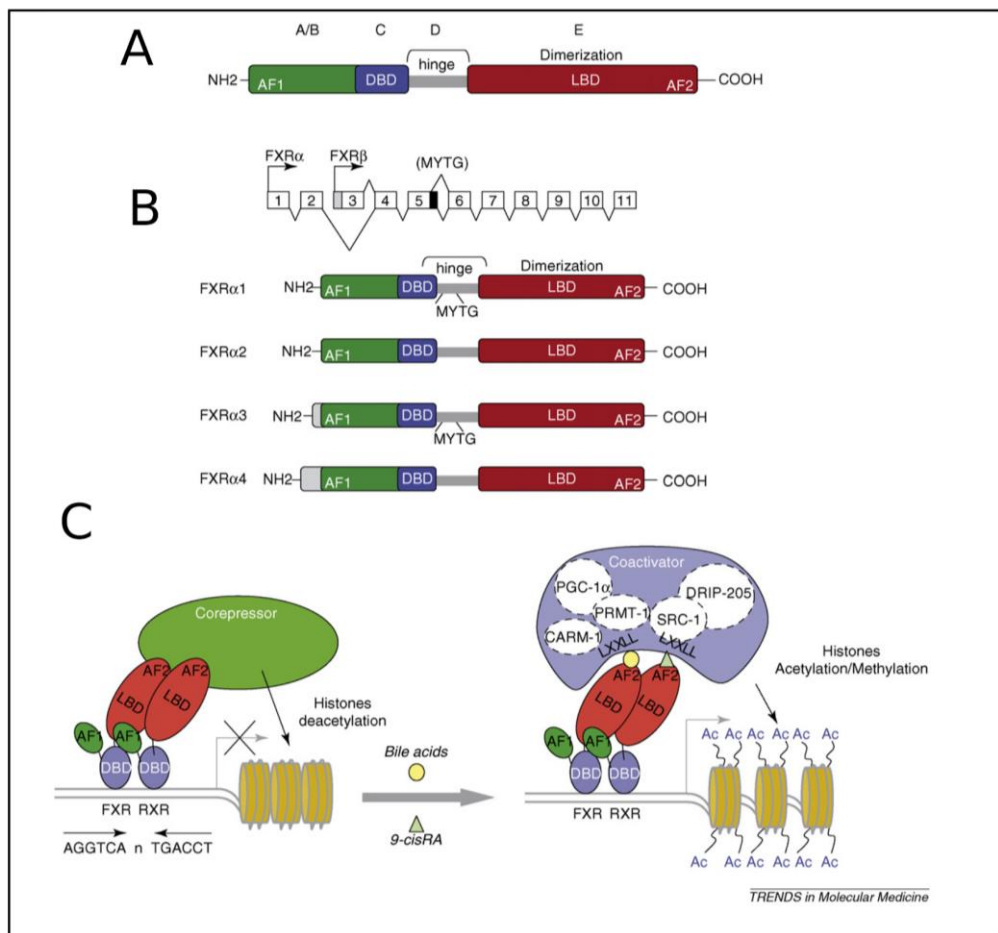
Fig.1.3.1.3.1. F2. **Farnesoid X receptor molecular structure, isoforms and binding sites**. A. The molecular structure of FXR, FXRα isoforms, and its signaling activation. A. Basic structure of nuclear hormone receptor

FXR with several functional domains like variable NH2 (N-terminal region A/B) that contains ligand-independent AF-1 transactivation domain, a central DNA binding domain (DBD) or region C which recognizes specific DNA sequences, region D which is highly variable hinge region that links DBD to region E that contains the ligand-binding domain (LBD), dimerization surface and ligand-dependent AF-2 in the region E close to at the C-terminal COOH. B. Schematic representation of the exon-intron organization of FXRα gene and its related isoforms. FXRα isoforms are generated by use of promoter (arrows) and alternative splicing of the gene (linked exons). FXRα1 and α3 have an insertion of 4 amino acids (MYTG) which is a result of alternative splicing of the 12-base pair at the 30th end of exon 5 in the region D of the FXR. C. FXR activation and repression by coactivator/corepressor complex. When ligands (BAs) are absent the FXR/RXR heterodimer is associated with corepressor complex which recruits histone-deacetylase activity that leads to compaction of chromatin and repression of transcription. Receptor activation results in the release of the corepressor complex and AF-2-dependent recruitment of coactivator complex which contains at least p160 co-activator (such as SRC-1). These proteins possess histone-acetyltransferase activity that allows chromatin decompaction and gene activation. Multiple protein-protein interactions exist among the FXR and other coactivators like protein arginine R methyltransferase-1 (PRMT-1), coactivator-associated arginine methyltransferase-1 (CARM-1), PPAR-gamma coactivator-1a (PGC-1α) and vitamin-D-receptor-interacting protein-205 (DRIP-205) which induce histone methylation.

The activation of FXR is promulgated through its binding of bile acids via its LBD. Hydrophobic BAs like CDCA are potent ligands of FXR with an EC_{50} of ~ 10 µmol/L. FXR is also activated by to a lesser extent by free bile acids, conjugated bile acids, e.g. LCA, DCA, CA but not activated by hydrophilic bile acids such as MCA or UDCA (J. Y. L. Chiang, 2013). Indeed, certain bile acids such as UDCA, Tauro-β-MCA function as antagonists of FXR, presumably occupying the LBD but preventing the conformational changes of the AF-1/2 regions that lead to the active heterodimeric state of the protein.

Due to the importance of FXR in bile acid homeostasis, a number of synthetic FXR agonists and antagonists have been identified. The most commonly used synthetic FXR agonist is GW4064 (EC_{50} ~ 0.059µmolar) (Fiorucci et al., 2012). The most commonly used synthetic antagonists include DY268 and the naturally occurring plant steroid guggulsterone (Fiorucci et al., 2012; Meng et al., 2015,).

The molecular characteristics of FXR hint at the reasons for the importance of FXR in the regulation of bile acid synthesis and transport. As a protein that controls transcription of various genes in response to the concentration of bile acids, FXR remains the only known intracellular sensor of bile acid concentrations. Essentially, FXR forms the primary input in a cell's response

to changing bile acid levels. It's role in bile acid homeostasis is described in detail in the following sections.

FXR activation and Bile acid synthesis

One of the target genes of FXR transcriptional regulation is the nuclear receptor small heterodimer partner (SHP). FXR activation due to bile-acid binding induces SHP expression, which in turn interacts with the repressed transcriptional activator liver-related homolog-1 (LRH-1). LRH-1 binds to the CYP7A1 gene promoter and stops the transcription of the CYP7A1 in the liver (Goodwin et al., 2000) (Fig.1.2.3.1.2). As described previously, the CYP7A1 enzyme is the rate-limiting step in bile acid biosynthesis. Thus, this set of protein interactions constitutes a negative feedback loop within the cell that regulates the synthesis of bile acids. Increased bile acid levels lead to increased FXR-binding/activation, which eventually translates to reduced CYP7A1 activity and attenuation of bile acid synthesis. The bile acid levels in the cell are therefore regulated such that toxic thresholds are not exceeded.

Effect of FXR activity on Bile acid transport

FXR not only controls the synthesis of bile acids but also modulates the expression of membrane transporters for bile acids. In general, when intracellular bile acid levels are high, the effect of FXR is to modify transporter activities so as to facilitate the evacuation of bile acids from the cell.

In the liver, enhanced FXR activity due to high bile acid levels *increases* expression the apical membrane efflux transporters such as BSEP, MRP2 which transport conjugate bile acids out of the cell and into the canalicular lumen to be excreted as bile. Concurrently, FXR activity also *represses* (via SHP) the basolateral membrane uptake transporters NTCP/OATP, ensuring that in no additional bile acids are imported from the blood into the hepatocyte cytoplasm if an excess already exists. Under conditions of chronically high bile acid levels in the hepatocyte cytoplasm, FXR eventually induces the expression of basolateral efflux transporters MRP3 and OST α/β to further aid in the removal of bile acids from the cell to the blood. In the intestine, kidney, and cholangiocytes, activation of FXR due to high bile acids represses the apical membrane uptake transporter ASBT and induces the basolateral efflux transporters OST α/β

and MRP3. Thus, FXR facilitates the removal of bile acids from the intracellular compartments of all tissues and their transfer to blood circulation.

The combined effect of reducing bile acid synthesis and their transport to blood is thought to be protective against bile acid toxicity. It is presumed that high levels of bile acids in the cytoplasm is more detrimental than their high levels in the blood. For this reason, FXR is thought to play a protective role in pathologies associated with high bile acid levels. The critical role of FXR in the coordination of bile acid synthesis, biliary bile acid secretion, intestinal bile acid reabsorption and secretion, and bile acid uptake into hepatocytes, has invoked substantial interest in the therapeutic modulation of FXR in liver disease (de Aguiar Vallim et al., 2015; Fiorucci et al., 2012; Guo et al., 2016).

1.3.1.3.2. The FGF15/19 'Gut-Liver' axis

While FXR represents the intracellular control node for bile acid biosynthesis, a second control mechanism operates at the level of the two tissues that are regularly exposed to bile acids and participate in their enterohepatic circulation (section 1.3.1.). Bile acid homeostasis is established through communication between the liver as bile-producer and the intestine as bile-absorber, mediated by members of the FGF cytokine family. Bile is released into the intestine to facilitate digestion, and the constituent bile acids are absorbed by intestinal cells. High levels of bile acids in intestinal cells induce the production and secretion of FGF15/19 from these cells into the blood. In an example of evolutionary elegance, this is achieved because FGF15/19 are themselves target genes of none other than FXR. High bile acid levels in intestinal cells activate FXR in these cells, which induces the transcription of FGF15/19 (Kliewer & Mangelsdorf, 2015). These growth factors are transported to the liver via portal vein blood and bind to the membrane-bound heterodimeric core-receptor (β-klotho/FGF4) (1.3.1. F3). FGF15/19 bound to the FGFR4/b-Klotho complex signals the cascade of reactions inside the hepatocytes involving JNK and ERK activation, and subsequent c-Fos induction which eventually represses CYP7A1 expression. Once again, the repression of CYP7A1 leads to the reduction of bile acid synthesis. Thus, FGF15/19 act as endocrine hormones, that exert a negative feedback regulation of the synthesis of bile acids on a systemic level - if the intestine is sensing high bile acid levels, there is no further requirement to synthesize them.

1.3.2. Functions of bile acids

In addition to the autoregulatory and hormonal functions (Kliewer & Mangelsdorf, 2015; C. Thomas et al., 2008), the bile acids also play important role in several other physiological processes such as cholesterol homeostasis, inflammation, lipid metabolism, glucose, and energy metabolism (J. Y. L. Chiang, 2013). Bile acids also help in intestinal calcium absorption, regulate pancreatic enzyme secretion and cytokinin release. Thus, bile acids function as not only regulators of their own synthesis but also are general metabolic controllers.

1.4. Toxicity of bile acids

Depending on the concentration of the bile acids, they have the potential to disrupt the cellular structure, tissue architecture and affect the function of the liver. This property of bile acids forms the basis of a variety of so-called '**cholestatic liver diseases'**, with significant clinical implications.

1.4.1. Clinical occurrence of Cholestasis

Cholestasis is defined as a decrease in bile flow due to impaired secretion of bile by the hepatocytes or due to obstruction in the flow of bile via intra or extra-hepatic ducts due to blockage. Cholestasis can be a result of genetic disorders, drug-induced toxicity, intestinal infections or during pregnancy, mechanical aberrations or physical obstructions like tumors or stones. Cholestasis leads to the accumulation of excess bile acids in the liver. When bile acids in the liver exceed the normal levels due to an impairment in the bile flow through the biliary tree, it is termed **extrahepatic cholestasis.** Accumulation of bile acids may also occur within the hepatocytes due to disruption of the bile acid transporters. This is termed as **intrahepatic cholestasis**.

Extrahepatic cholestasis occurs due to biliary tract abnormalities such as blockage of bile flow in the functional conduits 'bile ducts' of the liver as observed in primary biliary cholangitis (PBC), the formation of tumors or gallstones in the duct such as in chronic pancreatitis (Krishnamurthy & Krishnamurthy, 2000). Intrahepatic cholestasis occurs due to the

accumulation of excess bile acids in the hepatocytes due to the loss of transporters in hepatic tissue (hepatocyte, cholangiocytes) as observed in familial intrahepatic cholestasis.

Depending on the duration and concentration of exposure to bile acids, cholestasis can be classified as '**acute**' and '**chronic**' (Verhaag et al., 2016). The pathological feature of acute cholestasis is increased serum BAs, inflammation and oxidative damage due to reactive oxygen species (ROS) and lastly hepatocyte death. Chronic cholestasis is characterized by decreasing levels of inflammatory cytokines, ROS over time and constant unchanged high levels of serum and hepatic bile acids.

These clinical manifestations indicate a chronic pathological diseased state that is accompanied by large changes in the tissue architecture of the liver and alterations of hepatocyte function.

1.4.2. Tissue Manifestations of Cholestasis

In the liver parenchyma, the acute cholestatic liver disease manifests as large necrotic patches of hepatocytes, that subsequently accumulate bile acids. These 'bile infarcts' are repeatedly resolved due to the regenerative capacity of the liver. Therefore, while bile infarcts may not be visible in histopathology of chronic cholestasis. The repeated formation of bile infarcts exacerbates the development of peri cellular fibrosis and finally cirrhosis. Besides the formation of the bile infarcts, the most conspicuous change observed in the liver architecture is that of the bile ducts. Bile ducts form a complex network of functional conduits in the liver (1.2. Microanatomy of the liver). In response to cholestasis, the cells that line these conduits (cholangiocytes) undergo a highly specific reaction called the '**ductular reaction**' that does not occur spontaneously under normal conditions (Jörs et al., 2015).

A ductular reaction is characterized by cell proliferation of cholangiocytes that begins instantly after cholestatic injury and reaches a peak at 1-day post-injury (Shannon S. Glaser a,b,∗, Paolo Onorif , Candace Wise b, Fuguan Yang b,d, Marco Marzioni e, Domenico Alvarog, Antonio Franchitto h, Romina Mancinelli h, Gianfranco Alpini a,b,c, Md. Kamruzzaman Munshi b, Eugenio Gaudio h,∗∗, 2010). Marked inflammation occurs due to release of various cytokines such Il-3/6/8. An especially conspicuous clinical finding is the distension and enlargement of the large bile ducts as observed in CT or sonographic examination. Histopathological

investigation shows a significant increase in the number of duct lumens per periportal field surrounded by fibroblasts and extracellular matrix depositions. All these changes serve as a diagnostic marker for cholestatic liver disease in clinical examinations. Increase in serum markers like ALT, AST and bile acid levels are biochemical changes which occur as a response to ductular reactions.

The formation of necrotic areas and release of cytokines trigger a simultaneous immune system response involving the activation and recruitment of blood-derived immune cells along with activation of tissue-resident cells such as Kupffer cells and Stellate cells. The immune response associated with cholestasis is typically a secondary event to the ductular reaction and infarct formation and therefore beyond the scope of this work. The changes at the tissue level associated with cholestasis are summarized below (1.4.2.F1).
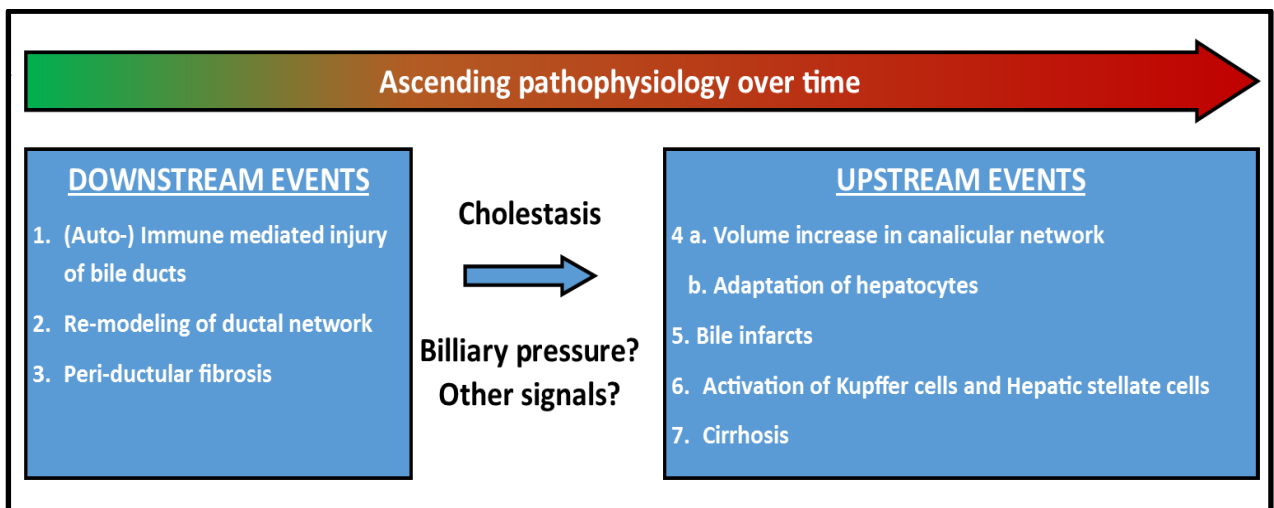
Fig.1.4.2. F1. Downstream and upstream events induced by bile acids. Image adapted from (Jansen et al., 2017)

1.4.3. Cellular manifestations of cholestasis.

Each of the alterations in the tissue architecture can be traced to specific cellular changes or responses. Depending on the concentrations and exposure period, bile acids (BAs) have different interactions with various cellular components (1.4.F1).
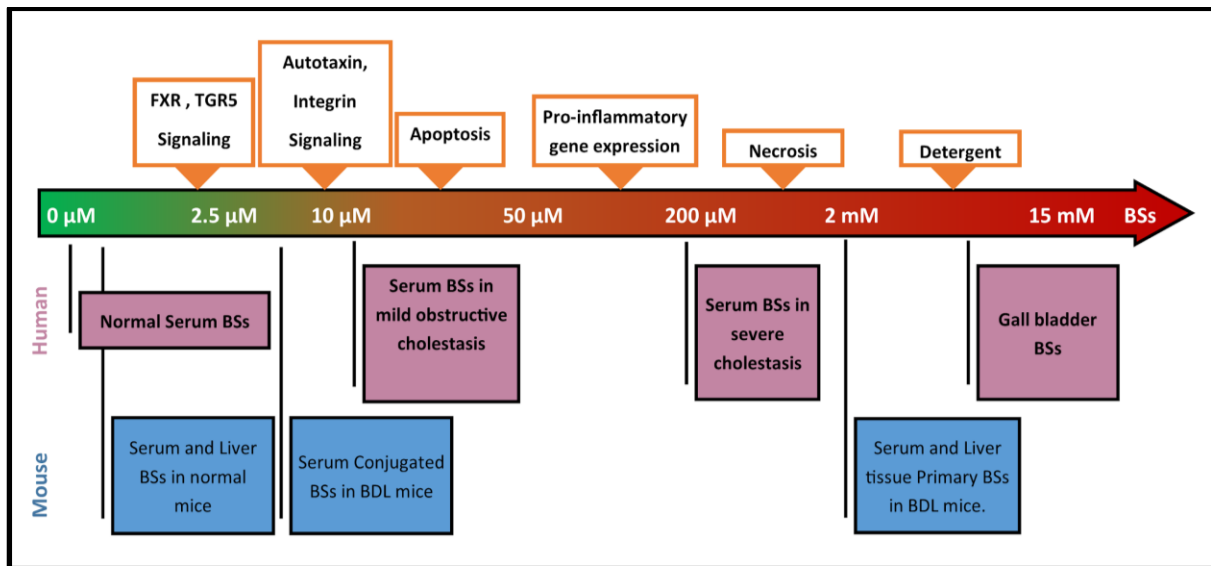
Fig.1.4.F1. Concentration-dependent actions of bile salts (BSs) or bile acids (BAs). Toxicity spectrum (green-red) of bile salts and their levels found in humans and mice. Image reused and adapted from (Jansen et al., 2017).

As previously described, under physiological conditions bile acids already interact with nuclear receptor FXR at concentrations up to 2.5 µM. At higher concentrations of BAs, a wide variety of non-physiological interactions becomes possible. These interactions are postulated to be responsible for the cytotoxic effects of bile acids at high concentrations. In vitro studies indicate that bile salts or bile acid at concentrations of 15-25 µM interact with autotaxin and integrins to influence the cytoskeletal structure and dynamics. At concentrations between 10 to 50 µM, they can induce apoptosis either by causing loss of mitochondrial membrane potential or inductions of TNF-α (Palmeira & Rolo, 2004; Yang et al., 2010). Bile acids at concentrations of 50- 200 µM activate proinflammatory gene expression by inhibiting IL-6 signaling. Necrotic cell death is induced when the concentration of bile acids exceeds 200 µM which is thought to be mediated by RIPK1 and RIPK3 signaling (Chen Long, 2014). Bile acids behave as detergents at concentrations higher than 2 mM and may dissolve and disrupt multiple cellular and tissue membranes at such concentrations (Attili, Angelico, Cantafora, Alvaro, & Capocaccia, 1986). However, bile acids can exist physiologically at these concentrations only in the gallbladder.

The parenchymal tissue of the liver is mainly composed of hepatocytes that uptake, modify, secrete and transport bile acids (see section 1.2.2). The high concentration of bile acids in cholestasis induces alterations in expression of transporters like NTCP, BSEP located on the hepatocytes through the FXR signaling pathway (section 1.3.1.2.). The changes in the synthesis

and transport kinetics of bile acids represent a significant departure from the physiological liver function. During cholestasis, transporter changes on hepatocytes effectively sequester bile acids in blood - the primary cause of cholestatic symptoms such as pruritus and renal trauma (Arrese & Trauner, 2003). At the cellular level, cholestasis eventually leads to excess bile mediated toxicity of hepatocytes, leading to the formation of large necrotic infarcts known as '**bile infarcts**' in the liver parenchyma (see section 1.4.2). In general, necrotic cell death may arise from a variety of causes, but eventually results in loss of plasma membrane integrity, structural rigidity and disruption of vesicular transport processes. These are accompanied with a reduction in the ATP/ADP ratio due to loss of mitochondrial function. Bile acids have been implicated in each of these processes depending on the specific concentration of exposure to hepatocytes [Fig.1.4.2.F1].

However, the hepatocyte is a polarized cell, and the apical membrane of hepatocytes form canaliculi - the compartment with the highest concentration of bile acids in the liver parenchyma. The pericanalicular cytoskeletal cortex is made up of actin-filaments and actin-binding proteins (Tsukada, Ackerley, & Phillips, 1995). It is also the site where tubulin filaments facilitate a complex co-ordination of the localization of bile-associated transporter proteins from juxtaposed vesicles (Oda et al. 1995). Disruption of the peri-canalicular cortex is therefore expected to have drastic consequences in the hepatocyte in terms of regulating bile secretion and preventing exposure to the toxic bile in the canalicular lumen. The canalicular membrane and its associated cytoskeleton would therefore appear to be the proverbial Achilles' heel of the hepatocyte with regard to bile acid toxicity in cholestasis.

Indeed, previous work has shown that bile acids can cause actin cytoskeletal disorganization (Thibault, Claude, & Ballet, 1992; Zhou et al., 2013), leading to a loss of apical microvilli, dilated lumens of the bile canaliculi, leaky tight junctions, and loss of α-catenin (Herr et al., 2014). While these observations have not been directly linked to bile-acid mediated toxicity, they support the hypothesis that bile acid toxicity may be a result of the disruption of the cytoskeletal components in the hepatocyte.

In the cells of the biliary tree, i.e. cholangiocytes, the excess amount of bile acids occurring in cholestasis leads to gene expression changes. For example, the secretin receptor, which normally is required for bile secretion from the duct, is upregulated (Yang et al., 2010). Increased expression of the secretin receptor predisposes cholangiocytes to undergo neoplastic

transformation and develop cholangiocarcinoma (Humphreys, Williams, Adams, & Afford, 2010). Calcium signaling in cholangiocytes is important for their resistance to bile acids but is disrupted in cholestasis due to loss of InsP3R/Ca release channel. Effects on Ca-signaling in cholangiocytes have wide-ranging effects on all cellular functions.

Taken together, bile acids can induce several downstream and upstream events such as architectural modifications, intracellular changes, and gene level alterations that can alleviate or enhance cholestatic liver damage.

1.5. Rodent model of cholestasis

Extrahepatic cholestasis is relatively easily simulated in rodents by interruption of bile flow through the biliary tree. A commonly used model is bile duct ligation (**BDL**) in mice or rats (Heinrich et al., 2011; Nakano, Haratake, & Hashimoto, 1995). The surgical procedure of BDL involves the complete obstruction of the common bile duct by ligation with the help of sutures (Tag et al., 2015).

The phenotypic, histological and serum characteristics of mice that undergo BDL have been extensively investigated. It is apparent that the profile of cellular and tissue alterations induced by BDL does not match the changes seen in chronic cholestasis, thus making BDL an unsuitable model for chronic cholestasis. However, the morphological and cellular events observed in BDL are the presence of massive ductular reactions, infarct formation, inflammation, increased serum biochemical constituents like alanine aminotransferase (ALT), aspartate aminotransferase (AST) and bile acids (Zhang et al., 2012). These phenotypic changes, as well changes in gene expression are similar to the those observed in acute cholestasis in humans. Hence **BDL** is a suitable model to study '**acute cholestasis**'. BDL also induces similar changes as observed in human biliary cirrhosis, albeit without the induction of fibrosis.

Models of intrahepatic cholestasis are substantially more difficult to establish. Recently, knockout mice lacking apical membrane BA transporters in hepatocytes have been suggested to replicate some features of human intrahepatic cholestasis. It remains to be clarified how faithfully these models recapitulate the clinical features of the human disease.

2. SCOPE AND AIM OF THE WORK

A commonly occurring pathological condition that results in hepatotoxicity is cholestasis. Cholestasis leads to increase in systemic blood concentrations of bile acids and their accumulation in the liver tissue.

In this pathological condition, the morphology and functionality of bile ducts and bile canaliculi network are altered. The changes pertaining to bile ducts are termed as the '**ductular reaction**' of the liver in response to cholestatic liver injury. The ductular reaction is well described in 2D histopathological samples, typically reported as an increase in the number of bile ducts per periportal field. However, several features of this ductular response remain unclear. For instance, bile ducts are in reality 3D conduits that establish specific links to the bile canalicular network in the liver parenchyma. Alterations of the 3D structure of bile ducts with reference to changes in their convolution, branching, surface alterations have thus far not been elucidated. Moreover, it remains unclear whether bile ducts stay in close proximity to the portal vein or whether they infiltrate into the liver parenchyma.

In the present work, these questions are addressed with the help of confocal microscopy, detailed morphometric image analysis, and 3D tissue surface reconstructions.

Besides, the above-mentioned tissue level changes, the intracellular mechanism of hepatotoxicity induced due to excess bile acids is also unclear. Bile acids have direct or indirect ability to induce effects such as cell death, alterations of the actin cytoskeleton and regulation of the intracellular bile acid signaling via nuclear receptor 'FXR'. Such effects are not only concentration but time-dependent for different bile acids that are synthesized in the liver.

FXR is widely studied and is an important pharmacological target in cholestasis treatment. It can directly bind to bile acids and play a role in their homeostasis. In most cases, FXR is hepatoprotective in nature but some literature also has reported that it can induce toxicity (Cheng et al. 2015). Therefore, it remains unclear if FXR activation due to bile acids during

cholestasis is protective or can induce or enhance the in vitro cytotoxicity due to excess accumulated bile acids. Can such activation in the FXR is related to the alterations of actin cytoskeleton induced by bile acids or it is an independent mechanism of hepatotoxicity?

Although the cytotoxic ability of bile acids to induce hepatocellular injury is known, the exact mechanism of liver damage is a complex process involving the interplay between all the above-mentioned intracellular factors. Thus, the objective of this work is to find the exact mechanism underlying hepatocellular toxicity or liver damage in cholestatic disorders. What are the main events and the order in which such changes occur during cholestatic liver injury? Lastly, if these events are interlinked with each other or have independent contributions by different mechanisms that result in hepatotoxicity.

In order to answer and verify these scientific goals, this study focused on the following questions:

1. What are the tissue level changes induced during cholestasis?
2. Is there a relation between tissue and intracellular events that occur as a response to cholestatic liver injury?
3. What are the cytotoxic concentrations of different bile acids?
4. Is cytotoxicity induced only at high concentrations of bile acids? Or hepatocellular death is also observed at low concentrations of bile acids?
5. What is the status of FXR activity at such bile acid concentrations?
6. Are there any alterations in the cortical actin cytoskeleton of the cells exposed to these bile acid concentrations when FXR is active?
7. Are these alterations or changes in the actin cytoskeleton and FXR correlated? Or these are two independent unlinked mechanisms?
8. Are cytoskeletal perturbations or dynamics altered by bile acids in liver cells exposed to micellar bile acid concentrations? What exact changes are observed, and do they result in cell death or hepatocellular toxicity?
9. What is the order? Is alteration of cytoskeleton or dynamics preceding the cell death or is it vice versa?
10. Are there any additional factors such as changes in expression of membrane proteins like alpha-catenin or alterations in tubulin network or change in the mitochondrial membrane potential?

3. MATERIALS AND METHODS

3.1. Materials

All the chemicals and reagents used in this study were of high purity laboratory grade.

3.1.1. Animals: Housing and ethics

To study the changes induced by bile duct ligation (BDL), C57BL/6N male mice of 8-12 weeks were used and purchased from Jackson Laboratory. The mice were fed with ad libitum water and standard pellet diet (ssniff, spezialdiäten, GmbH, Germany). The mice were kept under normal laboratory conditions and 12-hour light/dark cycles with regulated humidity ($45\pm5\%$) and temperature (21°C). All the experimental procedures were in accordance with the guidelines for animal care and use of experimental animals and the study was approved by the Animal Care Committee from the German government (EU).

3.1.2. Antibodies

Both primary and secondary antibodies were used for basic liver architecture visualization.

Table.3.1.2.1 Primary antibodies: Source and concentrations used

Primary antibody	Antibody raised in species	Catalogue. No	Company	Concentration used (dissolved in reagent F)
Monoclonal anti-BrdU antibody	Mouse	M0744	Dako, Hamburg, Germany	1:50
Goat anti-mouse DPP4/CD26 ectodomain	Goat	AF954	R&D Systems	1:100
Anti-rabbit glutamine synthetase	Rabbit	G2781	Sigma Aldrich, Missouri, USA	1:2000
KRT19 rabbit Polyclonal antibody	Rabbit	14965-1-AP	Proteintech Europe	1:50

Table.3.1.2.2. List of secondary antibodies used for immunofluorescence

Secondary antibody	Antibody raised in	Catalogue. No.	Company	Concentration (dissolved in reagent F) used
Alexa fluor®488-conjugated Affinipure Fluor F(ab')2 fragment donkey anti-goat IgG (H+L)	Donkey	705-546-147	Jackson Immunoresearch Laboratories UK (Dianova GmBH, Hamburg, Germany)	1:100
Cy™3-conjugated Affinipure F(ab')2 fragment donkey anti-rabbit	Donkey	711-166-152	Jackson Immunoresearch Laboratories UK (Dianova GmBH, Hamburg, Germany)	1:200
Alexa Fluor®647-conjugated Affinipure F(ab')2 fragment donkey anti-mouse IgG (H+L)	Donkey	715-606-150	Jackson Immunoresearch Laboratories UK (Dianova GmBH, Hamburg, Germany)	1:500

3.1.3. Buffers and commonly used solutions

3.1.3.1. Acetic acid solution (0.2%)

Add 200 µL of glacial acetic acid to 99.80000 mL of sterile distilled water. Filter this solution through 0.22 µm filter.

3.1.3.2. Bromodeoxyuridine (BrdU) solution

BrdU is a synthetic analog of thymidine. It is used in detection of cell proliferation as it incorporates selectively into cellular DNA during S-phase. 5 to 80 mg/kg of this reagent per body weight of a mice is used the detection of cell proliferation (Hammad et al., 2014). For in vitro use of BrdU, it was dissolved in sterile double-distilled water to a final concentration of 500 mmol/L.

3.1.3.3. DAPI solution

1 µL of 4',6-Diamidino-2-phenylindole (DAPI) was diluted in 10 ml of distilled water. The solution was used to stain nucleic acid.

3.1.3.4. CaCl$_2$ sterile filtered solution (19 g/l CaCl$_2$*2 H$_2$O)

19 grams of calcium chloride was added to 1 L of sterile distilled water. This solution was filtered through a 0.22 µm filter and stored at 4°C. Freshly prepared before every isolation.

3.1.3.5. EGTA pH 7.6

3.8035 grams of EGTA was added to 1 liter of deionized water to get a 10 mM solution. The final pH was adjusted to 7.6 and this solution was then filtered through a 0.22 µm sterile filter. Stored at 4°C.

3.1.3.6. Glucose solution (9 g/l)

9 grams of glucose was weighed and further dissolved in 1 liter of sterile distilled water. This solution was also freshly prepared and stored at 4°C after filtering through a 0.22 µm membrane filter.

3.1.3.7. Glucose solution (30%)

300 gm of D-(+)-glucose anhydrous was dissolved in 1-liter distilled water.

3.1.3.8. HEPES pH 7.6 (without carbogen equilibration)

60 grams of HEPES (free acid) was added to 1 liter of sterile filtered distilled water. The pH was measured and adjusted to a final value of 7.6 using 1M NaOH. The solution was then filtered through a 0.22 µm filter and stored at 4°C.

3.1.3.9. HEPES pH 8.5 (60 gm/l)

60 grams of HEPES (free acid) was added to 1 liter of sterile filtered distilled water. The pH was measured and adjusted to a final value of 8.5 using 1M NaOH. The solution was then filtered through a 0.22 µm filter and stored at 4°C.

3.1.3.10. KH buffer pH 7.4

Chemical name	Amount added/ weighed
Potassium chloride (KCl)	1.75 grams
Potassium dihydrogen phosphate (KH_2PO_4)	1.6 grams
Sodium chloride (NaCl)	60 grams

Dissolve the contents in 1 liter of deionized distilled water while adjusting the pH to 7.4. This solution was then sterile filtered using a 0.22 µm sterile filter. It was always freshly prepared and stored at 4°C.

3.1.3.11. L-glutamine (7 g/ml)

7 grams of L-glutamine was weighed and added to 1 liter of distilled water. This solution was also filtered through 0.22 µm membrane filter and stored at 4°C.

3.1.3.12. $MgSO_4$ sterile filtered solution (24.6 g/l $MgSO_4$*7 H_2O)

24.6 grams of magnesium sulphate was weighed and added to 1 liter of sterile filtered deionized water under sterile conditions i.e under a laminar flow cabinet.
The solution was also filtered through a 0.22 µm membrane filter and stored at 4°C.

3.1.3.13. 1M NaOH

4 gm of sodium hydroxide was dissolved 99.6 mL distilled water. Sterile filter this solution through a 0.22 μm filter. Store at 4°C. Use only under sterile conditions.

3.1.3.14. Phosphate buffered saline (10✕ PBS)

For 5 liters of 10✕ PBS:

Chemical name	Amount added/ weighed
Potassium Chloride	10 gm
Potassium dihydrogen phosphate	10 gm
Sodium chloride	400 gm
Disodium hydrogen phosphate anhydrous	46 gm

Above mentioned chemicals were dissolved in 5 liters of distilled water. The pH was calibrated to 7.4.

3.1.3.15. Reagent A (1X PBS)

100 ml of 10✕ PBS was diluted in 900 ml of distilled water.

3.1.3.16. Reagent B (Preservation Buffer)

For 1 liter of the buffer:

Chemical name	Amount used/liter
30 % glucose solution	500 ml
Roti-Histofix 4% (PFA)	500 ml

The glucose-PFA solution was the stored at 4°C. This solution was always prepared fresh before each fixation experiment.

3.1.3.17. Reagent C (Antigen retrieval buffer)

Chemical name	Amount/ liter
Citric acid monohydrate	2.1 gm
Distilled water	800 ml

All the above-mentioned chemicals were dissolved in 800 ml of distilled water and the final volume was brought to 1 liter. The pH was measured and adjusted to 6.0.

3.1.3.18. Reagent D (DNA denaturation agent)

10 ml of HCl was diluted in 10 ml of distilled water (1:1) to get the final concentration as 2M HCL.

3.1.3.19. Reagent E (Blocking Buffer)

Chemical name	Amount/100 ml
Albumin BSA	3 gm
Tween 80	3 ml
Reagent A (1X PBS)	97 ml

Finally, the reagent mixture was aliquoted as independent 10 ml solution and was stored at -20°C for long term use.

3.1.3.20. Reagent F (Dilution Buffer)

Chemical name	Amount added /100 ml
Albumin BSA	0.3 gm
Tween 80	3 ml
Reagent A (1X PBS)	97 ml

The buffer can be stored as 10 ml aliquots and preserved at -20°C for long term use.

3.1.4. Chemicals

All the chemicals and reagents listed in table below were of laboratory grade.

Table 3.1.4.1. List of all the chemicals used for the scientific work

Chemical name	Manufacturer	Article/Catalogue no.
Acetic acid	Carl-Roth, GmbH Karlsruhe, Germany	3738.5
Albumin bovine fraction V	Serva, Heidelberg-Germany	150216
5-Bromo-2'-deoxyuridine (BrdU)	Sigma-Aldrich	59-14-3
Citric acid monohydrate≥99.5% p.a., ACS; ISO	Carl-Roth, GmbH Karlsruhe, Germany	3958.2
4', 6-Diamidino-2-phenylindole (DAPI)	Invitrogen, Darmstadt-Germany	898934/D3571
D-(+)-glucose monohydrate anhydrous (≥99.9%)	Carl-Roth, GmbH Karlsruhe, Germany	101533270
Disodium-hydrogen phosphate anhydrous (Na_2HPO_4)	Carl-Roth, GmbH Karlsruhe, Germany	P030.2
Ethyl alcohol (ethanol)	Carl-Roth, GmbH Karlsruhe, Germany	9065.4
Fluorpreserve^{TM} reagent	Calbiochem	345787
Hydrochloric acid	Carl-Roth, GmbH Karlsruhe, Germany	No.76.1

Table.3.1.4.1. List of all the chemicals used for the scientific work (continued)

Chemical name	Manufacturer	Article/ catalogue no.
Isopropanol (2-propanol 99.8%)	Carl-Roth, GmbH Karlsruhe, Germany	6752.1
Paraffin	Leica-Microsystems, Wetzlar, Germany	39602012
Potassium chloride (KCl)	Carl-Roth, GmbH Karlsruhe, Germany	6781.1
Potassium dihydrogen phosphate (KH_2PO_4)	Carl-Roth, GmbH Karlsruhe, Germany	3904.1
Roti-Histofix 4% (Paraformaldehyde-PFA)	Carl-Roth, GmbH Karlsruhe, Germany	6640
Sodium chloride (NaCl)	CARL ROTH	3957.2
Sodium Hydroxide (NaOH)	Merck KGaA, Darmstadt, Germany	B239682/ 1.06482.1000
Tween 80	Add company name	P1754-500M

3.1.5. Cell culture: cell lines, cultivation media, perfusion buffers, reagents

All the cell lines were maintained under S1 safety regulations and were authenticated by DNA fingerprinting at the Leibniz-Institute DSMZ-German Collection of Microorganisms and Cell cultures.

Table.3.1.5.1. Eukaryotic cell lines and primary cells

Cell line	Type	Donor/ Source	Catalogue no.	Cell Bank
HepG2	Adherent epithelial cell line	Liver tissue of a 15-year old Caucasian male suffering from HCC	ATCC®HB-8065™	ATCC
Freshly isolated mouse hepatocytes (PMH)	Primary cells	8-12 weeks male C57BL/6N mice	In house isolation	IfADo, Germany

Table.3.1.5.2. List of cell culture cultivation medium for cell lines

Cell line	Culture Media	Amount added	Catalogue no.	Manufacturer
HepG2	Dulbecco's modified eagle's Medium (DMEM) with 4.5 g/l glucose, 3.7 g/l NaHCo3, with stable glutamine	450 mL	P04-04500	PAN-Biotech
	+1%-Penicillin-streptomycin 10 mg/ml (1%)	5 mL	P06-07100	PAN-Biotech
	+ 10%- Fetal bovine serum (FBS)	50 mL	42F6663K	GIBCO-One shot FBS

Table 3.1.5.3. List of cell culture cultivation medium for primary cells

Cell line	Culture medium	Amount added	Catalogue/ Lot no.	Manufacturer
Freshly isolated mouse hepatocytes	**Hepatocytes seeding medium:** William's E medium (2.24 g/L NaHCO$_3$) and:	500 mL	P04-29510/ 8610517	PAN-Biotech GmbH, Germany
	+ Gentamicin (10 µg/ml)	500 µL	P06-03001	PAN-Biotech GmbH, Germany
	+ Dexamethasone (100 nM)	500 µL	-	Sigma-Aldrich Corp.USA
	+ Stable L-glutamine (2mM)	5 mL	P04-82100	PAN-Biotech GmbH, Germany
	+ Insulin/ ITS liquid media Supplement (100X)	5 µL	SLBQ5376V	Sigma-Aldrich Corp. USA
	+ Penicillin- streptomycin (10 mg/ ml)	5 mL		PAN-Biotech GmbH, Germany
	+ FCS/ FBS (10%)	1:10	P170208, P170512	Sera Plus

Table 3.1.5.3. List of cell culture cultivation medium for primary cells (continued)

Cell line	Culture medium	Amount added	Catalogue/ Lot no.	Manufacturer
Freshly isolated mouse hepatocytes	**Hepatocytes wash Medium:** William's E medium without additives	500 mL	P04-29510/ 8610517	PAN-Biotech GmbH, Germany
Freshly isolated mouse hepatocytes	**Hepatocytes maintenance medium:** William's E medium with additives:	500 mL	P04-29510/ 8610517 P06-03001	PAN-Biotech GmbH, Germany PAN-Biotech GmbH, Germany
	+ Gentamicin (10 µg/mL)	500 µL		
	+ Dexamethasone (100 nM)	500 µL	-	
	+ Stable L-glutamine (2mM)	5 mL		PAN-Biotech GmbH, Germany
	+ Insulin/ ITS Liquid media Supplement (100 X)	5 µL	SLBQ5376V	Sigma-Aldrich Corp.USA
	+ Penicillin-streptomycin (10 mg/ ml)	5 mL	P170208, P170512	PAN-Biotech GmbH, Germany

Table.3.1.5.4. Perfusion buffers for primary cell isolation

Buffer name	Amount added	Product code/ Catalogue no.	Company
Collagenase buffer for primary mouse hepatocytes isolation:			
+ Amino acid solution	30 ml	SO-33100	PAN-Biotech
+ $CaCl_2$ sterile filtered solution (19 g/l $CaCl_2$*2 H_2O)	10 ml	See section 3.1.3.4	
+ Collagenase type 1	80 mg	SCR103	SIGMA-
+ Glucose solution (9 g/l)	155 ml	Section 3.1.3.6	ALDRICH
+ L-Glutamine (7 g/ml)	2.5 ml	Section 3.1.3.11	
+ HEPES pH 8.5 (60 g/l)	25ml	Section 3.1.3.9	
+ KH buffer pH 7.4 (40 g/l)	25 ml	Section 3.1.3.10	
Add collagenase to the buffer during EGTA perfusion			
EGTA-perfusion buffer:			
+ Amino acid solution	60 ml	SO-33100	PAN-Biotech
+ EGTA solution (47.5 g/l)	1.6 ml	Section 3.1.3.5	
+ Glucose solution (9 g/l)	248 ml	Section 3.1.3.6	
+ L-glutamine (7 g/ml)	4 ml	Section 3.1.3.11	
+ HEPES pH 8.5 (60 g/l)	40 ml	Section 3.1.3.9	
+ KH buffer pH 7.4	40 ml	Section 3.1.3.10	

Table.3.1.5.4. Perfusion buffers for primary cell isolation (continued)

Buffer name	Amount added	Catalogue/ Lot no.	Company
Suspension buffer for freshly isolated primary mouse hepatocytes:			
+ Albumin fraction V, Protease-free	400 mg	150834	SERVA
+ Amino acid solution	30 ml	SO-33100	SIGMA-ALDRICH
+ $CaCl_2$ sterile filtered solution (19 g/l $CaCl_2$*2 H_2O)	1.6 ml	Section 3.1.3.4	
+ Glucose solution (9 g/l)	124 ml	Section 3.1.3.6	
+ L-glutamine (7 g/ml)	2 ml		
+ HEPES pH 7.6 (60 g/l) (without carbogen equilibration)	20 ml	Section 3.1.3.8	
+ KH buffer	20 ml	Section 3.1.3.10	
+ $MgSO_4$ sterile filtered solution (24.6 g/l $MgSO_4$*7 H_2O)	0.8 ml	Section 3.1.3.12	
Add BSA during EGTA or collagenase perfusion.			

Table.3.1.5.5. Cell culture reagents

Chemical	Company	Lot/ catalogue No.
Acetic acid sterile filtered (0.2%)	See section 3.1.3.12	-
Amino acid solution	PAN-Biotech	SO-33100
Calcium chloride	CARL-ROTH	CN93.1
Cell Titer-Blue® Cell Viability Assay reagent kit	Promega Corporation	0000201957
Dimethyl sulfoxide Hybri-Max^{TM}, sterile Filtered (DMSO)	SIGMA Life Science	D2650-100ML
DEPC-Treated Nuclease-Free water, autoclaved, Filtered, 0.2 µm.	Ambion®, THE RNA COMPANY	1509057
DMEM Low Glucose (1.0 g/l) 10✕ concentrated	BioConcept	1-25K03-I / LA07698P
10✕ PBS	See section 3.1.3.14	-
Rat collagen lyophilized (10 mg)	Roche Diagnostic Mannheim	11171179001, 11179179001
Stable glutamine (200 mM)	PAN-BIOTECH	P04-82100
Trypan blue (0.4%)	Sigma-Aldrich Corp., St. Louis, MO, USA	T8154

3.1.6. Consumables

Table.3.1.6. List of consumables

Product	Manufacturer
Cell culture flasks for adherent cells (TC Flask 75)	Sardstedt
Cutfix scalpel blades	B. Braun Melsungen AG-Germany
CryoPure Tube 1ml mix color, sterile, Non-pyrogenic	SARSTEDT
Eppendorf tubes (0.5, 1 and 2 ml)	Sarstedt, Nümbrecht-Germany
µ-Slide, 8-Well ibiTreat chambers for live cell imaging (1.5 polymer coverslip, tissue culture treated, sterilized)	ibidi GmbH; Germany
µ-Slide, 4-Well, collagen IV coated chambers for live cell imaging (1.5 polymer coverslip, sterilized)	ibidi GmbH; Germany
Microscope cover slips (24x 50, 60 mm)	Thermo Fisher scientific, Gerhard Menzel, Braunschweig-Germany
Glass-slides	Thermo scientific, Gerhard Menzel, Braunschweig-Germany
Glass Bottom µ dishes (35mm petri dish, 14mm Microwell, No.1.5 cover glass [0.16-0.19mm])	MatTek CORPORATION, USA
Paraffin embedding tissue Loc cassettes	Thermo Fisher scientific
Parafilm® M All-Purpose Laboratory Film	Sigma-Aldrich/ Merck, Germany

Table. 3.1.6. List of consumables (continued)

Product	Manufacturer
Pipettes (0.5, 1, 10, 1000, 5000 µl)	Eppendorf, Germany
Pipette Tips	Sarstedt, Nümbrecht-Germany
PIPETMAN® Classic	Gilson International B.V. Deutschland Limburg-Offheim
Serological Pipettes (5, 10, 25, 50 ml)	Sarstedt, GmbH, Germany
TC-Flasche T75, Stand.,Bel.Ka, Tissue culture flasks (T75)	Sarstedt, GmbH, Germany
Vibratome feather blades VT	Leica Microsystems, Wetzlar, Germany

3.1.7. Compounds and Drugs

Table.3.1.7. List of bile salts, drugs and test compounds

Compound Name	Manufacturer	Batch/Lot.no./ Product code	Stock solution
Chenodeoxycholic acid	SIGMA Life Sciences	MKBS2816V	1mM, 10mM, 100mM in DMSO
Deoxycholic acid	SIGMA Life Sciences	BCBQ4388V	1mM, 10mM, 100mM in DMSO
Sodium taurocholate hydrate	SIGMA Life Sciences	BCBQ4207V	1mM, 10mM, 100mM in DMSO
Ursodeoxycholic acid	SIGMA Life Sciences	SLBH7529V	25 mM, 50mM, 100 mM
Tauro-β-muricholic Acid	Toronto Research Chemicals, Canada	T009135	25 mM, 50 mM, 100 mM
GW4064	SIGMA Life Sciences		10mM stock in DMSO
(Z)-Guggulsterone	SIGMA Life Sciences	SLBN3567V	10mM stock in DMSO

3.1.8. Equipment and Imaging modalities

Equipment/Imaging Modality	Company
Analytical balance BL150S	Sartorius AG, Goettingen-Germany
Bright field microscope BX41	Olympus GmbH, Hamburg-Germany
Bright field microscope Eclipse TS100	Nikon
Bright field microscope Primo Vert	Carl Zeiss, GmbH, Jena-Germany
Casy cell counter	Roche
Centrifuge (Avanti JXN-26)	BECKMAN COULTER, USA
Confocal laser scanning microscope	Olympus GmbH, Hamburg-Germany
Confocal laser scanning microscope for live cell imaging (LSM 880)	Carl Zeiss, GmbH, Jena-Germany
CO_2 cell culture incubator	Binder GmbH, Tuttlingen-Germany
Mettler Toledo Seven Easy pH meter (PH S20)	SIGMA-ALDRICH, Germany
Microwave Oven	Sharpe Electronics, Germany
Microplate reader (Infinite 200Pro)	TECAN,
Microtome (microm-HM450)	Microm, Walldorf-Germany
Nanodrop ND-100	Thermo Fisher Scientific
Orbital Incubator Shaker (Ecotron)	INFORS HT, GmbH, Einsbach, Germany
Rotatory shaker	Edmund Buhler, Hechingen- Germany
Time-lapse Imaging system BX 81	Olympus GmbH, Germany

3.1.8. Equipment and Imaging modalities (continued)

Equipment/Imaging Modality	Company
Vibrating blade microtome- Leica VT1000S	Leica Microsystems, Wetzlar-Germany
Water Bath	Labortechnik

3.1.9. Imaging software and License

Software	License company
Fluoview 1000	Olympus GmbH, Hamburg
Fiji-Image J	National Institute of Health (NIH)
GIMP 2	GNU Image Manipulation Program, Copyright © 1995-2017, Spencer Kimball, Peter Mattis and the GIMP Development Team
Image J	National Institute of Health (NIH)
Imaris 7.4	Bitplane, Zurich
Inkscape 0.91 www.inkscape.org	Open software (Proprietary, GNU GENERAL PUBLIC LICENSE Version 2, June 1991 Copyright (C) 1989, 1991 Free Software Foundation, Inc. 59 Temple Place, Suite 330, Boston, MA 02111-1307 USA)
MATLAB	MathWorks®
OriginPro 2016 (64-bit) b9.3.226	OriginLab EULA for Origin 2016 and/or OriginPro 2016

3.1.10. Plasmid preparation

Mammalian Plasmids

LifeAct TagRFP

The mammalian expression plasmid pCMV–LifeAct®–TagRFP used in this study was commercially purchased from ibidi GmbH. The fluorescent protein TagRFP codon with its sequence was optimized for expression in mammalian cells and allowed the labelling of filamentous actin (F-actin) in living cells. The backbone constituted of an immediate early promoter of cytomegalovirus (PCMV IE) for protein expression and simian Virus 40 (SV40 polyadenylation signals A) downstream of the coding sequence. Bacterial selection is mediated by neomycin resistance gene (NeoR) in E.coli.

CytoBAS

pCMV CytoBAS (CBAS), the fluorescent bile acid sensor that allowed spatiotemporal monitoring of bile acid transport in living cells was based on FRET and was a gift from Stan van de Graaf (van der Velden et al., n.d.). The sensor is also commercially available from Addgene Europe (Addgene plasmid # 62860). This plasmid was later transformed in E.coli for further use. The vector backbones constituted of synthetic DNA construct encoding BAS-1 that was cloned into pECFP-C1, replacing ECFP, to generate NucleoBAS. CytoBAS was created by KpnI digestion of NucleoBAS, which removed the nuclear localization signal or sequence (NLS). The mammalian expression was verified further by transient transfection of the CytoBAS in HepG2.

The FRET-based sensor was a fusion protein consisting of two fluorescent domains: donor-cerulean and an acceptor-citrine (Fig.3.1.10.F1.A). It was also made up of a ligand binding domain (LBD) and a peptide derived from NCoA2 which was the FXR activator protein. The peptide contained an LXXLL motif. Bile acids induced the interaction between the ligand binding domain of the FXR and the peptide NCoA2. This disrupted the interaction between donor and acceptor thus in turn causing a decrease in the FRET between bile acid-bound and unbound state.

In presence of bile acids, the LXXLL motif could bound to the ligand binding domain of the FXR thus resulting in an conformational change in the sensor and reduced the energy transfer i.e. FRET between cerulean and citrine. The design of the sensor was also exclusive, because in ligand or bile acid unbound state the sensor always maintained maximal FRET efficiency. This was possible due to the presence of two mutations: Q204F and V224L (Fig.3.1.10.F1.B).
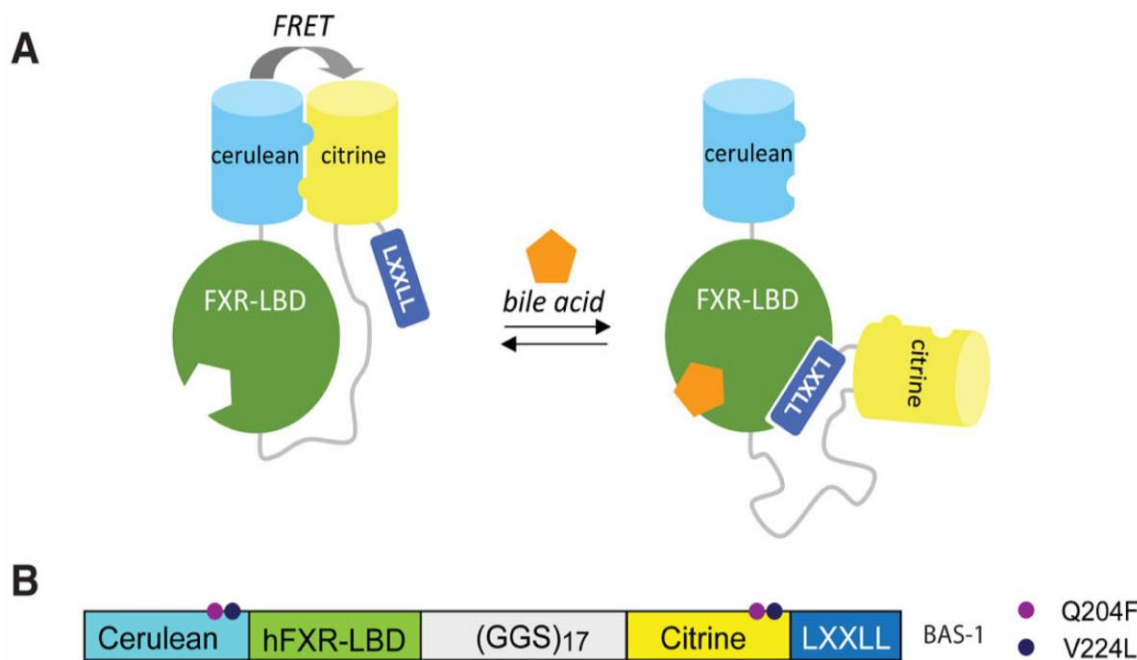
Fig.3.1.10.F1. Bile acid sensor. A. Structural design of the bile acid-FRET based sensor. Cerulean (donor fluorophore) and citrine (acceptor fluorophore) is the FRET pair linked to FXR-cofactor peptide LXXLL motif via the ligand binding domain or bile acid domain of the FXR. In bile acid bound state (right) the LXXLL motif will bind the FXR and reduce the FRET between cerulean and citrine by disrupting their interaction. B. The domain architecture of the bile acid sensor consisting of two mutations Q204F and V224L. These two domains promote the intramolecular interactions between the donor and acceptor proteins. The cytosolic version of this sensor CytoBAS construct lacks the c-terminal nuclear localization signal (NLS) which is present in the NucleoBAS. The CytoBAS is only seen to be localized to the cytosol thus allowing spatial-temporal determination of the intracellular concentrations of bile acids in living cells.

3.1.11. Transformation and Transfection: Antibiotics, competent cells, plasmids, isolation kits, transfection reagent

3.1.11.1. List of all the products used for bacterial plasmid isolation

Name	Company	Catalogue/Lot.no.
Agar-agar		
Ampicillin Sodium Cell Culture tested	SIGMA-ALDRICH Chemie, GmbH, Germany	065M4777V
Effectene Transfection reagent kit 1ml	Qiagen	301425
Kanamycin sulfate from Streptomyces kana	SIGMA-ALDRICH Chemie, GmBH, Germany	SLBR0055V
LB Broth Lennox, Animal Free (Powder)	Biomol	
LB Agar plates (100 µg/ml ampicillin resistant), 20 plates	TEKnova	L1004
LB Agar plates (50 µg/ml kanamycin resistant), 20 plates	TEKnova	L1025
MAX Efficiency™ DH5α™ Competent Cells	ThermoFisher Scientific	18258-012
Plasmid Isolation Maxi Kit (10)	Qiagen	154013121
Petri dishes (94 × 16 mm) with VENTS, Sterile	Greiner bio	633181
14 ml Polystyrene Round-Bottom Tube (17 × 100 mm), Non-pyrogenic, Sterile	FALCON® A Corning Brand	352051

3.1.11.2. List of all the plasmids, transfection reagent, fluorescent dyes and labels used in vitro experiments

Plasmid	Company	Catalogue/ Lot.no.	Expression in biological Organelle
pCMV CytoBAS	Addgene	62860	Cytoplasmic fluorescent bile acid sensor (BAS) to monitor bile acid transport in single living cells using FRET
pCMV-LifeAct-TagRFP plasmid, lyophilized, 20 µg	ibidi GmbH, Germany	60102	F-actin
Effectene Transfection reagent 1 mL	Qiagen	301425	Lipid based reagent to incorporate DNA into mammalian cells
SiR-actin	SPIROCHROME	CY-SC013	Far-red silicon rhodamine (SiR) fluorophore analogue SiR700-actin and actin binding natural product jasplakinolide which label endogenous F-actin in live cells with high specificity and low background without the need for genetic manipulation or over-expression.

3.2. Methods

3.2.1. Animal experiment and bile duct ligation surgery

Male C57BL/6N mice were weighed and anesthetized by injecting 0.5 L/min oxygen and 3% Isoflurane in an induction chamber. The abdomen was sterilized using povidone-iodine (Betaisodona) and then shaved to remove any extra fur coat which may interfere during surgery. The animal was fixed on a small operation table. Thereby, physical stress was carefully minimized. The mouse was in a supine position and was stabilized on the platform with the help of stripes of tape. The mouth and the nose of the mice was placed in a small animal anesthesia mask connected to an isoflurane-vaporizer (Sigma Delta, UK) with a maintained continuous rate of 0.5 L/min oxygen and 3% isoflurane. The breathing rate and heart rate of the animal were continuously monitored by the surgeon during the entire surgery to maintain optimal operative conditions and avoid stress to the mice. After disinfection of the abdomen, a sterilized operating area was created by placing a sterile gauze around the sterilized skin. A transverse incision was then made in the upper third part of the abdomen with the help of sterilized micro-instruments. Bleeding from the muscle was controlled with a bipolar coagulation device (ERBE, VIO 50C). The liver was carefully and gently lifted and exposed by lifting of the xiphoid process by a suture line fixed to the anesthesia mask and both the costal arches were retracted with the help of two mini hooks attached to the two columns.

The common bile duct located just above the pancreas was identified and gently isolated from surrounding fat tissue about 0.5 cm away. Three ligatures (silk 6-0) were placed around the common bile duct and each ligature was closed with 3 knots without any physical or mechanical stress. The common bile duct was then cut between the middle and the distal ligature. The entire procedure was carefully performed under a microscope to avoid any damage to the vasculature i.e. hepatic artery or portal vein and pancreatic tissue. After ligation, the situs was checked for any possible biliary leakage caused due to the surgery. The mice were then sutured back by closing the layer of skin with the help of two-layer running suture (Prolene 6-0). The bile duct ligation procedure was not performed for sham-operated animals that were used as controls for the study, rest all surgical operations were the same on the sham-operated as performed for bile duct ligated mice. Immediately, post-surgery all the mice from each experimental condition were treated with analgesic procedures and buprenorphine (0.05 mg/kg BW, Temgesic) was injected subcutaneously twice a day during the first two postsurgical days.

The mice were routinely observed for their clinical and physical conditions at least once in a day.

3.2.2. Blood collection and clinical chemistry

Blood was collected via the intrahepatic vena cava for the analysis of the liver enzymes such as aspartate aminotransferase (ASAT), alanine aminotransferase (ALAT) and alkaline phosphatase (ALP) determined by using an automated analyzer (Selectra).

3.2.3. BrdU administration, excision and fixation of the liver tissue

Sham-operated animals and animals from various time points post BDL were injected intravenously 1 hour before tissue harvest and blood collection with 5-bromo-2'-deoxyuridine (BrdU, Sigma-Aldrich, St. Louis, USA) in a dose of 5 mg/kg per body weight (dissolved in sterile NaCl 0.9%). The mice were then sacrificed by exsanguination under anesthesia and the liver tissue was harvested at all the relevant time points post bile duct ligation (Fig.3.2.3.F1).

Timepoint post Bile duct ligation

0.25 day (6 hours)

1 day

3 days

7 days

14 days

28 days
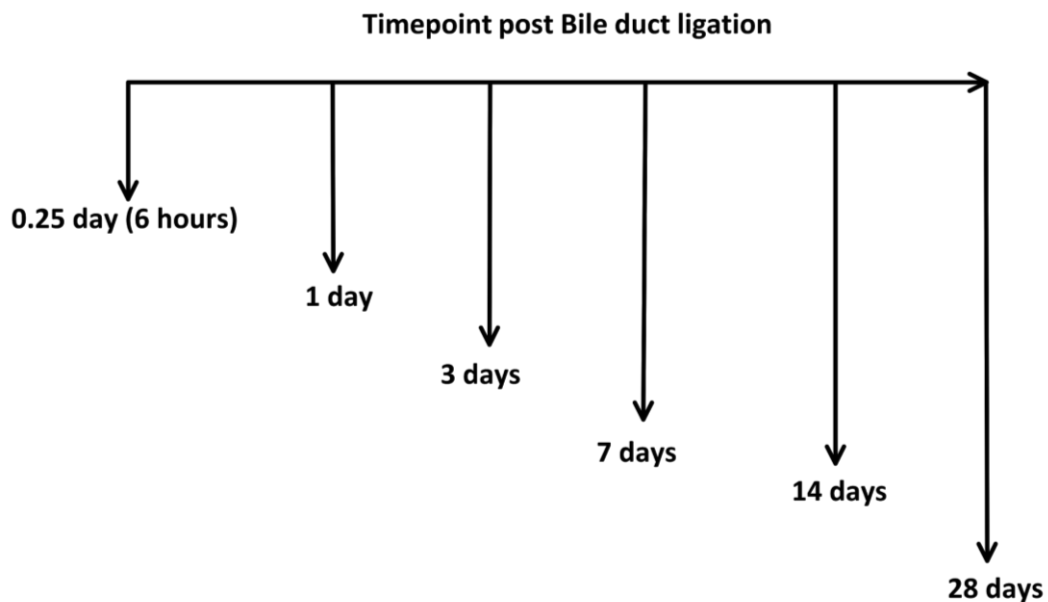
Fig.3.2.3.F1. Experimental design and time points post bile duct ligation. Six mice per time point were analyzed.

A small incision was made just below the thorax and the abdominal cavity was immediately opened. The entire liver tissue comprising of 5 liver lobes was removed carefully. The weight

of each liver lobe comprising the liver tissue was recorded and the tissue was then separated into two parts. The first part was preserved in 4% paraformaldehyde (PFA) solution in paraffin embedding cassettes at 4°C for 48 hours and these were further used for paraffin tissue embedding. The second part was preserved in 4% PFA for three days at 4°C (Hammad et al., 2014; Hoehme et al., 2010) followed by long term storage in preservation buffer i.e. reagent B (2% PFA, 15% glucose) which were then used for architecture-based immunofluorescence staining's.

3.2.4. Immunohistochemistry and Immunofluorescence of liver lobes

3.2.4.1. BrdU staining for cell proliferation index

The liver lobes preserved for paraffin tissue embedding were washed with $1\times$ PBS for 48 hours and dehydrated by ascending order of ethanol series, i.e. 5 minutes incubation in each 70%, 90% and 100% ethanol three times in the closed glass coplin jars. The liver sections were then incubated for 4 hours in xylene and then incubated overnight in xylene/paraffin (1:1) at 60°C and the tissue specimens were incubated with paraffin at 60°C twice for 3 hours. Finally, the tissues were embedded using the MicromSTP (name of the instrument and company).

Post paraffin embedding thin 4µm tissue sections were cut using a microtome (microm-HM450, Walldorf-Germany) and mounted on microscope glass slides (Thermo scientific) for further immunohistochemistry procedures. Two slides per mice per time point were prepared. The first slide had slices from three liver lobe slices (RSL, RIL, LLL) while the second slide was mounted with slices from two liver lobes (RML, LML) and a sample of duodenum which was the positive control for the BrdU staining. BrdU proliferation staining was based on a modified protocol of Sigma Inc and protocol for immunostaining of paraffin sections (Hammad et al., 2014; Hoehme et al., 2010). Post deparaffinization with roti histol 4 times and rehydration followed by incubation with descending concentrations of alcohol (xylene 30 minutes, 100% ethanol for 3 minutes, 70% ethanol for 3 minutes, distilled water wash for 3 minutes and TBS for 3 minutes). The deparaffinized tissue sections were then treated with 0.1% pre-warmed trypsin solution (Sigma, St. Louis, MO) and incubated at 37°C for 40 minutes. This was then followed by DNA denaturation with treatment of liver slices with 2N HCl (Merck, Darmstadt, Germany) for 30 minutes at 37°C.

Primary antibody, mouse monoclonal anti-BrdU (Dako, Hamburg, Germany) was used to stain the tissue sections for 1 hour at 37°C. Tissue sections were then incubated for 1 hour at room temperature with an alkaline-phosphatase labelled secondary anti-mouse antibody (Power Vision, Immunovision Technologies, USA). Fast Red Substrate System (sensitive from Dako, Hamburg, Germany) was then used to carry out the color reaction for 10 minutes followed by counterstaining with Mayer's Hemalaun (Merck, Darmstadt, Germany) for 10 seconds. Finally, the tissue slices were mounted with the help of Immu Mount (Shandon, Pittsburgh, PA).

The whole slide was then scanned using a whole slide scanner (Nanozoomer, Hamamatsu Electronic Press Co., Ltd, Lwata, Japan). A custom-made automated analysis routine was used to identify the liver lobes on the slides, portal fields within these liver lobes and bile ducts within the portal fields that comprise the liver lobules of the liver lobes and finally measure the number of BrdU-positive biliary epithelial cells lining the bile ducts. The bile duct cell proliferation index was determined for various time points including day 28 post BDL.

3.2.4.2. Liver architecture immunofluorescence staining

The liver lobes were harvested in the preservation buffer reagent B (Roti-Histofix 2% PFA with 15% glucose). The left liver lobe was then fixed on the buffer tray S of the vibratome (Leica VT1000S-vibrating blade microtome, cat. No. 047235613, Leica Biosystems, Wetzlar, Germany) with the help of glue (Histoacryl R Gewebekleber, B.Braun GmbH, Melsungen, Germany, 9381104). The fixed specimen was kept hydrated by filling the tray with 1✕PBS solution during the sectioning procedure. 75-100 µm thick tissue slices were prepared with the help of vibratome feather blades (VT, Leica Microsystems, Wetzlar, Germany, 14020542056) with a sectioning speed of 0.125mm/sec and vibratome sectioning frequency of 80 Hz.

Liver vibratome sections were then used for architecture specific immunofluorescence staining (Hammad et al., 2014). Tissue sections were washed three times with 1✕ PBS for 10 minutes at room temperature. The tissue slices were then further washed 9 times for 2 minutes with prewarmed reagent C (10mM citric acid, pH 6.0) solution also known as antigen retrieval process. The vibratome slices are then incubated in reagent E (3% BSA, 1% Tween 80, 1✕ PBS, 2h, room temperature, 150 rpm) to block any unspecific binding sites. Tissue sections are then incubated in primary antibodies (see Table.3.1.2.1) diluted in reagent F (0.3% BSA, 1% Tween 80, 1✕ PBS) overnight at 4°C on a rotating shaker in the dark room to preserve fluorescence. Next day, the tissue slices were washed with 1✕ PBS three times and incubated

with secondary antibodies (see Table.3.1.2.2) diluted in reagent F at 4°C on a rotating shaker for 2 days in dark. On day 4 post antibody incubation, the tissue sections were washed with 1✕ PBS three times and incubated with DAPI at 25°C on a rotating shaker at 150 RPM. Before mounting the slices were washed again with 1✕ PBS to remove any excess nuclear stain and mounted on a glass slide with the FluorpreserveTM reagent. The slide was finally covered with a thin coverslip without moving the tissue and allowed to dry for minimum 2 days before image acquisition. For long-term preservation, the tissue slides were stored at 4°C.

3.2.5. Image acquisition for Immunofluorescence

3.2.5.1. Z-stack acquisition

The architecture of the liver such as the bile canaliculi network, bile ducts, Hering canals were visualized by acquiring immunofluorescence micrographs and Z-stacks from the immunostained slides using a laser scanning confocal microscope (Olympus Fluoview™ FV1000, Germany). All the data was acquired using this microscope which has an HCL Apochromat 60x oil immersion objective (UPLSAPO 60XO NA: Olympus Fluoview™ FV1000, Germany) and appropriate laser excitation lines: 405 nm (UV-diode), 458, 488 and 514 nm (Argon) and 561, 633 nm (He-Ne).

The immunofluorescence micrographs and Z-stacks were acquired at: 1024×1024-pixel frame size; 207 nm pixel size; 540 nm Z-distance between two sections and a 4 µs/pixel scan speed with sequential scanning mode set to line scan. The images were acquired avoiding saturation and at optimized balanced intensity and less background noise for each slice of the Z-stack by adjusting the HV (Voltage), gain and offset parameters. These parameters were controlled by adjusting their values within integrated bright Z-stack function in the FV10-ASW (Olympus) imaging software. Z-stacks were saved as 16-bit TIFF (OIF format) and an accessory file (OIB file). The Z-stacks were also exported as AVI files.

Table. 3.2.5.1. List of various fluorophores and their spectral details used for the Z-stacks and Immuno-micrographs

Fluorophore	Excitation (nm)	Emission bandpass (nm)
DAPI	405	415-470
Alexa 488	488	500-550
Cy3	561	575-610
Alexa 647	633	645-700

3.2.5.2. Deconvolution

Deconvolution was further performed on the acquired Z-stacks by using AutoQuant X3 (Bitplane). The deconvolution method used was Adaptive PSF (Blind) deconvolution with the theoretical PSF as 10 iterations and medium noise. The deconvolved z-stack was then stored as a 32-bit floating point file in an Imaris file format (IMS). This format was compatible to IMARIS (Bitplane) software, which was used to generate the 3D surface reconstructions.

3.2.5.3. 3D surface reconstructions

The iso-surfaces were generated using the global intensities from the fluorescence staining's of the z-stacks. Appropriate thresholds were adapted to remove background noise. 3D surface of sinusoids was generated using the intensity values from donkey anti-mouse IgG signal using the Imaris surface function integrated in the IMARIS 6.4. (Bitplane) software.

The biliary network, i.e. bile ducts, canal of Hering and bile canaliculi were isolated by masking the 3D sinusoidal surface from the DPP4 channel. DPP4 marks the sinusoids along with the biliary network.

Depending on the individual intensities, the fine structural details were preserved by removing any artifacts or background noise or out of focus light acquired while imaging. Median filter (3x3x1 kernel) was applied to remove such artifacts. The link connecting the bile ducts to the bile canaliculi network, i.e. the canal of Hering was represented by yellow and white colors after isolation from the masked channel of the biliary network based on DPP4 intensity.

3.2.6. Image processing, 3D surface reconstruction and quantification

3.2.6.1. Image formats derived from the microscope and their conversion

All the images and z-stacks recorded on the microscopes were always stored in proprietary formats by vendor supplied acquisition software which is compatible to the instrument. The immuno-micrographs and z-stacks acquired from the immunofluorescence architectural staining's were from an Olympus FV1000 confocal microscope. The microscope is configured with FV10-ASW software that outputs the data as a *.OIB file, which contains acquisition metadata as well as the image frames. The data can also be stored as an *.OIF file format by this software. This format saves the data as a single file containing metadata and an accompanying directory which contains all acquired image frames as individual *.TIFF files.

All the data i.e. OIB and OIF files was converted to 32-bit OME-TIFF hyper stacks in the order XYZCT using the Bio-formats library for ImageJ. The TIFF files contained the metadata in the headers, which could then be further analyzed as required.

3.2.6.2. Evaluation of the duct diameter, eccentricity, length, tortuosity and volume

3.2.6.2.1. Isolation of individual bile ducts

3D-channel intensity of the anti-DPP4 that marked the apical surface of the bile ducts was used to measure the duct diameter. The z-stacks were processed, and bile ducts were isolated from each such stack and manually cropped to the region of interest containing the isolated bile ducts as an separate z-stack. This was stored again in Fiji. Thus, this resulted in a single unbifurcated section of the bile duct.

This step was very crucial in finding the duct orientation which was determined through principal component analysis.

Such processed z-stack data containing only the bile ducts required less memory and computationally low cost as compared to that acquired by the raw data.

3.2.6.2.2. Z-stack processing and diameter measurements

All the isolated bile ducts containing z-stacks were processed through a step-by step established analysis:

1. The background values were set to 0 and bile duct values were set to 1 by the Otsu thresholding method in the z-stack with the isolated bile duct.

2. Binary 3D-hole filling was done with a 4x4x4 px kernel to patch any holes that may have occurred due to poor immunofluorescence signal and thresholding.

3. PCA (principal component analysis) of the 3D intensity data was used to yield PCA coefficients and scores of the data.

4. These PCA coefficients represented the rotated axes such that the maximum variation of the data occurs along the new X, Y, Z, axes. The so called 'Varimax rotation' provides the orientation of the duct. For an approximately cylindrical shaped duct segment, the direction of the highest variation represents its length.

5. Affine transformation i.e. translation to center, rotation by PCA coefficients, and translation to original coordinates of the 3D data yields a Z-stack of the duct with the length of the duct aligned with the Z-axis.

6. Grayscale morphological region detection in all the Z-planes provides the centroids, area and perimeter of all duct cross-sections along the Z-axis of the entire stack.

7. Measurement of duct diameters is directly obtained from the perimeter measurements of each individual pixel pair.

8. Eccentricity is calculated as the ratio of the maximum and minimum diameter values.

9. Duct length is calculated from the line connecting the centroids of cross-sections of each slice of the isolated bile duct in the Z-stack.

10. Tortuosity is calculated as the ratio of the straight-line distance between end-points of this line and the duct length.

11. Curvature is the mean angle between segments connecting each point on the line to the previous and the next points on the line.

12. Summation of all the cross-sectional areas along the Z-axis provides the volume of the duct.

A MATLAB routine called '**Diaduct**' was written which implemented the above algorithmic steps. The output of the analysis by Diaduct is shown below:

3.2.6.3. Measurement of bile duct branching and biliary tree network complexity

Duct branching was measured from the anti-KRT19 immunofluorescent signal of the bile ducts. Anti-KRT19 marked the cytoplasm of the cholangiocytes that line the bile ducts. This measure was an accurate representation of the 3D-profile of the bile duct albeit compromising the identification of the duct luminal surface. However, the luminal surface of the duct has no bearing on its skeleton. Anti-KRT19 is bile duct specific, thus segmentation of the duct is simplified.

3.2.6.3.1. Steps involved in the 3D-image processing for branching and skeletonization

1. Reny-Entropy thresholding was used to set the background values to NaN (not a number) and the KRT19 bile duct signal to 1.
2. Gaussian filter with radius 5 px and binary hole filling was done using kernel of 2x2x2 px.
3. Skeletonization of the duct was performed to obtain single pixel traces of the bile duct.
4. Terminal points and node detection was carried out. Trimming of spurious branches was done based on branch length limit of 10 µm.
5. Strahler analysis of curated nodes and terminal points was used to obtain the biliary tree representation.
6. The final step was the collation of the data from various time points and the calculation of the mean branch length, frequency of the nodes and ramification ratio.

The above steps are implemented as chained Fiji macros: preprocess.ijm, SkeleAnalyse.ijm and StrahlerAnalysis.bsh.

3.2.6.4. Surface area and roughness measurements

Surface area was determined from the anti-DPP4 intensity. The anti-DPP4 surfaces of the manually segmented bile ducts were used to generate a triangle mesh using the Marching Cubes algorithm implemented in Python scikit-image package. The surfaces of the duct were further processed using the steps described below:

1. Triangle meshes are composed of the triangles, which are represented by their vertices. The vectors between these vertices were determined. The maximum resolution of the data is determined by the size of the pixels while the unit vector magnitudes are simply the pixel dimensions.

2. The cross product of any two triangle vectors is determined to obtain the normal (area) vector.

3. The normal vectors represent the orientation of the respective triangles in 3D space, while their magnitudes represent the extent of the surface which exists in that orientation.

4. The dot product of the normal vectors with a diagonal vector spanning the cuboidal 3D-space allows us to find the angle of orientation along with respect to the diagonal.

5. The variance of these angles indicates the variance in orientations of the bile duct surface i.e. frequency of corrugation. This frequency increases with the increased roughness.

6. Magnitude of the dot product is an indication of how far the surface translates at that triangle. The magnitude of the dot product represents the 'elevation' or 'amplitude' of the corrugation.

7. The area of all the triangles is calculated by Heron's formula and summed to calculate the area of the entire bile duct in the Z-stack.

This analysis routine is performed as the Python files: Roughness.py along with the initialization file Run.py. The duct surfaces and normal vectors resulted from this analysis may be visualized using the included Paraview pipeline 'VisualizerPipeline.pvsm'. The Python routine output creates CSV files containing all the measured quantitative parameters can then be collated to one file.

3.2.6.5. Simulation of corrugated surfaces

To evaluate the effect of corrugations on the surface area of the duct, simulations were performed with different frequency and amplitude values. A rectangular grid mesh was generated in a 3D space, with each cuboid equivalent to the X, Y pixel dimensions in the data.

Corrugations are introduced along the Z-axis according to a sinusoidal pattern with varying angular frequency and amplitudes from 10-50° and 0-50 µm, respectively. Gaussian noise equivalent to 10% of the x, y, z-values is added to the grid to stimulate biological variability.

From the resulting surface, the area is then calculated as the double integral along the X, Y dimensions. The dependence of the area on the angular frequency, corrugation amplitude and noise are then determined. This simulation routine is available as the Python routine:SurfaceSim.py

3.2.6.7. Computation of the portal vein diameter and distance of the bile ducts from the portal veins

The following step by step procedure was used to measure the distance of the bile duct from the portal vein:

1. The portal veins were manually segmented in 3D confocal stacks using the anti-Mouse IgG signal. The anti-Mouse IgG is specific for endothelial cells.
2. 'Diaduct' program described in detail in section 3.2.6.2.2 was used to determine the portal vein boundaries, diameters and centroids.
3. Diaduct is also designed to perform morphometry on any ductular shaped structure and the analysis is not relevant or dependent on the biological function of the structure.
4. Isolated and segmented bile ducts from anti-KRT19 staining as described in section 3.2.6.3 were used to determine the distance between every bile duct pixel and the closet portal vein centroid.

5. Distance of the bile duct pixels from the portal vein walls was similarly determined.
6. The mean of all the quantitative parameters for all the experimental timepoints was calculated and this analysis was then implemented in Python routines as: PVPreprocess.py, PVRemovesmallobjects.py, CollateBDPVdist.py

3.2.6.8. Measurement of the frequency of the canal of Hering's

The canal of Hering (CoH) was defined as the junction between the bile duct branches and the bile canalicular network. The canal of Hering appeared as a KRT19-positive bile duct branch lined by cholangiocytes. This branch joined the DPP4-positive bile canaliculi present between hepatocytes to the bile ducts.

CoHs were then manually identified and segmented and then subjected to further morphometric analyses as described earlier in section 3.2.6.1, 2, 3, 4, 5 performed for the bile ducts. Entire

KRT19-positive branch or the CoH was included in the analysis. The number of CoH in as Z-stack was normalized to the total length of the bile duct and the portal veins present per stack.

All the results were collated using the Python routines:
CollateCoH.py, CollateCoHPV.py, MapCoHPV.py

3.2.6.9. Cell proliferation rates measurements

The rate of cellular proliferation of the bile duct cells was determined from the BrdU staining's. The images of anti-BrdU stained tissue slices were generated using a whole slide scanner (Nanozoomer) equipped with a Hamamatsu CCD camera and archived in NDP2 file format. The high-resolution TIFF files were extracted from the NDP2 files and subjected to object detection and filtering algorithms that isolated the liver lobes.

To reassure the correspondence in the liver regions that were used for cellular proliferation rate determination and 3D-morphometry, only the region corresponding to the outer 200 µm of each liver lobe was used for further analysis.

The portal vein luminal cross-sections were identified as 'empty circles' of 30-50 µm while the bile duct luminal cross-sections were identified as 'empty circles' of 5-20 µm diameter within 25 µm of the portal veins. These range limits were deduced from the measurement of the portal vein diameters, bile duct diameters and bile duct to portal vein distance determined as described in sections 3.2.6.2 and 3.2.6.7. BrdU-positive bile duct cells i.e. the cholangiocytes were identified through the color-based thresholding as being 'brown' spots of 5-15 µm that lined the lumen of the bile duct.

The frequency of these BrdU-positive cells per bile duct per portal vein was determined for all the time points post BDL with the help of custom automated analysis of all the portal fields in the liver tissues. This analysis and preprocessing routines are available as the Python scripts: Extract_NDP2.py, Extract_lobes.py and BrdUCounter.py.

3.2.6.10. Code and Dependencies for data quantification

All the programs and scripts required for the computation and generation of data described above are open source and can be found on http://vartak.org/liver

3.2.7. Molecular Biology Techniques

3.2.7.1. Bacterial transformation and selection

200 µl of dense chemically competent E.coli cultures were incubated with plasmid DNA products on ice for 10 mins. The bacterial culture was then allowed to recover in Super Optimal Broth (SOB) for 1h at 37°C. Finally, these cultures were plated on the LB-agar plates containing the specific antibiotics such as Kanamycin (30 µg/ml) or Ampicillin (50 µg/ml), depending upon the selection marker on the plasmid DNA, and incubated overnight at 37°C.

Individual bacterial colonies were then picked and added to the 2ml starter cultures containing LB-medium with the selection marker or antibiotics as on the agar plates. The steady cultures obtained after overnight growth at 37°C, 180 rpm were then used to prepare batch cultures and glycerol stocks. The batch cultures were prepared by addition of 500 µl of starter bacterial culture to 500 ml of LB-medium with selection marker or specific antibiotic. The batch culture was allowed to grow overnight 37°C, 180 rpm for 12-16h and further used for plasmid extraction and isolation. The remaining starter culture was stored as glycerol stocks ("Addgene: Protocol - How to Create a Bacterial Glycerol Stock," n.d.) which can be used again for plasmid production.

3.2.7.2. Extraction, Isolation and storage of the plasmid DNA

Batch cultures of bacteria harvested overnight were used to extract the plasmid DNA by the following extraction procedure:

1. Harvest the overnight bacterial culture by centrifuging at 6000 × g for 15 mins at 4°C.
2. Resuspend the bacterial pellet in 10 ml Buffer P1 containing RNase A (resuspension buffer) of the Qiagen Plasmid Maxi Kit.
3. Add 10 ml of Buffer P2 to the resuspend the bacterial pellet in Buffer P1. Mix thoroughly by vigorous inverting of the tube containing the bacterial solution 4-6 times. Incubate at room temperature (15-25°C) for 5 min. The solution will turn blue, in presence of LyseBlue reagent and this is an indication that the lysis is complete.
4. Add 10 ml of pre-chilled Buffer P3, mix thoroughly by vigorously inverting 4-6 times. Incubate on ice for 20 mins.

5. Centrifuge at $\geq 20,000 \times$ g for 10 min at 4°C. Re-centrifuge the supernatant at $20,000 \times$ g for 15 min at 4°C if the supernatant is not clear.

6. Meanwhile equilibrate a QIAGEN-tip 500 by applying 10 ml Buffer QBT and allow column to empty by gravity flow.

7. Apply the supernatant from step 5 to the QIAGEN-tip and allow it to enter the resin by gravity flow.

8. Wash the QIAGEN-tip with 2×30 ml Buffer QC. Allow Buffer QC to move through the QIAGEN-tip by gravity flow.

9. Elute DNA with 15 ml Buffer QF into a clean 50 ml vessel. For DNA constructs larger than 45 kb, prewarming the elution buffer to 65°C may help to increase the yield.

10. Precipitate DNA by adding 10.5 ml room temperature isopropanol to the eluted DNA and mix. Centrifuge at $\geq 15,000 \times$ g for 30 min at 4°C. Carefully decant the supernatant.

11. Wash the DNA pellet with 5 ml room-temperature 70% ethanol and centrifuge at $\geq 15,000 \times$ g for 10 minutes. Carefully decant the supernatant.

12. Air-dry pellet for 5-10 minutes and redissolve DNA in a suitable volume of appropriate buffer (e.g., TE buffer, pH 8.0 or DNase/RNase free distilled water).

13. Measure the concentration of the plasmid DNA using nanodrop.

3.2.8. In vitro experimentation

3.2.8.1. Maintenance and Propagation, transfection of cell lines

3.2.8.1.1. Thawing of the cell lines

Thawing of the frozen vials of HepG2 and HeLa was done at 37°C (~ 2mins). In order to reduce the possibility of any contamination during this process, the O-ring and cap of the vial was kept above the surface of the water in the water bath.

Once thawed, the vials were removed from the water bath and sterilized from outside with 70% ethanol before transferring under the laminar cabinet. The contents of the vial were immediately transferred to a 10 mL falcon tube containing 9ml complete culture medium. The cells are then spin down at ~125g for 5 to 7 mins in an centrifuge to remove any DMSO remaining from the freezing medium. Prior to adding the cells, the culture flask containing the respective amount of culture media was placed inside the incubator for 15 mins to avoid the excessive alkalinity of the medium during the recovery of the cells and allow the culture

medium to reach its normal pH (7 to 7.6). The cell pellet is then resuspended in complete culture medium containing and dispense into an 75cm^2 flask. The cells are then maintained under sterile conditions in incubator at 37°C, 5% CO_2. The medium is changed at least twice a week during the propagation period.

3.2.8.1.2. Sub-cultivation of cell lines: HepG2 and HeLa

HepG2 and HeLa cells were cultured and maintained throughout the experimental periods at 37°C, 5% CO_2 under sterile conditions of S1. Both of these cell lines were cultured in Dulbecco's modified eagle's medium (DMEM) containing 4.5g/L Glucose, 10% FBS (GIBCO, Invitrogen) and Penicillin-streptomycin (PAN-BIOTECH). Once confluent about (90- 95%), the cells were needed to be split and sub-cultured to maintain their respective phenotype and guaranteed constant growth (ideally Passage 24 for both cell lines). The cell lines were split and maintained at least twice a week with the help of sterile materials and solutions under a laminar flow cabinet. Splitting of cells included, the aspiration of the old media, washing of the monolayer of cells one time with 1×PBS and incubation for 5-7 mins with trypsin/EDTA (PAN-BIOTECH) typically (3ml for a 75 cm^2 cell culture flask) at 37°C, 5% CO_2 inside the incubator to detach the monolayer of cells. Once detached (as visualized under a standard phase contrast microscope) the cells were resuspended with full growth medium with antibiotics. Further, the cells were subsequently diluted with new cell growth medium with antibiotics (preferably 1:4 or 1:6 ratio) in an T75 cell culture flask maintained at 37°C, 5% CO_2.

3.2.8.1.3. Freezing of cell lines

Once recovered, the first few passages (P4 to P7) of the cell lines were cryopreserved and stored at -70°C in liquid nitrogen tank for long term use. The confluent cells are washed one time with 1x PBS, trypsinized in 3 ml trypsin/EDTA, diluted in complete growth medium (~9ml) and centrifuged at 125g for 5-7mins. They are then further resuspended in cryopreservation medium with 5% (v/v) DMSO and are flash freeze by storing them at liquid N_2 tank.

3.2.8.1.4. Cell counting and seeding of cell lines for live cell imaging experiments

90-95% confluent cell culture were used for all the cell morphology, toxicity and live cell imaging-based experiments. The cells from confluent flask where diluted post trypsinization with help of complete culture growth media (3ml trypsinized cell suspension in 7ml DMEM containing FBS and antibiotic: solution A). Cells per ml were counted using 1x 102 dilution i.e. 100 of solution A in 10 ml of CASYton buffer using a CASY cell counter (3.2.8.1.4.F1).
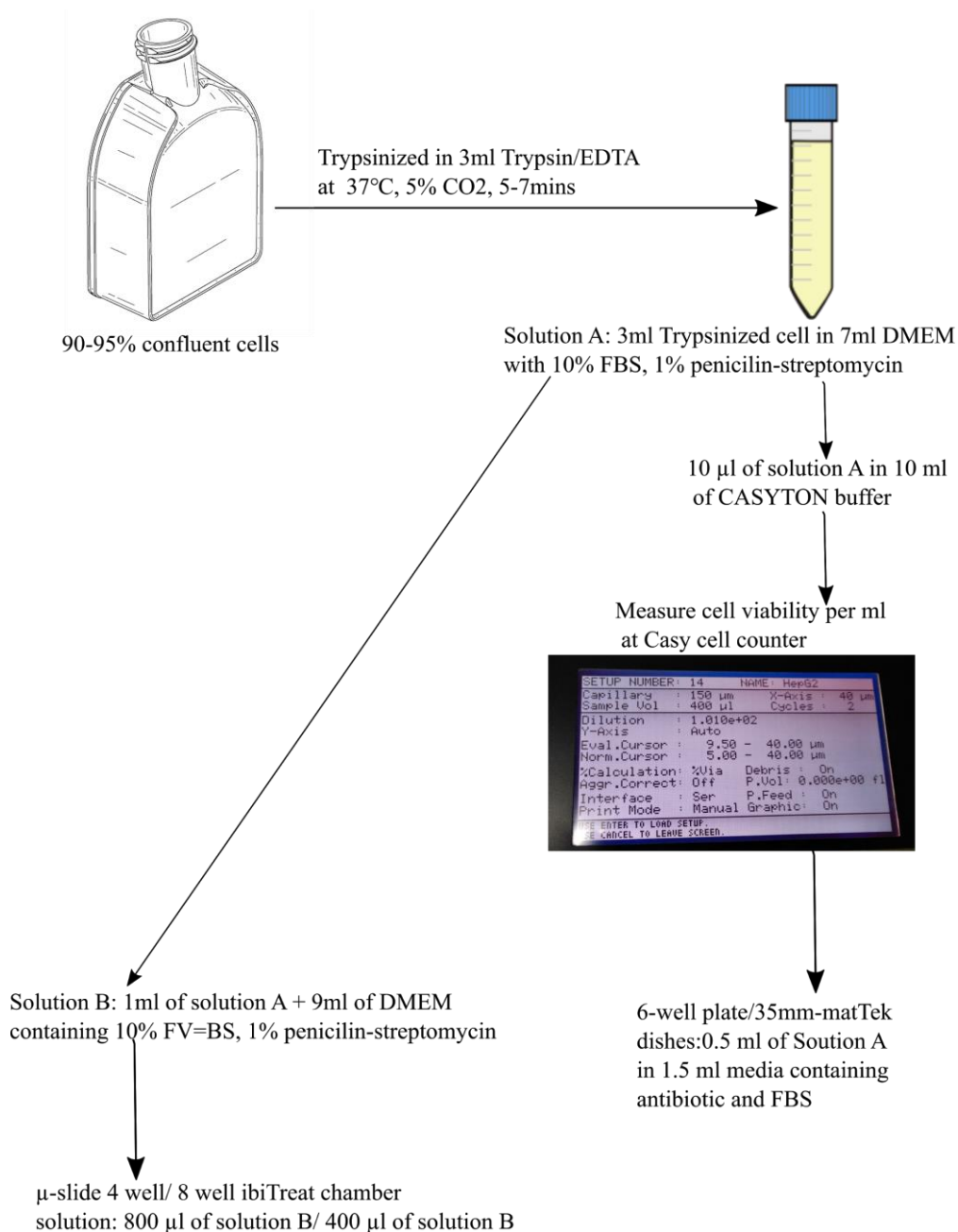

Fig.3.2.8.1.4.F1. Workflow of cell counting and seeding for cell lines

Depending on the format of well plate used for experiments, the cells were further diluted using the complete culture growth medium (Table.3.2.8.1.4.T1). Appropriate volume of the resuspended cells is then seeded in dishes and incubated at least for 5 to 6 hours at 37°C, 5% CO_2 before being transfected or used for any assay.

Table.3.2.8.1.4. Cell culture seeding conditions for cell line

Culture well format	Cell number/well	Medium & additives	Culture type and experiment
35mm- MatTek glass bottom dishes	2×10^5- 5×10^5 cells per/well	1.5 ml	Dose response FRET experiments in HepG2
µ-slide, 8-well ibiTreat chamber	a. 25000-50000 cells/well	400 µl	CTB assay HepG2, Live cell imaging HepG2, Time-lapse imaging
	b. 10000-15000 cells/ well	700 µl	CTB assay PMH, Live cell and time-lapse imaging

3.2.8.1.5. Transient transfection of cell lines: HepG2 and HeLa

For live cell microscopy of actin cytoskeleton / FRET signal and bright field imaging, both cell lines i.e. HepG2 and HeLa cells were seeded in a µ-slide 8-well, chambered glass ibiTreat:#1.5 polymer coverslip, tissue culture treated, sterilized and 35mm- glass bottom dishes (MatTek). After roughly 6 hours post seeding, the cells were transfected with the plasmid of interest using non-liposomal lipid-based transfection reagent effectene (Qiagen). The appropriate amount of DNA-transfection mix was calculated as per the concentration of the DNA and the well format in which cells were seeded (Table.3.2.8.1.5).

Table. 3.2.8.1.5. Amount and list of transfection constituents

Reagent	Volume added/well of a 6 well plate or 35 mm-MatTek glass bottom dish Format	Volume added/well of a µ-slide 4 well ibiTreat chamber
EC Buffer	100 µl	50 µl
DNA amount	1µg/µL	1µg/µL
Enhancer	1 µg DNA to 8 µl Enhancer	1 µg DNA to 8 µl Enhancer
Vortex for 2 seconds and incubate at RT for 5 mins		
Effectene transfection reagent	5 µl	2.5 µl
Vortex for 2-5 seconds, incubate at RT for 15-20 minutes to allow the transfection-DNA mix to form		
Final amount added	114 µl	61.5 µl

The detailed steps involved in the transfection were as follows:

1. 0.25 µg DNA per construct was diluted in Buffer EC to final volume of 100 µl.
2. [8 x Net amount of DNA used (µg)] µl of Enhancer reagent was added to the DNA-EC Buffer mixture.
3. The mixture was then vortexed for 1 second and incubated at RT for 2-5mins.
4. The effectene transfection reagent (5 µl per MatTek dish) was then added to the above mixture. This transfection mix was vortexed again for 1-2 seconds and incubated at RT for 5-15 mins.
5. During the incubation period, the old medium was aspirated and new complete culture growth medium with antibiotic was added in the MatTek (1.5 to 2.0 ml) and µ-slide, 8-well ibidi chambers (400 to 450µl).
6. Depending on the well format (Table.3.2.8.2.3) the DNA-transfection complex was added to the dishes.

7. The cells were then incubated at 37°C, 5% CO_2. Cell lines expressed protein 6 to 7 hours after transfection. Overnight incubation only maximized expression.

8. Next day, the cells were used for live cell imaging experiments.

3.2.8.2. Isolation and cultivation of primary mouse hepatocytes

3.2.8.2.1. Protocol for isolation of primary mouse hepatocytes

Perfusion apparatus

The primary mouse hepatocytes were freshly isolated from C57BL/6N mice using in-house well-established two-step perfusion protocol which is based on an isolation method described by (Seglen, 1976). The perfusion apparatus includes setting up of an infusion pump as per the manufacturer's protocol. The first step was to remove the small plastic from one end of the apparatus and was fixed to the 3 way stop cock, while the other end of the plastic tube was placed into a reservoir containing the perfusion buffer which was immersed in a 37°C-water bath. Opposite to the tube, the infusion tube extension was connected with the 3 way stop cock. The other end of this tube extension carries a blunt cannula which will later be injected into the blood vessel. The tube is spirally coiled on the heating element to ensure warming of the appropriate perfusion buffer before entering the liver through the needle. The third conjunction of the 3 way stop cock is fixed to another connection tubing i.e. "Heidelberger extension". This conjunction enables pressure release in case the pressure in the perfusion system is too high. The system needs to be rinsed once with EGTA perfusion buffer before usage to avoid air bubbles in the tubes that might perturb the liver perfusion. During the entire perfusion process the flow rate is set to 15 mL/min.

Mouse surgery and isolation of cells

8 to 12 weeks old mice were allowed to acclimatize under laboratory conditions and exposed to 12-hour light/ dark cycle with ad libitum food and water. The mice were anaesthetized via an intraperitoneal injection of a mixture consisting of Xylazine (Rompun® 2%, Bayer, Leverkusen, Germany) and ketamine (Ratio pharm, Ulm, Germany). The amount of ketamine-xylene mixture was carefully administered in appropriate amounts as mentioned in the table 3.2.8.2.1.T1.

Table.3.2.8.2.1. Dosage of anesthesia administered in mice

Drug	Amount per anesthetic compound administered in mice
Ketamine	61.5 mg/kg of the body weight
Rompun	20 mg/kg of the body weight
Needle	BD microlance 3, 26G x 5/8, 0.45 mm x 16mm
Syringe	BD 1ml syringe (REF 300013)

The effect of anesthetic was regulated by checking the eyelid reflex by touching with a soft brush and the pain sensitivity via the pedal reflex by checking with pressing the feet in between blunted forceps. The mice were then fixed on a grid table in the dorsal position resting on the grid (3.2.8.2.1.F1.A). The abdominal cavity was then opened longitudinally using sterile dissecting material. Vena cava of the mouse was then incised, and a blunted needle was inserted into the vena cava. This needle was connected to a sterilized flexible plastic tube that was controlled through a pump and placed in the appropriate perfusion buffer (3.2.8.2.1.F1.B).

The liver was first carefully perfused with pre-warmed EGTA-buffer. The flow rate during the perfusion was maintained to 9 ml/min. The perfusion was carried out for 10 to 15 mins to remove any blood and Ca^{2+} dependent adhesion factors. Collagenase buffer pre-warmed to 37°C was then exchanged with the EGTA-buffer. The collagenase buffer digested the extracellular matrix and reduced the cell-cell adhesion contacts, thus helping in a homogenous suspension of cells. Depending on the activity of the collagenase in the buffer, the flow rate was maintained to 9 ml/ min during the perfusion. The perfusion was stopped once the liver changed its color from dark red to a soft pale-yellow color, marking the end of successful perfusion (3.2.8.2.1.F1.C). The liver was then carefully excised with the help of blunt pincers and forceps near the thoracic blood vessels. It was then placed in a sterile petri plate (3.2.8.2.1. F1.D) under laminar flow cabinet immediately and immersed in ~50 ml suspension buffer (3.2.8.2.1.F1.E). The capsule was removed by gently shaking the liver slowly in the buffer. The suspended cells were then filtered through a 100 μm cell strainer. This suspension was then centrifuged in a 50 ml falcon tube for 5 mins at 4°C, 50 g. This process helped in the

removal of any non-parenchymal cells (NPCs) from the hepatocytes. The supernatant was then discarded, and the pellet was resuspended gently without any stress to hepatocytes in 10 ml suspension buffer by gently inverting the falcon tube several times and avoiding any pipette up down method. The cells were then placed on ice till they were used for plating for the experiment.

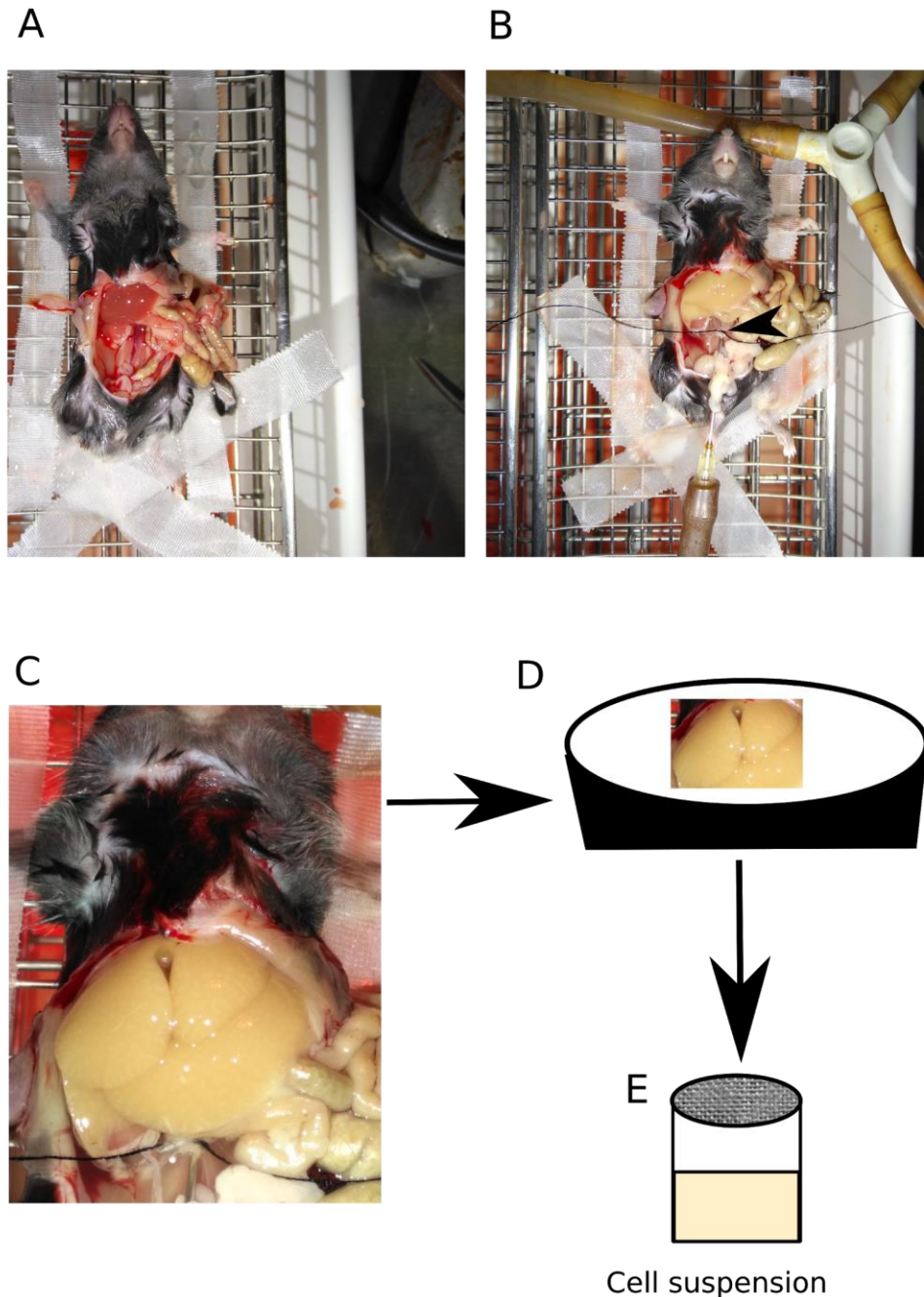Fig.3.2.8.2.1. Isolation procedure of primary mouse hepatocytes. A. Dorsal view of mouse with dissected abdominal cavity. B. Vena cava inserted with a blunt needle (black arrow), which is continuously supplied with hepatocytes perfusion buffer. C. Perfused liver lobes of the mice. D. Petri-dish containing the dissected liver lobes. E. Cell suspension containing hepatocytes passed through the sterile filter membrane (gray grid).

3.2.8.2.2. Cell viability and cell counting of primary mouse hepatocytes

To check the cell viability of the freshly isolated mouse hepatocytes before being used for any cytotoxicity assay, healthy living cells were counted using trypan blue staining method. 400 µl of isolated cell suspension was diluted in 100 µl of 0.4% sterile trypan blue solution with the help of wide-bore pipette tips. The tube was inverted gently and roughly 50 µl of this cell suspension in trypan blue was loaded onto a Neubauer counting chamber. The amount of viable and dead (blue) cells were counted rapidly within 5 minutes after dilution process, as the trypan blue can affect the viability of the cells itself. Cells were counted under a bright field microscope in both the chambers of the Neubauer chamber which contained 4 quartiles in both the chambers of the Neubauer chamber. Each quartile consisted of 4 x 4 small squares (3.2.8.2.2.F1).
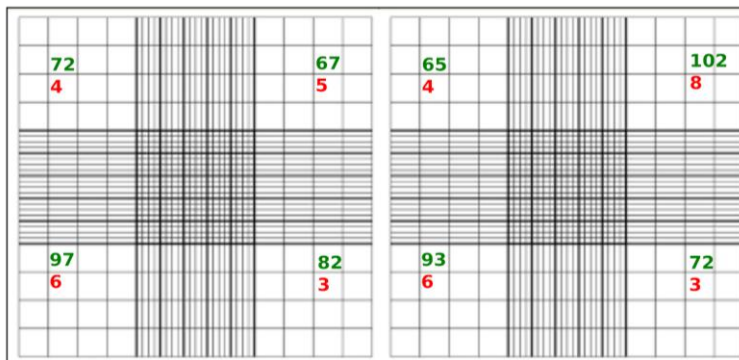
Living cells in total: 72+67+82+97+65+102+93+72 =650
Dead cells in total: 4+5+3+6+4+8+3+6=39

Average living cells per quartile: 650/8=81.25
Average dead cells per quartile: 39/8= 4.875

Average of total cells per quartile: 81.25+4.875=86.125

$$Viability = \frac{average\ living\ cells\ per\ quartile}{average\ of\ total\ cells\ per\ quartile} \times 100\%$$

Viability = 81.25/86.125 x 100% =94.3%

Fig.3.2.8.2.2. F1. Neubauer cell counting chamber (0.100mm depth) and cell viability measure.

The average of both viable and dead (blue) cells per quartile was determined and the viability was measured as ratio of average of living cells per quartile / average of total cells per quartile multiplied by 100 to get the percentage. The total amount of living cells per ml were measured as: **Cells per ml= average living cells per quartile x dilution factor x 10.000**

For all the cytotoxicity assays, FRET and cytoskeleton imaging primary mouse hepatocytes viable less than 60% were not used. Only cells with viability higher than 60% were seeded and plated for any experiments in this study.

3.2.8.2.3. Cultivation and seeding of primary mouse hepatocytes for long term live cell imaging.

In the following study, primary mouse hepatocytes were cultured in both sandwich and monolayer depending on the type of assay, biological or cellular function to be observed post drug treatment. The number of cells seeded was dependent on the type of culture system and the assay as mentioned below (Table.3.2.8.2.3.T1). Primary mouse hepatocytes were cultivated in William's E Medium supplemented with growth factors and antibiotics (Table.3.1.5.2) and maintained under sterile conditions at 37°C, 5% CO_2 during the entire period of experimentation.

Table.3.2.8.2.3.T1. Cell culture seeding condition for primary cells

Culture well format	Cell number/well	Collagen 1 mg/ ml	Medium & additives	Culture type and Experiment
μ-slide, 4-well ibiTreat chamber	a. 3×10^5 cells per/well b. 140900 cells/ well	Pre-coated 200 µl	700 µl 700 µl	Monolayer (CTB assay) Sandwich (Live cell imaging)
μ-slide, 8-well ibiTreat chamber	c. 25000-50000 cells/well d. 169076 cells/ well	- Pre-coated	400 µl 700 µl	CTB assay HepG2, Live cell imaging HepG2, Time-lapse imaging CTB assay PMH, Live cell and time-lapse imaging

3.2.8.2.3.1. Cultivation of primary mouse hepatocytes in collagen monolayer system

Primary mouse hepatocytes were cultivated in pre-coated μ-slide, 4 well Collagen IV pre-coated coated dishes (Art.Nr.80422, ibidi GmbH; Martinsried, Germany). 300000 cells/well were suspended in 700μl hepatocytes seeding medium (Table.3.1.5.2) to obtain a confluent culture which was used for bile acid toxicity experiments and actin cytoskeleton imaging. The cells were then incubated for 3hr at 37°C, 5% CO_2 in order to allow their attachment and growth. After 3hrs, the medium was aspirated off to remove the FCS and stop de-differentiation of hepatocytes. The cells were then washed carefully 3 times with hepatocyte washing medium (Table.3.1.5.2) in to remove any dead cells or debris. Fresh hepatocytes culture medium was added to each well and the cells were incubated at 37°C, 5% CO_2 at least for 2-3 hours before the imaging and experimentation. In monolayer, the primary mouse hepatocytes can be used until 24 hours post seeding are optimal for any relevant experimental observations. Post 24 hours, primary mouse hepatocytes start de-differentiating.

3.2.8.2.3.2. Cultivation of primary mouse hepatocytes in collagen sandwich system

Primary mouse hepatocytes were cultivated and seeded depending on the type of culture format (Table.3.2.8.2.3.1) between two soft layers of rat tail type I collagen.
The lyophilized collagen (10 mg, Roche) was dissolved night before or minimum 3 hours before plating in 10 ml of 0.2% sterile filtered acetic acid solution and was stored at 4°C. Depending on the type of culture format used (Table.3.2.8.2.3.2.1) the collagen was prepared for first layer on ice and was mixed with appropriate amount of 10x DMEM and the pH was adjusted using 1M NaOH.

E.g. For each well of a 6-well plate, 250 μl of dissolved collagen (1mg/ml)- DMEM mixture is used. The pH of this mixture is adjusted by adding ~150 μl of 1M NaOH.

This was prepared by diluting 3 ml of sterile collagen (1 mg/ml) with 1/10nth of 10x DMEM i.e. 350 μl in a 50ml falcon tube placed on ice under sterile conditions of a laminar air flow cabinet. The DMEM-collagen mixture was then gently mixed by avoiding any bubbles. The pH of this mixture was neutralized by adding dropwise 1M NaOH until the color of the mixture

turns from yellow to pink. The final concentration of the collagen per well was always 1 mg/ml. This mixture was prepared always fresh and used within 1hr from the preparation time.

The mixture was then carefully added to the wells (250 µl/well of a 6-well plate) and distributed evenly either by quick movements of a cell scraper or by gentle shaking of the plate up and down, side to side until the bottom of the well was evenly completely covered with DMEM-collagen mixture. While shaking, care was taken to avoid any air bubbles in the layer as this may interfere with the cell growth.

The plates were covered and allowed to dry ~5-10 mins till the collagen gel mixture was polymerized. The remaining solution was kept as a check for the end point of polymerization. Once polymerized, the plates were seeded with appropriate number of cells depending on the culture format and condition in prewarmed hepatocyte seeding medium i.e. William's E medium supplemented with additive and FCS. The plates were gently shaken in EWNS direction for distributing the cells evenly. The amount or number of hepatocytes, seeding medium and HepG2 cells seeded was as described in Table.3.2.8.2.3.2.1.

E.g. For a 6-well plate, 2 ml of seeding medium is required per well. 12 ml of seeding medium is required, hence an additional amount i.e. 20 ml is prepared by diluting 20 ml of Hepatocyte culture medium with 2 ml of 10% FCS.

The plates were then transferred to an incubator with constant temperature of 37°C and 5% CO_2 at least for 3 hours before adding the second layer of the collagen. The plates were intermittently shaken at least 2 to 3 times in EWNS direction to avoid cell aggregation in the center of the well which can affect the cell growth.

Post 3 hours the attached hepatocytes were washed with hepatocyte washing medium i.e. William's E medium without additional additives and FCS 3 times to remove any unattached or dead cells before adding the second layer of the collagen. The appropriate amount of DMEM-collagen mixture was then added as a second layer (Table.3.2.8.2.3.2.1) and the plates were then transferred to the incubator immediately after evenly distributing the collagen gently by shaking. The second layer roughly needed 15-30 mins to polymerize. Once polymerized, hepatocyte culture medium was added to each well of the plate and the cells were incubated at 37°C, 5% CO_2 for optimal growth.

3.2.9. Cytotoxicity estimation with cell viability assay

To determine the cytotoxic concentrations of different bile acids in cells, the Cell Titer-Blue® viability assay kit was used. The assay is based on a dark blue indicator dye called resazurin that can measure the metabolic capacity of cells. Resazurin is reduced to resorufin, which is highly fluorescent in nature. Viable cells can retain the ability to reduce the resazurin whereas the nonviable cells will have reduced resorufin production thus indicated by no strong fluorescent signal.

For this assay, the primary mouse hepatocytes were cultivated as monolayer (300000 cells per well) in a collagen type IV coated 4-well IBIDI chambers (see section 3.2.8.2.3.1). While the HepG2, were cultivated in µ-slide 8-well ibiTreat cell culture treated chambers (see section 3.2.8.1.4.).

Once allowed to adhere, i.e. minimum 6 hours for primary mouse hepatocytes and 24 hours for HepG2, the cells were incubated with different concentrations of different bile acids diluted in cell culture medium (WEM with additives/ DMEM with additives). After 24 hours incubation with bile acids, the cells were washed one to three times with pre-warmed $1\times$ PBS. Depending on the volume of the dish, pre-warmed Cell Titer-Blue reagent and medium (1:4) was added (Table.3.2.9.T1).

Table.3.2.9.T1. Cell Titer-Blue reagent concentrations

Culture format	Cell Titer blue reagent (µl)/well	Medium (µl)/well
µ-slide, 4-well ibiTreat chamber	100 µl	400 µl
µ-slide, 8-well ibiTreat chamber	40 µl	200 µl

The medium from the well which was untreated i.e. without any bile acid and the well which was incubated with vehicle control i.e. solvent in which the bile acid stocks were made, was also incubated with the Cell Titer-Blue® and used as a separate measure for control. An

additional solvent control was hepatocyte cultivation medium incubated with Cell Titer-Blue® reagent.

After 60 minutes incubation for HepG2 and 90 minutes incubation for PMH at 37°C, 100 µL of Cell Titer-Blue® reagent-media mixture or the supernatant from each well was transferred to a well of a 96-well microtiter plate with black walls and a flat, transparent bottom. For each treatment/ bile acid concentration, ~ two to four technical replicates were prepared within the experiment. The fluorescent signal was then measured at $579_{Ex}/584_{Em}$ nm of each well using a microtiter plate reader (Infinite M200 Pro, TECAN) and readings were stored in an excel file.

3.2.10. Imaging modalities and Microscopy methods

3.2.10.1. Time-lapse microscopy

Time-lapse microscopy was performed on both HepG2 and primary mouse hepatocytes (PMH) to capture cell death events over 24 hours after exposure to different bile salts. Environmentally controlled Olympus IX 81 inverted wide-field microscope equipped with UPLFLN 10x objective, with motorized stage, shutters, filter wheels with CCD camera (Olympus XM 10T, Hamamatsu ORCA-R2) was used (3.2.10.1.F1A).

The system was calibrated at least 3 hours before experiment and adjusted for constant temperature of the imaging chamber to 37°C, 5% CO_2 and 60% humidity by setting the required values in the climatization control (3.2.10.1.F1B). Both liver cell line and primary cells i.e. HepG2 (50000 cells in 400 µl of DMEM supplemented with 10% FBS and 1% pen-strep medium per well) and primary mouse hepatocytes (300000 in 700 µl of WEM supplemented with additives and antibiotics per well) were seeded (see section 3.2.8.1.4. And 3.2.8.2.3.1).

In case of HepG2, the cells were allowed to grow and adhere for a period of 5 to 24 hours post seeding. Whereas the primary mouse hepatocytes seeded as monolayer were allowed to grow and attach at least for 3 hours at 37°C, 5% CO_2 before the experiment began. Once the cells reached 80-95% confluency, the chambers were used for experiment.
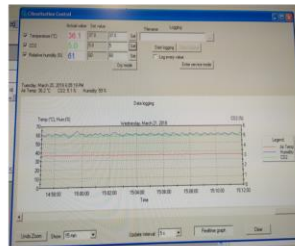
The chambers containing the cells were allowed to equilibrate in the time-lapse imaging system at least for 1 hour at 37°C, 5% CO_2, 60% humidity before start of the experiment (3.2.10.1.F1.C). Four positions per well were marked and saved as a list using the stage window integrated in the Xcellence rt imaging software of the microscope (3.2.10.1.F1.D). Bright-field images of all the marked positions were captured by the integrated Hamamatsu camera using a UPLFLN 10x objective, U-PH1 condenser at exposure time of 35 milliseconds.

The old media was removed, and appropriate bile salt working solutions were added to the respected wells of the chamber. The imaging chamber was immediately transferred back to the microscope imaging chamber. Any corrections for focus drifts and XYZ change in the position of the cells were made and the new positions were stored as a new list. For each such experiment, a database was created, and images were taken 100 cycles every 30 minutes after addition of the bile salts (3.2.10.1.F1.E).
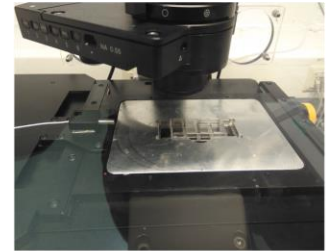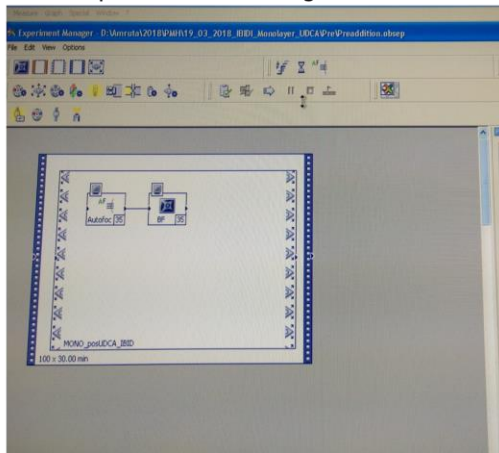

Fig.3.2.10.1.F1. Steps in acquisition of data on time lapse imaging microscope. A. Setup of basic time-lapse microscopy imaging unit. B. Integrated software controlled climatization. C. Imaging chamber inside a routine time lapse imaging unit. D. Representative image of one such experiment with list of different positions across well to be imaged. E. Final experimental manager or database containing the details of the imaging parameters.

3.2.10.2. Confocal microscopy

Point-scanning confocal microscopy was performed by using the Zeiss LSM 880 laser scanning confocal microscope equipped with a Zeiss Plan Apochromat 63x/water immersion objective. The stage of the microscope was automated and enclosed in a CO_2/Humidity/Temperature controlled incubator. Cells were maintained inside this imaging chamber of the microscope throughout the experimental duration at temperature of 37°C and constant supply of 5% CO2.

3.2.10.2.1. *Fluorescence resonance energy transfer (FRET) in single cells*

The fluorescence resonance energy transfer is a measure of energy transfer between two fluorophores, in this case CFY-YFP (see section 3.1.9). The FRET value is a direct measure of any posttranslational modifications, conformational change or protein-protein interactions in living cells at subcellular resolution.

Here, ratiometric FRET was measured in HepG2 cells treated with different bile salts. The cells were cultivated in µ-slide 8 well ibiTreat chambers (see section 3.2.8.1.4). 5 hours post seeding the cells were transiently transfected with CytoBAS, a genetically encoded bile acid sensor that can measure the bile acid concentrations in the cytosol (see section 3.2.8.1.5).

Next day, the cells were adhered and ready for imaging. The old medium was replaced from all the wells, after washing the cells 3 times with 1✕ PBS. Fresh DMEM with phenol red and antibiotic was added to each well. The pH of the cells was constantly monitored throughout the experiment as the sensor is pH sensitive. Bile acids were diluted in DMEM containing phenol red, FBS and antibiotics in desired concentrations and volume.

The microscope was equipped with a 63X/1.20 W M27 immersion objective and appropriate laser excitation lines: 405 nm (UV-diode), 458, 488 and 514 nm (Argon) and 561, 633 nm (Helium-Neon).

For single cell imaging of FRET in live cells, following settings were applied:

1. The acquisition mode was xyt (time-lapse imaging of a single focal plane).
2. Pinhole was adjusted to 1 Airy unit, 512 x 512 frame size and 2 averaging.
3. The bit depth was 12 with scanning mode as frame mode and averaging method was mean.
4. Two independent tracks were set. Track 1 include activated laser lines 458 at 8% and a TPMT channel that acquired a bright field image. The ECFP and EYFP channels were used to detect the fluorescent intensity of donor i.e. cerulean 450-520 and acceptor i.e. citrine: 520-580 nm in the same cell.
5. Track 2 included 514 nm laser line at 5%, that acquired the intensity of only the acceptor-acceptor i.e. the citrine: 520-580 nm.
6. Images were acquired of at least 5-6 cell clusters containing 3-4 cells for all 3 channels per condition before adding bile acids. For each cell cluster the gain and offset of each channel was adjusted to distinguish the signal from the background while remaining below the saturation for all the pixels in the cells images.
7. All cells with similar fluorescence intensity, average shape and size of the CBAS were chosen. The positions of these cell clusters were saved as a list.
8. Relevant bile acid stock solutions were then added to the edge of the 8 well chamber without moving the dish or changing the focus.
9. Immediately post addition at an interval of 2 minutes, 100 cycles for each such cell cluster per concentration of bile salt was acquired.
10. Images were also captured post 5 mins and 24 hours of same cell clusters to measure the ratiometric FRET after bile acid exposure.
11. At the end of each experiment, the data was saved as an experiment and exported into a CZI file.

3.2.10.2.2. Live cell imaging of detection of intracellular bile acid concentrations and cortical F-actin using FRET Biosensor and actin-binding domains

For visualizing the endogenous F-actin in cells after exposure to different bile salts, a genetically encoded actin-binding domains LifeAct, a short 17-amino acid peptide derivative from yeast fused to RFP was used (Riedl et al., 2008).

HepG2 were seeded in µ-slide 8 well ibiTreat chambers as described previously in section 3.2.8.1.4 and then transfected with LifeAct TagRFP and CBAS (section 3.2.8.1.5). The images were acquired using standard laser scanning confocal microscope from Carl Zeiss, LSM 880 equipped with a 63X/1.20 W Korr M27 immersion objective.

The imaging parameters to measure the FRET and visualize the cortical F-actin were as follows:

1. The acquisition mode was xyt (time-lapse imaging of a single focal plane).
2. The dish was allowed to equilibrate inside the imaging chamber at 37°C, 5% CO_2 at least for a hour before the start of the experiment.
3. Images were captured at frame size of 512X512, 12 bits as the bit depth, averaging of 4 and method of averaging was mean, and mode was line. The pinhole was adjusted to 120.1 AU.
4. The laser lines used were 458, 514 and 633 nm. The intensity of laser lines was 488: 4.5%, 514: 1% and 633: 0.5%.
5. The gain and offset were adjusted for all the three laser lines, to avoid any background interference while controlling degree of saturation of all the pixels of cell images.
6. 3 independent tracks were selected using the ZEN blue imaging software. Track 1 used laser line 458 nm with channels ECFP and EYFP. The ECFP acquired images of the donor-donor intensity of the CBAS while EYFP image was the donor-acceptor intensity. The beam splitter was MBS 458/514.
7. Track 2 captured image of the acceptor-acceptor intensity that was acquired by excitation of the acceptor i.e. citrine alone by laser line 514 nm. Beam splitter 458/514 was used to select the light that could pass. It also consisted of an additional bright field image acquired by TPMT.
8. Track 3 of the imaging setup included activation of laser line 633 nm, with a beam splitter MBS 488/561/633 nm. This channel had settings as use for Alexa Fluor 647 and it acquired images of the F-actin signal in the cortex of the cell.
9. A single image consisting of donor-donor intensity, donor-acceptor intensity, acceptor-acceptor intensity, F-actin network and bright field image of the same cell was acquired before addition of any bile acids.

10. Bile acids were then added to the edge of the well and images were acquired of the same cell clusters after 5 mins post BA addition and imaging was continued overnight > 24 hours.

11. After 24 hours exposure to bile acids, timeseries with 64 cycles every 5 seconds were also acquired.

12. The data was stored as a CZI file format and later quantified using ImageJ and in house written analysis plugins.

3.2.10.2.3. Live cell imaging of actin dynamics using cell permeable small molecule dye SiR-actin

The use of life act to visualize endogenous actin requires transfection and limits to determining the total F-actin network in the cells. LifeAct is also known to have a high affinity to bind the globular actin and create background fluorescence (Melak, Plessner, & Grosse, 2017).

In order to study actin dynamics in a living cell, we utilized a small molecular weight dye: SiR-actin (D'Este, Kamin, Göttfert, El-Hady, & Hell, 2015; Lukinavičius et al., 2014). The dye is highly specific for F-actin thus can accurately predict the dynamics of actin upon exposure to drugs. It is derived from a natural F-actin binding toxin jasplakinolide (***marine sponge Jaspis johnstoni***). A staining protocol was first established in primary mouse hepatocytes to visualize the F-actin network and dynamics using SiR-actin. 500-1000 nM of SiR-actin for 4 to 12 hours incubation were the best optimal conditions for visualization of the actin.

The primary mouse hepatocytes were incubated with SiR-actin in suspension (500 nm, 4°C, 4h). These stained hepatocytes were then plated in a sandwich culture (37°C, 5% CO_2, >3h). Sandwich culture hepatocytes were then exposed to ~EC_{50} concentrations of bile acids along with pre and post BA addition imaging. The dish was allowed to equilibrate inside the microscope incubation chamber (37°C, 5% CO_2, >1h) before imaging was started. The imaging parameters were as follows:

1. The acquisition mode was frame wise, xyt. The images were acquired using air objective EC Plan-Neofluar 20x/0.50 M27. The frame size was 512X512, 8-bit depth and 2x line average. The pinhole was set to 1 Airy unit.

2. The imaging rate was 1 frame per 5 minutes.

3. The SiR-actin is based on fluorophore silicon rhodamine dye and can be visualized using the far-red emission wavelength or laser line Helium-neon 633 nm.

4. The laser intensity was set to 1.8% and the filter used was MBS 488/561/633 nm beam splitter.

5. The gain and offset were adjusted for all the three laser lines, to avoid saturation and background interference.

6. There was only one track selected which included excitation of the 633 nm laser line that acquired image of the actin network and TPMT that acquired the bright field image of the same cell utilizes to check the morphological status of the cell throughout imaging.

7. Imaging was continued overnight after bile acid addition. The data was saved as a CZI file.

3.2.10.2.4. *Live cell imaging of peri-canalicular actin and tubulin in primary mouse hepatocytes*

1. To visualize cytoskeletal components: actin and tubulin in same living cell, the primary mouse hepatocytes (PMH) were incubated with 100 nM of SiR-actin dye in suspension for 12 hours at 4°C and then were cultured as collagen sandwich. After washing and addition of the second layer of collagen, the cultivation medium in the well containing attached cells was supplemented with Tubulin Tracker Green reagent dye (1000 nM) and SiR-actin (100 nM). The cells were incubated overnight at 37°C, 5% CO_2 for incorporation of the dye and optimal labeling of the tubulin and actin. Day 1 post plating, the PMH were homogeneously labeled with a peri-canalicular actin and tubulin. The imaging chamber of the microscope was set to have a constant temperature of 37°C and CO_2 concentration of 5%. The imaging dish with cells was allowed to equilibrate inside the microscope incubation chamber (37°C, 5% CO_2, >1h) before imaging was started. Before addition of the bile acids, at least 2 cycles with a rate of every 10 mins were captured at imaging settings below. The cells were treated with different bile acids and imaging of the cytoskeleton dynamics was carried out. The imaging parameters were as follows:

2. The acquisition mode was frame, xyt. The frame size was 512 X 512, 8-bit depth and line average of 4 with mean averaging method was use. The mode was line. Pinhole was opened and adjusted to 2.68 AU. The air objective used was EC Plan-Neofluar 20x/0.50 M27.

3. The imaging rate was 1 frame per 10 minutes.

4. The Tubulin Tracker Green reagent dye is conjugated with the Oregon Green 488 fluorophore and can be visualized using the Argon 488 laser line. The SiR-actin is based on fluorophore silicon rhodamine dye and can be visualized using the far-red emission wavelength or Helium-Neon 633 nm laser line. The filter set was MBS 488/561/633.

5. The laser intensity for the argon and helium-neon was set to 1.8% and 2.8% and appropriate Fluorescence emission was captured setting the filters to 498-560 nm and 643-735 nm wavelength for both the laser lines respectively.

6. The gain and offset were adjusted for all the laser lines and the DIC/ TPMT channel to avoid phototoxicity, saturation and background interference.

7. Imaging was continued overnight after bile acid addition at above settings. The data was saved as a CZI file.

3.2.11. Image analysis and Quantification methods

3.2.11.1. Cell Titer blue viability assay

The values of fluorescence ($579_{Ex}/584_{Em}$) obtained from the excel file were organized as per the condition in a new excel sheet. R programming language-based algorithm was applied to these values and the EC_{50} values were determined for each bile acid and respective cell line or primary cells. The detailed analysis is described below.

Preprocessing the data

The mean of the vehicle control values called 'c' and the mean of the CTB + Medium (WEM/DMEM) called 'low' is calculated and used as 100% and 0% viability respectively. All the other values are scaled accordingly to these values (by: (value-low)/(c-low)) and multiplied with 100 to obtain percentages.

Fitting the curve

A four-parameter-log-logistic curve (4pLL) is fitted to the data using the statistical software programming language R, version 3.4.4 with additional packages drc (R Core Team, n.d.; Ritz, Baty, Streibig, & Gerhard, 2015).

The model is given by:

$$f(x, (b, c, d, e)) = c + \frac{d - c}{1 + exp(b(log(x) - log(e)))}$$

The parameter *b* describes the steepness of the curve, *d* and *c* the upper and lower asymptotes and e the EC_{50} value.

To estimate the parameters for given dose levels, the reading of the CTB assay was fitted to the above equation numerically with minimization using the Gauss-Newton algorithm.

Estimation

The EC_{50} value is calculated as the concentration, where the 4pLL curve attains the value 50. Confidence intervals are calculated using the delta method.

3.2.11.2. Automated analysis and calculation of FRET efficiency

FRET efficiency for the FXR activation experiments (section) was calculated in an automated manner using a custom python script implementing the following algorithmic steps:

1. Image and metadata extraction from the proprietary file format (CZI) of the three channels:

    DD: Donor-excitation (458 nm, CFP), Donor emission (468-504nm, CFP)
    DA: Donor-excitation (458 nm, CFP), Acceptor emission (524-551nm, YFP)
    AA: Acceptor excitation (514nm, YFP), Acceptor emission (524-551nm, YFP)

2. Background subtraction of all 3 channels.

3. Segmentation of cells using the Otsu or Yen threshold masks of the AA channel.
4. For time-lapse experiments, correction for monitor bleaching of the fluorophores was performed using the DD and AA channels for the donor and acceptor respectively.
5. Application of the derived cell masks to all 3 channels, along with removal of zero-zero pixels.
6. Pixel-wise division of the masked DA and DD or AA channels, to obtain the ratio DA/DD or DA/AA, representing the FRET efficiency for each pixel.
7. Determination of mean, standard error of the mean and median for all pixels in the FRET ratio image.
8. For dose-dependent measurement of FRET, normalization of all FRET values to the FRET value of the vehicle control to obtain fold-change in FRET.
9. For time-lapse measurement of FRET, normalization of all FRET values to the pre-bile acid addition FRET value, to obtain the fold change in FRET.
10. Calculation of the mean propagated standard error of the mean and median for all technical replicates of each condition.

These steps yielded tables containing the change in FRET efficiency after exposure to varying BA concentrations, or over time after exposure to bile acids (BAs). Statistical comparison was performed using the Wilcoxon Sign-rank test with p value ≥ 0.05 considered significant.

Determination of binding affinity for performed by non-linear least squares fitting the normalized FRET values in the dose-response curve to a saturable 3-parameter logistic equation:

$$l_t = \frac{L_{inf}}{1 + e^{-k(t-1)}}$$

The script was implemented in Python 3.4 (http://www.python.org) with the following external dependency packages: czifile (C. Goehlke), tifffile, numpy-mkl, SciPy, pandas.

3.2.11.3. Actin cytoskeleton analysis

LifeAct-RFP transfected cells were utilized to visualize the actin cytoskeleton in cells. Quantitative analysis of the actin cytoskeleton in the cortex was performed using two independent parameters:

Cortical enrichment - relative intensity of actin in the cortex versus the cell

1. Image and metadata extraction from the proprietary file format (CZI) of the LifeAct channel

2. Background subtraction of all 3 channels.

3. Segmentation of cells using the Otsu or Yen threshold to yield masks of the high intensity cortical actin region (cortex mask).

4. Segmentation using BG+30% threshold to yield masks of the entire cells including the cortical actin region (cell mask).

5. Subtraction of the cortex mask from the cell mask to yield a cytoplasm mask.

6. Application of the cortex and cell masks to the LifeAct channel including removal of zero-zero pixels.

7. Determination of the mean, standard error of the mean and median value of the cortex and cell LifeAct intensity.

8. Ratio of the cortex and cell LifeAct intensity yielded cortical enrichment of actin.

Actin coherency in the cortex

Coherency is a measure of the number of clearly defined structures in an image. In the case of actin, coherency may be used to differentiate between long isolated filaments (high coherency) versus short grid-like meshes (low coherency). Coherency of the actin filaments in the cortex was quantified using the method described previously (Weichsel, Herold, Lehmann, Kräusslich, & Schwarz, 2010).

Mathematically, coherency is defined as:

$$Coherency = \frac{\lambda 1 - \lambda 2}{\lambda 1 + \lambda 2}$$

where $\lambda 1$ and $\lambda 2$ are the large and small eigenvalues of the structure tensor respectively.

The structure tensor of the image defines the intensity gradients seen in a pixel neighborhood of a given size. The following algorithmic steps was utilized to quantify actin cortex coherency in the LifeAct-RFP images:

1. Image and metadata extraction from the proprietary file format (CZI) of the LifeAct channel.
2. Background subtraction of the channel.
3. Segmentation of cells using the Otsu or Yen threshold to yield masks of the high intensity cortical actin region (cortex mask).
4. Determination of the structure tensor of the LifeAct-RFP channel masked and segmented for the cortex for pixel neighborhood's in the range 0.1 to 5 μm^2 in steps of 0.1 μm^2.
5. Calculation of the eigenvalues of the structure tensor and determination of the coherency as above for all pixel neighborhood sizes.
6. Normalization of the total coherency with the total area of the cortex to account for differences in relative pixel size with biological structures.
7. Coherency showed a saturation behavior at pixel neighborhood sizes greater than 3.0 μm^2, with similar relative differences at all lower values. Hence, the pixel neighborhood size of 2.0 μm^2 was chosen for further analysis.
8. Calculation of mean, standard error of the mean of the coherency per unit area.

The mean cortical enrichment and mean coherency of LifeAct-RFP stained actin was plotted for various bile salts and concentrations. Statistical comparisons were made using the Wilcoxon sign-rank test, with $p \geq 0.05$ considered significant.

4. RESULTS

4.1. Architectural changes in the liver under cholestasis

This section is adapted and re-written from a manuscript **"Vartak, N., Damle-Vartak, A., Richter, B., Dirsch, O., Dahmen, U., Hammad, S., & Hengstler, J. G. (2016). Cholestasis-induced adaptive remodeling of interlobular bile ducts. Hepatology (Baltimore, Md.), 63(3), 951–964. http://doi.org/10.1002/hep.28373"** with permission.

4.1.1. BDL-induced cholestasis and its effect on biochemical and cellular markers

Cholangiocytes are the cells of the ducts which proliferate during cholestasis. This proliferation response is known as '**ductular reaction**'. Anti-BrdU staining of liver slices from BrdU-treated (injection 1hr before harvest) and bile duct ligated mice showed an increased cellular proliferation rate of cholangiocytes in terminal bile ducts (4.1.1.F1.A). The rate of proliferation was highest at day 3 post-BDL and decreased at later time points until day 28 post-BDL (4.1.1.F1.B). Analysis of the serum from sham-operated and bile duct ligated mice showed an in increase in the levels of relevant biomarkers for acute injury such as alanine aminotransferase (ALAT), aspartate aminotransferase (ASAT), alkaline phosphatase (ALP) (4.1.1.F1.C, D, E) at early time points BDL induced cholestasis. The serum bilirubin increased until day 14 and plateaued between day 14 to 28 post-BDL (4.1.1.F1.F). This plateaued effect could be a phase of chronic liver injury. Thus, bile duct ligation was efficient in inducing cholestasis and the consequent ductular reaction in mouse livers.
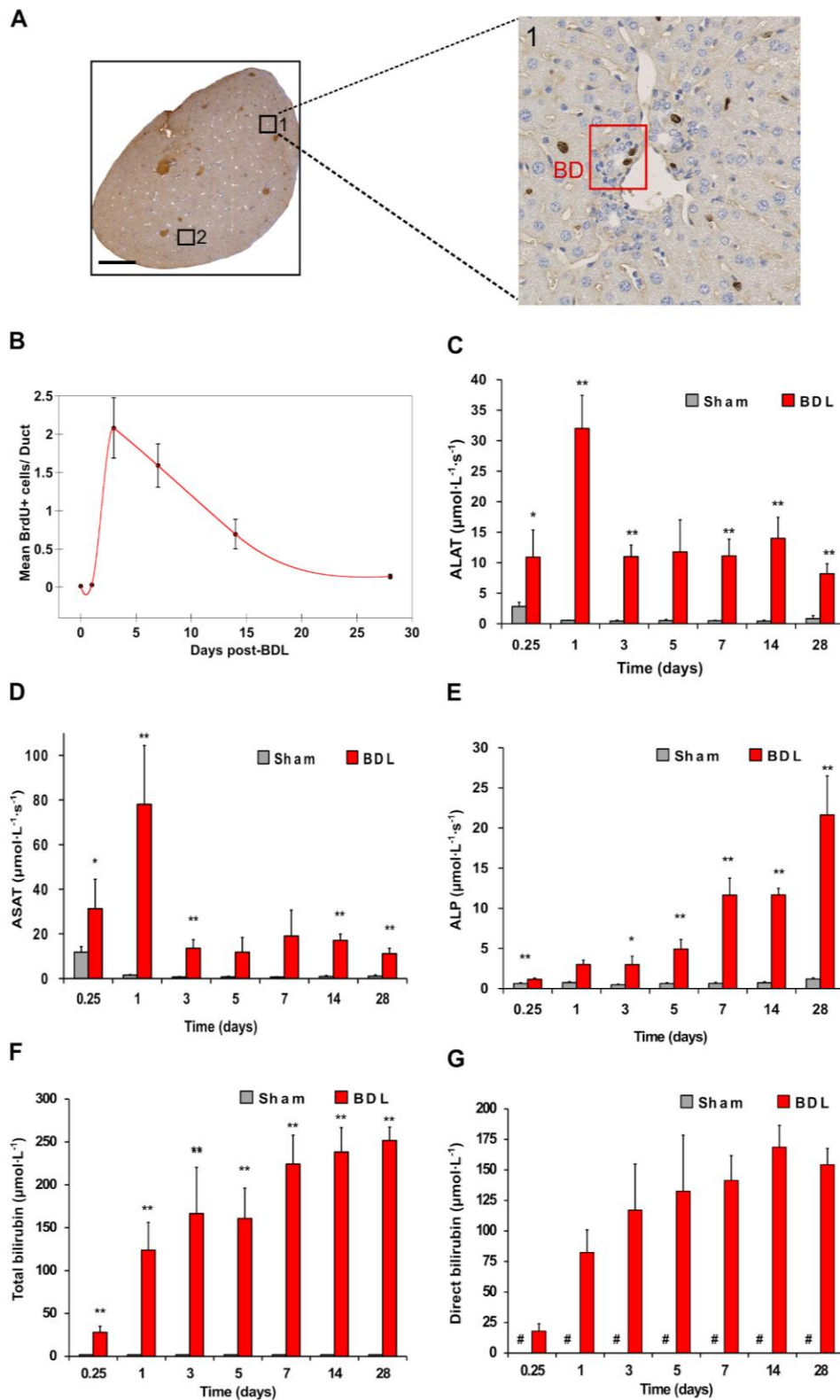
Fig 4.1.1.F1. A. Representative anti-BrdU-stained lobular tissue section with periportal fields as indicated by insets 1 and 2. Top left: Magnified view of one of the portal fields in panel A with BrdU-positive cells (dark brown) and insets showing bile duct cross-sections. B. Quantification of proliferation indices (BrdU-positive cells) in bile ducts on various days post-BDL correspond to rate of proliferation. Points indicate the mean ± standard error of the mean per time point, respectively. The trend line indicates the non-rounded Akima spline. C. Serum

levels of Alanine Aminotransferase (ALAT). D. Serum levels of Aspartate Aminotransferase (ASAT). E. Alkaline Phosphatase level (ALP) in Serum. F. Total bilirubin in the serum. G. Direct (conjugated) bilirubin in serum of sham-operated and bile-duct ligated mice. Values indicate Mean ± SEM of N=6 per time point. The number of asterisks (*) indicates statistical significance as units of SEM, while hash (#) indicates sham-operated set for each time-point. **Figure reused and reproduced from (Vartak et al., 2016).**

4.1.2. Biliary network and architecture is intact post bile duct ligation.

Ductular reactions occurring in cholestasis diseases such as PBC are known to adversely affect the architecture of the liver, one of the effects being the loss of the connectivity of the canaliculi network to the bile ducts. To visualize the 3D spatial-temporal pattern of these reactions in terms of biliary tree alterations, we took vibratome liver slices (4.1.2.F1.A) from healthy and bile duct ligated mice and immunostained them with, DPP4 (Gene ID NCBI:1803) which marked the apical membrane of cholangiocytes, hepatocytes, luminal surface of sinusoidal network and anti-mouse IgG that marked the lobular sinusoidal network (4.1.2.F1.B.[Left panel]). In normal healthy mouse liver slices, all the relevant architectural features i.e. the interlobular bile ducts and their link to the lobular canalicular network were well preserved (4.1.2. F1.B.[Middle and Right panel]). The gross architecture of the liver remained intact over time post bile duct ligation (4.1.2. F1.C). The average diameter of the bile canaliculi was increased by 30% with bleb like protrusions which could intrude into the hepatocyte cytoplasm appeared after 3,7,14 and 2 days post bile duct ligation.
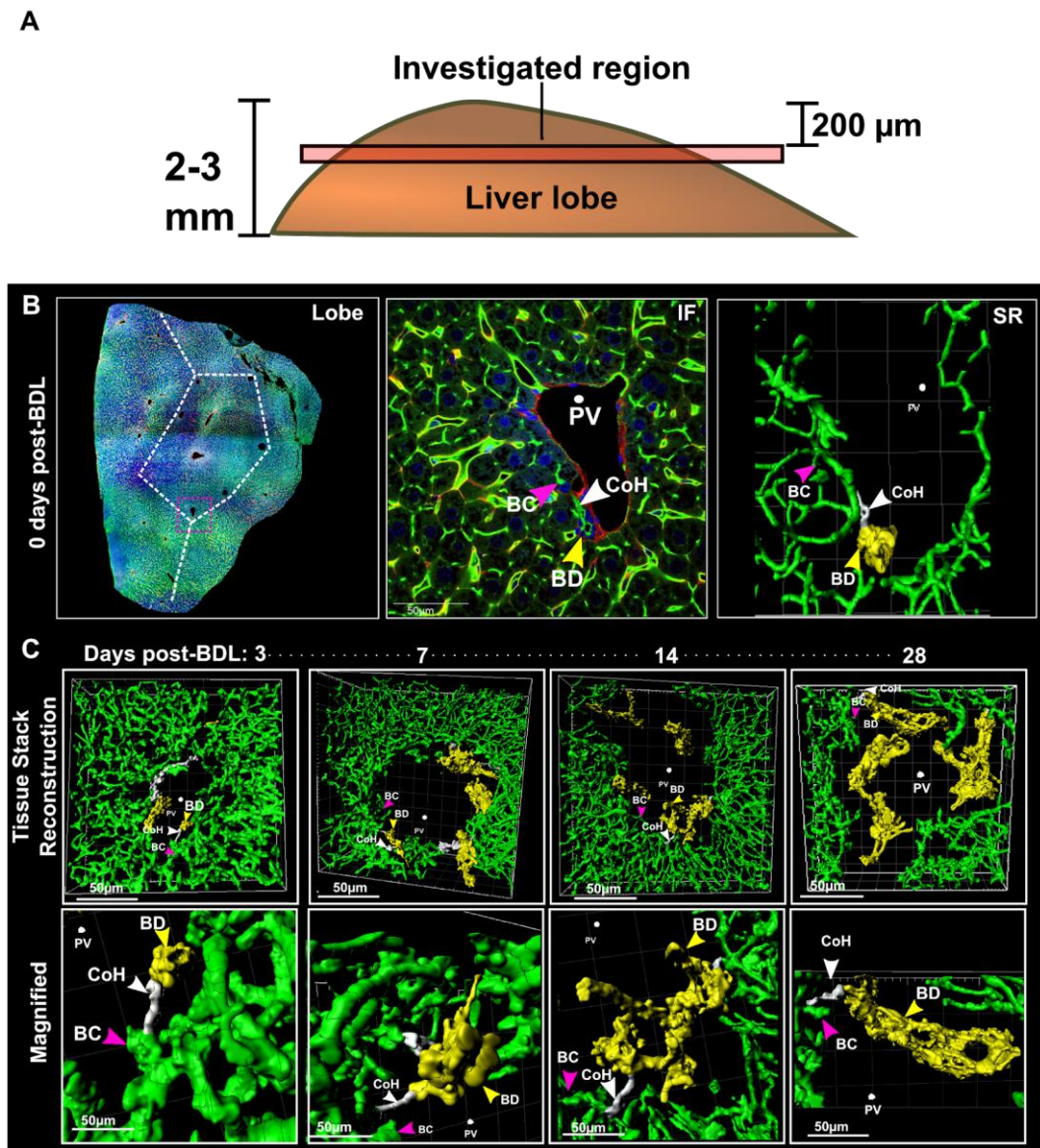
Fig 4.1.2.F1. A. Location of vibratome tissue sectioning in the liver lobe (red bar) that was investigated. B. Representative confocal immuno micrograph of the liver tissue section stained with architectural markers (red, anti-mIgG [sinusoids]; green, anti-DPP4 [apical membranes including ducts, canaliculi and sinusoids]; gray, anti-GS [pericentral area]; blue, DAPI [cell nuclei]) showing a putative liver lobule (white dotted lines) based on field arrangement. The inset (pink dotted lines) indicates a single portal field. Centre panel: Magnified view of the architectural immunofluorescence (IF) of the inset showing the portal vein (PV), bile canaliculi (BC) connected to the bile ducts (BD) via canals of Hering (CoH). Right panel: 3D surface reconstruction (SR) of the same features corresponding confocal Z-stack seen in IF. C. Top row: Representative 3D surface reconstructions of confocal Z-stacks from various days post-BDL showing the presence of intact biliary tree network i.e. bile ducts (BD, green), bile canaliculi (BC, green) and canals of Hering (CoH, white). Bottom row: Magnified view of the same structures indicated in the top row showing that the link of the duct network (BD) is connected with the canaliculi network (BC) via intermediate bridge canals of Hering (CoH) and the ductular network is denser with dilated canaliculi post-BDL. Scale bars: 50µm. **Figure reused and reproduced from (Vartak et al., 2016).**

4.1.3. Denser biliary network as a result of bile duct branching and elongation

Bile duct ligation results in an increase in ductular tissue or dense biliary network, often characterized in 2D histology as increased number of ducts per periportal field. To confirm this, we first investigated the 3D duct morphology of anti-DPP4 marked interlobular bile ducts which were isolated and reconstructed (4.1.3.F1.A) over time post-BDL. The reconstructed duct surface analyzed for morphometric parameters like length, eccentricity, tortuosity with the help of automatic analysis (Supplementary information chapter 3) showed an increase in duct length between days 3 and 7 as well as days 7 and 28 post-BDL (4.1.3.F1.B) in a biphasic manner, leaning towards ductular elongation following injury to the biliary tree.

The increased duct length could be a result of convolution i.e. "twistedness" or duct branching. Convolution measured in terms of 'curvature' of duct along its length i.e. angle at which the duct bends and 'tortuosity' as a measure of ratio of the duct length to the straight-line distance between its endpoints indicated that the interlobular bile ducts (IBDs) have some inherent twistedness and curvature, but both these parameters do not change substantially over 28 days post-BDL (4.1.3.F1.C and D). Instead the duct length increased due to branching of the IBDs. The number of branches per duct increased during day 3 to day 14 post-BDL (4.1.3.F1.E), with maximal branch formation occurring at 6.7 days and remained constant between day 14 to day 28.

The Hill coefficient yielded from fitting of branch frequency data to a logistic equation was 3.73 that indicated a strong cooperative effect in branch formation, showing that existing duct branches tend to produce more branches. The interlobular bile ducts undergo morphological changes post-BDL injury and increase ductular tissue by duct branching and not by duct convolution. This observation is similar to that observed in rats following ANIT (α-napthylisothiocyanate) toxicity, were sprouting of new duct branches occur. This anatomical remodeling of duct could be the first mechanism by which ductular tissue increases post injury to alleviate cholestasis.

A
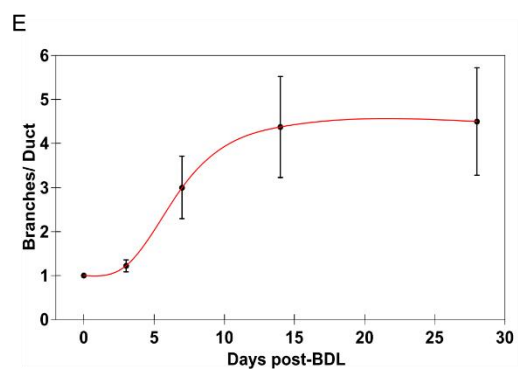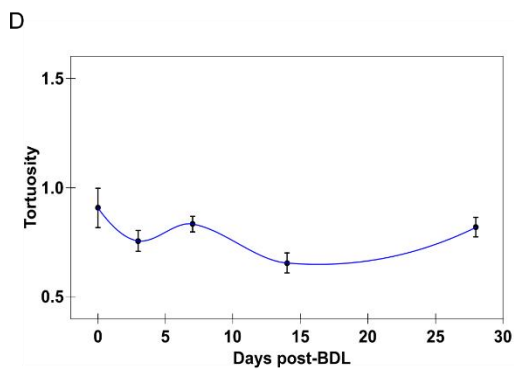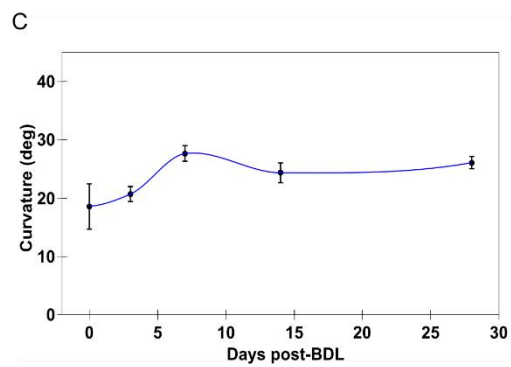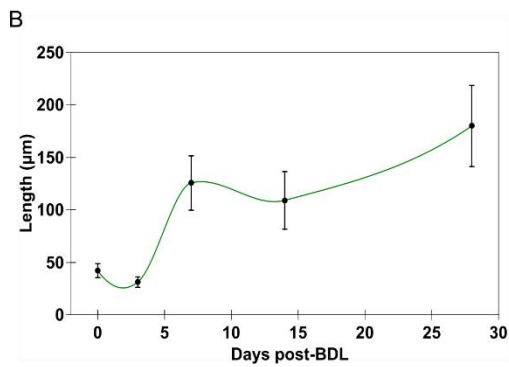Segmented 3D Reconstructions: anti-DPP4 staining the apical membrane
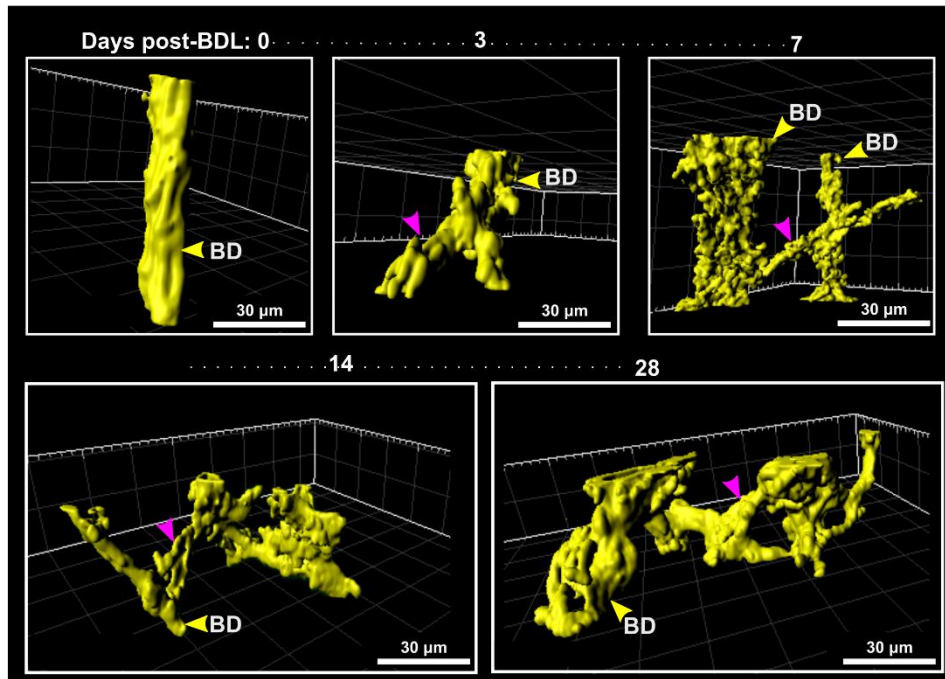
Fig.4.1.3.F1.A. Representative interlobular bile ducts isolated from immunostained biliary network.3D surface reconstructions of the luminal surface of the ducts marked with anti-DPP4 in healthy and various days post-BDL treated liver tissue. Bile ducts (yellow arrows) parallel to the portal vein are shown with their interconnecting

branches (magenta arrow). Scale bars: 30µm. B. Quantification of mean duct length of the interlobular bile ducts at various days post-BDL showing biphasic increase. C. Bile duct curvature along its axis at various days post-BDL. D. Quantification of bile duct tortuosity over time BDL. E. Branches per bile duct various days post-BDL showing a logistic increase (Hill coefficient [p],3.73; half-max[x_0],6.73 days). Points indicate the mean ± standard error of the mean per time point, respectively. The trend line indicates the non-rounded Akima spline for B to D. The line in E indicates regression fit of the data to y= y_{min} + (y_{max}-y_{min})/[1 - (x-x_0)^p] with R^2 = 0.99. **Figure reused and reproduced from (Vartak et al., 2016).**

4.1.4. Loop formation and rejoining of branched interlobular ducts within a restricted volume

The interlobular bile ducts increased ductular tissue post cholestasis by forming a branched network. Branching continued over time till day 14 parallel to the increase in ductular tissue but remained constant between day 14 and 28 post BDL also shown by branch frequency (4.1.3.F1.E), although during this period there was a significant increase in cell proliferation (4.1.1.F1.B) and duct elongation (4.1.3.F1.B). To resolve this discrepancy and investigate what factor contributes to the duct elongation, when the branching is constant, we further classified the branching into two types of branch formation, i.e. bifurcations and trifurcations.

Strahler analysis was performed on anti-KRT19 (Gene ID NCBI: 3880) immunostained bile ducts (4.1.4. F1.A), which were analyzed by skeletonization of the duct profile, by pixel removal from all sides until only a single pixel trace is left (4.1.4.F1.B). The results showed an increase in number of bifurcations and trifurcations of the ductular tree by day 3 followed by a decrease at later time-points (4.1.4. F1.C). Other parameters like branch length, ramification ratio (i.e. number of order of branches that occur in the duct per unit of its length) and probability of loop formation i.e. (rejoining of the branches to itself or to the duct) were also measured. Average branch length increased steadily over 28 days post-BDL that accounted for the increase in overall duct length during this period (4.1.4. F1.D). The overall complexity of the duct measured as ramification ratio (number of features per unit length of the duct did not change significantly over 28 days post-BDL (4.1.4. F1.E). Although the average branch length increased during this period (4.1.4. F1.D). The average duct branches were of first and the second order, suggesting that most branches arise from the original unbifurcated duct or from the first-order branches. The second order branches rarely branched further but re-joined to the original duct while maintaining a constant ramification ratio. Rejoining of the branches to

establish a circular feature is defined as "loop formation". This is excluded from the branch count. The second order branches did not branch further, instead they are re-joined either to the first order or main duct branch and are reflected by the increase observed in the probability of loop formation being maximum at day 14 and increased with the number of branches (4.1.4.F1.F) and length of the branches (4.14.F1.D). This increase in rejoining of the branches from day 3 post-BDL onwards might be the early sign of retransformation of existing bile duct branches to form more branches to outsource the bile while circumventing the potential blockages or dysfunctional duct segment. However, the rejoining would also reduce the chances of finding an alternative pathway to eject bile if it occurs to a blocked or dysfunctional duct. This feature of the duct to rejoin might be a consequence of ductular elongation within a constrained space between the parenchyma and the portal vein.

A

| anti-DPP4 | anti-KRT19 | anti-DPP4 /anti-KRT19 |

B

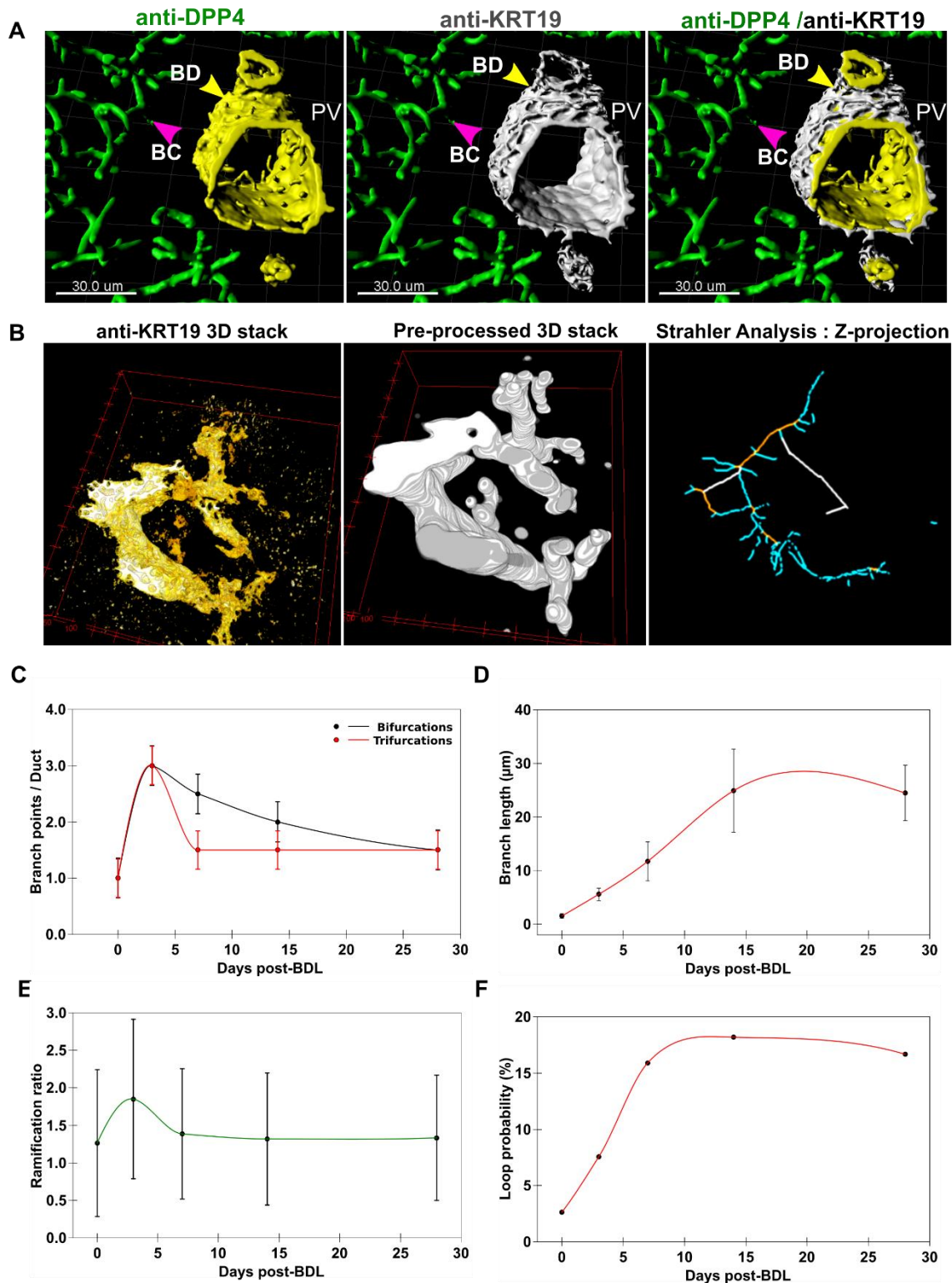| anti-KRT19 3D stack | Pre-processed 3D stack | Strahler Analysis : Z-projection |

Fig.4.1.4.F1.A. Representative surface reconstructions of DPP4 (left) and anti-KRT19 (right) immunostained interlobular bile duct. DPP4 marks the luminal membrane surface of the duct and KRT19 represents cytoskeletal secondary filaments of cholangiocytes as shown in overlay (right). B. Left: raw 3D-confocal data of a

representative anti-KRT19 stained bile duct (yellow). Center: Gaussian filtered volumetric representation of the bile duct (pre-processed). Right: Strahler analysis of the skeletonized processed bile duct, image yields branched orders (color-coded), branch points, branch lengths. C. Number of branch points: bifurcations and trifurcations per duct over time post-BDL showing branching occurs mostly between day 3 and 14. D. Quantification of branch length shows that branch length increases up to day 14 contributing to duct elongation. E. Duct complexity quantified as ramification ratio does not change significantly over time post BDL. F. Loop formation probability (self-joining of branches to themselves) increased up to day 14 and remain constant between day 14 and 28. Points in all graphs indicate the Mean ± SEM for bile ducts per time point in C to E. Points in panel F indicate ratio of loops to bile ducts per time point. Trend lines in all graphs indicate the non-rounded Akima spline. **Figure reused and reproduced from (Vartak et al., 2016).**

4.1.5. Mechanistic restraints on duct remodeling post bile duct ligation

Diameter increase, or tube widening is a very common way to accumulate larger volumes of fluid. Increase in diameter of the common bile duct is a very common diagnostic feature observed after injury and obstruction of the biliary tree. This might be related to the accommodation of the excess biliary fluid in the biliary tree during cholestasis. BDL induced cholestasis can also lead to an increase in hydrostatic pressure created by accumulated biliary fluid in the biliary tree. Increase in the duct diameter across all the relevant branches of the biliary tree can increase the ductular volume to accommodate the excess biliary fluid.

We therefore investigated if after BDL induced cholestasis, the increase in the ductular tissue is due to increased duct diameter. Such an increase in IBD diameter can result further into the widening of the bile duct lumen that may increase the volume of the biliary tree to neutralize the excess pressure created by the accumulated excess biliary fluid and reabsorb toxic bile salts.

The segmented intensity of anti-DPP4 stained bile ducts (4.1.5. F1.A) was used to measure morphometric parameters like automated mean duct diameter and eccentricity (4.1.5.F1.B,C). BDL-induced cholestasis did not lead to an increase in diameter of the interlobular bile ducts (4.1.5. F1.B), keeping it constant (approx. 10µm) over 28 days post-BDL. Area measurements were also performed on cross-sectional planes of the duct perpendicular to the long axis to ensure that perspective and skewing effects do not lead to over- or underestimation of the duct diameter (see section 5.1.). The results indicated that there was no significant change in the diameter of the IBDs during cholestasis and is an entirely different response than the large bile ducts. This invariant diameter could be also due to the changes in the cross-sectional

eccentricity as the duct is not a perfect smooth cylinder. The eccentricity which is deviation of a duct from a circular shape can be a way to increase cross-sectional diameter of the duct and/or its branches without affecting the mean diameter to increase the ductular volume. The results showed that, the average duct cross-section is eccentric, but there were no significant changes in eccentricity over time BDL of the entire dataset comprising 39 ducts and their branches from 3 mice per time point (4.1.5. F1.C).
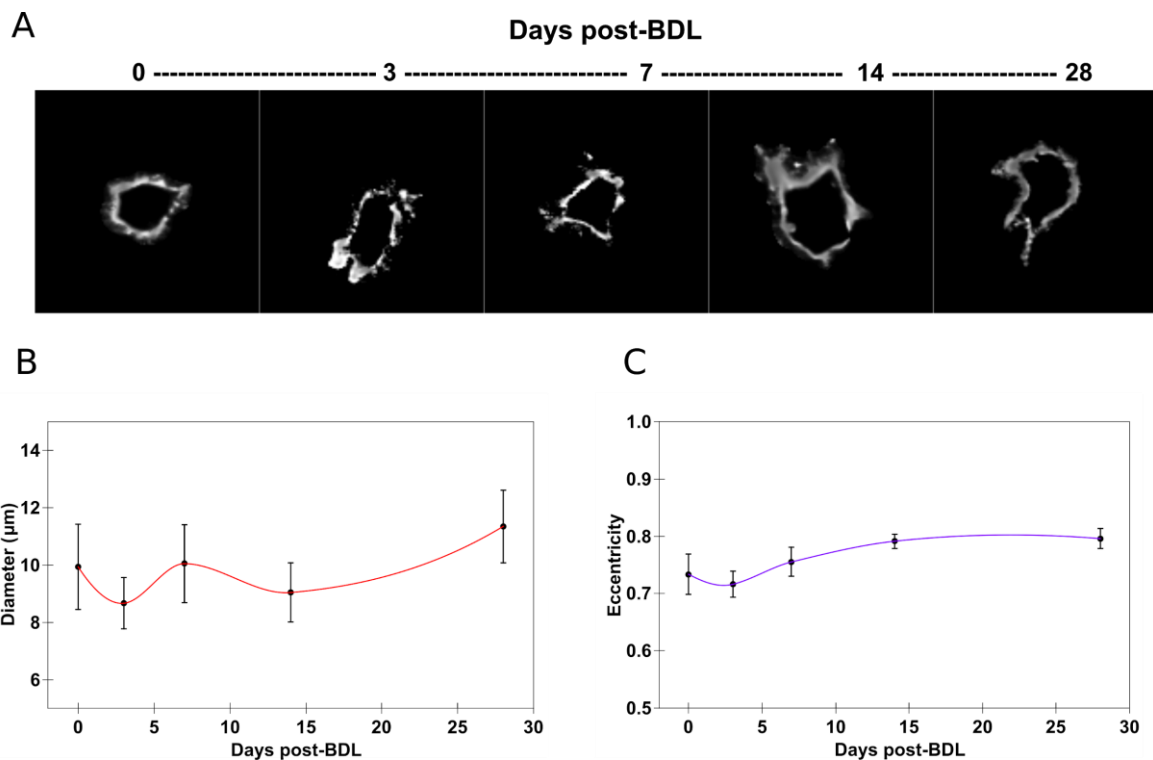

Fig.4.1.5. F1.A. Representative segmented cross-sections of the interlobular bile ducts from various days post-BDL. Scale bar: 10µm. B. Bile duct diameter showing no significant change over time BDL. C. Quantification of bile duct eccentricity (i.e. deviation from a perfect circle) indicates no significant change post-BDL. Points in graphs B and C indicates mean ± SEM for the bile ducts per time point. **Figure reused and reproduced from (Vartak et al., 2016).**

Therefore, the interlobular bile ducts were not a perfect circle but had some minimum eccentricity. The eccentricity did not increase later over 28 days after BDL, thus negating its role to affect the invariant diameter.

Therefore, increased cholangiocytes proliferation post BDL is directed towards elongation of the ductular network by branching and re-looping and by increasing the duct diameter to release existence of any minimum hydrostatic pressure caused by duct obstruction or toxic bile salts

created on duct. This diagnostic feature showed clear mechanistic difference observed between the interlobular bile ducts from the large bile ducts.

4.1.6. Volumetric expansion of the biliary network as a result of increased length and duct complexity

The interlobular bile ducts remodel themselves by undergoing branching thus in turn leading to the enlargement of the biliary network as seen from the increased duct length post cholestasis (see section 4.1.3). Enlargement of the network can be achieved either by expansion of the existing ducts by increasing their diameter or by increasing their volume. This volumetric increase of the biliary tree can then help to accommodate the excess accumulated toxic bile acids.

We investigated, if this increase in the duct length via branching has any effect on the volume of the IBDs, as the duct diameter remained constant over time and did not contribute in the enlargement of the biliary network post cholestasis. We measured the expected ideal volume of the interlobular bile duct as '$\pi r^2 L$', considering that the duct is a perfect cylinder. We further compared these values with the values obtained as an integration of the cross-sectional areas determined from the 3D DPP4-based intensities of the ducts (4.1.6.F1).

We observed a 5-fold bi-phasic increase in the volume of the duct that continued until 28 days after BDL as compared to control dataset. The first increase was observed between day 3 and day 7 while the volume expansion continued increasing as a second phase between day 7 and day 28 post BDL. This measured volume over time after BDL followed closely the same trend of escalation as seen from the ideal cylindrical with some positive offset between the absolute values. The constant positive offset could be due to the constant non-zero eccentricity (see section 4.1.3.F1.D) and tortuosity (4.1.5.F1.C) of the ducts. We concluded, that the bile duct volume changes over time post BDL and is linear to the duct length while being close to the volume of a perfect cylinder. Therefore, the bile duct is not a geometrically ideal perfect cylinder.
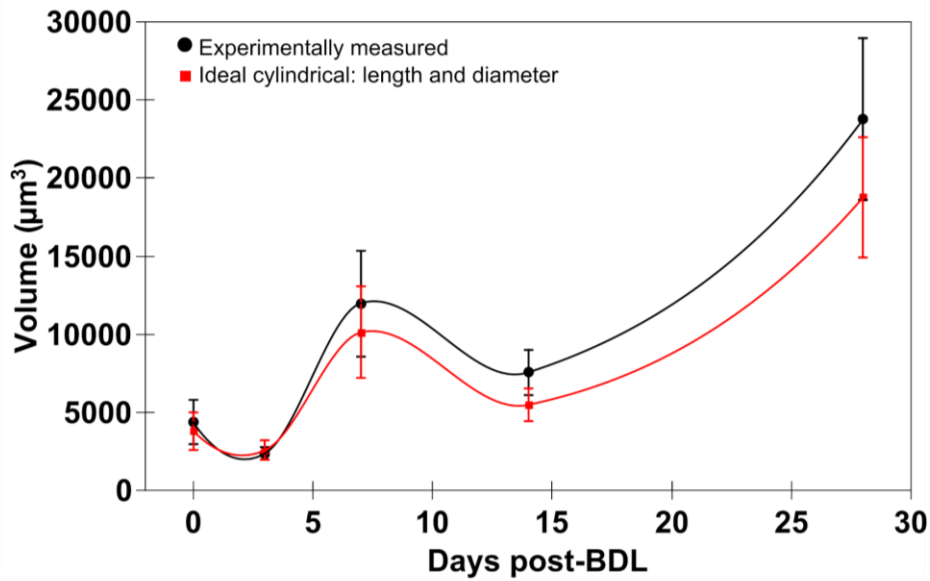
Fig.4.1.6.F1. Volume of bile duct determined experimentally (black line) and considering as an ideal cylinder (red line) from the DPP4 based luminal intensity. Bile duct volume shows a biphasic increase with the first phase seen between day 3 and day 7 while the second is marked between day 7 to day 28 post-BDL. **Figure reused and reproduced from (Vartak et al., 2016).**

4.1.7. Surface area along with corrugations contribute and enhance the absorption capacity of bile ducts

Suboptimal increase in volume due to increase in ductular length is not sufficient to alleviate cholestasis. Effective reabsorption of the accumulated bile acids together with increased ductular tissue or biliary volume can alleviate cholestasis through the cholehepatic shunt pathway (G. Alpini et al., 1997, 1998).

One of the well-known functions of the cholangiocytes is modification of the biliary fluids by reabsorption and secretion of bile salts, water and electrolytes (Xia, Francis, Glaser, Alpini, & LeSage, 2006). This function is majorly catalyzed by different bile acid transporters and enzymes that are located on the apical membrane of the cholangiocytes which the luminal surface of the duct is also.

As observed previously, high rate of cholangiocytes proliferation is one of the response post BDL (see section 4.1.1.). This increased cell proliferation might also mean that there are more no of cholangiocytes per duct. The enlargement of the interface between the cholangiocytes

apical membrane and ductular bile thus can be a functional adaptation to help in ductular bile absorption.

In order to find if there is any correlation of high cellular proliferation to the enhancement of the luminal surface area of the duct, we measured the surface area of the interlobular bile ducts. For this, we utilized isosurface tessellations of the DPP4 stained luminal membrane of the segmented bile ducts.

28 days post-BDL showed a five-fold increase in the luminal surface area of the bile duct as compared to untreated ducts (Fig.4.1.7.F1.A). Similar to the volume measurements (see section 4.1.6) we measured the surface area of the duct considering it as an ideal cylindrical form. The ideal cylinder surface area was calculated from the length and the diameter measurements as **"$2\pi rL$".** We observed, that the measured surface area of the bile duct was 4-fold higher than the surface area when it is considered as an ideal cylinder (Fig.4.1.7.F1.A).

Thus, the increased surface area post-BDL is not only due to increased bile duct length, but the large difference might indicate the presence of an unknown parameter that can directly contribute in the escalation. The unknown parameter could be presence of small node like structures "corrugations" or wrinkling which is observed on the luminal surface of the bile duct (Fig.4.1.7.F1.B).

We observed that such corrugations occur only post-BDL and are absent on the surface of the bile ducts from untreated livers. These corrugations hence may serve to contribute in the disproportionate increase in the surface area. Thus, analogous to villi of the intestine and sulci of the brain. Thus, expansion in the surface area or absorptive and cortical surface area within a restricted volume by formation of such ex or invaginations on the 2D planar tissue into 3D could be the way to enhance functional capacity of bile reabsorption.

We further investigated the degree of corrugations in alleviating bile acid toxicity, by determining the average elevation (amplitude) and angular variation (frequency) over all timepoints post-BDL. For this, we utilized the duct surface isosurfaces. The isosurfaces were generated for the surface area measurements and were comprised of individual triangles for which the orientation vectors and normals were calculated (4.1.7.F1.C).

Average elevation (amplitude) is the extent of displacement of a surface from an ideal planar surface at that point which is measured from the magnitude of the normals. Angular variation (frequency of corrugations) is the direction of the normals i.e. the angle of displacement. Thus, the extent of corrugations is a combined measure of angular elevation and variation.

The results from this study, show that the angular variation of the corrugations (or roughness) increased and peaked at day 3 post-BDL and returned back to normal levels until 28-day post-BDL (4.1.7.F1.D). Whereas the angular elevation increased in a biphasic manner i.e. between day 3 to day 7 and day 14 to day 28 post ligation (4.1.7.F1.E). This increase followed the same trend as increase in the length, volume and surface area of the bile duct.
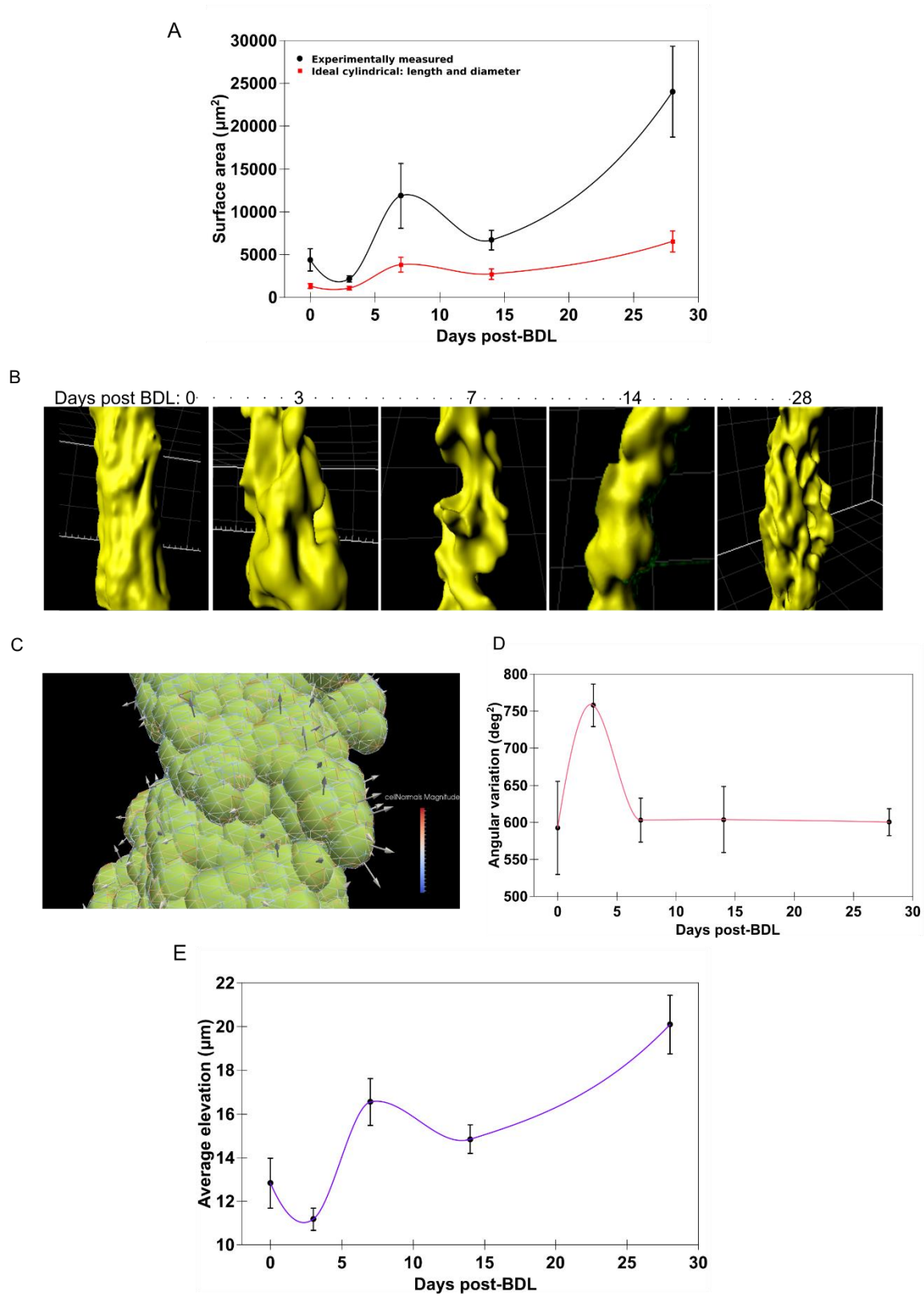
Fig.4.1.7.F1.A. Surface area of the interlobular bile ducts determined experimentally (black line) and surface area of the same duct considered as an ideal cylinder (red line) over time until 28 days post-BDL. The experimentally determined surface area is the measure of summation of triangle areas together constituting the bile duct surface

in the 3D reconstructed z-stacks. The ideal cylindrical surface area is calculated as '2πrL' from the length, diameter values of the duct. Both the experimental and ideal surface area show a biphasic increase from day 3 to day 7 and day 7 to day 28 post-BDL. B. Representative images of surfaces of various bile ducts generated from the anti-DPP4 immunostainings post various days BDL. The surface of untreated ducts more or less resembles to a smooth planar surface while the surface of the bile ducts post injury has presence of corrugations on the luminal duct surface. C. Automated tessellations and normals computation (arrows) to quantify surface corrugations on a bile duct. D. Measure of angular variance between normal vectors at different day post injury. E. Measure of average elevation of the bile duct surface (corrugation amplitude) from the normal vector magnitudes overtime post-BDL. **Figure reused and reproduced from (Vartak et al., 2016).**

In order to investigate if the increase in the degree of corrugations, with simultaneous increase of duct length can justify and contribute in the increase in the surface area of the bile duct post injury, we generated simulations of the surfaces with varying length and corrugations values (4.1.7.F2.A).

We observed that the simulated surface area of the bile ducts varied in direct proportion to the average elevation or amplitude of the corrugations and periodically with the angular variation of the roughness or corrugations (4.1.7.F2.B). The calculated surface area is the function of length, diameter, angular variation and elevation. This calculated surface area from the analytically determined values resulted in a close proximation to the measured surface area at these time points post-BDL (4.1.7.F2.C) and cancelled out any plausible discrepancy between the measured and ideal cylindrical surface area.
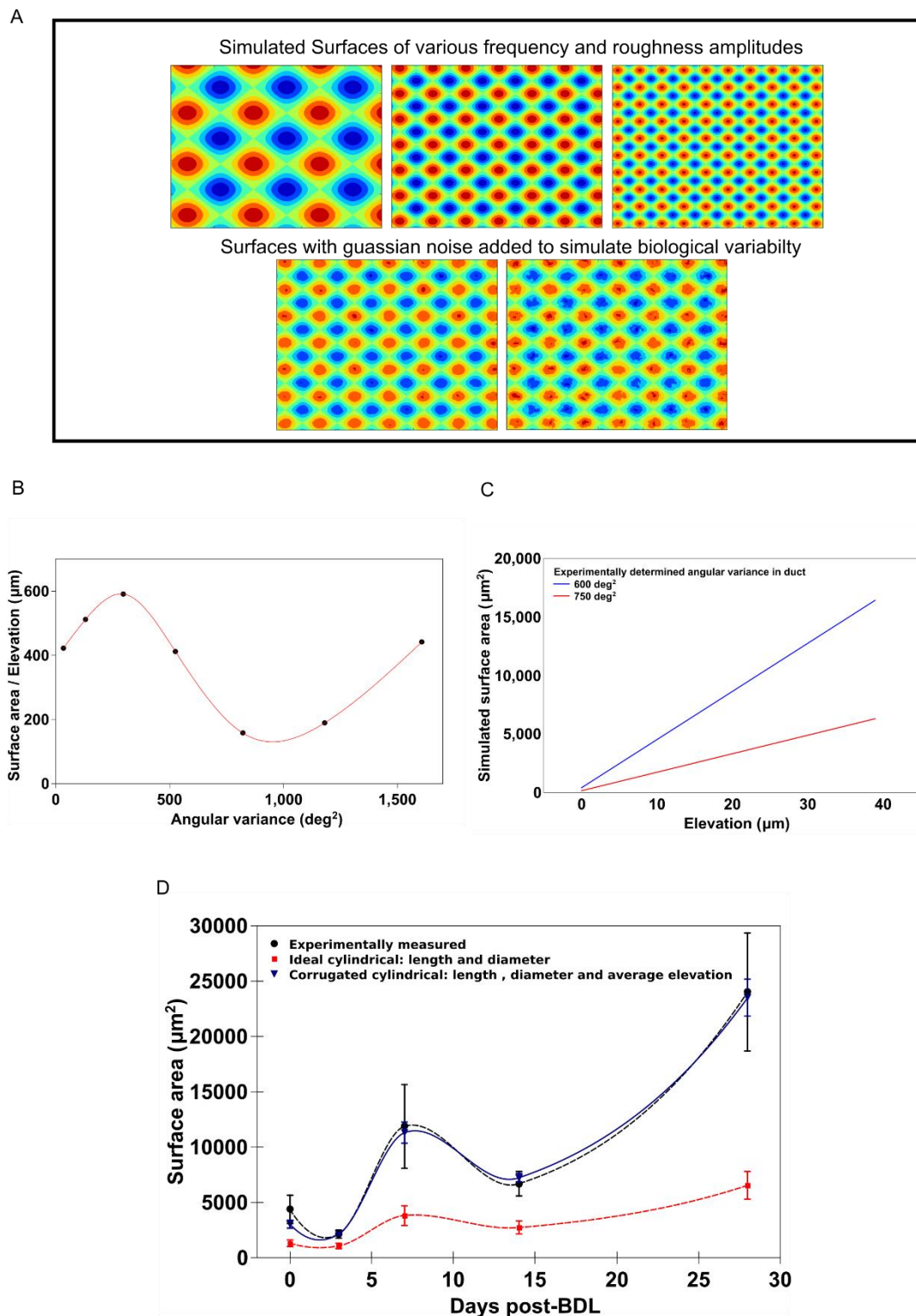
Fig.4.1.7.F2.A. Illustrative simulated surfaces of the bile ducts generated using various frequencies and amplitudes with and without stochastic noise. B. Periodic variation of the luminal surface area of the duct/unit elevation of corrugations with increasing angular variance in angle of the normal vectors. C. Linear increase in

the simulated surface area along with increased angular elevation of corrugations for various experimentally observed angular variances (red, blue). N=1000 simulation runs. D. Bile duct surface area calculated from the experimental (black line) and ideal cylindrical (red line) along with the cylindrical surface area with corrugations (blue) calculated from the average elevation values (4.1.7.F1.E). Near perfect match can be seen between the experimentally determined and corrugated cylindrical surface area of the duct. This approximation indicates that the increase in the surface area occurs due to increase in angular elevation. Mean ± SEM of bile ducts per time point is indicated by points in all the graphs. Trend lines in the graphs indicate the non-rounded Akima spline. **Figure reused and reproduced from (Vartak et al., 2016).**

4.1.8. BDL does not lead to any increase in draining capacity of the liver lobules
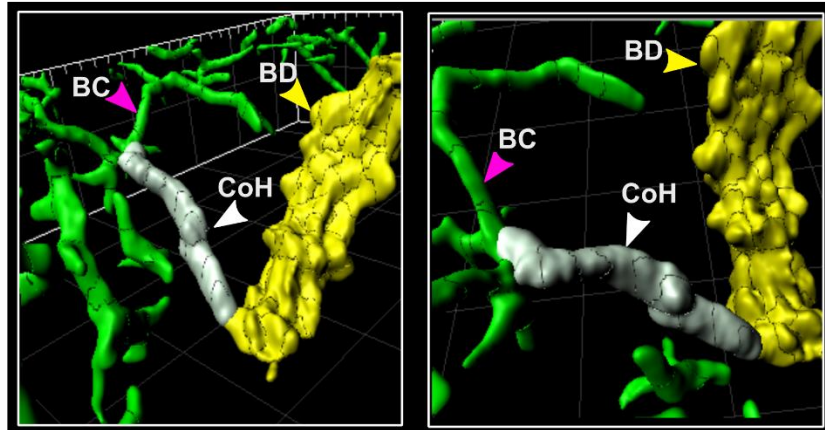
BDL-mediated cholestasis does not alter the amount of biliary fluid generated in the lobular bile canalicular network but can affect the bile salt concentrations by affecting their metabolism especially by affecting the hepatocytes and the cholangiocytes. Therefore, in order to avoid the accumulation of such altered bile salts and eliminate their cytotoxicity, it is very important to drain them out of the hepatic lobular network.

In normal liver lobular architecture, small conduits termed as the 'canals of Hering' connect the canalicular network and the interlobular bile ducts thus aid in draining the hepatocyte-generated biliary fluid (4.1.8.F1.A).

Although it is reported that such functional conduits are damaged post various liver injuries such as primary biliary cirrhosis (Saxena, Hytiroglou, Thung, & Theise, 2002; Theise et al., 1999) thus affecting the lobular draining capacity. It is still unclear what happens to such conduits post cholestatic liver injury.

In order to verify if the connectivity of the lobular bile canalicular network is enhanced i.e. there is an increase in the number of canal of Hering and if the increased overall ductular length and number of duct branches can also lead to an increase in number of such conduits, we measured the frequency of the canals of Hering on the interlobular bile ducts (4.1.8.F1.B).
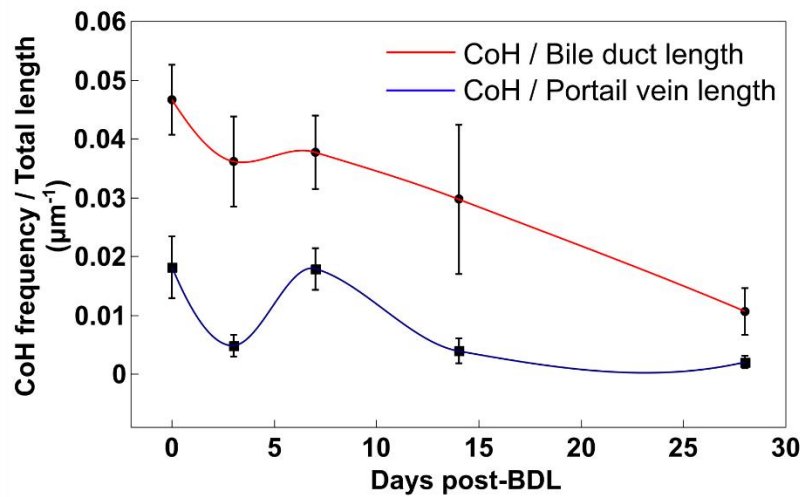
Fig.4.1.8.F1. A. Representative images of 3D surface reconstruction of an isolated canal of Hering (CoH) connecting the bile duct (BD) with the bile canalicular network (BC). B. Quantified frequency of canal of Hering per unit length of the bile duct (red line) and per unit length of the portal vein (blue line) over time BDL. The density of the Hering canals is decreased per unit length of the bile duct. Points in the graphs indicate the mean ± standard error of the mean (SEM) per time point BDL. Trend line represent the non-rounded Akima spline. **Figure reused and reproduced from (Vartak et al., 2016).**

The frequency of the Hering canals per unit length of the bile duct decreased over 28 days post-BDL (~5 in every 100 µm of the duct to ~1 in every 100 µm of the duct). The frequency of Hering canals per unit length of the portal vein was also measured to cancel any plausible effect or contribution of bile duct elongation on the decreased connectivity of duct-canalicular network. Results show the frequency of the Canals of Hering per unit length of the portal vein

remained at a constant value (1 to 2 for every 100 µm of the portal vein until day 7) and decreased at day 14 and day 28 post-BDL. Although the ductular network was elongated, no *denovo* formation of CoH occur post-BDL. The relative capacity of the hepatic lobule to drain the biliary fluid from the canalicular network was reduced thus indicating a response to reduce the elevated bile salt concentrations in the duct during BDL-induced cholestasis.

4.1.9. Enlarged biliary network is a mesh confined to the portal tract post BDL

While the duct diameter remains invariant without any increase in biliary fluid draining capacity, but the ductular tissue is increasing by branching, it is possible that these elongated duct branches may invade the liver parenchyma and move away from the portal tract to accumulate the excess ductular tissue and biliary fluid.

It is known that chronic cholestasis conditions eventually result in fibrosis (Tag et al., 2015). One of the features seen in such conditions are **'*fibrotic streaks*'** i.e. invasion of the duct into the parenchyma that therefore also results in interconnecting two different portal tracts (Tannuri et al., 2012). This ductular invasion into the liver parenchyma is a way that has been reported, possibly to deliver hepatic progenitors through small penetrating ducts when hepatocyte regeneration is impaired following chemical injury (Gouw, Clouston, & Theise, 2011; Kaneko, Kamimoto, Miyajima, & Itoh, 2015).

To visualize the presence of any such phenomenon independent ducts or their branches and their invasion into the parenchyma post-BDL induced cholestasis, we measured the pixel wise distance between the bile ducts and the portal vein (4.1.9.F1.A). We observed that bile ducts maintain a constant distance within 10 to 15µm from the walls of the portal vein throughout 28 days post-BDL.

Although we observe some isolated KRT19-positive cells as in control (4.1.9.F1.B) they do not result in individual new duct branches or connect the existing duct branch and invade the parenchyma of the liver. BDL does not induce any change in the diameter of the interlobular bile ducts or in the diameter of the portal vein. The excess ductular tissue increased post-BDL

is only by duct branching and lengthening while keeping the ductular mesh in close proximity to the portal vein.
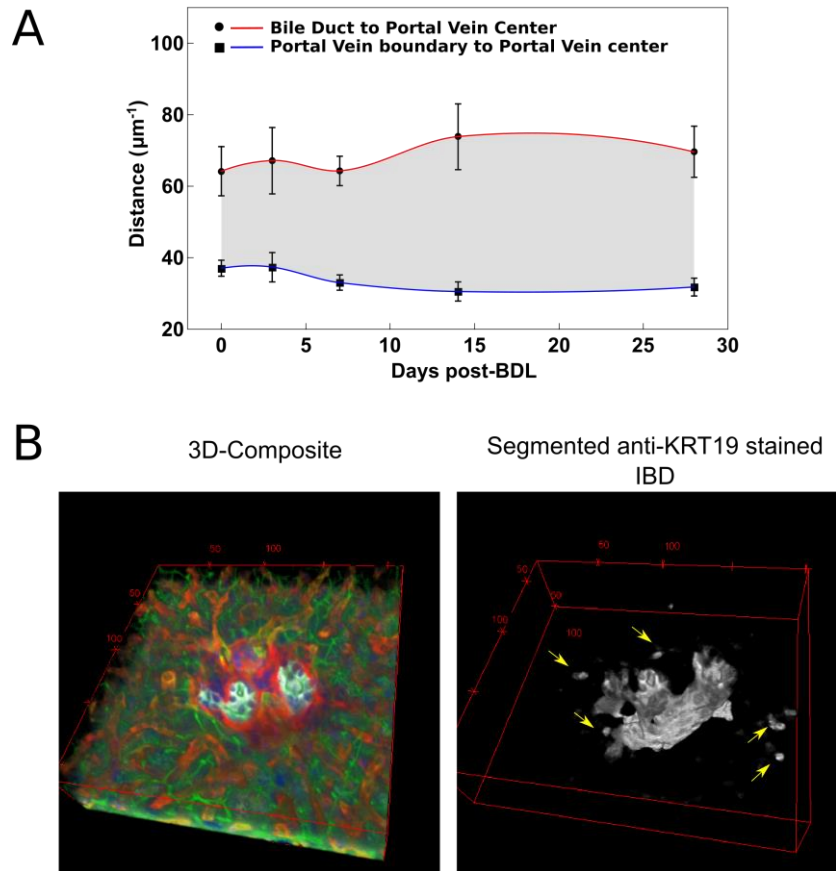

Fig.4.1.9.F1.A. Measured distance of the bile ducts to the portal vein (red line) and the radius of the portal vein (blue) i.e. the distance between the portal vein center to the wall of the portal vein. Gray area represents the difference between the radius of the portal vein and the distance of the bile duct to the portal vein, showing that a constant distance is maintained between the portal vein and the bile duct at various time points post-BDL. B. Left:3D-stack of the bile duct in B showing the entire stack (left) and segmented 3D bile duct (right). Isolated KRT19-positive cells (yellow arrows) that are sometimes also present in the portal tract or do not form any connections to the other IBDs network along the portal vein. Points in the graphs indicate the mean ± SEM for the bile ducts over time BDL. Trend lines in all the graphs indicated the non-rounded Akima spline. **Figure reused and reproduced from (Vartak et al., 2016).**

4.1.10. Remodeling of the lobular bile canaliculi network post BDL

Bile canaliculi represent the most upstream part of the biliary tree. They are responsible for collecting and draining the lobular bile salts from hepatocytes and transport them to the interlobular bile ducts.

The apical membrane of hepatocytes together results in a bile canaliculus and this canaliculus is the first compartment where enrichment of extracellular bile salts or bile acids occur. Therefore, the primary aim of this work was to study whether the architecture of the bile canaliculi is altered by exposure to high levels of accumulated bile salts. The following work also focused on if the canalicular network is altered due to the interrupted bile flow during cholestasis induced by BDL.

For this purpose, liver tissue sections were obtained from bile duct ligated mice and immunostained for apical membrane marker such as DPP4 (UniProtKB-P28843) to visualize bile canaliculi. 3D immuno-micrographs were generated using confocal microscopy and 3D reconstructions were performed to generate isosurfaces of the canaliculi. The resulting 3D isosurfaces were utilized to analyze several morphometric parameters such as canalicular diameter, network nodes, and surface topography. In mice, treated with BDL, the bile canalicular network showed characteristic morphological alterations with formation of spine or bleb-like projections on their surface that intrude the hepatocyte cytoplasm (4.1.10.F1.B, C, D, E). Such projections were not observed in untreated liver tissue samples (4.1.10.F1.A).
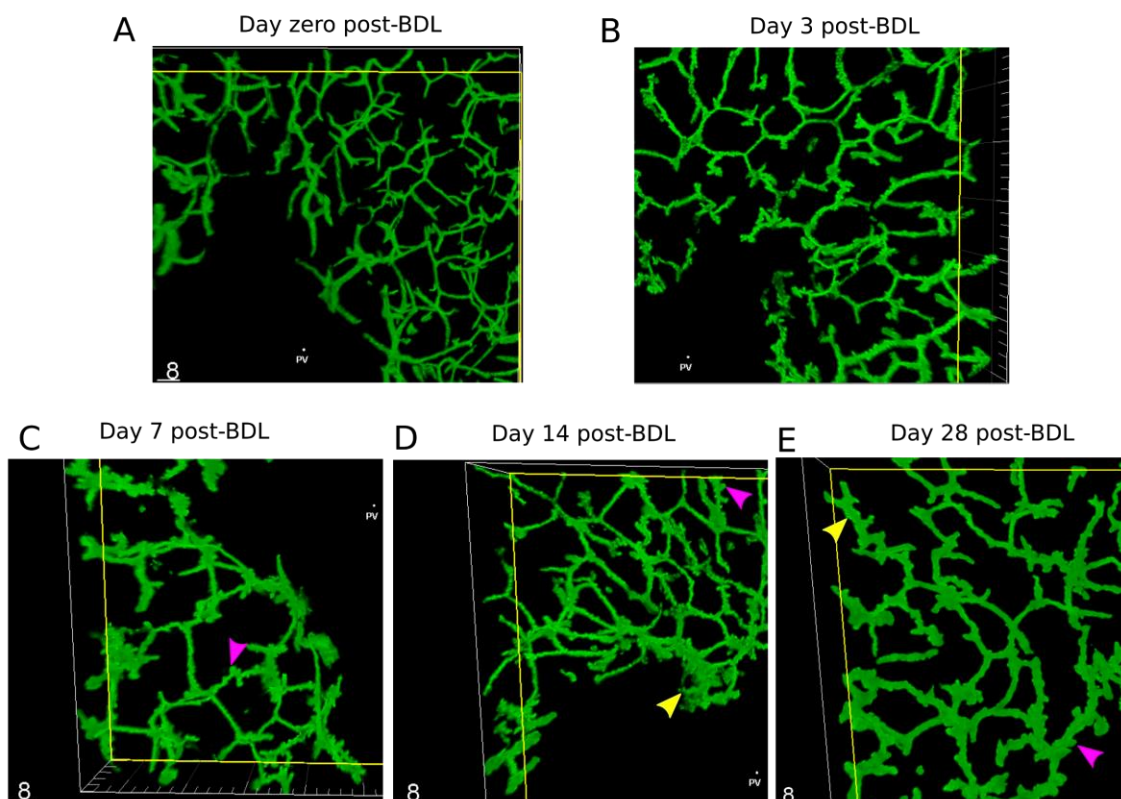

Fig.4.1.10.F1. Bile canaliculi network in untreated and bile duct ligated mice liver. A. DPP4 marked canalicular network of sham-operated mice liver shows a smooth surface. B. Bile canalicular network after 3 days BDL. C. Day 7 post BDL, the canaliculi have small spine or bleb like protrusions on their surface (magenta arrow). D. The

canaliculi also dilate (yellow arrow) and have small bleb like structures after 14 days BDL. E. 28 days after BDL, the bile canalicular network is dense with irregular spiny projections (magenta arrow). **Figure reused and reproduced from (Jansen et al., 2017).**

The bile canaliculi were widened or dilated after BDL. The projections on the surface of the canaliculi may have contributed in increase in the area by widening or dilation. This morphological alteration was observed to be correlated with the 30% increase seen in the outgrowth length after 28 days BDL (4.1.10. F2. A).

A two-fold increase in the roughness or angular variance in radians of the bile canaliculi was also observed (4.1.10.F2.B). Further, an increase of the average canalicular diameter by 30% was also seen post 28 days BDL (4.1.10.F2.C).
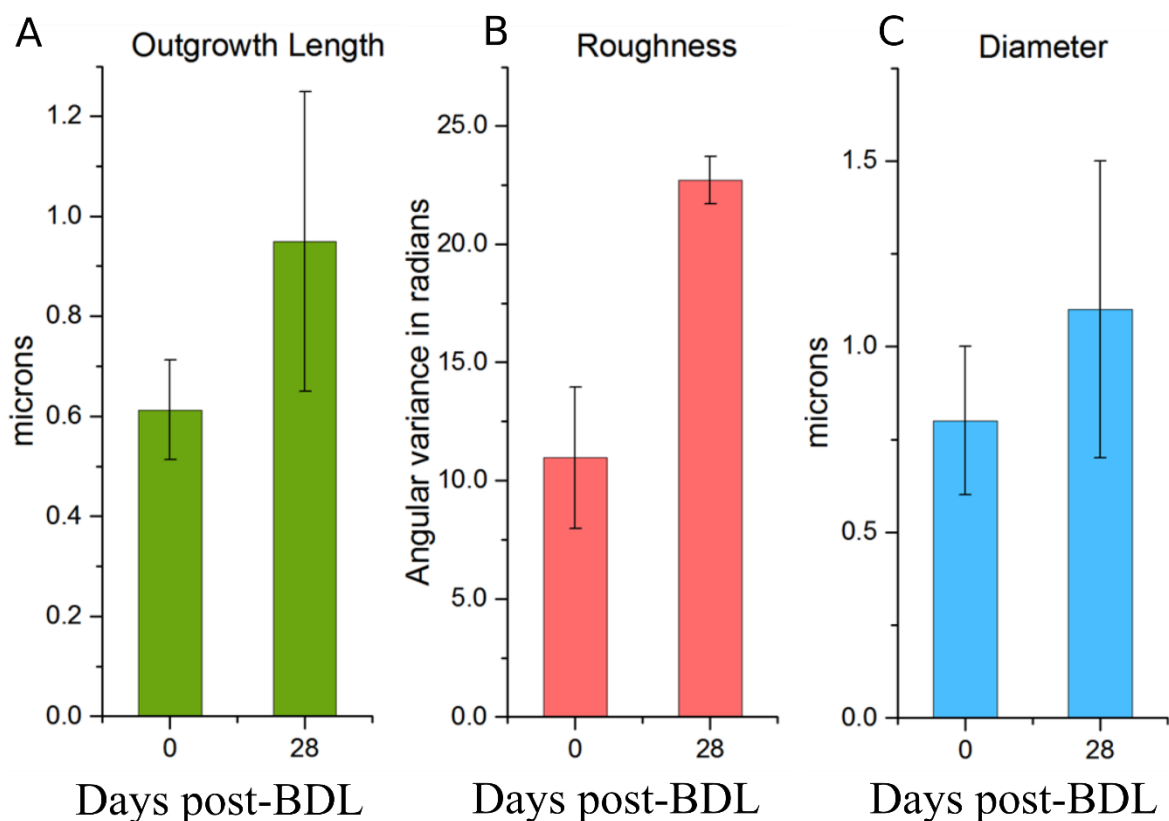

Fig.4.1.10.F2. Quantification of bile canalicular network in cholestasis. A. Length of outgrowths or blebs on the surface of bile canaliculi. B. angular variance in radians or roughness of the canalicular surface. C. Average diameter of the bile canaliculi in sham-operated and BDL mice. **Figure reused and reproduced from (Jansen et al., 2017).**

In conclusion, the bile canalicular network adapts by undergoing major alterations in cholestasis. Dilation or widening of the canalicular lumen reflected by the increased diameter and increased outgrowth length or roughness may contribute to resolve and reabsorb excess bile salts.

Spine or fish bone like projections and increased length of the entire network is also observed after cholestatic liver injury. This spatial-temporal response on the tissue level of the canalicular surface to cholestasis can be related to the cellular response of the peri-canalicular actin that provides cellular stability and is also known to be altered during cholestasis (Gupta et al., 2016).

4.2. Intracellular response to bile acid induced toxicity in cholestatic liver injury after BDL

Results described so far, focused on the changes of the biliary tree at the tissue scale in response to cholestasis. However, the ultimate target of bile salt toxicity are the hepatocytes. To further study bile acid-induced toxicity in vitro and compare them to the in vivo situation, we isolated primary hepatocytes from C57BL6/N mice and determined cytotoxic concentrations of different bile acids. One of the major function of the hepatocytes is the synthesis of bile acids. When in excess, the synthesis of bile acids by hepatocytes is also regulated by a nuclear receptor 'FXR'. We then measured intracellular levels of bile acids by measuring the FXR activity in the cells exposed to bile acids.

Further, we visualized the overall cortical F-actin network and cytoskeletal dynamics with a focus on the peri-canalicular actin marked by 'LifeAct' and a small molecule dye 'SiR-actin'. The analyses were performed at concentrations of beginning cytotoxicity. These concentrations are relevant to the in vivo situation, because they may occur in severe cholestasis.

4.2.1. Cytotoxicity and cell death in relation to bile acids

Four bile acids were selected based on their abundance (DCA, TCA), molecular interactions (CDCA) and clinical relevance (UDCA). TβMCA, the most abundant bile acid found in the mouse liver was also included in morphology-based cytotoxicity experiments.

4.2.1.1. Cytotoxic bile acid concentrations that induce death in hepatocytes

The cytotoxicity of these four bile acids was initially evaluated from the cellular morphology of hepatocytes by time-lapse imaging. Approximate cytotoxic concentration ranges for different bile acids were estimated based on the morphological changes such as nuclear fragmentation, cell blebbing or detachment from the dish observed during time lapse imaging (4.2.1.F1.F2, F3, F4, F5). These changes correlated with the cytotoxicity of bile acids reported in the literature in hepatocytes (Woolbright et al. 2015; Woolbright et al. 2016).

Deoxycholic acid at a concentration of 250 µM induced cell death indicated as round circular hepatocyte with black cytoplasmic debris or nuclear fragmentation within 12 to 24 hours after exposure (4.2.1.F1.A). Taurocholic acid induced cytotoxicity only at the high concentration of 10000 µM between 6 to 12 hours post exposure (4.2.1.F2.B). The cytotoxic concentration of choleretic bile acid such as ursodeoxycholic acid in hepatocytes was 500 µM within 12 to 24 hours after exposure. UDCA treatment also resulted in changes in the bile canaliculi, such as dilation (4.2.1.F3.C). The FXR ligand CDCA showed first signs of cytotoxicity at 250 µM within 6 hours of exposure (4.2.1.F4.B). Finally, mouse bile acid TβMCA at 250µM induced cytotoxicity within 12 to 24 hours similar as observed in hepatocytes treated with deoxycholic acid (4.2.1.F5.B). On the other hand, TCA did not induce any major cytotoxicity until concentrations as high as 3000 µM. CDCA and UDCA induced cell death over 24 hours at concentrations of 100-500 µM and 250-750 µM, respectively.
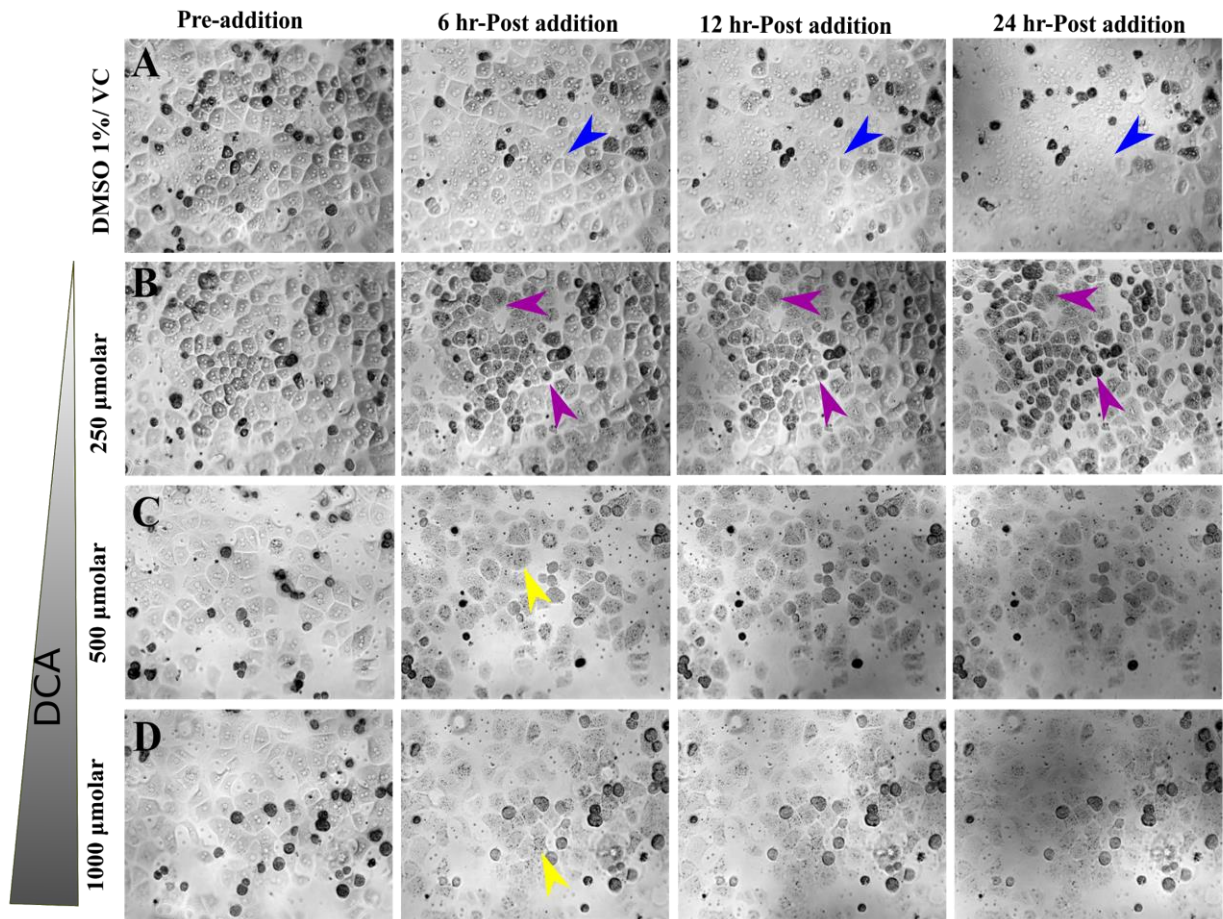
Fig.4.2.1.1.F1. Morphological changes induced after deoxycholic acid exposure in primary mouse hepatocytes. A. Top row: Primary mouse hepatocyte morphology before and after (6, 12, 24 hours) exposure to DMSO 1% (vehicle control) show dedifferentiated hepatocytes (blue arrow). B. Deoxycholic acid induced cytotoxicity over 24 hours at 250 µmolar with nuclear fragmentation and eventually cell death or dead round hepatocytes (magenta arrow). C and D. High concentrations of DCA i.e. 500 and 1000 µmolar induced cytotoxic effect such as cell death early around 6 hours of bile salts exposure (yellow arrow).
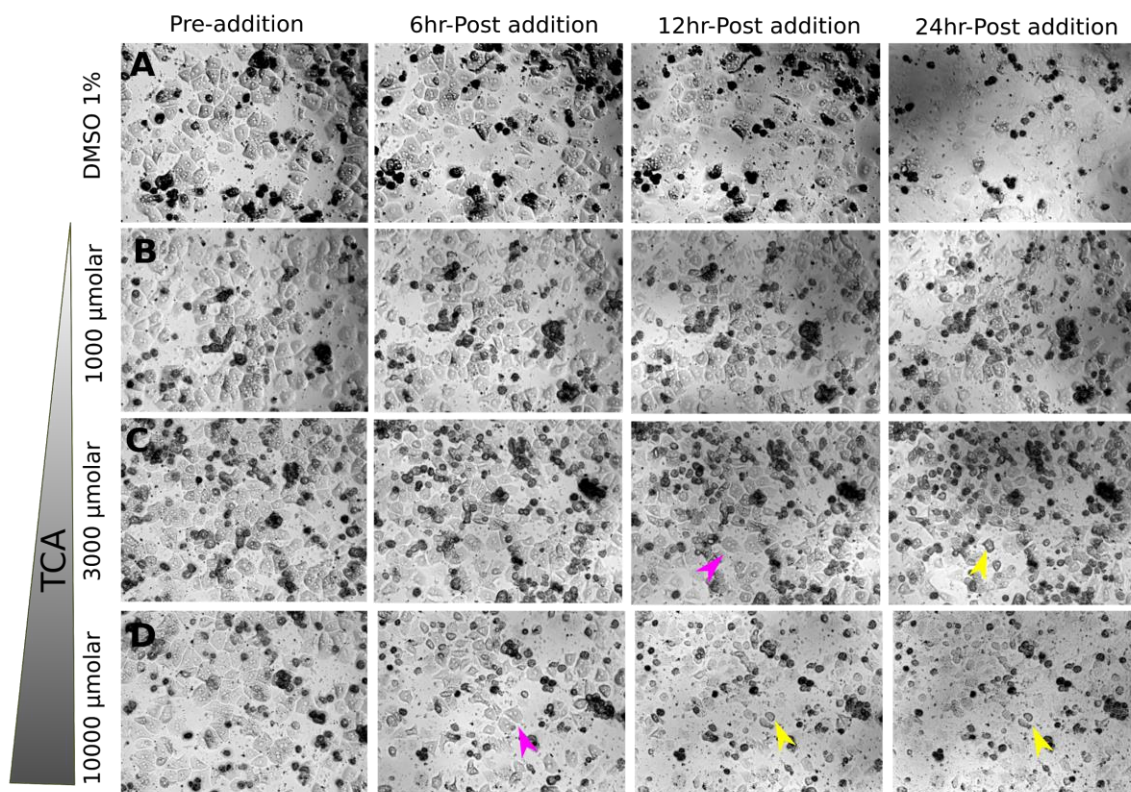
Fig.4.2.1.1.F2. Morphological changes induced after exposure of primary mouse hepatocytes to taurocholic acid (TCA). A. Top row: Primary mouse hepatocyte morphology after exposure to DMSO 1% (vehicle control). B. TCA at high concentration as 1000 µmolar did not induced cell death over 24 hours. C. TCA 3000 µM showed minor cytotoxicity. One such representative healthy hepatocyte (magenta arrow) after exposure to TCA 3000 µM responded to bile acid with change in cell shape (yellow arrow) initiated between 12 to 24 hours. D. Millimolar concentration of TCA i.e. 10000 µmolar induced major cytotoxic effects or cell death between 6 to 12 hours of bile salts exposure (yellow arrow).
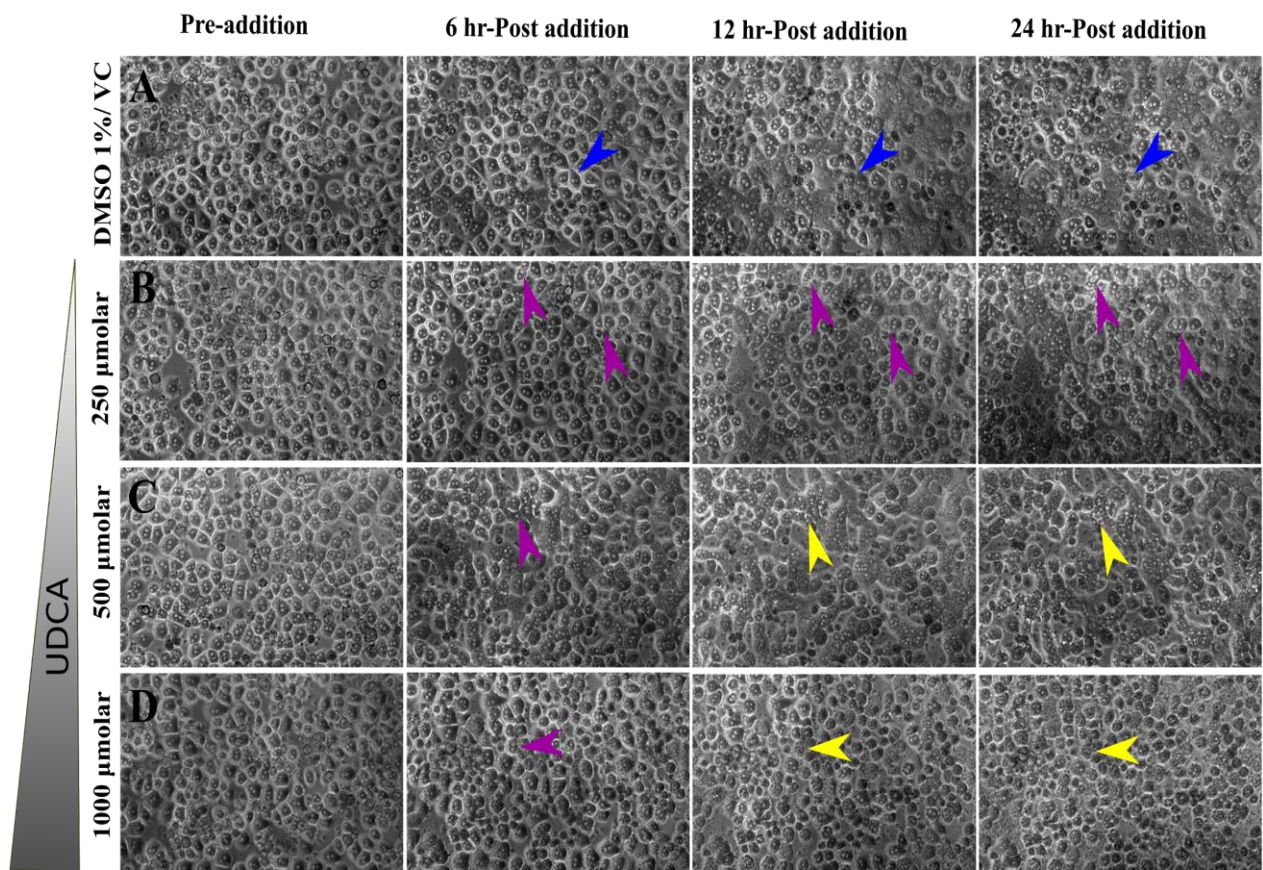
Fig.4.2.1.1.F3. Morphological changes induced after exposure of primary mouse hepatocytes to the choleretic agent-UDCA. A. Top row: Primary mouse hepatocyte morphology before and after (6, 12, 24 hours) exposure to DMSO 1% (vehicle control) show dedifferentiated hepatocytes (blue arrow). B. UDCA 250µM resulted in dilation of the bile canaliculus (magenta arrow) within 12 to 24 hours of exposure. C. 500µM of UDCA also resulted in dilation of single tube-like canaliculi (magenta arrow) between two hepatocytes within 12 to 24 hours of bile acid treatment (yellow arrow). D. High concentration such as 1000 µM caused cytotoxicity/cell death between 6 to 12 hours of bile acid exposure (yellow arrow).
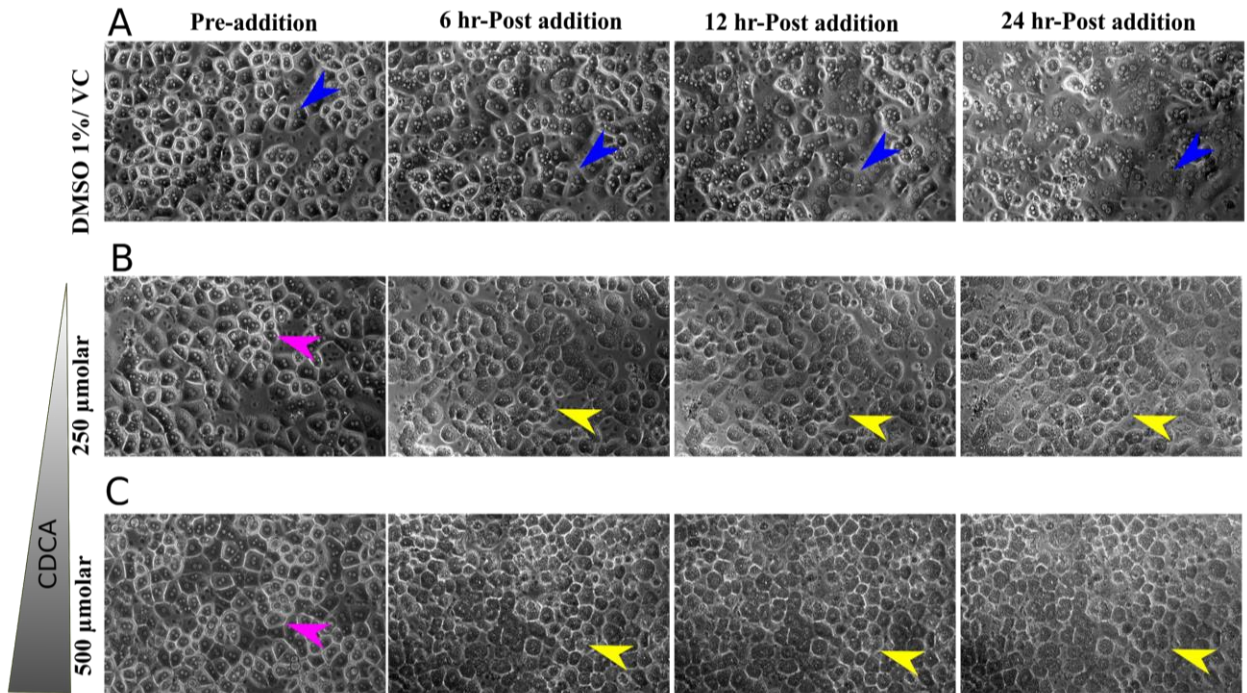
Fig.4.2.1.1.F4. Morphological changes induced after exposure of primary mouse hepatocytes to CDCA. A. Top row: Hepatocyte morphology before and after (6, 12, 24 hours) exposure to DMSO 1% (vehicle control) show healthy and de-differentiated hepatocytes (blue arrow). B. CDCA 250µM induced cytotoxicity within 6 hours post exposure (yellow arrow). C. 500µM of bile salt CDCA also resulted in cell death within 6 hours of exposure with nuclear fragmentation or black small circular debris inside the cell (yellow arrow).
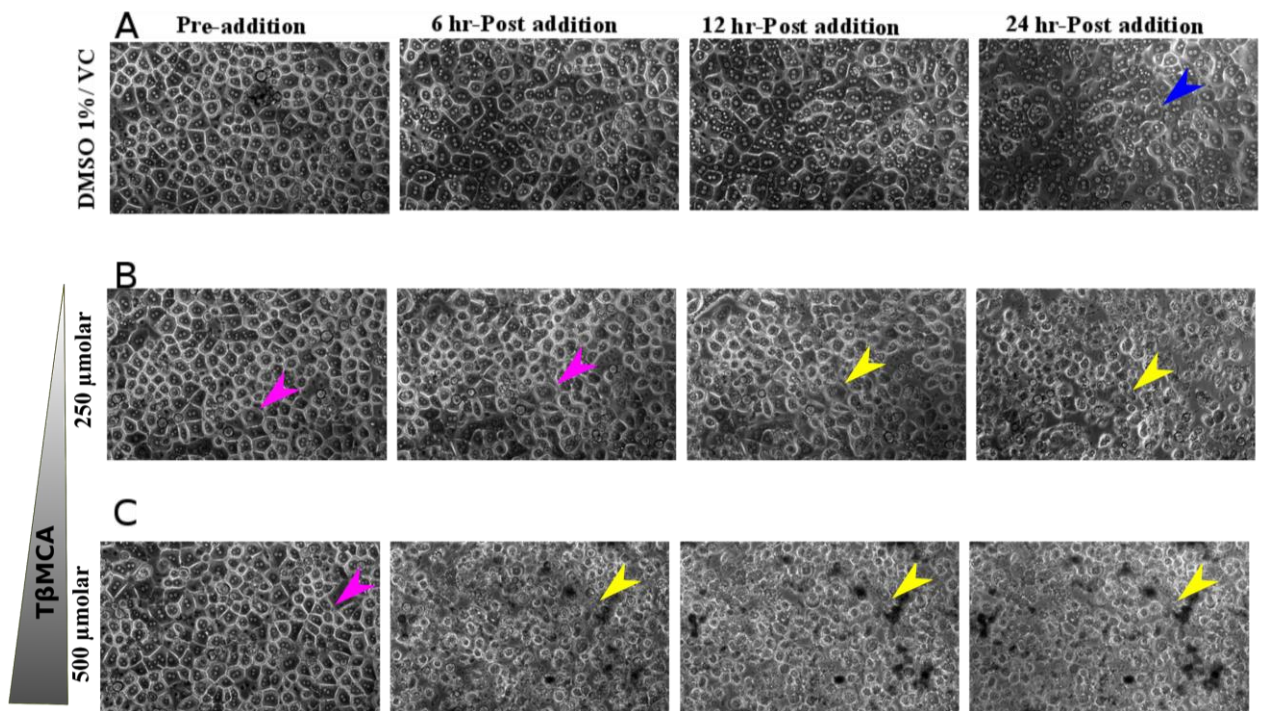

Fig.4.2.1.1.F5. Morphological changes induced after exposure of primary mouse hepatocytes to bile acid TβMCA. A. Top row: Hepatocyte morphology before and after (6, 12, 24 hours) exposure to DMSO 1% (vehicle control) show healthy hepatocytes (blue arrow) B. TβMCA 250µM induced cytotoxicity within 12 to 24 hours post

exposure (yellow arrow). C. 500µM of bile acid, TβMCA induced cell death within 6 hours of exposure depicted as healthy cuboidal hepatocytes (magenta arrow) dead and indicated as a round dead hepatocyte (yellow arrow).

4.2.1.2. Cytotoxic bile acid concentrations that induce death in HepG2 cells

HepG2, a well-differentiated adherent epithelial-like cell line derived from hepatocellular carcinoma is a common in vitro model cell system used in toxicity studies of drugs and xenobiotics and liver metabolism research. This cell line is maintaining morphological and functional characteristics known from hepatocytes, such as bile canaliculi. They are also known to synthesize unconjugated bile acids. To estimate which bile acids are cytotoxic and to determine the cytotoxic concentration range, we concentration dependently treated HepG2 cells with four different bile acids (DCA, CDCA, UDCA, TCA). Deoxycholic acid was the most cytotoxic bile acid, followed by CDCA, UDCA, TCA. DCA induced cell death at 500 µM within 12-24 hours of exposure and within 6 hours post 750 µM (4.2.1.2.F1).

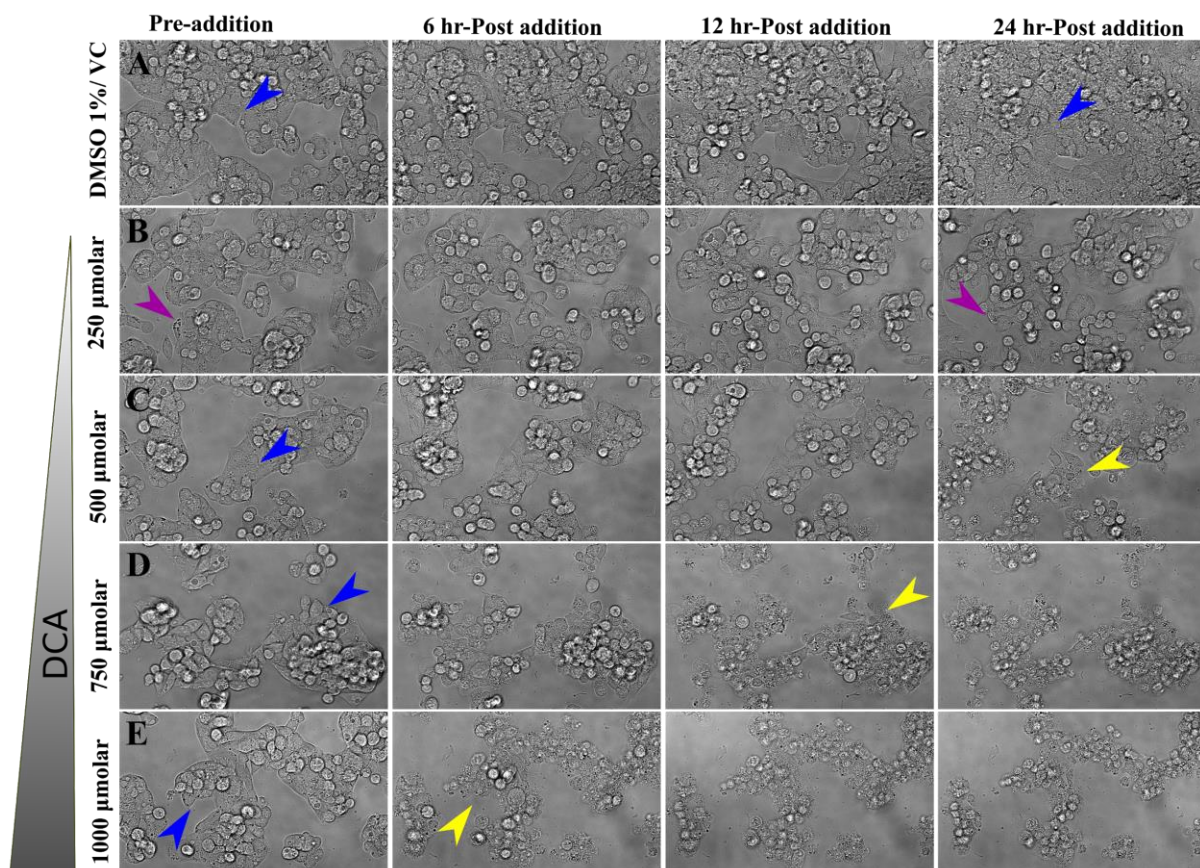Fig.4.2.1.2.F1. Morphological changes induced after exposure of HepG2 to bile acid DCA. A. Top row: Normal epithelial conical shaped morphology before and after (6, 12, 24 hours) exposure to DMSO 1% (vehicle control) show healthy proliferated cell clusters (blue arrow) B. DCA 250 µM has almost 0.1% cytotoxicity within 24 hours post exposure as observed in one dead cell (magenta arrow). C. 500 µM of DCA induced cell death within

12-24 hours of exposure seen as round cell with black fragmented nucleus (yellow arrow). D. DCA 750 µM induced cytotoxicity between 6-12 hours of exposure. E. Millimolar concentration of DCA i.e. 1000 µM induced immediate cytotoxicity as observed, a healthy cell cluster (blue) within 6 hours of exposure to round dead cells (yellow arrow).

CDCA was the second most toxic bile acid that resembled the cytotoxic activity of DCA i.e. cell death with blebbing and nuclear fragmentation, which was observed at 500 µM within 12-24 hours post exposure (4.2.1.2.F2).
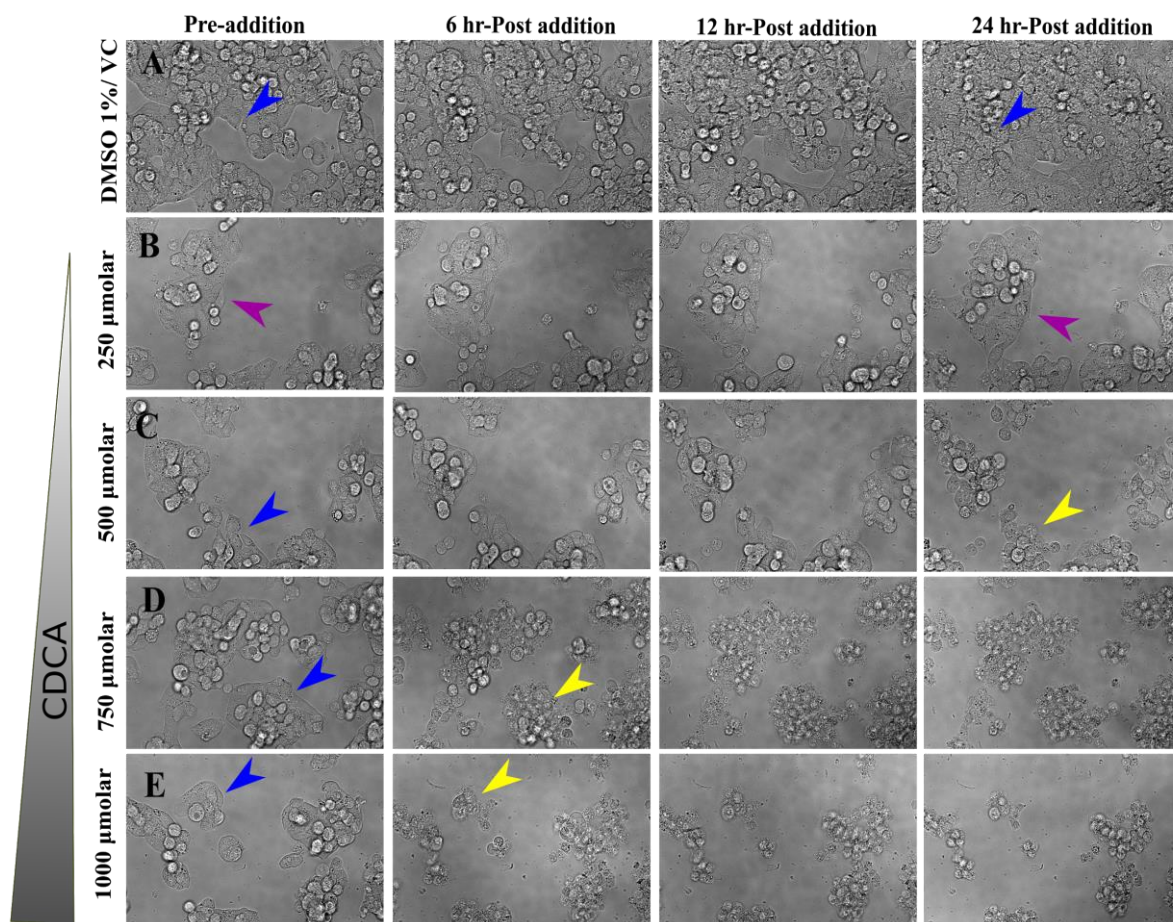

Fig.4.2.1.2.F2. Morphological changes induced after exposure of HepG2 to bile acid CDCA. A. Top row: Cluster of healthy HepG2 (blue arrow) before and after (6, 12, 24 hours) exposure to DMSO 1% (vehicle control) show healthy proliferated cell clusters (blue arrow) and no cell death. B. CDCA 250 µM did not exert cell death within 24 hours post exposure with healthy conical shaped proliferated cell clusters (magenta arrow). C. 500 µM of CDCA induced cell death within 12-24 hours of exposure. Healthy cell clusters were dead after 24 hours of exposure with CDCA and cells were round and dead still attached with each other (yellow arrow).D. CDCA 750 µM induced cytotoxicity between 0-6 hours of exposure. E. Millimolar concentration of CDCA i.e. 1mM/ 1000 µM induced immediate 100% cytotoxicity as observed with 750 µM.

Ursodeoxycholic acid had a cytoprotective role and resulted in cytotoxicity only about 0.1% over a period of 24 hours only at high concentrations of 500, 750 and 1000 µM (4.2.1.2.F3). UDCA may inhibit cell proliferation in HepG2 cells as observed in a previous study (Kim, Cho, Kim, & Kim, 2017).

Fig.4.2.1.2.F3. Morphological changes induced after exposure of HepG2 cells to the bile acid UDCA. A. Top row: Cluster of healthy HepG2 (blue arrow) before and after (6, 12, 24 hours) exposure to DMSO 1% (vehicle control) show healthy proliferated cell clusters (blue arrow) and no observed cell death. B. UDCA 250 µM did not exert cell death within 24 hours post exposure with healthy conical shaped proliferated cell clusters (magenta arrow). C. 500 µM of CDCA induced cell death within 12-24 hours of exposure. Healthy cell clusters were dead after 24 hours of exposure with CDCA and cells were round and dead still attached with each other (yellow arrow).D. CDCA 750 µM induced cytotoxicity between 0-6 hours of exposure. E. Millimolar concentration of CDCA i.e. 1mM/ 1000 µM induced immediate 100% cytotoxicity as observed with 750 µM.

Taurocholic acid was observed as the least cytotoxic bile acid with only little cytotoxicity induced even at the high concentration of 8 millimolar after 12 hours exposure (4.2.1.2.F4).
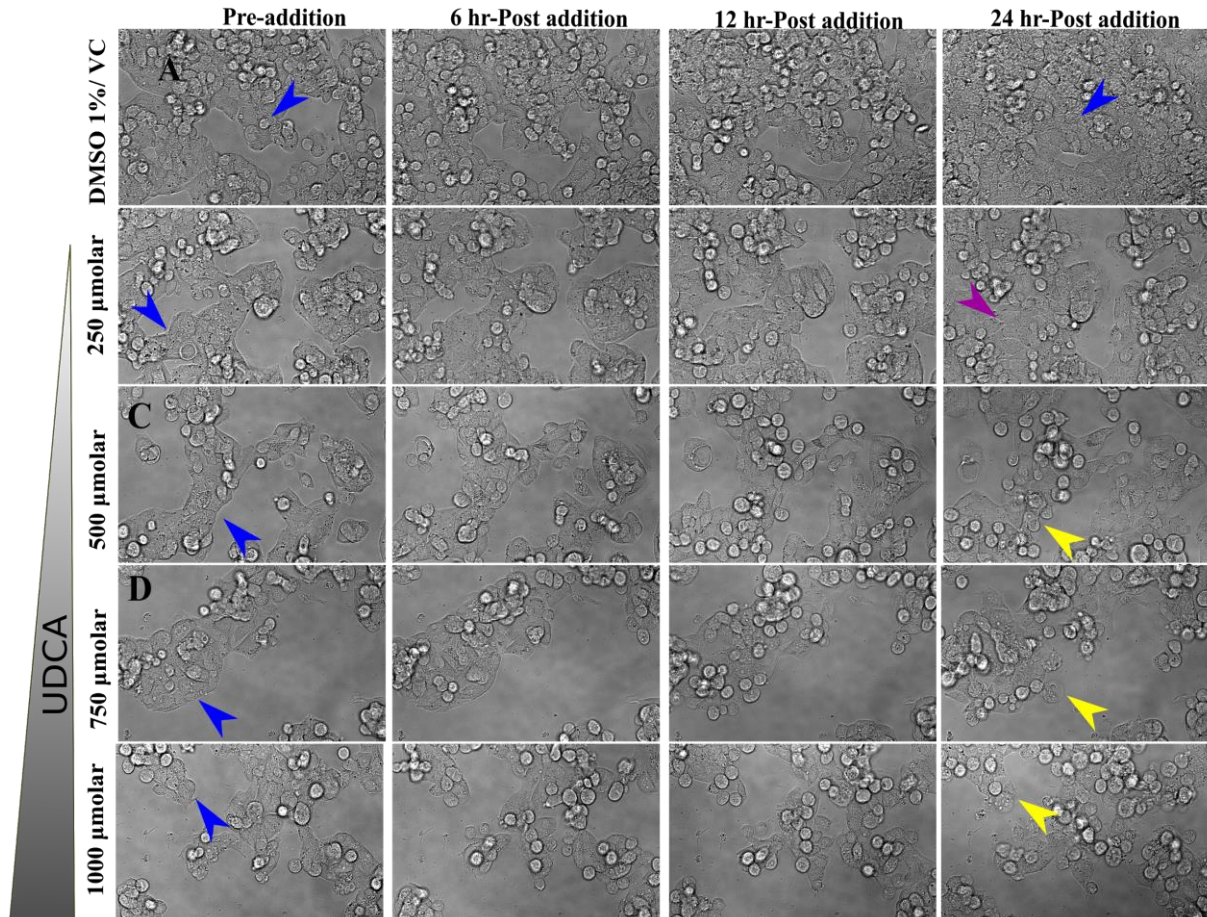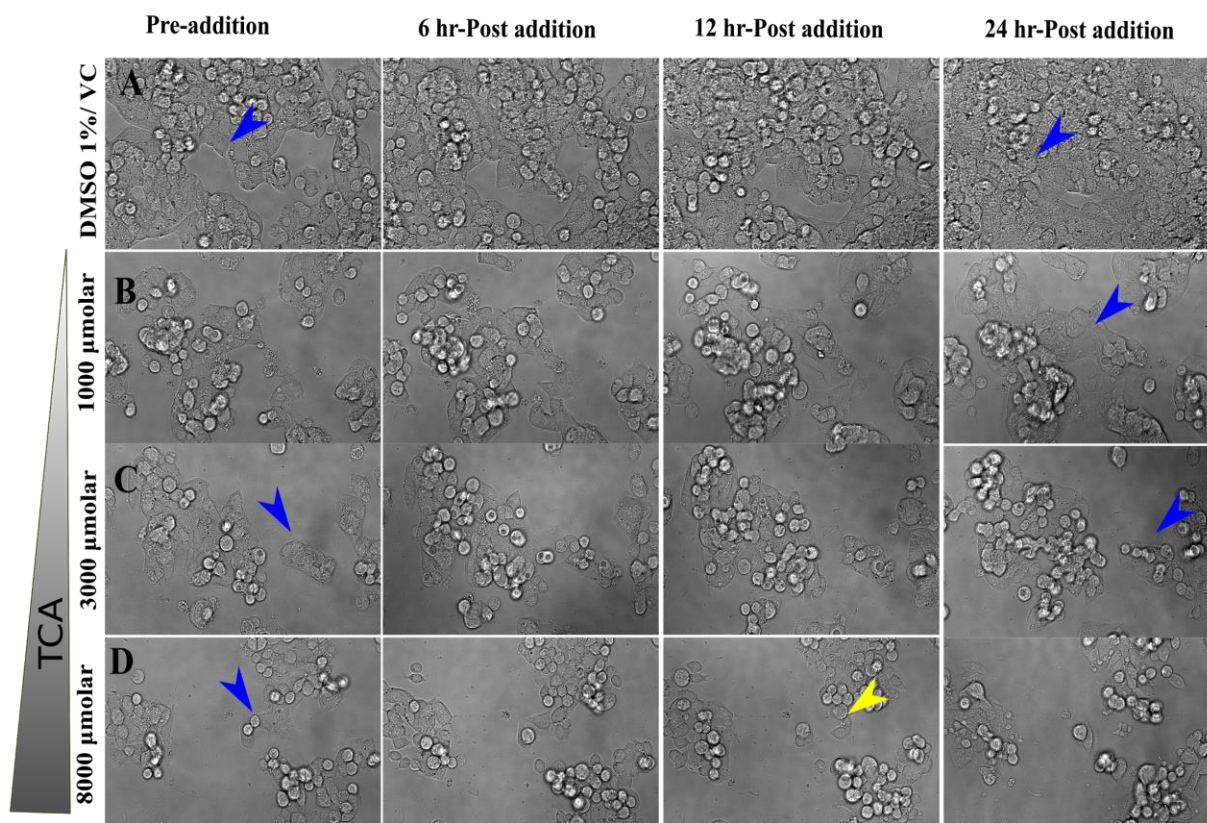
Fig.4.2.1.2.F4. Morphological changes induced after exposure of HepG2 cells to the bile acid TCA. A. Top row: Cluster of healthy HepG2 (blue arrow) before and after (6, 12, 24 hours) exposure to DMSO 1% (vehicle control) show healthy proliferated cell clusters (blue arrow) and no observed cell death. B. TCA 1000 µM did not exert cell death within 24 hours post exposure with healthy conical shaped proliferated cell clusters (blue arrow). C. 3000 µM of TCA was also observed to not cytotoxic and did not induced cell death within 24 hours of exposure (blue arrow). D. TCA 8000 µM induced cytotoxicity between 6-12 hours of exposure at rate of 0.1% observed with presence of round dead cell (yellow arrow).

The examples presented above showing the lowest and the highest concentrations of bile acids that induced morphological changes led further to the identification of accurate concentration ranges by the CTB assay as described in the next chapter.

4.2.2. Cytotoxicity as a measure of cell viability after exposure to bile acids

To confirm the above morphological changes observed from the real-time imaging of cell death using time-lapse and determine the viability of the bile acid treated primary mouse hepatocytes and HepG2 cells, we used a cell viability assay (Cell Titer-Blue®/ CTB: Cell Viability Assay, Promega). After 24 hours of concentration dependent exposure to bile acids, the cell viability was quantified based on the ability of the cells to metabolize CTB. We further calculated the EC_{50} of each analyzed bile acid (4.2.2.F1).

Fig.4.2.2.F1. Bile acids reduce the cell viability of primary mouse hepatocytes. A. Deoxycholic acid (DCA); B. Taurocholic acid (TCA); C. Chenodeoxycholic acid (CDCA); D. Ursodeoxycholic acid (UDCA). The vertical lines indicate the EC_{50} and its 95% confidence interval.

The dose-dependent cytotoxicity of bile acids in primary mouse hepatocytes was then compared to the dose-dependent cytotoxic activity of bile acids in HepG2 cells (4.2.2.F2).
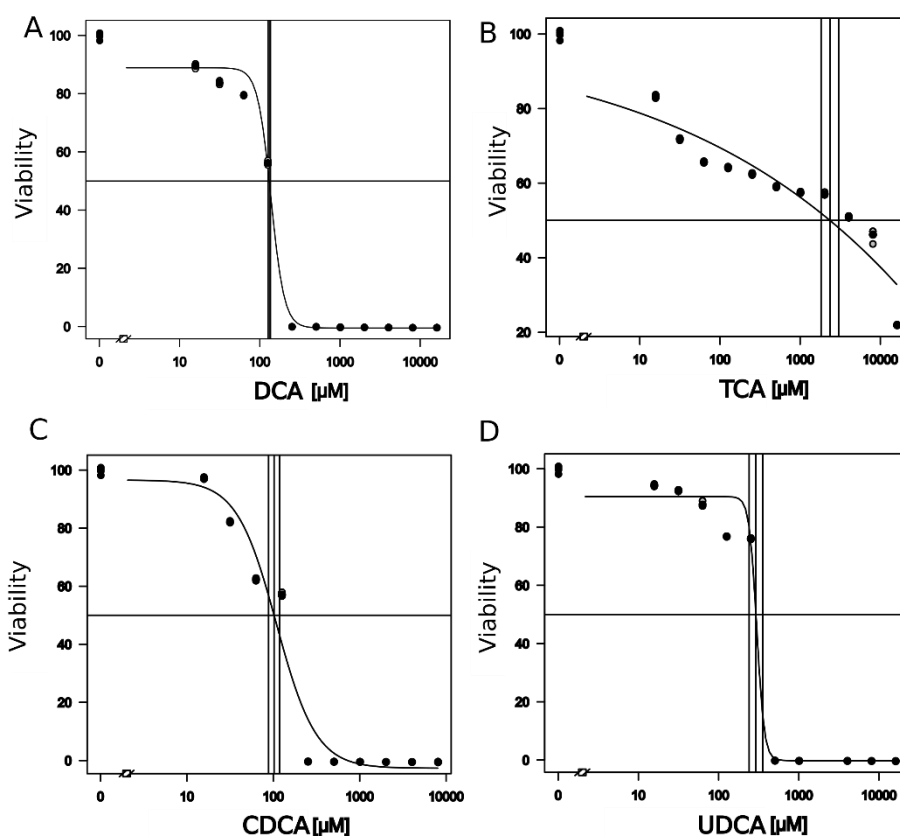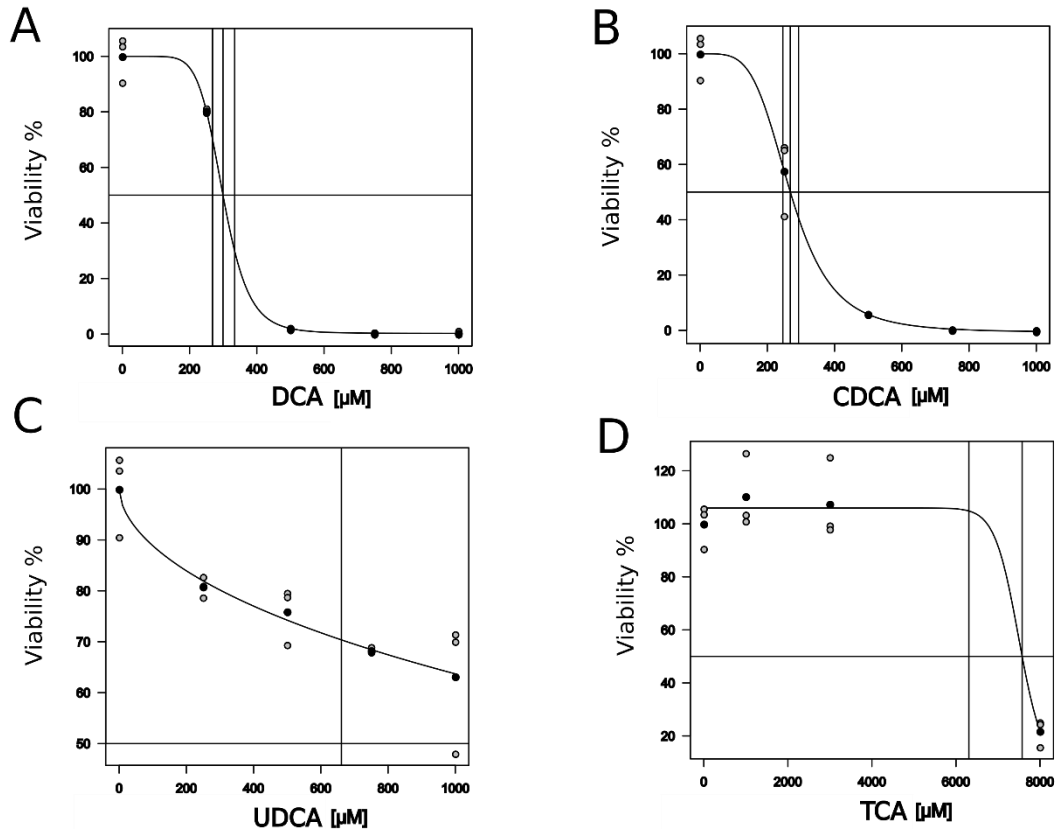
Fig.4.2.2.F2.Bile acids reduce the cell viability of HepG2 cells. A. Deoxycholic acid (DCA); B. Taurocholic acid (TCA); C. Chenodeoxycholic acid (CDCA); D. Ursodeoxycholic acid (UDCA). The vertical lines indicate the EC_{50} and its 95% confidence interval.

The results identified CDCA as being the most cytotoxic bile acid followed by DCA > UDCA > TCA in both, the primary cells and the liver-specific cell line (HepG2). The effective concentrations (EC_{50}) of different bile acids were determined in both PMH and HepG2 cells from the CTB assay (Table.4.2.2.T1). Although the order of toxicity in HepG2 cells and the effects on morphology induced by bile acids were similar as observed in primary mouse hepatocytes, HepG2 cells required two to three-fold higher concentrations to induce cytotoxicity. This difference could be the lack of bile acid transporters in HepG2 cells. In conclusion, the morphology based on time-lapse imaging and the standardized cell viability assay narrow down the concentration range of bile acids that are toxic. These concentrations were the basis of all the further experiments related to cytoskeleton dynamics in bile acid-induced toxicity.

Table.4.2.2.T1. Effective concentrations of bile acids that induced cytotoxicity in PMH and HepG2

Cell line / Primary cells	Bile acid	EC$_{50}$ concentration (μM)	C.I.Lower	C.I.Upper
PMH	CDCA	102	88	118
	DCA	131	126	137
	UDCA	292	240	356
	TCA	2352	1827	3027
HepG2	CDCA	268	246	293
	DCA	299	268	334
	UDCA	1975	661	5901
	TCA	7475	6307	9097

PMH: primary mouse hepatocytes, C.I: confidence interval, EC: effective concentration

4.2.3. Propensity of different bile acids to activate intracellular FXR

In order to quantitatively determine FXR activity, we utilized a FRET-based sensor derived from the bile acid binding domain of FXR. HepG2 cells were transfected with this CFP-YFP FRET sensor variant CBAS which localizes to the cytoplasm. The sensor shows changes in FRET (van der Velden et al., n.d.) upon bile-acid binding, indicating that FXR has been activated by bile acids. To determine the responsive range of the sensor and FXR activation, HepG2 cells were exposed to the most potent ligand of FXR, CDCA at different concentrations. The activity of FXR was measured and found to reach maximal values at 10 μM of CDCA (4.2.3.F1.A) over approximately 5 hours in HepG2 cells (4.2.3.F1.B). We measured a binding constant of 3.1 μM for CDCA and FXR in live cells. These data are in agreement with previous

studies using purified FXR in biochemical assays [3 µM, (Mi et al., 2003)]and X-ray crystallography [2.4 µM (van der Velden et al., n.d.)].
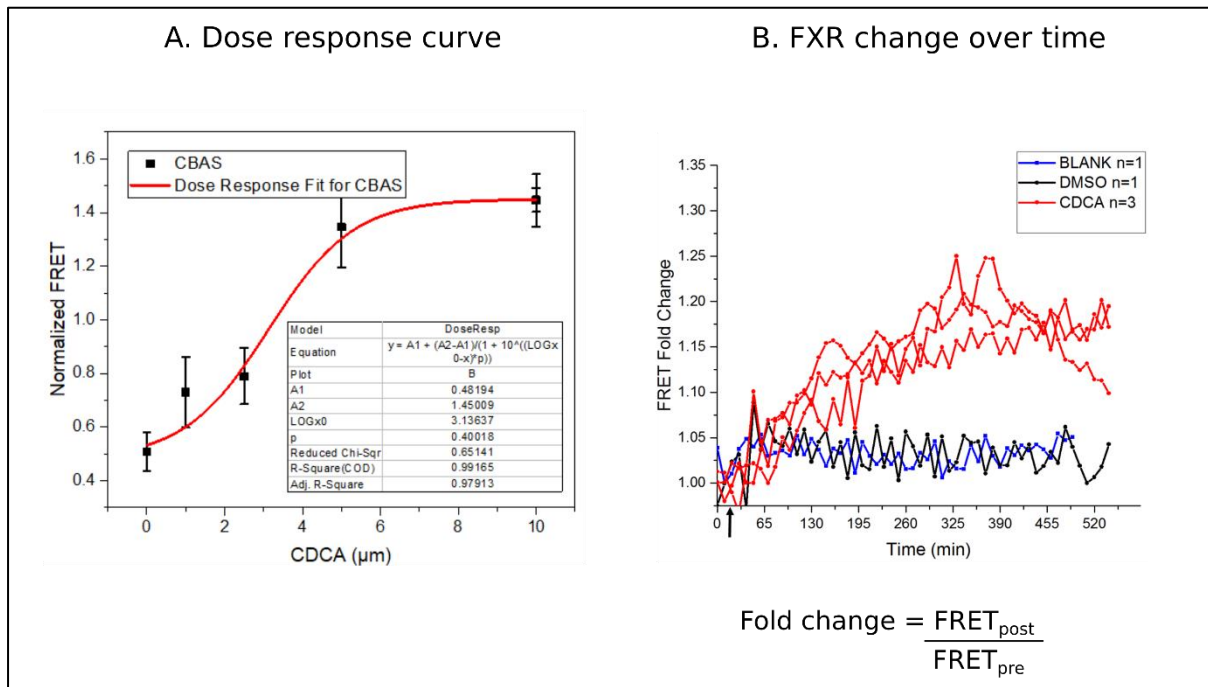

Fig.4.2.3.F1. Dose and time-dependent response of FXR in HepG2 cells to bile acid CDCA. A. Normalized FRET values over increasing concentration of CDCA and dose-response fit the same. Error bars indicate Mean ± SEM. The table shows the best-fit parameters. B. FRET fold change i.e. the ratio of FRET post bile acid addition vs FRET pre-bile acid addition, over time in HepG2 cells incubated with 12.5 µm CDCA. Each line indicates an independent cell cluster that is made of at least five to six cells.

We then tested the effect of DCA and TCA on FXR activation in HepG2 cells exposed to these bile acids over a period of 24 hours. At 100 µM of DCA, TCA or UDCA, FXR activity had reached maximal values. The results show that FXR activation is initiated at concentrations up to several fold lower than the EC_{50} value of the toxicity of these bile acids. Since bile acids seem to activate FXR at concentrations where they are not-toxic, it is unlikely that cytotoxicity is directly proportional to FXR activation. Rather, active FXR initiates transcriptional changes in cells and creates the cellular context in which bile acid toxification leads to cell death. The direct mechanism of bile-acid induced toxicity, however, remains unclear. Active FXR is known to modulate Wnt/beta-catenin signaling, a pathway that is known to have significant effects on the cellular cytoskeleton (Thompson et al., 2018). Bile acids themselves are known to interact with actin in vitro (Gupta et al., 2016), and circumstantial evidence exists showing that canalicular dynamics originating from actin-myosin interactions are altered upon bile acid

exposure. We, therefore, investigated if bile acid causes cytotoxicity by directly interfering with the cellular cytoskeleton.

4.2.4. Cortical actin cytoskeleton network is changed after bile acid exposure

The cytoskeleton comprises of at least 3 main structural elements: actin, tubulin and intermediate filaments. The actin cytoskeleton can be classified based on the spatial arrangement of microfilaments into two types, the cytoplasmic cytoskeleton which comprises of structural components such as stress fibers and the cortical cytoskeleton that juxtaposed with the plasma membrane. In hepatocytes, the cortical actin is localized to the canaliculi and provides structural rigidity. In order to visualize the endogenous F-actin network, HepG2 cells were transfected with a 17 amino acid peptide called LifeAct-RFP which binds specifically to actin (Riedl et al., 2008). These cells were then exposed to different bile acids (DCA, TCA) over a period of 24 hours. F-actin network after bile acid exposure was evaluated as a measure of cortical enrichment of F-actin and coherency within the cortical actin network.

DCA 100 µM over a period of 24 hours reduced the cortical F-actin significantly as compared to bile acid untreated cells (4.2.4.F1.A). Low concentration of DCA i.e. 10 µM which activate the FXR did not reduce or significantly changed the cortical actin network (4.2.4.F1.A). On the other hand, high and low concentrations of TCA i.e. 10 and 100 µM had minor effects on the cortical F-actin enrichment (4.2.4.F1.A). The results were confirmed as observed again in an experimental repeat (4.2.4.F1.B).

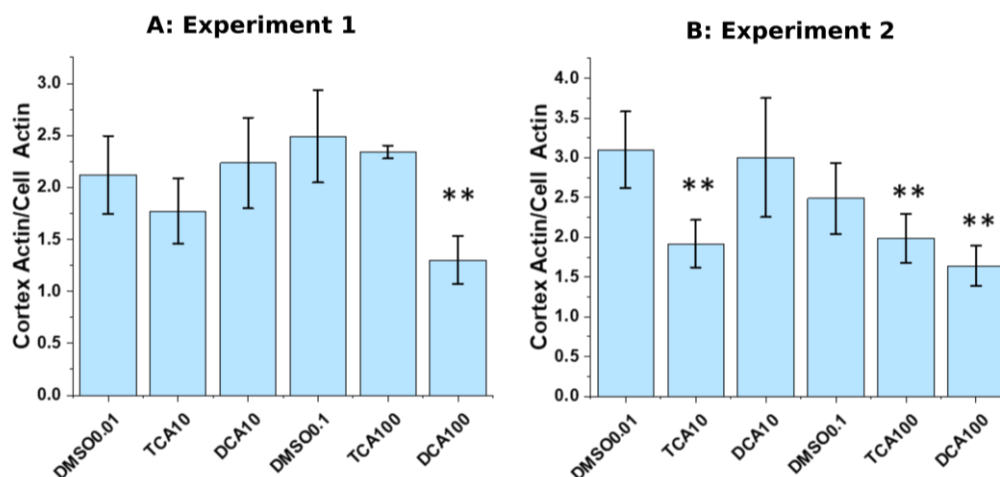Cortical F-actin enrichment after 24 hours of bile acid exposure

Fig.4.2.4.F1. Cortical enrichment of actin in HepG2 after exposure to bile acids. A. Graph showing decrease in the cortical F-actin i.e. the ratio of actin in cortex verses actin in the cell/cytoplasm after 24 hours exposure to DCA 100 µM. B. Experimental repeat confirms the same result as seen in A but TCA 100 µM also induced minor reduction of the cortical F-actin over 24 hours.

Actin coherency is increased by both high and low concentrations of bile acids, DCA and TCA after 24 hours (4.2.4.F2.A and B).
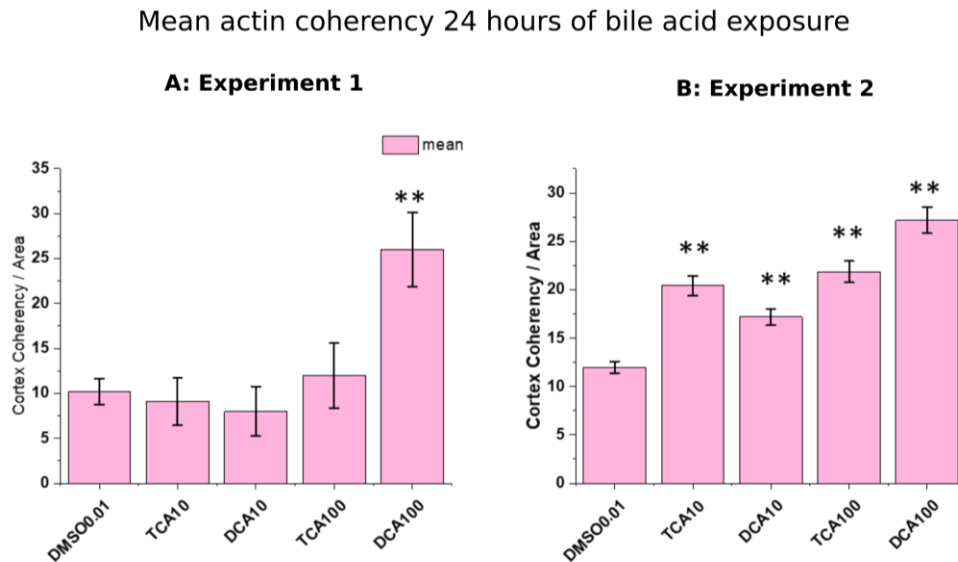
Fig.4.2.4.F2. Mean coherency of F-actin after exposure to bile acids. A. DCA 100 µM exposure resulted in an 2-fold increase in the mean coherency of F-actin after 24 hours. B. Experimental repeat also show significant changes in the mean actin coherency in cells exposed to low concentrations of TCA and DCA. Asterix points in the graphs indicate level of significance with the mean ± SEM.

Thus, after exposure to bile acids, the cortical actin decreases and exists in the state of long fibers which may indicate indirectly the depolymerization of actin thus altering cell dynamics.

4.2.5. FXR activation is not correlated with changes in cortical actin network in cells exposed to different bile acids

The experiments to evaluate the changes in actin cytoskeleton in HepG2 cells (see section 4.2.4) were performed with simultaneous co-transfection of the FRET-based FXR activity sensor CBAS. This allowed us to determine if FXR activation by the different bile acids is correlated with changes induced in the actin cytoskeleton.

As suspected due to the maximal activity of FXR observed at low bile acid concentrations (see section 4.2.3), we show that changes in the actin cytoskeleton are not correlated with the degree of FXR activation (4.2.5.F1.A).

As an internal control, we measured the correlation between FXR activity in the cytoplasm and that within the cortical cytoskeleton (4.2.5.F1.B).
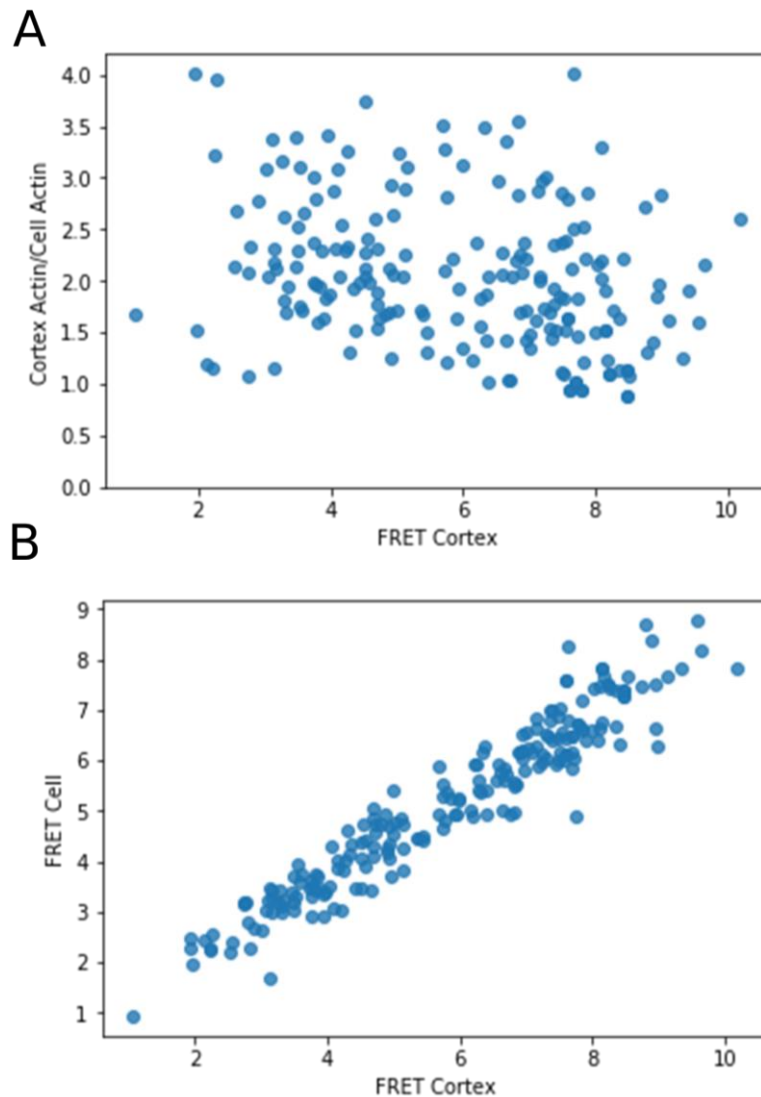
Fig.4.2.5.F1. Correlation maps of FXR activity and actin cytoskeleton in HepG2 treated with bile acids. A. Correlation map shows FXR activity in the cortex is not correlated with the actin cytoskeleton changes. Each point B. Correlation map of FXR activity in the cortex versus FXR activity in the cytoplasm indicates a strong correlation.

The strong correlation in FXR activity between these two regions indicate that bile acids activate FXR homogeneously and spatial differences do not explain the lack of correlation between FXR activity and cortical actin disruption.

4.2.6. Bile acids induced toxicity is associated with alterations in the cytoskeleton

The cytoskeleton provides cell shape, stability, and basic cytoskeletal support; however, the cytoskeleton is dynamic with individual actin fibers undergoing repeated rounds of polymerization and depolymerization (Lodish et al. 2000). In addition to the actin network, the cytoskeleton also has microtubular network of tubulin that interacts with actin and provides the molecular pathways for transport of regulatory proteins, structural proteins of the tight junctions, etc. (Tzanakakis, Hansen, & Hu, 2001). The peri-canalicular space or bile canaliculus is surrounded by actin filament network (Segawa et al., 1993; Tsukada et al., 1995).It is no surprise, that the movements of canaliculi in hepatocytes termed canalicular dynamics are intimately dependent on actin and tubulin dynamics (Dugina et al., 2016; Tsukada et al., 1995).

To visualize the subtle changes in the cytoskeleton and dynamics of the peri-canalicular actin cytoskeleton after bile acid exposure, we utilized primary mouse hepatocytes cultivated in a sandwich culture which form functional bile canaliculi (Reif et al., 2015). However, primary mouse hepatocytes are not easily transfectable. We, therefore, developed a method based on a fluorogenic probe called '***Sir-actin***', that allows us to visualize the actin dynamics in live primary mouse hepatocytes. Primary mouse hepatocytes showed specific localization of this small molecule dye at the peri-canalicular and cortical area of hepatocytes (see section 3.2.10.2.3) after 4 hours of incubation (4.2.6.F1).
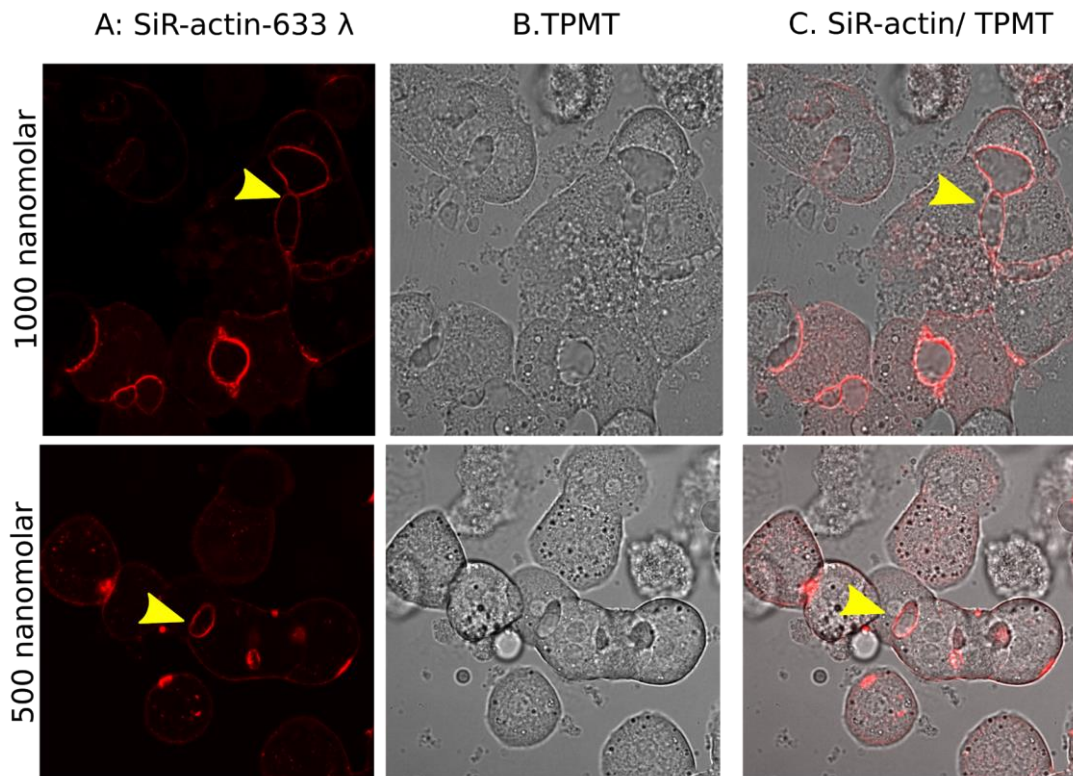
Fig.4.2.6.F1. Staining of pericanalicular and cortical actin in live primary mouse hepatocytes. A. The pericanalicular space between three adjacent hepatocytes positive for SiR-actin (yellow arrow) labeling after an incubation for 1 hours with 1000 nM. B. Primary mouse hepatocytes incubated with 500 nM SiR-actin for 4 hours at 4 °C in suspension and seeded as sandwich culture also show a positive labeled bile canaliculus (yellow arrow).

All the further experiments after treatment with bile acids were carried out in cells incubated with 500 nM of the dye in primary mouse hepatocytes and actin dynamics were recorded using live cell imaging.

4.2.6.1. Bile acid toxicity results from destabilized bile canaliculi as a result of depleted pericanalicular actin

Functional bile canaliculi are required for normal bile acid efflux from hepatocytes (Watanabe et al., 2006). These canalicular structures have the ability to secrete many liver-specific proteins such as albumin and bile acids (Dunn, Tompkins, & Yarmush, 1991). Functionality of the bile canaliculi depends on their stability and expression of important apical membrane anchored transporter proteins such as BSEP, NTCP. During the establishment of the bile canaliculi in vitro in sandwich cultures, bile canaliculi exhibit dynamic motility, such as rhythmic contractions and dilations of the apical membrane (Reif et al., 2015). Upon establishment and formation of tight junctions between two hepatocyte apical membranes, canaliculi enter a structurally stable phase. This dynamic to stable transition of the canaliculus is dependent on the phosphorylation/dephosphorylation of the myosin light chain (MLC) subunit 2 and on the acto-myosin pathway. It is also known that certain cholestatic drugs can increase the motility of bile canaliculi via the Rho kinase (ROCK)/myosin light chain kinase (MLCK) pathway (Burbank et al., 2016; Sharanek et al., 2016). Although the signaling pathway involved is studied in detail, its involvement in sensitizing the cell and induce hepatotoxicity remains to be explored. Therefore, we investigated if changes in canalicular stability also play a role in bile acid mediated toxicity, similar to effects caused by cholestatic drugs. Actin, that is one of the filaments that form the cytoskeleton has been reported to be localized circumferentially at the canalicular membrane (Tsukada et al., 1995). Here, it plays an important role in providing stability to the cell. We therefore, further studied if any alterations in the peri canalicular actin can weaken the cytoskeleton and result in bile acid induced toxicity.

For this, we incubated live cells with a fluorogenic actin specific probe and exposed them to evaluated ~EC_{50} concentrations of 4 physiologically important bile acids (CDCA, DCA, UDCA, TCA). We observed that, CDCA the potent FXR ligand, induced hepatotoxicity at 100 µM over a period of 48 hours of exposure (4.2.6.1.F1). The different events included depletion of the pericanalicular actin, with canalicular dynamics, collapse of the bile canaliculus, redistribution of actin in the cortex, membrane rupture and eventually cell death.
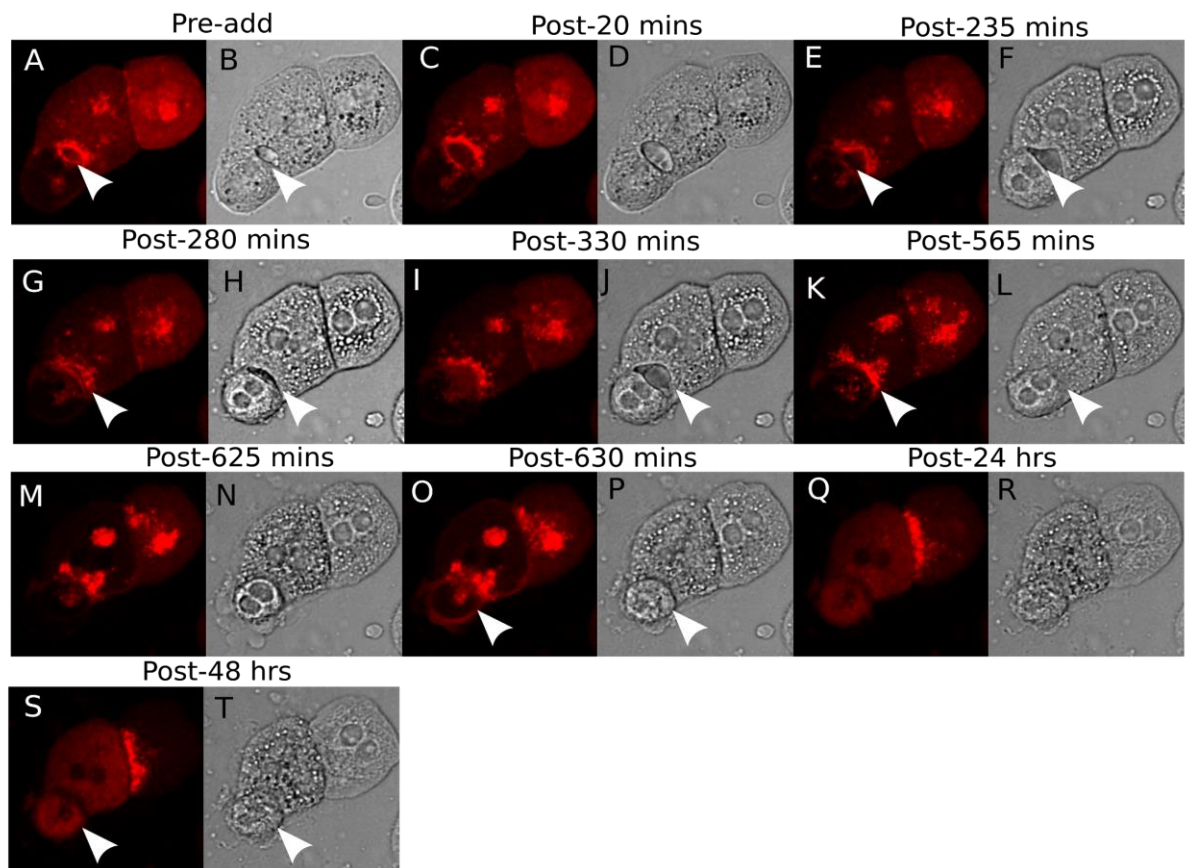
Fig.4.2.6.F1. **CDCA induced changes in peri-canalicular actin cytoskeleton of PMH.** 20 X magnification of primary mouse hepatocytes in SiR-actin and DIC channels imaged for 48 hours. A,B: Show some healthy adjacent hepatocytes with bile canaliculi (white arrow). C-F: Loss of pericanalicular actin after incubation with 100 µM bile acid. Canalicular dilation (white arrow, F) of the same cell of which the pericanalicular actin is depleted. G-L: Altered canalicular dynamics of the hepatocytes showing canalicular constriction-dilation with collapse bile canaliculi. M-P: Membrane rupture of the hepatocyte and redistribution of the actin to the cortex. Q-T: Cell death of the adjacent hepatocyte and complete loss of the pericanalicular actin (white arrow).

At 100 µM, DCA also induced similar cytotoxic effects as observed with CDCA (4.2.6.1.F2). Reduction in the pericanalicular actin intensity (4.2.6.1.F2.E,G,I,K: white arrow) and canalicular dynamics such as constriction-dilation were observed post incubation with the bile acid DCA. Collapse of the bile canaliculi with membrane rupture and redistribution of the actin to the cortex was observed over a period of 48 hours.

Fig.4.2.6.1.F2. **DCA induced peri-canalicular actin cytoskeletal changes in PMH.** 20 X magnification of primary mouse hepatocytes in SiR-actin and DIC channels imaged for 48 hours. A,B: Healthy adjacent hepatocytes with bile canaliculi (white arrow) prior to bile acid exposure. E-N: Depletion of pericanalicular actin following 100 µM DCA-exposure with altered canalicular dynamics (white arrow: dilation, F; constriction, I, J, L; redilation, N) seen in the same field of view. O-R: Canalicular collapse (white arrow) and subsequent cell death (white arrow). Q-V: Membrane rupture of the hepatocyte and redistribution of the actin to the cortex. Cell remnants of the adjacent dead hepatocytes with eventual washout of the staining dye and complete loss of the pericanalicular actin (white arrow).

Choleretic bile acid UDCA, have been reported to induce formation of inward blebs from the peri-canalicular membrane that may help to regurgitate bile and alleviate cholestasis (Gupta et al., 2016). But its cytotoxic effect has been poorly understood. We observed, that the ~EC_{50} value of UDCA also resulted in depletion of the pericanalicular actin and induced cytotoxicity (4.2.6.1.F3).
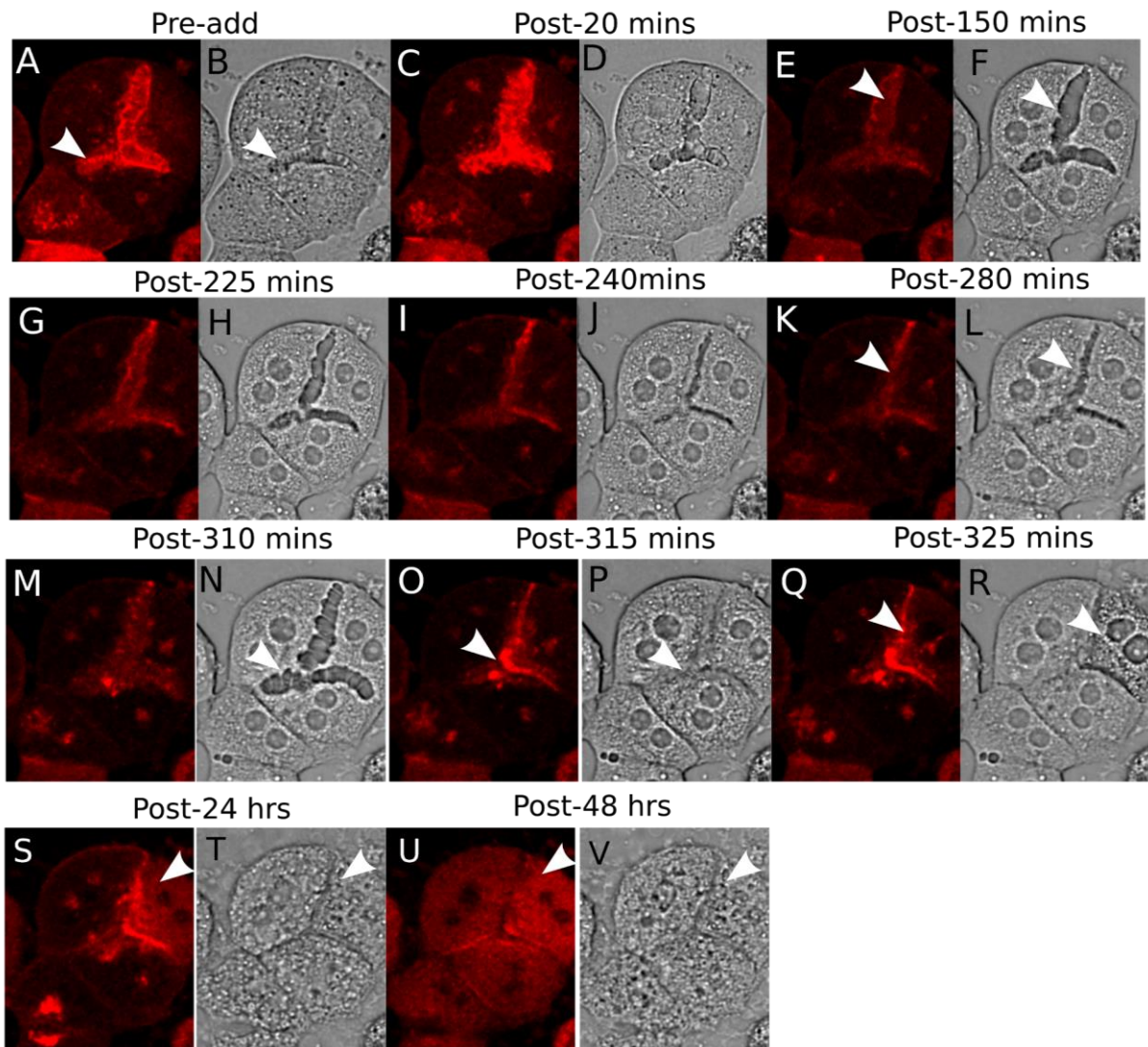
Fig.4.2.6.1.F3. **UDCA induced peri-canalicular actin cytoskeletal changes in PMH.** 20 X magnification of primary mouse hepatocytes in SiR-actin and DIC channels imaged for 48 hours. A,B: Healthy adjacent hepatocytes with bile canaliculi as seen in DIC and SiR-actin channels prior to bile acid exposure. C-N: Depletion of pericanalicular actin following UDCA-exposure with oscillatory altered canalicular dynamics (white arrow: dilation, F; constriction, G,) and canalicular collapse (white arrow, J) seen in the same field of view. K-P: Subsequent cell death along with membrane rupture following actin depletion of the adjacent hepatocytes. Q-V: Redistribution of the actin to the cortex with eventual washout of the staining dye from the cortex and complete loss of the pericanalicular actin (white arrow).

Taurocholic acid resulted in cytotoxicity in primary mouse hepatocytes at high millimolar concentrations (4.2.6.1.F4). The events involved in inducing cytotoxicity followed similar pattern as observed with other bile acids, but the concentration of TCA was about 10-fold higher i.e. 2000 µM to induce any changes on the pericanalicular actin or cell survival.
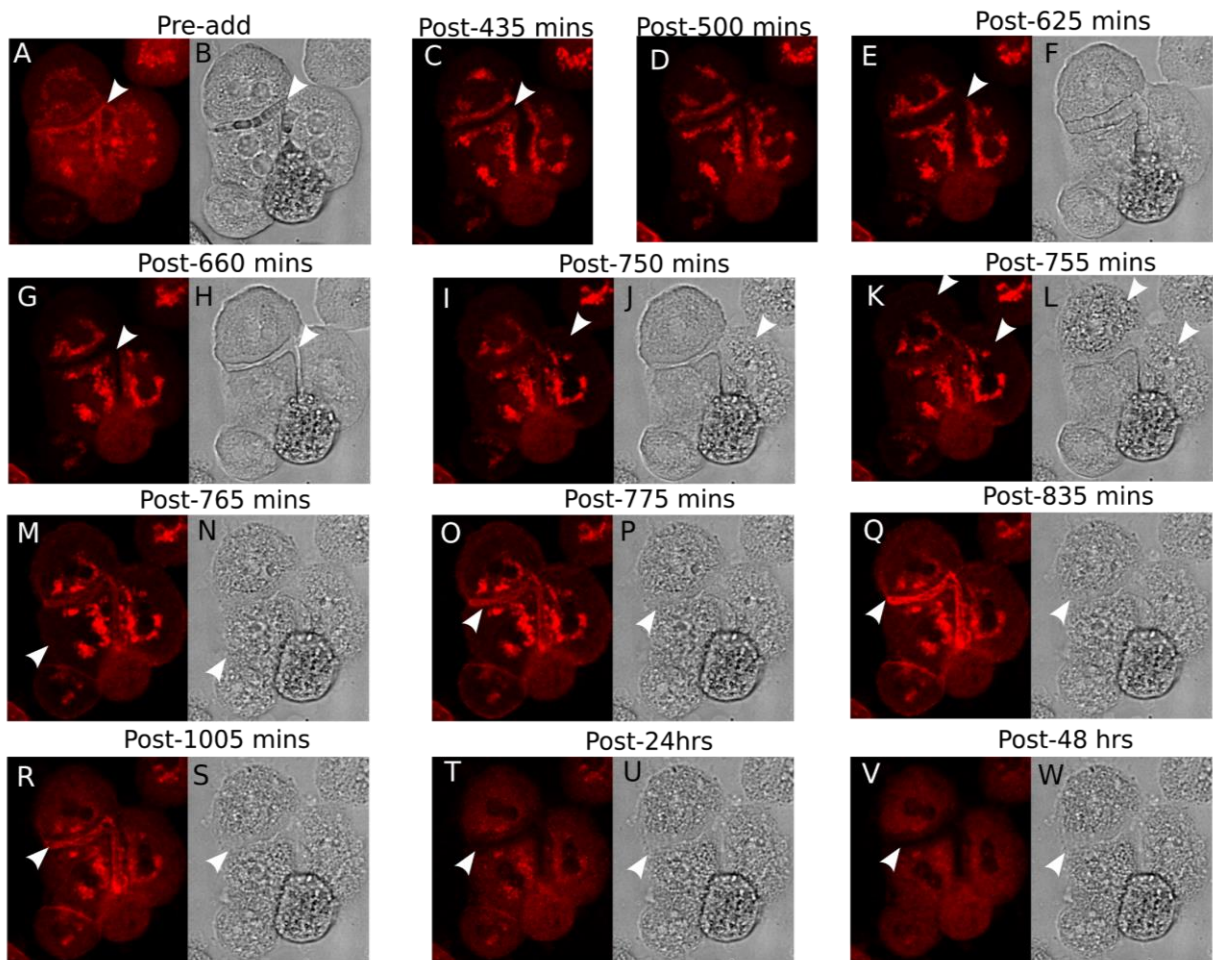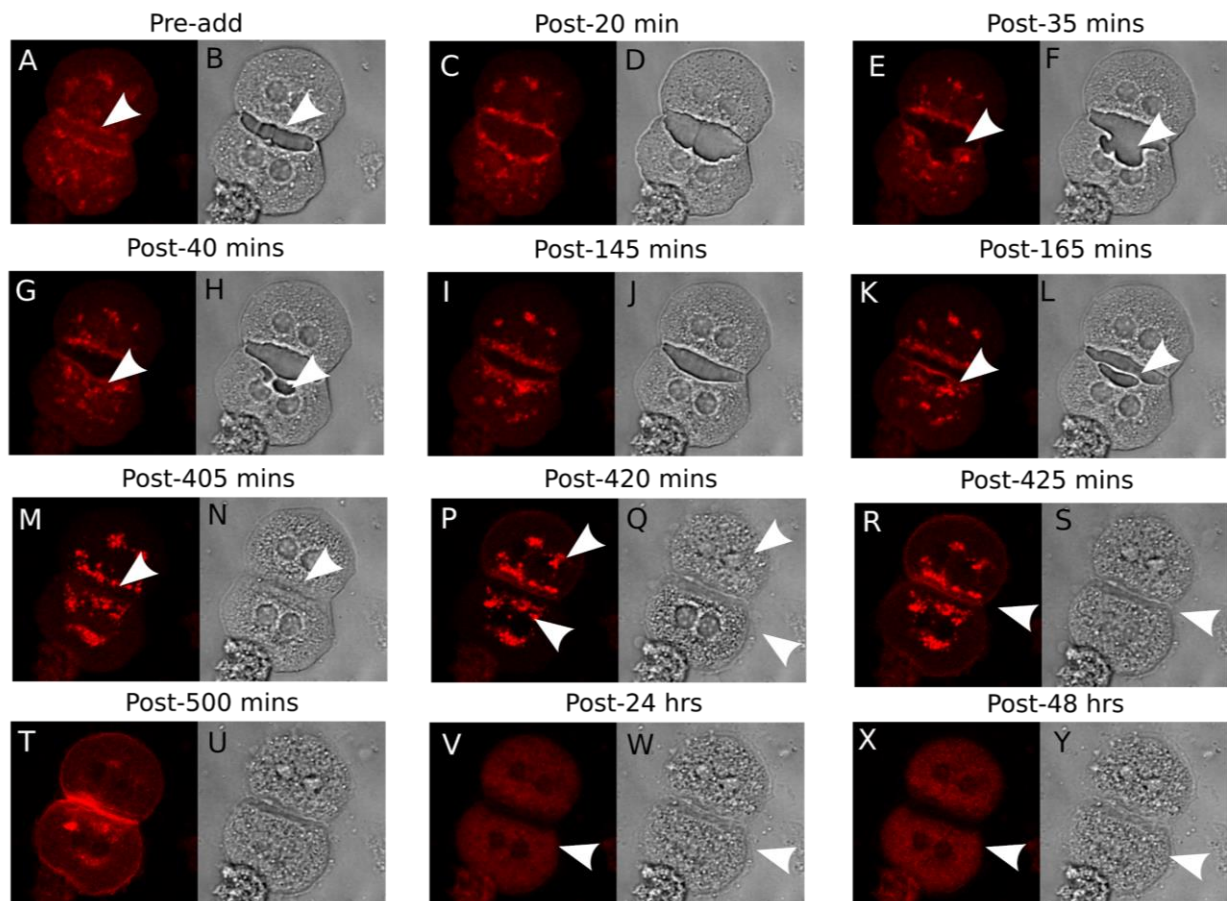
Fig.4.2.6.1.F4. **TCA induced peri-canalicular actin cytoskeletal changes in PMH.** 20 X magnification of primary mouse hepatocytes in SiR-actin and DIC channels imaged for 48 hours. A, B: Healthy adjacent hepatocytes with bile canaliculi with pericanalicular SiR-actin labeling and DIC image of same cells prior to bile acid exposure. C-L: Altered canalicular dynamics with dilated bile canaliculus (white arrow, C), bile canalicular vesicle (BCV) formation with canalicular constriction (white arrow, E-L), along with depletion of peri-canalicular actin following UDCA-exposure. M-Q: Subsequent cell death after peri-canalicular actin depletion with membrane rupture. R-Y: Redistribution of the actin to the cortex with eventual washout of the staining dye from the cortex and complete loss of the pericanalicular actin (white arrow).

Bile acids were dissolved using DMSO as solvent. To confirm if the vehicle control or solvent induced any cytotoxicity independent of the bile acids, primary mouse hepatocytes were incubated with equivalent concentration of DMSO 1% as used for bile acid solutions. DMSO 1% did not induce any cytotoxicity in the observed imaging period of 48 hours (4.2.6.1. F5).
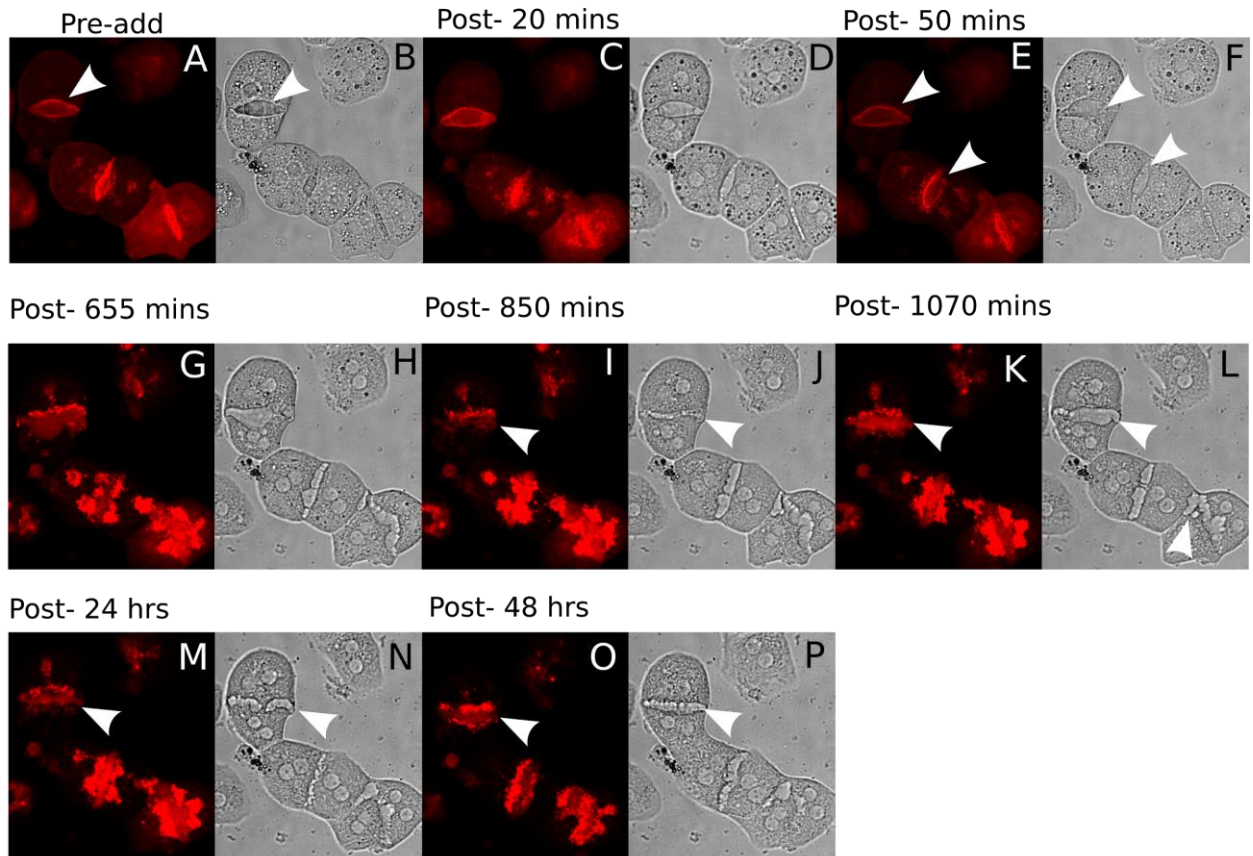
Fig.4.2.6.1.F5. **Hepatocyte survival post exposure to vehicle control or DMSO.** A, B: Healthy hepatocyte as seen in SiR-actin and DIC channels prior to bile acid exposure. C, E, G, I: Pericanalicular actin is not depleted even over the period of 48 hours after incubation with the vehicle control. D, F, H, J: DIC channels show the healthy hepatocytes with canalicular dynamics of constriction-dilation of the bile canaliculi.

4.2.6.2. Tubulin-actin interplay in relation to bile canalicular dynamics

The actin and tubulin networks are interdependent on each other and tubulin is known to play a role in self-assembly of the hepatocytes and vesicular transport (Oda et al., 1995; Tzanakakis et al., 2001). To visualize, if the altered actin network after bile acid exposure has any repercussions on the microtubule or tubulin network, '***Tubulin Tracker Green reagent***', an uncharged, non-fluorescent compound that can easily pass through the plasma membrane of live cells was used. Once crossed the membrane the lipophilic blocking group on this compound is cleaved and green fluorescence is seen. This compound allowed uniform selective labeling of the polymerized tubulin in the live cells ("Tubulin Tracker Oregon Green 488 Taxol, Bis-Acetate), for live-cell imaging," n.d.; Wu et al., 2011). Incubation with 1000 nM Tubulin Tracker Green reagent for 30 mins of PMH incubated with 100 nM SiR-actin for ~12

hours and seeded as sandwich layer, showed a uniform selective labeling of the peri-canalicular tubulin and actin in sandwich cultivated primary mouse hepatocytes (4.2.6.1. F1.A-A3). In contrast to the actin cytoskeleton labeling, tubulin labeling was also prominent in the cell membrane.

Thus, the experimental data showed that the tubulin network corresponds to the actin cytoskeleton network and is present at the peri-canalicular membrane (4.2.6.2. F1.A-A3). At cytotoxic concentrations i.e. 100 µM of bile acid such as CDCA, the pericanalicular actin diminishes which coincides with an overall depletion of the pericanalicular tubulin and finally results in cell death (4.2.6.2.F1.C-J).
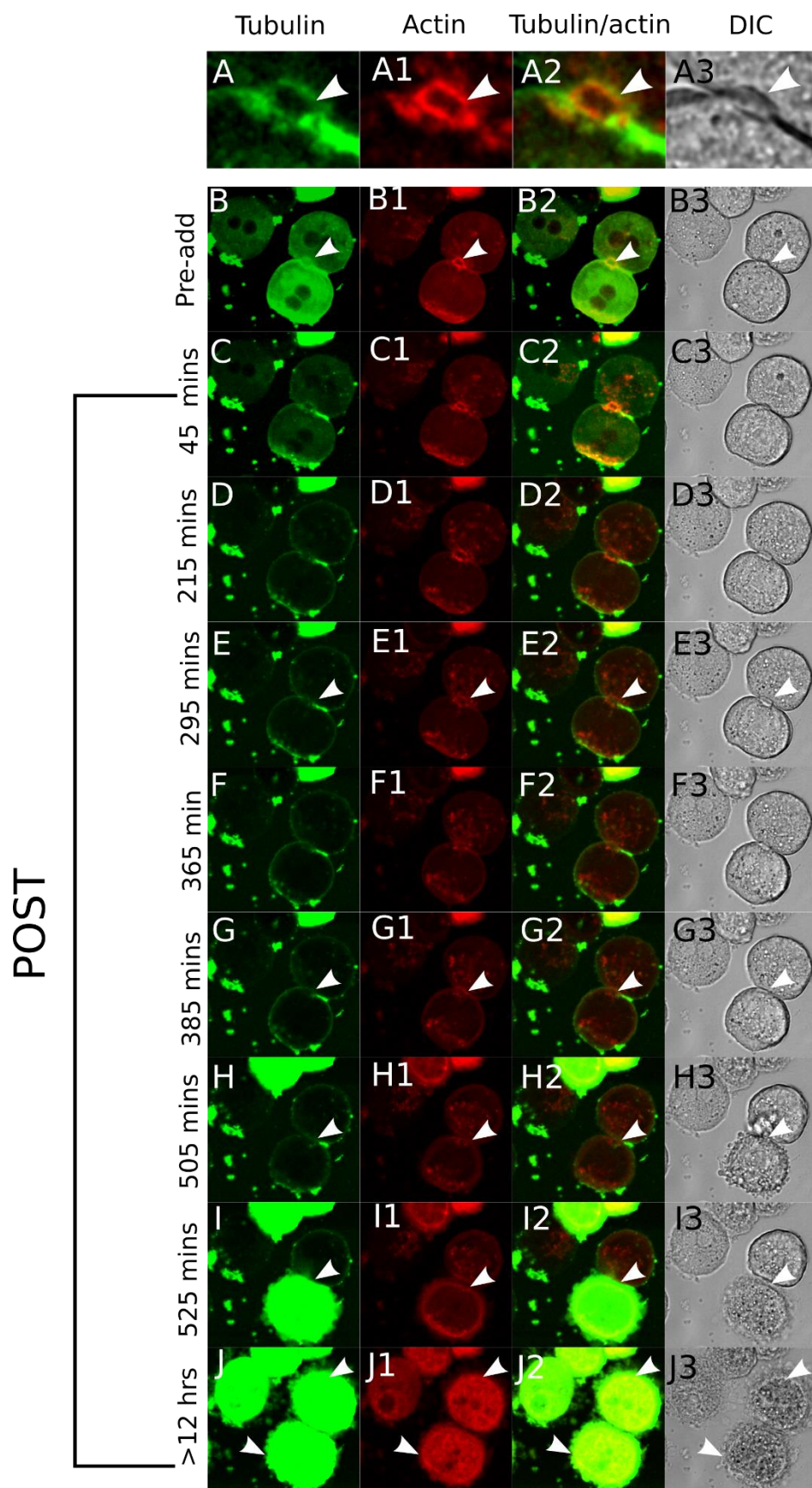
Fig.4.2.6.2. F1. **Actin-tubulin network is altered after exposure to CDCA.** A-A3: Magnified view of the peri-canalicular actin and tubulin network, which correspond to each other. E-E3: CDCA treated PMH show a

depletion in the pericanalicular actin and tubulin network. G-G3: Collapse of the bile canaliculi as clearly observed in the DIC image (white arrow) follows the depletion in the pericanalicular cytoskeletal network (G, G1, G2, white arrow). H-H3: Cell blebbing (H3, white arrow) with a collapsed bile canaliculus (H1, white arrow). I-I3: Membrane rupture immediately results in cell death (white arrow, I3) with redistribution of actin along the cortex (I1, white arrow) and flooding of the cell with tubulin tracker dye (I2,white arrow) is observed. J-J3: Cell death with similar pericanalicular actin depletion and collapse of the bile canaliculus with flooding of the tubulin tracker is observed in the adjacent hepatocyte (white arrow) over a period of at least 12 hours of incubation with CDCA.

At 100 µM of DCA, the peri-canalicular actin also depletes and coincides with an overall depletion of the pericanalicular tubulin, which together finally result in cell death (4.2.6.2.F2). Reduction in the pericanalicular actin and alterations in the canalicular dynamics such as constriction-dilation were observed post incubation with DCA. Collapse of the bile canaliculi with membrane rupture and redistribution of the actin to the cortex was observed over a period of at least 12 hours.

Fig.4.2.6.2.F2. **DCA induced alterations in the cytoskeleton of the PMH.** 20 X magnification view of primary mouse hepatocytes pre-addition to bile acid. A-A3: The pericanalicular actin and tubulin network, which

correspond to each other in healthy primary mouse hepatocytes. C-C3: DCA treated PMH show a depletion in the pericanalicular actin and tubulin network. D-D3: Collapse of the bile canaliculi as clearly observed in the DIC image (white arrow) follows the depletion in the pericanalicular cytoskeletal network (G, G1, G2, white arrow). E-E3: Canalicular dilation response post actin depletion prior to death (E3, white arrow) with a collapsed bile canaliculus. G-G3: Cell shrinkage after membrane rupture immediately results in cell death with redistribution of actin along the cortex (white arrow, G3). H-H3: Flooding of the cell with tubulin tracker dye (H2, white arrow) along with redistribution of actin along the cortex marks the signature of a dead cell with disrupted cytoskeleton (H1, white arrow). I, J-I3, J3: Cell death with similar pericanalicular actin depletion and collapse of the bile canaliculus with flooding of the tubulin tracker is observed in the adjacent hepatocyte (white arrow) over a period of at least 12 hours.

Ursodeoxycholic acid disrupted the cytoskeleton at an EC_{50} of 350 µM with depletion of the pericanalicular actin-tubulin and eventually lead to cell death (4.2.6.2. F3).
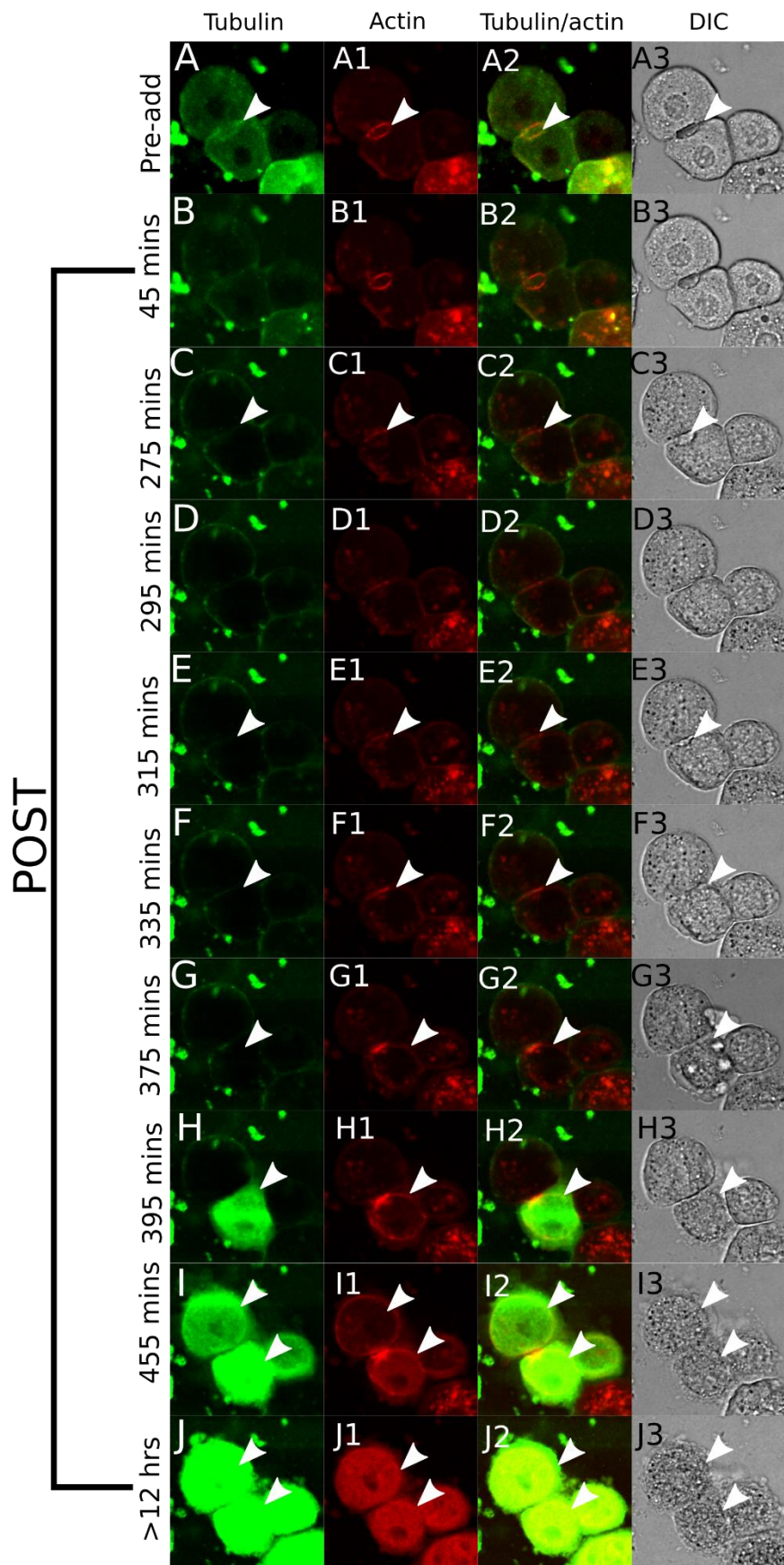
Fig.4.2.6.2. F3. **UDCA induced alterations in the cytoskeleton of the PMH.** 20 X magnification view of primary mouse hepatocytes pre-addition to bile acid. A-A3: The pericanalicular actin and tubulin network, which correspond to each other in healthy primary mouse hepatocytes. D-D3: Bile acid induced depletion in the pericanalicular actin and tubulin network of PMH. F-F3: Collapse of the bile canaliculi and membrane rupture as

clearly observed also in the DIC image with blebbed cell (white arrow, F3) follows immediately the depletion of pericanalicular cytoskeletal network. redistribution of actin to the cell cortex (white arrow, F1-F2) of the dead cell. G-J: Cell death of the adjacent hepatocyte with depletion of the pericanalicular actin-tubulin, cell shrinkage and blebbing, membrane rupture, cortical actin redistribution and flooding of the dead hepatocyte with tubulin tracker dye over a period of at least 12 hours due to UDCA exposure.
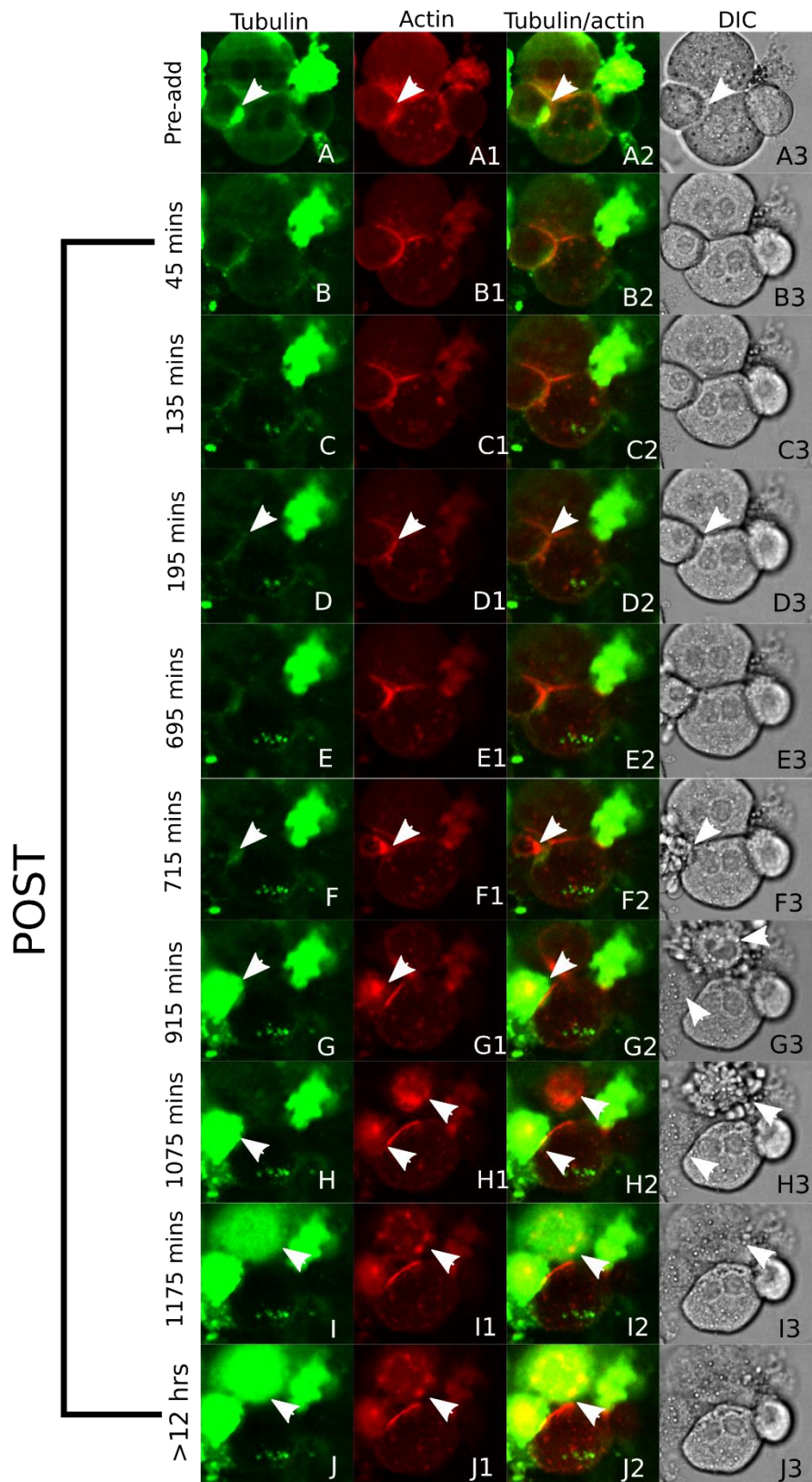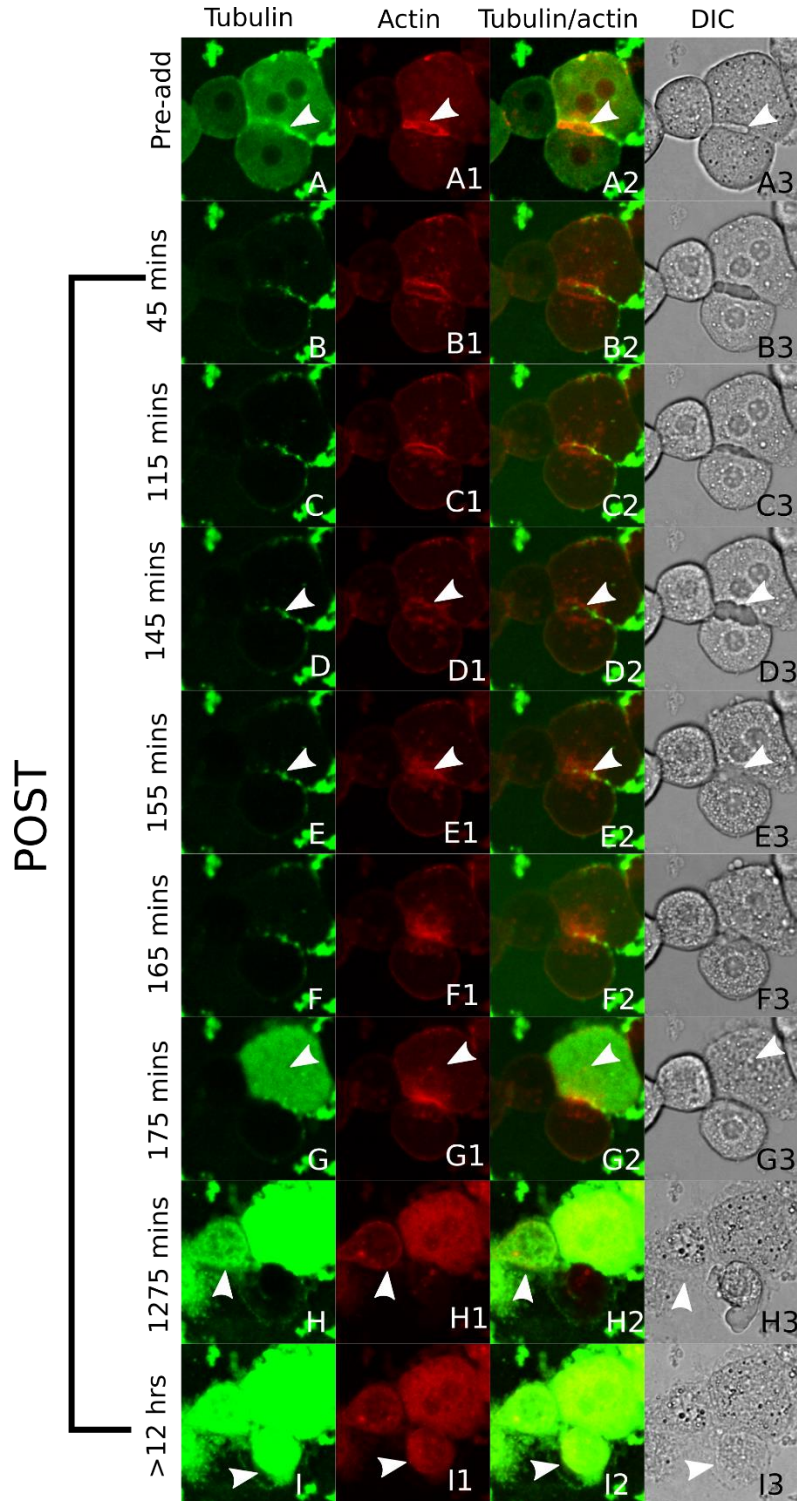

Fig.4.2.6.2. F4. **TCA induced alterations in the cytoskeleton of the PMH at high concentration.** 20 X magnification view of primary mouse hepatocytes pre-addition to bile acid. A-A3: The pericanalicular actin and

tubulin network, which correspond to each other in healthy primary mouse hepatocytes. D-D3: Bile acid induced depletion in the pericanalicular actin and tubulin network of PMH. E-E3: Collapse of the bile canaliculi and blebbing of cell membrane induces the death event as also observed in the DIC channel image (white arrow, E3) follows immediately the depletion of pericanalicular cytoskeletal components. G-G3: Redistribution of actin to the cell cortex of the dead hepatocyte (white arrow, G1) and flooding of the tubulin tracker dye marks the dead fate of the hepatocyte following BA exposure. H-I: Cell death of the adjacent hepatocytes observed over a period of at least 12 hours as an effect of TCA 2000 µM.

To ensure, that depletion of the cytoskeletal components, actin and tubulin is not an effect due to the solvent i.e. DMSO, PMH were incubated with equivalent concentration of solvent i.e. 1% and imaged for a period of 12 hours (4.2.6.2.F5).
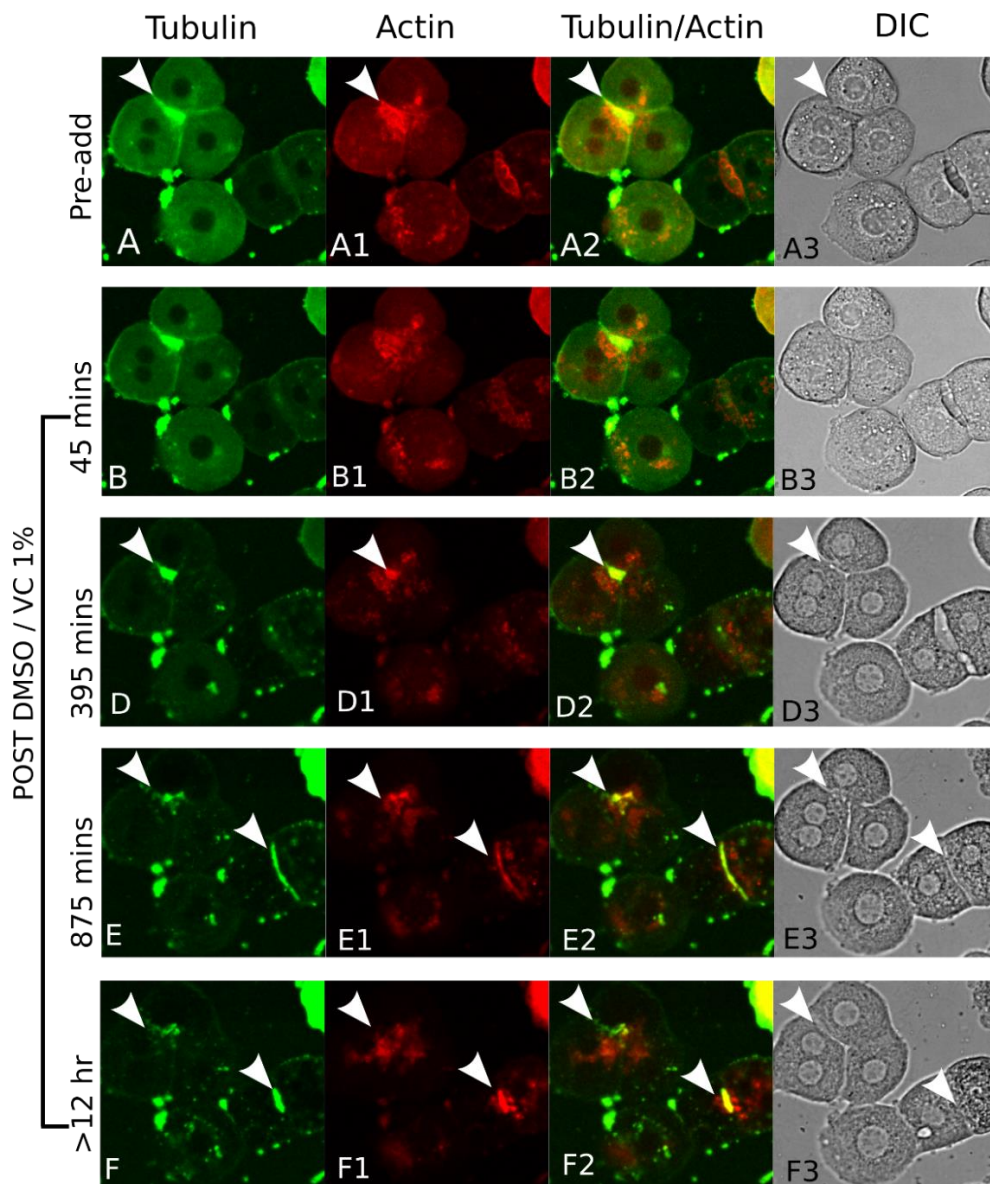

Fig.4.2.6.2. F5. **Cytoskeleton of the PMH treated with 1% solvent or vehicle control i.e. DMSO.** 20 X magnification view of primary mouse hepatocytes pre-addition to bile acid. A-A3: The pericanalicular actin and

tubulin network, which correspond to each other in healthy primary mouse hepatocytes. D-F: Bile canalicular dynamics i.e. dilation-constrictions with localized peri-canalicular actin-tubulin signal observed over a period of 12 hours incubation.

5. DISCUSSION

The work focuses on how the three main topological domains of the liver i.e. bile ducts, bile canaliculi and the hepatocytes respond and adapt to alleviate cholestatic liver injury. Cholestasis induced remodeling is a series of downstream and upstream events based on tissue and cellular level which help the system to survive, modulate and reabsorb the bile acids and reduced their cytotoxicity.

5.1. Tissue level adaptive response and remodeling of the hepatobiliary tree in cholestasis

Interlobular bile ducts in the liver tissue, are relatively smooth conduits which are lined by polarized epithelial cells '***cholangiocytes***'. During cholestasis, bile acids which are the end product of hepatocyte secretion are accumulated in the liver mainly the biliary tree due to impairment in the bile flow or defects in their export from the hepatocytes. These bile acids can cause a series of inflammatory and fibro genic episodes such as release of pro-inflammatory cytokines, infiltration of neutrophils, stellate cell activation with progressive fibrosis which result in liver failure and apoptosis or necrosis of hepatocytes. Cholangiocytes and hepatocyte proliferation is also an response that has been known to increase during cholestasis (Glaser, Gaudio, Miller, Alvaro, & Alpini, 2009). In healthy liver, cholangiocytes have a certain basal proliferation rate (see section 4.1.1.F1.B). Upon BDL induced cholestasis we observed that this rate of proliferation increases at least four-fold and reaches to maximal in the early phase of injury. (see section 4.1.1.F1.B).

The massive cell proliferation is also accompanied with an increase in liver biochemistry parameters such as ASAT (see section 4.1.1. F1.C, D, E) which mark the acute phase of early cholestatic injury induced by BDL. This response so far matches to what has been studied and reported in literature (Zhang et al., 2012), thus indicating that BDL reliably induces cholestasis

in mice and can be used as a model for the further experiments. These changes represent the cellular facet of a wide-spread response of the biliary tree known as the '**ductular reaction**'.

At the tissue level, this ductular reaction manifests as spatiotemporal alterations of the IBDs in response to cholestatic stress. A combination of 3D confocal imaging and computer aided isosurface reconstructions with automated morphometry yielded a detailed picture of the changes that occur in the IBDs in cholestasis. The morphometric parameters of the IBDs vary with experimental parameters as depicted in the correlation map (5.1.F1).
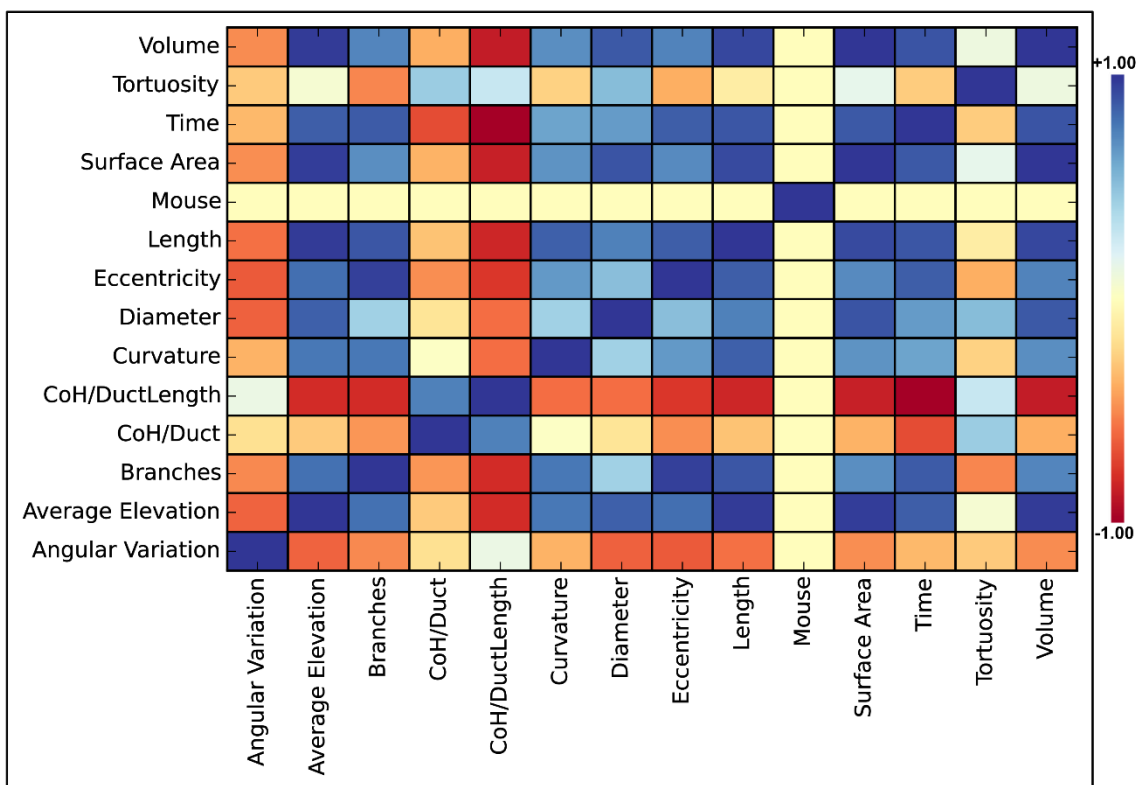
Fig.5.1.F1. **Correlation of all morphometric parameters depicted in a heat map.** A positive strong correlation (＞ 0.90) is observed between parameters such as average elevation of corrugations, length, surface area, time and volume. The occurrence of canals of Hering (CoH) per unit length of the bile duct is strongly negatively correlated (＜ -0.90) with time. Poor or no correlation is observed between all the other parameters measured. Heat map reused from publication (Vartak et al., 2016).

We discuss below the salient features of the remodeling of the IBDs that occur as part of a ductular reaction.

On branching and looping of IBDs

Previous reports have shown that in rats, the intrahepatic biliary tree undergoes elongation after BDL induced cholestasis which is triggered by cholangiocytes proliferation (T. V. Masyuk, Ritman, & LaRusso, 2001). In addition, the intrahepatic bile ducts sprout or form new branches. In this work, we confirm that such a response also occurs in mice. However, the superior reconstruction techniques utilized allow us a 3D high resolution insight into this process. We observe that the IBDs remodel from a simple pipe-like structure into a complex mesh that surrounds the portal vein (see section 4.1.3). The branching occurs through bifurcations and trifurcations with the former being more frequent. This ramified IBD network is a novel feature of the biliary tree that remains confined to the portal tract. After day 7, spatial restrictions force the formation of loops in this network through rejoining of new branches to pre-existing ones (see section 4.1.4). This reaches to a maximum at day 14 and invalidate any cooperative effect of branch formation. Loop formation, therefore, restricts the extent of branch formation thus regulating the formation of second-order branches. These changes are timed precisely with the cholangiocytes proliferation which is maximal up to day 7 after BDL, indicating that proliferation drives duct elongation and branching. This newly developed network of IBDs around the portal tract is then maintained further as cholestasis progresses into the chronic phase.

The existence of a ramified IBD network explains the observation in 2D histopathological staining's, were in an increase in the number of bile ducts per portal tract is reported (Muthukanagarajan, Karnan, Srinivasan, Sadagopan, & Manickam, 2016; Salvalaggio, Whitington, Alonso, & Superina, 2005). Our work shows that it is not the number of bile ducts which increases. Rather the histopathology merely depicts the cross section of the IBD network in 2D, appearing as multiple independent lumina from each of the sectioned branches.

On the diameter of IBDs

Previous studies have reported dynamic changes such as dilation of the bile ducts post obstructive cholestasis (G. Alpini et al., 1996). However, findings from this work show that the diameter of the interlobular bile ducts remains constant and does not change over 28 days post-BDL (see section 4.1.5). This discrepancy is explained, in part by the distinct domains of the biliary tree that were investigated in previous studies. The studies reported until so far

focused on the large bile ducts (~200 µm) observed by using imaging modalities like surgical or radiological approaches. Large bile ducts indeed undergo dilation upon cholestatic injury.

However, the methods utilized to observe large bile ducts have a resolution limit e.g. in case of micro-CT which has a limited resolution and can visualize only structures larger than 30 µm and fail to capture the events in the range of smaller bile ducts that are more complex. Our work focused on the morphometric changes of the IBDs with normal diameters not exceeding 15 µm. These IBDs therefore show a distinct response, namely maintenance of a constant diameter than that of the large bile ducts to cholestasis.

On the other hand, studies where traditional 2D histopathological sections of the liver are investigated, IBDs are visible as 2D lumina around the portal tract. Unfortunately, such data are limited to a projection of the 3D architecture of the lobule thereby losing detailed morphometric changes. As a result, 2D sectioning can introduce bias in the morphometry of IBDs, as the more complex a 3D mesh becomes in cholestasis, the less likely it is to find a single sectioning plane which is perpendicular to the long axis of all the branches of the interlobular ducts.

This bias was illustrated by using the 3D duct reconstruction based on thick about 75 µm z-thickness tissue blocks. The 3D stacks enabled diameter measurements with and without prior knowledge of the long axis of the duct thus illustrating clearing the bias in the duct diameter values based on the 2D sections (5.1.F2.A). This bias can be also observed in the data of duct diameters from day 7 to day 28 post-BDL analyzed in this study, which shows increased duct diameter of the duct when observed in 2D sections (5.1.F2.B).
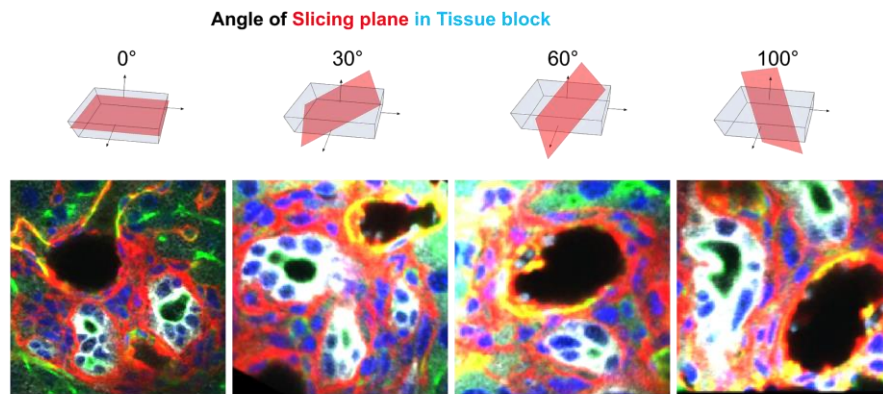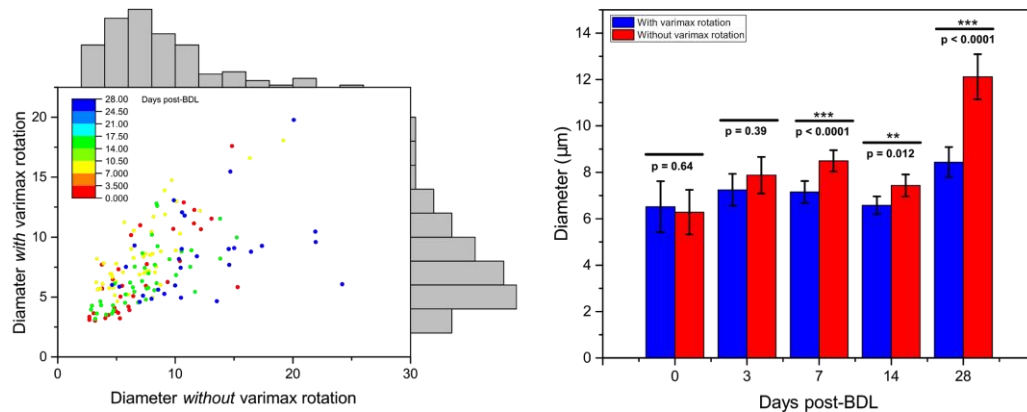
Fig.5.1.F1. Diameter measurements and bias in duct diameter in 2D of the interlobular bile ducts with and without varimax rotations. A. Different slicing angles during 2D sectioning of the tissue affect the measured diameter of the IBDs. B. Left: Duct diameter measurements represented as a large spread with and without varimax rotation. The oblique slicing of the duct can introduce bias as seen by the disparity between the diameter measurements in the graph. Right: The measured values of diameter of the interlobular bile ducts (µM) at different days after BDL, show statistically significant difference with a p value < 0.05, calculated by applying paired sample t-test from day 7 correlating with the increase in branching, between measurements varimax-rotated and unrotated bile ducts. Values are mean ± SEM and asterisks indicate SEM units for significance.

The results from this study are based on the 3D geometry and determine the long axis of the bile ducts prior to their diameter measurements thus mitigating the bias created from analysis based on the 2D sections which lead to the overestimation of duct diameter and increased branching frequency. This underscores the utility of 3 dimensional reconstructions in providing accurate tissue morphometry.

On the luminal surface area of IBDs

Cholestasis can be alleviated by modulating the concentrations of bile acids through their reabsorption by bile salt transporters on the cholangiocytes apical membrane (T. Roskams & Desmet, 1998; M. Strazzabosco, 1997). The cellular level adaptive response of the cholangiocytes to cholestatic stress via up-regulation of transporters and their recruitment to the apical membrane to reabsorb bile salts is well known (Xia et al., 2006). Thus, an increase in the surface area of the bile duct would be a favorable adaptation in alleviating cholestasis through cholangiocytes bile acid reabsorption.

Indeed, results from the morphometric analysis show that the luminal surface area of the IBDs does increase. However, this increase is far in excess of what may be expected proportionally from an increase in duct length and branching. Increasing the luminal diameter would, in theory, be a way to increase luminal surface area, thereby increasing the cholangiocytes-bile interface. However, we found counter-intuitively that IBDs do not increase their luminal diameter as a way to increase the cholangiocytes-bile interface.

Instead the luminal surface of IBDs forms several in- and extravagations, which we term as '*corrugations*'. These corrugations on the surface of the IBDs increase the surface area of IBDs, and thus the cholangiocytes-bile interface, without an increase in volume or diameter. We also show through simulations that the measured degree of corrugation (amplitude, frequency) explains the disproportionate excess of luminal surface area compared to that expected from mere elongation of the IBDs (See figure.4.1.7.F2). This mode of surface area increase of the IBDs is an hitherto unreported feature of the ductular reaction. This adaptive response is consistent with the architecture of the hepatic lobules which consists of several such IBDs that are spatially constrained to the vicinity of the portal vein within the portal tract. Corrugations of the IBDs to increase surface area is analogous to similar evolutionary adaptations with sulci of the brain or villi of the intestine.

By contrast to IBDs, the cholangiocytes of the large bile ducts have limited absorption capacity for bile salts. Large bile ducts are mainly water conduits and do indeed increase their volume by an increase in diameter, presumably facilitating excess flow (Glaser, Gaudio, Rao, et al., 2009). As a large number of lobules eventually drain into a larger bile duct, the increased

diameter and consequently increased volume supports the role of large ducts as temporary reservoirs of excess bile salts. IBDs, on the other hand are clearly adapting towards a resorptive goal as described before. This functional heterogeneity may be attributed to cellular heterogeneity between large cholangiocytes which form the large bile ducts versus small cholangiocytes which line small bile ducts (Maroni et al., 2015; T. A. Roskams et al., 2004).

On the canalicular connectivity of IBDs

A further way of alleviating cholestasis is to increase the connectivity of the IBDs to the canalicular network, thereby facilitating the drainage of bile into the biliary tree. The canal of Hering is a specialized conduit that links the IBDs to the lobular canalicular network. Previous work on the morphogenesis of bile ducts during embryonic development or chemically induced ductular reactions (Jörs et al., 2015; Takashima, Terada, Kawabata, & Suzuki, 2015), observed an increase in canalicular connectivity of the biliary tree. Such an increase might be a way to collect the excess accumulated bile acids and drain them out of the liver.

During embryonic stages, the duct formation begins initially by the formation of precursor cell clusters that elongate to form segments which then fuse in the end to generate a de novo bile duct together with all its branches. Along similar lines, individual KRT19-positive cholangiocytes form small ductules upon toxification by DDC or CDE. These ductules invade the lobular parenchyma and connect to the canalicular network to drain the excess bile accumulated in the lobule.

In contrast to these observations, we find that ***no new canals of Hering*** are formed in BDL-induced cholestasis despite an increase in the overall size of the interlobular biliary tree. Infact the number of CoH remains constant in spite of duct elongation and branching thereby reducing the relative frequency of canalicular-IBD connection points per unit length of the duct.

Although the data shows the presence of some solitary KRT19-positive cells, detailed 3D morphometric analysis rules out any chance of isolated cells forming ductules (see results 4.1.9.F1). The results suggest that the additional duct branches that arise as a response to cholestasis induced upon BDL can arise only from the preexisting bile ducts. No, *de novo* duct formation, neither from precursors nor from isolated cell fragments is observed.

Finally, compared to another 3D morphometric evaluation of mouse liver that was exposed to CCl$_4$ (Kaneko et al., 2015) which is a hepatotoxic chemical inducing pericentral necrosis. The authors show the remodeling of the hepatobiliary system by the invasion of biliary branching into the parenchyma. In the present study of cholestasis induced by BDL, observed dataset shows no such pericentral bile duct infiltration. The branching interlobular bile ducts are also always seen to be confined as a mesh close to the portal veins.

Thus, the de novo response of bile ducts in embryonic development or chemically-induced ductular reactions are clearly different from the response of adult bile ducts following BDL. In the absence of increased connectivity to the canalicular network, enhancement of bile reabsorption by an corrugation-mediated increase in surface area seems to be the 'preferred' way to tackle excess bile salts in the liver.

Relevance

The present study describes the response of the finite structures like canaliculi and ducts ranging from 0.207 to 30 µm with optimal resolution and details useful to quantify and analyze their 3D architecture. The observations from this study fill the gap between the large bile ducts and the lobular canalicular network and describe the functional adaptive feedback of the interlobular bile ducts located in this gap. The adaptive response of the liver tissue, mainly the bile ducts is finely tuned to coalesce the interface of duct lumen to the apical membrane of the cholangiocytes lining the duct.

Conclusion

The data analyzed and observed in this study shows detailed morphometry of the interlobular bile ducts which have not been studied so far post cholestatic liver injury. These bile ducts are the terminal most branches of the biliary tree which penetrate the functional unit of the liver-'*hepatic liver lobules*'. These lobules are only accessible in detail through 3D confocal microscopy.
Cholangiocytes proliferation leads to a series of tissue level adaptations which involve alterations in morphology of the interlobular bile ducts. This tissue-level response occurs in two major phases that are distinguished as an acute and chronic phase.

Figure (5.1.F2) graphically depicts the major findings of this work. The results from this study demonstrate a novel response of how an individual interlobular bile duct leads to a complex ductular network that elongates, corrugates and ramifies to alleviate cholestasis. This response is quantitatively and mechanistically independent from the large and embryonic bile ducts and is highly specific to the adult IBDs. It is an adaptive tissue response of IBDs that balances and enhances the cellular response of the functional cholangiocytes in bile acid reabsorption to alleviate cholestasis.
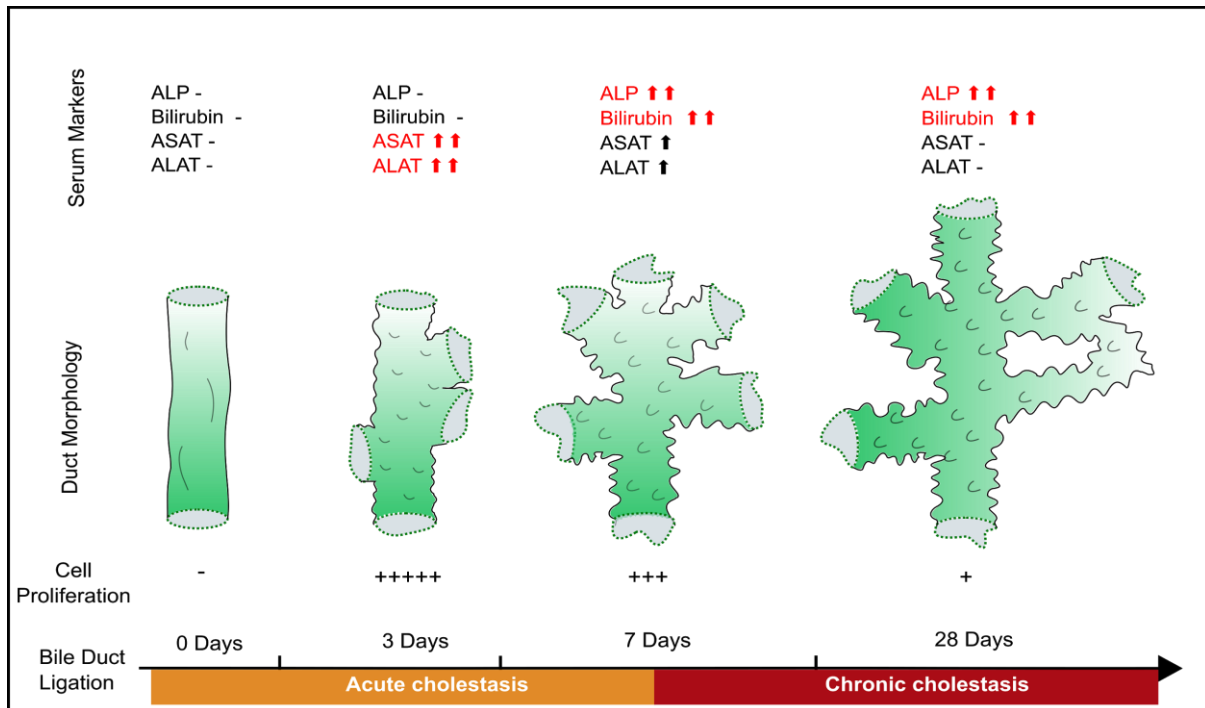
Fig.5.1.F2. **Graphical representation of the ductular reaction.** Depiction of cellular and tissue level changes that constitute the ductular reaction in the acute and chronic phases as defined by serum markers (ASAT, ALAT) of injury. Cellular proliferation is seen to be higher in acute cholestasis along with elongation of the duct. Branching of the IBDs, emergence and increase of corrugations on the luminal duct surface, increased duct surface area and volume is observed during the acute phase. Chronic cholestasis occurs between day 7 to day 28 post-BDL. This second phase begins is characterized by continued elongation of the duct. Additionally, loop formation by self-joining of the bile duct branches to the original duct segment is observed. There is an increase in amplitude of corrugations on the surface of the bile duct with relatively reduced duct-to-canalicular network connections. Lastly, the serum biomarkers of acute cholestasis are replaced by those of jaundice in chronic cholestasis. Figure readapted and reused from (Vartak et al., 2016) .

179

5.2. Hepatocellular response in relation to cytoskeleton and intracellular events involved in cell death during cholestasis

While cholangiocytes seem to adapt and remodel in response to high bile acid concentrations, cholestasis-mediated hepatotoxicity stems from the torment of another major cell type of the liver. Hepatocytes are the primary targets of toxicity induced during various cholestatic liver injuries. One of the key features of these cells is formation of a bile canaliculi on their apical surface. A key feature of hepatocytes is polarity, whereby the apical membrane forms the bile canaliculi. The bile canaliculi are surrounded by a network of actin fibers that are known as 'peri-canalicular actin cortex' (Tsukada et al., 1995). The actin cytoskeleton is involved in a myriad functions - providing cell shape and stability (Katsantonis et al., 1994; Szymanski & Staiger, 2018; Tranter, Sugrue, & Schwartz, 1991), supporting vesicular transport, recycling and degradation of proteins, maintaining cell polarity (Doctor & Nichols, 2004) etc. In hepatocytes, it plays a critical role in the bile acid transport processes in the biliary network (Chalut & Paluch, 2016; Doctor & Fouassier, 2002; Doctor & Nichols, 2004). During cholestasis, actin polymerization is known to be inhibited (Thibault et al., 1992) and the intracellular signaling of acto-myosin is enhanced (Gupta et al., 2016).

In light of these observations, disruption of the actin cytoskeleton seemed a likely candidate for the initiation or propagation of hepatocyte toxicity in cholestasis. Microscopic visualization of the actin cytoskeleton is challenging in primary hepatocytes for several reasons. Firstly, in an *in vitro* monolayer culture, primary hepatocytes tend to de-differentiate and lose cell polarity, consequently losing specialized bile transport functions and structures such as canaliculi in the duration required for transfection and ectopic expression of marker proteins. Secondly, while collagen layering on hepatocytes in the so-called 'sandwich culture' allows the maintenance of the differentiated state, the collagen presents a barrier for transfer of exogenous plasmid DNA to hepatocytes, resulting in poor transfection efficiency. On the other hand, well-differentiated live hepatocytes preserve their physiological xenobiotic expulsion functions, efficiently removing any small-molecule dyes from the cytoplasm and creating a catch-22 for small-molecule fluorescent marker such as phalloidin. To circumvent these technical challenges, a staining protocol was developed with careful standardization of dye-incubation procedures, as well as titration of the staining dye. This yielded an optimal staining protocol where the cytoskeleton of live differentiated primary hepatocytes could be visualized for durations up to 48 hours. The advantage of this protocol compared to the conventional

LifeAct technique (Riedl et al., 2008) is that actin cytoskeleton in live primary hepatocytes that have functional bile canaliculi is visualized for a period of at least 3 days in vitro without transfection and any changes to the morphological or phenotype of the cells. The dye used here is a silico-rhodamine derivative SiR-actin [Tebu-bio], with far-red fluorescence such that it remains compatible with conventional stains in the visible spectral range. Efficient actin staining can be achieved with sub-micromolar concentrations of SiR-actin. The actin binding moiety of SiR-actin is jasplakinolide which has no cytotoxic effects at these low concentrations (D'Este et al., 2015). Analysis of polarized hepatocytes stained with this protocol, showed that the peri-canalicular actin cytoskeleton is intensely marked, representing more than 80% of the visualized actin in a hepatocyte.

While the presence of peri-canalicular actin is reported (Tsukada et al., 1995), only a little is known about the second major cytoskeletal component in cells - tubulin. The tubulin network is indispensable in cellular transport processes, especially in transport of apical membrane proteins in polarized cells (Groebner & Tuma, 2015; Müsch, 2004; Oda et al., 1995; Shepard & Tuma, 2010). The staining protocol developed with SiR-actin for actin visualization could be adapted for simultaneous tubulin visualization by incorporation of a small molecule microtubule binding dye - Tubulin Tracker Green reagent [ThermoFisher] with green fluorescence. We observed an intricate organization of a microtubule network juxtaposed to the pericanalicular actin described above.

Hepatocytes incubated with cytotoxic concentrations of bile acids showed a highly reproducible sequence of events involving the pericanalicular actin and tubulin cytoskeleton, which eventually resulted in bile-acid induced hepatocellular death.

In normal healthy hepatocytes, bile canaliculi are surrounded by a dense actin-tubulin cytoskeletal network. Canaliculi are formed from the apical membranes of a hepatocyte couplet. Upon exposure to cytotoxic bile acid concentrations, canalicular dynamics (alternating constriction and dilations) increase in amplitude and frequency compared to those of untreated cells. A reduction of the pericanalicular actin occurs in at least one of the cells within the hepatocyte couplet. Depletion of the tubulin mess occurs almost simultaneously. While canalicular dynamics continue, loss of the pericanalicular actin-tubulin inevitably is followed by a canalicular collapse. The canalicular collapse is either accompanied or followed shortly by membrane rupture and cell death. In the event that only one of the hepatocytes in the couplet

undergoes this process, the second hepatocyte transiently survives the loss of its partner but eventually also enters the same spiral of death.

This process occurs with all bile acids tested. The morphological features of dead cells and duration of this process [minutes] suggests necrotic cell death. These characteristics are corroborated by the in vivo histopathology in cholestatic liver injury which presents as necrotic bile infarcts (Abshagen et al., 2015; Desmet, 1995; Harnoss, Heidecke, Vollmar, & Eipel, 2011).

This highly reproducible effect of the bile acids on both components of the cytoskeleton, namely depletion preceding cell death, is termed as the 'pericanalicular cytoskeleton depletion and collapse' (PCDC). A schematic representation of PCDC is provided below (5.2.F1).

1. Healthy hepatocyte with bile canaliculi and pericanalicular actin-tubulin

2. Depletion of the pericancliular actin-tubulin network

— Tubulin   — Actin

Bile acids

3. Asymmetric canalicular collapse

4. Cortical actin redistribution

5. Membrane rupture

6. Cell death
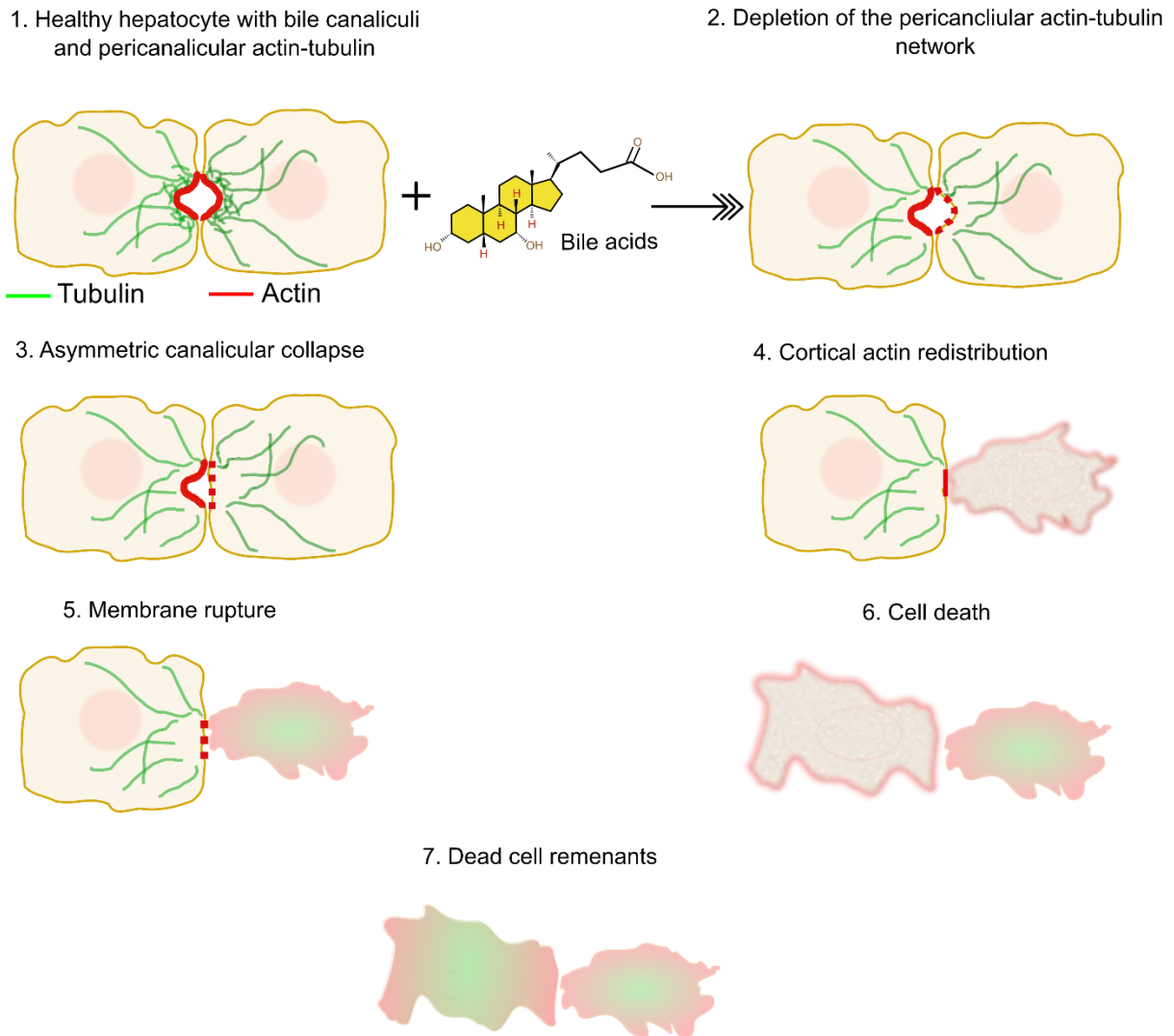
7. Dead cell remenants

Fig.5.2 .F1.Pericanalicular cytoskeleton depletion and collapse (PCDC) precedes membrane rupture and cell death upon bile acid exposure

Since PCDC is induced by bile acids we investigate if bile acid mediated signaling via FXR plays a role in this process. For this purpose, a FRET based sensor was used to determine the propensity of different bile acids to activate FXR signaling. These experiments demonstrated that FXR signaling was activated and saturated already at bile acid concentrations ($\sim 100\ \mu M$) far below the EC_{50} for bile acid toxicity. PCDC and subsequent bile acid toxicity occurs at higher concentration ranges ($100\text{-}2400\ \mu M$) for the four investigated bile acids. Therefore, cell death occurs at concentrations where FXR signaling is already activated. While it cannot be ruled out that FXR mediated transcriptional changes set the context for PCDC, it is clear that mere FXR activation is not sufficient to cause cell death.

To the knowledge of the author, neither the bile acid induced canalicular collapse events, nor the underlying disruption of the actin and tubulin networks have been previously described. However, the mechanism responsible for disruption of actin and tubulin remains to be elucidated. One possibility is a direct molecular interaction of bile acids with actin. This hypothesis is supported by a previous study that showed that bile acids inhibit polymerization of purified actin in vitro (Tuchweber et al., 1990). Whether this also occurs in living cells still remains to be explored. A second possible explanation is that actin polymerization is inhibited due to ATP depletion as a consequence of the well-known phenomenon of mitochondrial inactivation following exposure to bile acids (Palmeira & Rolo, 2004; Rolo, Palmeira, Holy, & Wallace, 2004). Therefore, a focus of future research should be to find out whether the loss of mitochondrial activity precedes and is necessary and sufficient to induce PCDC.

It also remains to be determined, why the canalicular collapse leads to cell death within a relatively short period of time. Canalicular dynamics are in general regulated by a balance of actomyosin mediated contractile forces and pericanalicular cortical actin mediated stabilization (Gupta et al., 2016). A plausible explanation is that the increased canalicular dynamics and collapse following bile acid exposure represents a myosin contractility run amok, in the absence of a stabilizing pericanalicular actin. Because the membranes of the neighboring cells are linked to each other by tight junctions, and moreover the tight junctions are linked to the pericanalicular cytoskeletal network (van Deurs, von Bũlow, Vilhardt, Holm, & Sandvig, 1996), it is likely that both hepatocytes in a couplet undergoes PCDC in a correlated.

Understanding, the role of actin-tubulin network in antagonizing bile acid toxicity suggests that pharmaceutical cytoskeletal modulators may ameliorate PCDC and thereby protect against bile acid mediated toxicity in cholestasis.

In conclusion, this study elucidated the consequences of exposure to high concentrations of bile acids of two major cell types of the liver, cholangiocytes which respond by adapting through ductular reactions and hepatocytes which fail to adapt and succumb to PCDC.

5.3. Outlook

In this work, the adaptive response of bile ducts was investigated at the architectural and the morphological level. In the second the phenomenon of PCDC was shown to play a critical role in bile acid toxicity. This opens a pandora's box of as yet unanswered questions that would form the basis of future investigations:

1) The functional aspects of cholangiocytes behavior in cholestasis in terms of transporter expression, resilience or susceptibility to high bile salt concentrations and their contribution to alleviating cholestasis remain to be investigated.

2) As shown in this work, the lobular architecture possesses complex architecture and remodeling behavior. Technical limitations did not allow the reconstruction of an entire lobule. Newly developed methods such as tissue clearing, label free imaging now may provide the opportunity to investigate the entire functional unit of the liver at subcellular resolutions.

3) In this work pericanalicular cytoskeletal depletion and collapse is described. However, the molecular mechanisms that initiate PCDC range from ATP depletion to direct modulation of actin dynamics. The use of advanced imaging methodologies such as speckle microscopy, mitochondrial potential imaging and super-resolution imaging may reveal the complete causality of PCDC and bile acid toxicity.

4) Whatever effect bile acids have in the cell, their entry into the cytoplasm remains mysterious. It is unclear if the cytotoxic concentrations of bile salts enter from the apical membrane where it is highest physiologically, or from the basolateral side where it is highest only in cholestasis. The possibility of induced or inadvertent vesicular uptake from either membrane has not been ruled out. Investigation of the mechanism of bile salt infiltration into the cytoplasm will help to clarify the pathogenesis of cholestatic liver disease.

5) Cholestasis often occurs secondary to other liver pathologies such as NASH, HCC, hepatitis and pharmaceutical toxicity. How these conditions affect the susceptibility of hepatocytes and cholangiocytes to PCDC remains to be explored.

6. REFERENCES

Abdel-Misih, S. R. Z., & Bloomston, M. (2010). Liver anatomy. *The Surgical Clinics of North America*, *90*(4), 643–653.

Abshagen, K., König, M., Hoppe, A., Müller, I., Ebert, M., Weng, H., … Dooley, S. (2015). Pathobiochemical signatures of cholestatic liver disease in bile duct ligated mice. *BMC Systems Biology*, *9*, 83.

Addgene: Protocol - How to Create a Bacterial Glycerol Stock. (n.d.). Retrieved December 8, 2017, from https://www.addgene.org/protocols/create-glycerol-stock/

Alpini, G., Glaser, S. S., Ueno, Y., Pham, L., Podila, P. V., Caligiuri, A., … LaRusso, N. F. (1998). Heterogeneity of the proliferative capacity of rat cholangiocytes after bile duct ligation. *The American Journal of Physiology*, *274*(4 Pt 1), G767–G775.

Alpini, G., McGill, J. M., & Larusso, N. F. (2002). The pathobiology of biliary epithelia. *Hepatology* , *35*(5), 1256–1268.

Alpini, G., Roberts, S., Kuntz, S. M., Ueno, Y., Gubba, S., Podila, P. V., … LaRusso, N. F. (1996). Morphological, molecular, and functional heterogeneity of cholangiocytes from normal rat liver. *Gastroenterology*, *110*(5), 1636–1643.

Alpini, G., Ulrich, C., Roberts, S., Phillips, J. O., Ueno, Y., Podila, P. V., … LaRusso, N. F. (1997). Molecular and functional heterogeneity of cholangiocytes from rat liver after bile duct ligation. *The American Journal of Physiology*, *272*(2 Pt 1), G289–G297.

Arrese, M., & Trauner, M. (2003). Molecular aspects of bile formation and cholestasis. *Trends in Molecular Medicine*, *9*(12), 558–564.

Attili, A. F., Angelico, M., Cantafora, A., Alvaro, D., & Capocaccia, L. (1986). Bile acid-induced liver toxicity: relation to the hydrophobic-hydrophilic balance of bile acids. *Medical Hypotheses*, *19*(1), 57–69.

Burbank, M. G., Burban, A., Sharanek, A., Weaver, R. J., Guguen-Guillouzo, C., & Guillouzo, A. (2016). Early Alterations of Bile Canaliculi Dynamics and the Rho Kinase/Myosin Light Chain Kinase Pathway Are Characteristics of Drug-Induced Intrahepatic Cholestasis. *Drug Metabolism*

and Disposition: The Biological Fate of Chemicals*, *44*(11), 1780–1793.

Bykov, I., Ylipaasto, P., Eerola, L., & Lindros, K. O. (2004). Functional Differences between Periportal and Perivenous Kupffer Cells Isolated by Digitonin-Collagenase Perfusion. *Comparative Hepatology*, *3 Suppl 1*, S34.

Cardinale, V., Wang, Y., Carpino, G., Mendel, G., Alpini, G., Gaudio, E., … Alvaro, D. (2012). The biliary tree—a reservoir of multipotent stem cells. *Nature Reviews. Gastroenterology & Hepatology*, *9*(4), 231–240.

Carpentier, R., Suñer, R. E., van Hul, N., Kopp, J. L., Beaudry, J.-B., Cordi, S., … Lemaigre, F. P. (2011). Embryonic ductal plate cells give rise to cholangiocytes, periportal hepatocytes, and adult liver progenitor cells. *Gastroenterology*, *141*(4), 1432–1438, 1438.e1–e4.

Chalut, K. J., & Paluch, E. K. (2016). The Actin Cortex: A Bridge between Cell Shape and Function. *Developmental Cell*, *38*(6), 571–573.

Chen Long, L. M. (2014). Bile Acids Induced Cell Necropotosis. *Journal of Cytology & Histology*, *s4*(01). https://doi.org/10.4172/2157-7099.S4-004

Chen, X.-M., O'Hara, S. P., & LaRusso, N. F. (2008). The immunobiology of cholangiocytes. *Immunology and Cell Biology*, *86*(6), 497–505.

Cheng, Q., Inaba, Y., Lu, P., Xu, M., He, J., Zhao, Y., … Xie, W. (2015). Chronic Activation of FXR in Transgenic Mice Caused Perinatal Toxicity and Sensitized Mice to Cholesterol Toxicity. Molecular Endocrinology, 29(4), 571–582. http://doi.org/10.1210/me.2014-1337

Chiang, J. Y. (1998). Regulation of bile acid synthesis. *Frontiers in Bioscience: A Journal and Virtual Library*, *3*, d176–d193.

Chiang, J. Y. L. (2013). Bile Acid Metabolism and Signaling. In *Comprehensive Physiology*. John Wiley & Sons, Inc.

Cubero, F. J., & Nieto, N. (2006). Kupffer cells and alcoholic liver disease. *Revista Espanola de Enfermedades Digestivas: Organo Oficial de La Sociedad Espanola de Patologia Digestiva*, *98*(6), 460–472.

de Aguiar Vallim, T. Q., Tarling, E. J., Ahn, H., Hagey, L. R., Romanoski, C. E., Lee, R. G., … Edwards, P. A. (2015). MAFG is a transcriptional repressor of bile acid synthesis and

metabolism. *Cell Metabolism*, *21*(2), 298–310.

de Aguiar Vallim, T. Q., Tarling, E. J., & Edwards, P. A. (2013). Pleiotropic roles of bile acids in metabolism. *Cell Metabolism*, *17*(5), 657–669.

Decker, K. (1990). Biologically active products of stimulated liver macrophages (Kupffer cells). *European Journal of Biochemistry / FEBS*, *192*(2), 245–261.

Desmet, V. J. (1995). Histopathology of cholestasis. *Verhandlungen Der Deutschen Gesellschaft Fur Pathologie*, *79*, 233–240.

D'Este, E., Kamin, D., Göttfert, F., El-Hady, A., & Hell, S. W. (2015). STED nanoscopy reveals the ubiquity of subcortical cytoskeleton periodicity in living neurons. *Cell Reports*, *10*(8), 1246–1251.

Doctor, R. B., & Fouassier, L. (2002). Emerging roles of the actin cytoskeleton in cholangiocyte function and disease. *Seminars in Liver Disease*, *22*(3), 263–276.

Doctor, R. B., & Nichols, M. (2004). 3. THE ACTIN CYTOSKELETON IN LIVER FUNCTION. In *Principles of Medical Biology* (Vol. 15, pp. 49–79). Elsevier.

Dugina, V., Alieva, I., Khromova, N., Kireev, I., Gunning, P. W., & Kopnin, P. (2016). Interaction of microtubules with the actin cytoskeleton via cross-talk of EB1-containing +TIPs and γ-actin in epithelial cells. *Oncotarget*, *7*(45), 72699–72715.

Dunn, J. C., Tompkins, R. G., & Yarmush, M. L. (1991). Long-term in vitro function of adult hepatocytes in a collagen sandwich configuration. *Biotechnology Progress*, *7*(3), 237–245.

Elsevier. (n.d.). Zakim and Boyer's Hepatology - 7th Edition. Retrieved August 21, 2017, from https://www.elsevier.com/books/zakim-and-boyers-hepatology/sanyal/978-0-323-44657-0

Esteller, A. (2008). Physiology of bile secretion. *World Journal of Gastroenterology: WJG*, *14*(37), 5641–5649.

Fava, G., Glaser, S., Francis, H., & Alpini, G. (2005). The immunophysiology of biliary epithelium. *Seminars in Liver Disease*, *25*(3), 251–264.

Fiorucci, S., & Baldelli, F. (2009). Farnesoid X receptor agonists in biliary tract disease. *Current Opinion in Gastroenterology*, *25*(3), 252–259.

Fiorucci, S., Mencarelli, A., Distrutti, E., & Zampella, A. (2012). Farnesoid X receptor: from

medicinal chemistry to clinical applications. *Future Medicinal Chemistry*, *4*(7), 877–891.

Fitz, J. G. (2002). Regulation of cholangiocyte secretion. *Seminars in Liver Disease*, *22*(3), 241–249.

Fox, S. I. (2015). *Human Physiology*. McGraw-Hill Education.

Glaser, S. S., Francis, H., Marzioni, M., Taffetani, S., Phinizy, J. L., LeSage, G., & Alpini, G. (2000). *Functional Heterogeneity of the Intrahepatic Biliary Epithelium*. Landes Bioscience.

Glaser, S. S., Gaudio, E., Miller, T., Alvaro, D., & Alpini, G. (2009). Cholangiocyte proliferation and liver fibrosis. *Expert Reviews in Molecular Medicine*, *11*, e7.

Glaser, S. S., Gaudio, E., Rao, A., Pierce, L. M., Onori, P., Franchitto, A., … Alpini, G. D. (2009). Morphological and functional heterogeneity of the mouse intrahepatic biliary epithelium. *Laboratory Investigation; a Journal of Technical Methods and Pathology*, *89*(4), 456–469.

Goodwin, B., Jones, S. A., Price, R. R., Watson, M. A., McKee, D. D., Moore, L. B., … Kliewer, S. A. (2000). A regulatory cascade of the nuclear receptors FXR, SHP-1, and LRH-1 represses bile acid biosynthesis. *Molecular Cell*, *6*(3), 517–526.

Gouw, A. S. H., Clouston, A. D., & Theise, N. D. (2011). Ductular reactions in human liver: diversity at the interface. *Hepatology* , *54*(5), 1853–1863.

Groebner, J. L., & Tuma, P. L. (2015). The Altered Hepatic Tubulin Code in Alcoholic Liver Disease. *Biomolecules*, *5*(3), 2140–2159.

Guo, H.-L., Hassan, H. M., Zhang, Y., Dong, S.-Z., Ding, P.-P., Wang, T., … Jiang, Z.-Z. (2016). Pyrazinamide induced rat cholestatic liver injury through inhibition of FXR regulatory effect on bile acid synthesis and transport. *Toxicological Sciences: An Official Journal of the Society of Toxicology*. https://doi.org/10.1093/toxsci/kfw098

Gupta, K., Li, Q., Fan, J., Fong, E. L. S., Song, Z., Mo, S., … Yu, H. (2016, January 1). *Actomyosin Contractility Drives Bile Regurgitation as an Early Homeostatic Response to Increased Biliary Pressure in Obstructive Cholestasis*. *bioRxiv*. https://doi.org/10.1101/077792

Hammad, S., Hoehme, S., Friebel, A., von Recklinghausen, I., Othman, A., Begher-Tibbe, B., … Hengstler, J. G. (2014). Protocols for staining of bile canalicular and sinusoidal networks of human, mouse and pig livers, three-dimensional reconstruction and quantification of tissue microarchitecture by image processing and analysis. *Archives of Toxicology*, *88*(5), 1161–1183.

Harnoss, J.-C., Heidecke, C. D., Vollmar, B., & Eipel, C. (2011). In vivo imaging of bile

    accumulation and biliary infarction after common bile duct ligation in rats. *European Surgical*

    Research. Europaische Chirurgische Forschung. Recherches Chirurgicales Europeennes, *47*(4),

    240–247.

Heinrich, S., Georgiev, P., Weber, A., Vergopoulos, A., Graf, R., & Clavien, P.-A. (2011). Partial bile

    duct ligation in mice: a novel model of acute cholestasis. *Surgery*, *149*(3), 445–451.

Henry Gray. 1918. Anatomy of the Human Body: Bibliographic Record. (n.d.). Retrieved August 30,

    2017, from http://www.bartleby.com/br/107.html

Herr, K. J., Tsang, Y.-H. N., Ong, J. W. E., Li, Q., Yap, L. L., Yu, W., … Thiery, J. P. (2014). Loss of

    α-catenin elicits a cholestatic response and impairs liver regeneration. *Scientific Reports*, *4*, 6835.

Hoehme, S., Brulport, M., Bauer, A., Bedawy, E., Schormann, W., Hermes, M., … Drasdo, D. (2010).

    Prediction and validation of cell alignment along microvessels as order principle to restore tissue

    architecture in liver regeneration. *Proceedings of the National Academy of Sciences of the United*

    States of America, *107*(23), 10371–10376.

Humphreys, E. H., Williams, K. T., Adams, D. H., & Afford, S. C. (2010). Primary and malignant

    cholangiocytes undergo CD40 mediated Fas dependent apoptosis, but are insensitive to direct

    activation with exogenous Fas ligand. *PloS One*, *5*(11), e14037.

Itoh, Y., Okanoue, T., Morimoto, M., Nagao, Y., Mori, T., Hori, N., … Kashima, K. (1992).

    Functional heterogeneity of rat liver macrophages: interleukin-1 secretion and Ia antigen

    expression in contrast with phagocytic activity. *Liver*, *12*(1), 26–33.

Jansen, P. L. M., Ghallab, A., Vartak, N., Reif, R., Schaap, F. G., Hampe, J., & Hengstler, J. G.

    (2017). The ascending pathophysiology of cholestatic liver disease. *Hepatology* , *65*(2), 722–

    738.

Jonker, J. W., Stedman, C. A. M., Liddle, C., & Downes, M. (2009). Hepatobiliary ABC transporters:

    physiology, regulation and implications for disease. *Frontiers in Bioscience* , *14*, 4904–4920.

Jörs, S., Jeliazkova, P., Ringelhan, M., Thalhammer, J., Dürl, S., Ferrer, J., … Geisler, F. (2015).

    Lineage fate of ductular reactions in liver injury and carcinogenesis. *The Journal of Clinical*

    Investigation, *125*(6), 2445–2457.

Kaneko, K., Kamimoto, K., Miyajima, A., & Itoh, T. (2015). Adaptive remodeling of the biliary architecture underlies liver homeostasis. *Hepatology* , *61*(6), 2056–2066.

Kang, L.-I., Mars, W. M., & Michalopoulos, G. K. (2012). Signals and cells involved in regulating liver regeneration. *Cells* , *1*(4), 1261–1292.

Kanno, N., LeSage, G., Glaser, S., & Alpini, G. (2001). Regulation of cholangiocyte bicarbonate secretion. *American Journal of Physiology. Gastrointestinal and Liver Physiology*, *281*(3), G612–G625.

Katsantonis, J., Tosca, A., Koukouritaki, S. B., Theodoropoulos, P. A., Gravanis, A., & Stournaras, C. (1994). Differences in the G/total actin ratio and microfilament stability between normal and malignant human keratinocytes. *Cell Biochemistry and Function*, *12*(4), 267–274.

Kim, E.-K., Cho, J. H., Kim, E., & Kim, Y. J. (2017). Ursodeoxycholic acid inhibits the proliferation of colon cancer cells by regulating oxidative stress and cancer stem-like cell growth. *PloS One*, *12*(7), e0181183.

Kliewer, S. A., & Mangelsdorf, D. J. (2015). Bile Acids as Hormones: The FXR-FGF15/19 Pathway. *Digestive Diseases* , *33*(3), 327–331.

Krishnamurthy, G. T., & Krishnamurthy, S. (2000). Extrahepatic Cholestasis. In *Nuclear Hepatology* (pp. 159–186). Springer, Berlin, Heidelberg.

Kulkarni, S. R., Soroka, C. J., Hagey, L. R., & Boyer, J. L. (2016). Sirtuin 1 activation alleviates cholestatic liver injury in a cholic acid-fed mouse model of cholestasis. *Hepatology* , *64*(6), 2151–2164.

Lee, F. Y., Lee, H., Hubbert, M. L., Edwards, P. A., & Zhang, Y. (2006). FXR, a multipurpose nuclear receptor. *Trends in Biochemical Sciences*, *31*(10), 572–580.

Lee-Montiel, F. T., George, S. M., Gough, A. H., Sharma, A. D., Wu, J., DeBiasio, R., … Taylor, D. L. (2017). Control of oxygen tension recapitulates zone-specific functions in human liver microphysiology systems. *Experimental Biology and Medicine* , 1535370217703978.

LeSage, G. D., Benedetti, A., Glaser, S., Marucci, L., Tretjak, Z., Caligiuri, A., … Alpini, G. (1999). Acute carbon tetrachloride feeding selectively damages large, but not small, cholangiocytes from normal rat liver. *Hepatology* , *29*(2), 307–319.

Lesage, G., Glaser, S. S., Gubba, S., Robertson, W. E., Phinizy, J. L., Lasater, J., … Alpini, G. (1996). Regrowth of the rat biliary tree after 70% partial hepatectomy is coupled to increased secretin-induced ductal secretion. *Gastroenterology*, *111*(6), 1633–1644.

Li, T., & Chiang, J. Y. L. (2014). Bile acid signaling in metabolic disease and drug therapy. *Pharmacological Reviews*, *66*(4), 948–983.

Li, Y., Tang, R., Leung, P. S. C., Gershwin, M. E., & Ma, X. (2017). Bile acids and intestinal microbiota in autoimmune cholestatic liver diseases. *Autoimmunity Reviews*, *16*(9), 885–896.

Loinder, K., & Söderström, M. (2003). The nuclear receptor corepressor (N-CoR) modulates basal and activated transcription of genes controlled by retinoic acid. *The Journal of Steroid Biochemistry and Molecular Biology*, *84*(1), 15–21.

Lukinavičius, G., Reymond, L., D'Este, E., Masharina, A., Göttfert, F., Ta, H., … Johnsson, K. (2014). Fluorogenic probes for live-cell imaging of the cytoskeleton. *Nature Methods*, *11*(7), 731–733.

Malarkey, D. E., Johnson, K., Ryan, L., Boorman, G., & Maronpot, R. R. (2005). New insights into functional aspects of liver morphology. *Toxicologic Pathology*, *33*(1), 27–34.

Maroni, L., Haibo, B., Ray, D., Zhou, T., Wan, Y., Meng, F., … Alpini, G. (2015). Functional and structural features of cholangiocytes in health and disease. *Cellular and Molecular Gastroenterology and Hepatology*, *1*(4), 368–380.

Maronpot, R. (2010, July 4). Proliferative and Nonproliferative Lesions of the Rat and Mouse Hepatobiliary System - Toxicologic Pathology. Retrieved September 1, 2017, from https://focusontoxpath.com/proliferative-and-nonproliferative-lesions-of-the-rat-and-mouse-hepatobiliary-system/

Maronpot, R. (n.d.). Quick Publishing. Retrieved August 22, 2017, from http://www.cacheriverpress.com/books/pathmouse.htm

Masyuk, A. I., Masyuk, T. V., Splinter, P. L., Huang, B. Q., Stroope, A. J., & LaRusso, N. F. (2006). Cholangiocyte cilia detect changes in luminal fluid flow and transmit them into intracellular Ca2+ and cAMP signaling. *Gastroenterology*, *131*(3), 911–920.

Masyuk, T. V., Ritman, E. L., & LaRusso, N. F. (2001). Quantitative assessment of the rat

intrahepatic biliary system by three-dimensional reconstruction. *The American Journal of Pathology*, *158*(6), 2079–2088.

McGill, J. M., Yen, M. S., Cummings, O. W., Alpini, G., LeSage, G., Pollok, K. E., … Stansfield, A. P. (2001). Interleukin-5 inhibition of biliary cell chloride currents and bile flow. *American Journal of Physiology. Gastrointestinal and Liver Physiology*, *280*(4), G738–G745.

Melak, M., Plessner, M., & Grosse, R. (2017). Actin visualization at a glance. *Journal of Cell Science*, *130*(3), 525–530.

Meng, Q., Chen, X., Wang, C., Liu, Q., Sun, H., Sun, P., … Liu, K. (2015). Protective Effects of Alisol B 23-Acetate Via Farnesoid X Receptor-Mediated Regulation of Transporters and Enzymes in Estrogen-Induced Cholestatic Liver Injury in Mice. *Pharmaceutical Research*, *32*(11), 3688–3698.

Mi, L.-Z., Devarakonda, S., Harp, J. M., Han, Q., Pellicciari, R., Willson, T. M., … Rastinejad, F. (2003). Structural Basis for Bile Acid Short Article Binding and Activation of the Nuclear Receptor FXR. *Molecular Cell*, *11*, 1093–1100.

Mitra, V., & Metcalf, J. (2009). Metabolic functions of the liver. *Anaesthesia & Intensive Care Medicine*, *10*(7), 334–335.

Monte, M. J., Marin, J. J. G., Antelo, A., & Vazquez-Tato, J. (2009). Bile acids: chemistry, physiology, and pathophysiology. *World Journal of Gastroenterology: WJG*, *15*(7), 804–816.

Müsch, A. (2004). Microtubule Organization and Function in Epithelial Cells: Microtubules in Epithelial Cells. *Traffic* , *5*(1), 1–9.

Muthukanagarajan, S. J., Karnan, I., Srinivasan, P., Sadagopan, P., & Manickam, S. (2016). Diagnostic and Prognostic Significance of Various Histopathological Features in Extrahepatic Biliary Atresia. *Journal of Clinical and Diagnostic Research: JCDR*, *10*(6), EC23–EC27.

Nakano, S., Haratake, J., & Hashimoto, H. (1995). Alterations in bile ducts and peribiliary microcirculation in rats after common bile duct ligation. *Hepatology* , *21*(5), 1380–1386.

Oda, H., Stockert, R. J., Collins, C., Wang, H., Novikoff, P. M., Satir, P., & Wolkoff, A. W. (1995). Interaction of the microtubule cytoskeleton with endocytic vesicles and cytoplasmic dynein in cultured rat hepatocytes. *The Journal of Biological Chemistry*, *270*(25), 15242–15249.

Palmeira, C. M., & Rolo, A. P. (2004). Mitochondrially-mediated toxicity of bile acids. *Toxicology*, *203*(1-3), 1–15.

Pellicciari, R., Costantino, G., & Fiorucci, S. (2005). Farnesoid X receptor: from structure to potential clinical applications. *Journal of Medicinal Chemistry*, *48*(17), 5383–5403.

Rappaport, A. M., & Wilson, W. D. (1958). The stuctural and functional unit in the human liver (liver acinus). *The Anatomical Record*, *130*(4), 673–689.

R Core Team. (n.d.). R: A language and environment for statistical computing. Retrieved 2018, from https://www.R-project.org/

Reif, R., Karlsson, J., Günther, G., Beattie, L., Wrangborg, D., Hammad, S., … Jirstrand, M. (2015). Bile canalicular dynamics in hepatocyte sandwich cultures. *Archives of Toxicology*, *89*(10), 1861–1870.

Reshetnyak, V. I. (2013). Physiological and molecular biochemical mechanisms of bile formation. *World Journal of Gastroenterology: WJG*, *19*(42), 7341–7360.

Riedl, J., Crevenna, A. H., Kessenbrock, K., Yu, J. H., Neukirchen, D., Bista, M., … Wedlich-Soldner, R. (2008). Lifeact: a versatile marker to visualize F-actin. *Nature Methods*, *5*(7), 605–607.

Ritz, C., Baty, F., Streibig, J. C., & Gerhard, D. (2015). Dose-Response Analysis Using R. *PloS One*, *10*(12), e0146021.

Rolo, A. P., Palmeira, C. M., Holy, J. M., & Wallace, K. B. (2004). Role of mitochondrial dysfunction in combined bile acid-induced cytotoxicity: the switch between apoptosis and necrosis. *Toxicological Sciences: An Official Journal of the Society of Toxicology*, *79*(1), 196–204.

Roskams, T. A., Theise, N. D., Balabaud, C., Bhagat, G., Bhathal, P. S., Bioulac-Sage, P., … West, A. B. (2004). Nomenclature of the finer branches of the biliary tree: canals, ductules, and ductular reactions in human livers. *Hepatology* , *39*(6), 1739–1745.

Roskams, T., & Desmet, V. (1998). Ductular reaction and its diagnostic significance. *Seminars in Diagnostic Pathology*, *15*(4), 259–269.

Salvalaggio, P. R. O., Whitington, P. F., Alonso, E. M., & Superina, R. A. (2005). Presence of multiple bile ducts in the liver graft increases the incidence of biliary complications in pediatric

liver transplantation. *Liver Transplantation: Official Publication of the American Association for the Study of Liver Diseases and the International Liver Transplantation Society*, *11*(2), 161–166.

Saxena, R., Hytiroglou, P., Thung, S. N., & Theise, N. D. (2002). Destruction of canals of Hering in primary biliary cirrhosis. *Human Pathology*, *33*(10), 983–988.

Segawa, O., Miyano, T., Fujimoto, T., Watanabe, S., Hirose, M., & Fujiwara, T. (1993). Actin and myosin deposition around bile canaliculi: a predictor of clinical outcome in biliary atresia. *Journal of Pediatric Surgery*, *28*(6), 851–856.

Seglen, P. O. (1976). Preparation of isolated rat liver cells. *Methods in Cell Biology*, *13*, 29–83.

Shannon S. Glaser a,b,∗, Paolo Onorif , Candace Wise b, Fuguan Yang b,d, Marco Marzioni e, Domenico Alvarog, Antonio Franchitto h, Romina Mancinelli h, Gianfranco Alpini a,b,c, Md. Kamruzzaman Munshi b, Eugenio Gaudio h,∗∗. (2010). Recent advances in the regulation of cholangiocyte proliferation and function during extrahepatic cholestasis. *Digestive and Liver Disease*. Retrieved from file:///C:/Users/Vartak/Documents/1-s2.0-S1590865810000125-main.pdf

Sharanek, A., Burban, A., Burbank, M., Le Guevel, R., Li, R., Guillouzo, A., & Guguen-Guillouzo, C. (2016). Rho-kinase/myosin light chain kinase pathway plays a key role in the impairment of bile canaliculi dynamics induced by cholestatic drugs. *Scientific Reports*, *6*, 24709.

Shepard, B. D., & Tuma, P. L. (2010). Alcohol-induced alterations of the hepatocyte cytoskeleton. *World Journal of Gastroenterology: WJG*, *16*(11), 1358–1365.

Sinal, C. J., Tohkin, M., Miyata, M., Ward, J. M., Lambert, G., & Gonzalez, F. J. (2000). Targeted disruption of the nuclear receptor FXR/BAR impairs bile acid and lipid homeostasis. *Cell*, *102*(6), 731–744.

Si-Tayeb, K., Lemaigre, F. P., & Duncan, S. A. (2010). Organogenesis and development of the liver. *Developmental Cell*, *18*(2), 175–189.

Strazzabosco, M. (1997). Transport systems in cholangiocytes: their role in bile formation and cholestasis. *The Yale Journal of Biology and Medicine*, *70*(4), 427–434.

Strazzabosco, M., & Fabris, L. (2008). Functional anatomy of normal bile ducts. *Anatomical Record* , *291*(6), 653–660.

Szymanski, D., & Staiger, C. J. (2018). The Actin Cytoskeleton: Functional Arrays for Cytoplasmic
Organization and Cell Shape Control. *Plant Physiology*, *176*(1), 106–118.

Tag, C. G., Sauer-Lehnen, S., Weiskirchen, S., Borkham-Kamphorst, E., Tolba, R. H., Tacke, F., &
Weiskirchen, R. (2015). Bile duct ligation in mice: induction of inflammatory liver injury and
fibrosis by obstructive cholestasis. *Journal of Visualized Experiments: JoVE*, (96).
https://doi.org/10.3791/52438

Takashima, Y., Terada, M., Kawabata, M., & Suzuki, A. (2015). Dynamic three-dimensional
morphogenesis of intrahepatic bile ducts in mouse liver development. *Hepatology* , *61*(3), 1003–
1011.

Tanimizu, N., Miyajima, A., & Mostov, K. E. (2007). Liver progenitor cells develop cholangiocyte-
type epithelial polarity in three-dimensional culture. *Molecular Biology of the Cell*, *18*(4), 1472–
1479.

Tannuri, A. C. A., Coelho, M. C. M., de Oliveira Gonçalves, J., Santos, M. M., Ferraz da Silva, L. F.,
Bendit, I., & Tannuri, U. (2012). Effects of selective bile duct ligation on liver parenchyma in
young animals: histologic and molecular evaluations. *Journal of Pediatric Surgery*, *47*(3), 513–
522.

Theise, N. D., Saxena, R., Portmann, B. C., Thung, S. N., Yee, H., Chiriboga, L., … Crawford, J. M.
(1999). The canals of Hering and hepatic stem cells in humans. *Hepatology* , *30*(6), 1425–1433.

Thibault, N., Claude, J. R., & Ballet, F. (1992). Actin filament alteration as a potential marker for
cholestasis: a study in isolated rat hepatocyte couplets. *Toxicology*, *73*(3), 269–279.

Thomas, A. M., Hart, S. N., Kong, B., Fang, J., Zhong, X.-B., & Guo, G. L. (2010). Genome-wide
tissue-specific farnesoid X receptor binding in mouse liver and intestine. *Hepatology* , *51*(4),
1410–1419.

Thomas, C., Pellicciari, R., Pruzanski, M., Auwerx, J., & Schoonjans, K. (2008). Targeting bile-acid
signalling for metabolic diseases. *Nature Reviews. Drug Discovery*, *7*(8), 678–693.

Thompson, M. D., Moghe, A., Cornuet, P., Marino, R., Tian, J., Wang, P., … Nejak-Bowen, K.
(2018). β-Catenin regulation of farnesoid X receptor signaling and bile acid metabolism during
murine cholestasis. *Hepatology* , *67*(3), 955–971.

Tranter, M. P., Sugrue, S. P., & Schwartz, M. A. (1991). Binding of actin to liver cell membranes: the state of membrane-bound actin. *The Journal of Cell Biology*, *112*(5), 891–901.

Trauner, M., & Boyer, J. L. (2003). Bile salt transporters: molecular characterization, function, and regulation. *Physiological Reviews*, *83*(2), 633–671.

Tsukada, N., Ackerley, C. A., & Phillips, M. J. (1995). The structure and organization of the bile canalicular cytoskeleton with special reference to actin and actin-binding proteins. *Hepatology* , *21*(4), 1106–1113.

Tubulin Tracker Green (Oregon Green 488 Taxol, Bis-Acetate), for live-cell imaging. (n.d.). Retrieved May 13, 2018, from http://www.thermofisher.com/order/catalog/product/T34075

Tuchweber, B., Roy, S., Desroches, S., Yousef, I. M., Gicquaud, C., Weber, A. M., & Loranger, A. (1990). Effects of bile acids on actin polymerization in vitro. *Life Sciences*, *47*(15), 1299–1307.

Tzanakakis, E. S., Hansen, L. K., & Hu, W. S. (2001). The role of actin filaments and microtubules in hepatocyte spheroid self-assembly. *Cell Motility and the Cytoskeleton*, *48*(3), 175–189.

van der Velden, L. M., Golynskiy, M. V., van Mil, S. W. C., Klomp, L. W. J., Merkx, M., & van de Graaf, S. F. J. (n.d.). Monitoring Bile Acid Transport in Single Living Cells Using a Genetically Encoded F€orster Resonance Energy Transfer Sensor.

van Deurs, B., von Bũlow, F., Vilhardt, F., Holm, P. K., & Sandvig, K. (1996). Destabilization of plasma membrane structure by prevention of actin polymerization. Microtubule-dependent tubulation of the plasma membrane. *Journal of Cell Science*, *109 (Pt 7)*, 1655–1665.

van Eyken, P., Sciot, R., van Damme, B., de Wolf-Peeters, C., & Desmet, V. J. (1987). Keratin immunohistochemistry in normal human liver. Cytokeratin pattern of hepatocytes, bile ducts and acinar gradient. *Virchows Archiv. A, Pathological Anatomy and Histopathology*, *412*(1), 63–72.

Vartak, N., Damle-Vartak, A., Richter, B., Dirsch, O., Dahmen, U., Hammad, S., & Hengstler, J. G. (2016). Cholestasis-induced adaptive remodeling of interlobular bile ducts. *Hepatology* , *63*(3), 951–964.

Verhaag, E. M., Buist-Homan, M., Koehorst, M., Groen, A. K., Moshage, H., & Faber, K. N. (2016). Hormesis in Cholestatic Liver Disease; Preconditioning with Low Bile Acid Concentrations Protects against Bile Acid-Induced Toxicity. *PloS One*, *11*(3), e0149782.

Vizcarra, J. (n.d.). Findings Suggest That RNA Molecule microRNA-122 (miR-122) Linked To Liver Cancer. Retrieved October 10, 2017, from http://www.quantumday.com/2012/07/findings-suggest-that-rna-molecule.html

Watanabe, M., Houten, S. M., Mataki, C., Christoffolete, M. A., Kim, B. W., Sato, H., … Auwerx, J. (2006). Bile acids induce energy expenditure by promoting intracellular thyroid hormone activation. *Nature*, *439*(7075), 484–489.

Weichsel, J., Herold, N., Lehmann, M. J., Kräusslich, H.-G., & Schwarz, U. S. (2010). A quantitative measure for alterations in the actin cytoskeleton investigated with automated high-throughput microscopy. *Cytometry. Part A: The Journal of the International Society for Analytical Cytology*, *77*(1), 52–63.

Wiley: Principles of Anatomy and Physiology, 14th Edition - Gerard J. Tortora, Bryan H. Derrickson. (n.d.). Retrieved August 23, 2017, from http://eu.wiley.com/WileyCDA/WileyTitle/productCd-EHEP002935.html

Wilton, J. C., Chipman, J. K., Lawson, C. J., Strain, A. J., & Coleman, R. (1993). Periportal- and perivenous-enriched hepatocyte couplets: differences in canalicular activity and in response to oxidative stress. *Biochemical Journal*, *292 (Pt 3)*, 773–779.

Wu, Y. C., Hour, M. J., Leung, W. C., Wu, C. Y., Liu, W. Z., Chang, Y. H., & Lee, H. Z. (2011). 2-(Naphthalene-1-yl)-6-pyrrolidinyl-4-quinazolinone inhibits skin cancer M21 cell proliferation through aberrant expression of microtubules and the cell cycle. *The Journal of Pharmacology and Experimental Therapeutics*, *338*(3), 942–951.

Xia, X., Francis, H., Glaser, S., Alpini, G., & LeSage, G. (2006). Bile acid interactions with cholangiocytes. *World Journal of Gastroenterology: WJG*, *12*(22), 3553–3563.

Yang, F., Gaudio, E., Onori, P., Wise, C., Alpini, G., & Glaser, S. S. (2010). Mechanisms of Biliary Damage. *Journal of Cell Death*, *2010*(3), 13–21.

Zhang, Y., Hong, J.-Y., Rockwell, C. E., Copple, B. L., Jaeschke, H., & Klaassen, C. D. (2012). Effect of bile duct ligation on bile acid composition in mouse serum and liver. *Liver International: Official Journal of the International Association for the Study of the Liver*, *32*(1), 58–69.

Zhou, Y., Maxwell, K. N., Sezgin, E., Lu, M., Liang, H., Hancock, J. F., … Levental, I. (2013). Bile acids modulate signaling by functional perturbation of plasma membrane domains. *The Journal of Biological Chemistry*, *288*(50), 35660–35670.

Zorn, A. M. (2008). Liver development. In *StemBook*. Cambridge (MA): Harvard Stem Cell Institute.

7. APPENDIX

7.1. Abbreviations

ACOX2   Acyl-coA oxidase 2

AKR1C4   Aldo-keto reductase family 1-member C4

ALB   Albumin

ALP   Alkaline phosphatase

ANIT   α-naphthylisothiocyanate

ASAT   Aspartate aminotransferase

AST   Aspartate transaminase

ASBT   Apical Sodium Dependent bile acid transporter

BA   Bile acid

BC   Bile canaliculi

BCV   Bile canalicular vesicle

BDL   Bile duct ligation

BECs   Biliary epithelial cells

BG   Background

BP   Biliary pigments

BrdU   5-bromo-2'-deoxyuridine

BSEP   Bile salt Export Pump

CA   Cholic acid

CDCA   Chenodeoxycholic acid

CD14   Cluster of differentiation 14

CK   Cytokeratin

CLSM   Confocal laser scanning microscope

CoH   canal of Hering

CYP   Cytochrome P

DBD   DNA binding domain

DCA   Deoxycholic acid

DIC   Differential interference contrast microscopy

DMSO   Dimethyl sulfoxide

DPP4   Dipeptidyl peptidase-4

ECM   Extracellular matrix

FXR	Farnesoid X Receptor
FGF	Fibroblast growth factor
FRET	Förster resonance energy transfer
GI	Gastrointestinal tract
GPCR	G protein-coupled receptor
HA	Hepatic artery
HCC	Hepatocellular carcinoma
HNF	Hepatocyte nuclear factor
IBD	Interlobular bile duct
IGF	Insulin-like growth factor
LB	Luria broth
LBD	Ligand binding domain
LCA	Lithocholic acid
LRH	Liver receptor homolog
LSEC	Liver sinusoidal endothelial cell
LXR	Liver X receptor
NASH	Non-alcoholic steatohepatitis
NLS	Nuclear localization signal or sequence
NR1H4	Nuclear receptor subfamily 1 group H member 4
NTCP	Na^{2+} or Sodium/taurocholate cotransporting Polypeptide
OATP	Organic-anion-transporting polypeptide
OST	Organic solute transporter
PCDC	Pericanalicular cytoskeleton depletion and collapse
PMH	Primary mouse hepatocyte
PV	Portal vein
RFP	Red fluorescent protein
SHP	Short heterodimer protein
SiR	Silicon rhodamine
SOB	Super optimized broth
SREBP	Sterol regulatory element-binding protein
TCA	Taurocholic acid
UDCA	Ursodeoxycholic acid
VC	Vehicle control

7.2. Publications, Posters and Workshops

7.2.1. Publications

Results, methodologies and computational algorithms presented in this thesis have been contributed to the following peer-reviewed publication:

- *Vartak, N., *Damle-Vartak, A., Richter, B., Dirsch, O., Dahmen, U., Hammad, S. and Hengstler, J. G. (2016), **Cholestasis-induced adaptive remodeling of interlobular bile ducts**. Hepatology, 63: 951-964. doi:10.1002/hep.28373
  *shared first co-authors

- Anna Lorentzen, Paul F. Becker, Jan Kosla, Massimo Saini, Kathrin Weidele, Paolo Ronchi, Corinna Klein, Monika J. Wolf, Felix Geist, Bastian Seubert, Marc Ringelhan, Daniela Mihic-Probst, Knud Esser, Marko Roblek, Felix Kuehne, Gaia Bianco, Tracy O'Connor, Quentin Müller, Kathleen Schuck, Sebastian Lange, Daniel Hartmann, Saskia Spaich, Olaf Groß, Jochen Utikal, Sebastian Haferkamp, Martin R. Sprick, Amruta Damle-Vartak, Alexander Hapfelmeier, Norbert Hüser, Ulrike Protzer, Andreas Trumpp, Dieter Saur, Nachiket Vartak, Christoph A. Klein, Bernhard Polzer, Lubor Borsig, Mathias Heikenwalder. **Single cell polarity in liquid phase facilitates tumour metastasis.** Nature Communications, 2018; 9 (1) DOI: 10.1038/s41467-018-03139-6

Other research publications included:

- Hammad S, Hoehme S, Friebel A, von Recklinghausen I, Othman A, Begher-Tibbe B, Reif R, Godoy P, Johann T, Vartak A, Golka K, Bucur PO, Vibert E, Marchan R, Christ B, Dooley S, Meyer C, Ilkavets I, Dahmen U, Dirsch O, Böttger J, Gebhardt R, Drasdo D, Hengstler JG. Arch Toxicol. 2014 May;88(5):1161-83. doi: 10.1007/s00204-014-1243-5. Epub 2014 Apr 19. **Protocols for staining of bile canalicular and sinusoidal networks of human, mouse and pig livers, three-dimensional reconstruction and quantification of tissue microarchitecture by image processing and analysis.** Archives of Toxicology, 88(5), 1161–1183. http://doi.org/10.1007/s00204-014-1243-5

- Reif, R.; Karlsson, J.; Günther, G.; Wrangborg, D.; Hammad, S.; Begher-Tibbe, B.; Vartak, A.; Hengstler, J. G.: **Bile canalicular dynamics in hepatocyte sandwich cultures.** Arch. Toxicol. 89: 1861-1870 (2015). http://dx.doi.org/10.1007/s00204-015-1575-9

7.2.2. Posters and Presentations

The work had been presented as poster at the following conferences:

- Reconstruction and quantification of periportal bile ducts and Hering canal after bile duct ligation - 31. Jahrestagung der Deutschen Arbeitsgemeinschaft zum Studium der Leber (GASL), München, 30.01.2015 to 31.01.2015.
- Remodeling of interlobular bile ducts after cholestasis -Practical course in current methods in cell biology, EMBL, European Molecular Biology Laboratory, Heidelberg, 13.09.2015.
- Cholestasis-induced adaptations in liver architecture and signaling- Tag der Chemie" at TU Dortmund, 24.02.2017.
- LiSyM-Midterm evaluation, Manheim, May 2018

7.2.3. Workshops

- Practical course in current methods in cell biology , EMBL, European Molecular Biology Laboratory, Heidelberg , 13.09.2015.
- Laboratory animal course -FELASA B certificate, Bayer AG Pharma, Wuppertal, February 2017.

7.3. Curriculum vitae

Name : Amruta Damle Vartak

Address: Hohe Str. 100, 44139 Dortmund, Germany

Telephone: +49-176-842-88114

Email: vartak@ifado.de

Date of Birth: 22 June 1986

Nationality: Indian

University Matriculation Number:

Education:

July 2004-November 2007- Bachelor of Science (Biotechnology)

University: Rashtrasanta Tukdoji Maharaj Nagpur University, Nagpur, INDIA

Grade: Division II with 50.73%

July 2008- July 2010- Master of Science (Zoology) specialization in Animal Physiology

University: Nowrosjee Wadia College, University of Pune, INDIA

Grade: First Class with 62.3%

Past employment:

August 2010-June 2011: Project Research Assistant

Institute: CSIR-NEERI (Council for scientific and industrial research- National Environmental Engineering Research Institute), Nagpur, INDIA

Department: Applied Aquatic Ecosystem Division

Project: Fish Melanophores as Cytosensors

April 2013-April 2014: Wissenschaften Hilfskraft

Institute: Leibniz-Institut für Arbeitsforschung an der TU Dortmund

Department: Systems Toxicology

7.4. Affidavit

Eidesstattliche Versicherung (Affidavit)

DAMLE-VARTAK, AMRUTA
_____
Name, Vorname
(Surname, first name)

211109
_____
Matrikel-Nr.
(Enrolment number)

Belehrung:	Official notification:
Wer vorsätzlich gegen eine die Täuschung über Prüfungsleistungen betreffende Regelung einer Hochschulprüfungsordnung verstößt, handelt ordnungswidrig. Die Ordnungswidrigkeit kann mit einer Geldbuße von bis zu 50.000,00 € geahndet werden. Zuständige Verwaltungsbehörde für die Verfolgung und Ahndung von Ordnungswidrigkeiten ist der Kanzler/die Kanzlerin der Technischen Universität Dortmund. Im Falle eines mehrfachen oder sonstigen schwerwiegenden Täuschungsversuches kann der Prüfling zudem exmatrikuliert werden, § 63 Abs. 5 Hochschulgesetz NRW.	Any person who intentionally breaches any regulation of university examination regulations relating to deception in examination performance is acting improperly. This offence can be punished with a fine of up to EUR 50,000.00. The competent administrative authority for the pursuit and prosecution of offences of this type is the chancellor of the TU Dortmund University. In the case of multiple or other serious attempts at deception, the candidate can also be unenrolled, Section 63, paragraph 5 of the Universities Act of North Rhine-Westphalia.
Die Abgabe einer falschen Versicherung an Eides statt ist strafbar.	The submission of a false affidavit is punishable.
Wer vorsätzlich eine falsche Versicherung an Eides statt abgibt, kann mit einer Freiheitsstrafe bis zu drei Jahren oder mit Geldstrafe bestraft werden, § 156 StGB. Die fahrlässige Abgabe einer falschen Versicherung an Eides statt kann mit einer Freiheitsstrafe bis zu einem Jahr oder Geldstrafe bestraft werden, § 161 StGB.	Any person who intentionally submits a false affidavit can be punished with a prison sentence of up to three years or a fine, Section 156 of the Criminal Code. The negligent submission of a false affidavit can be punished with a prison sentence of up to one year or a fine, Section 161 of the Criminal Code.
Die oben stehende Belehrung habe ich zur Kenntnis genommen:	I have taken note of the above official notification.

_____
Ort, Datum
(Place, date)

_____
Unterschrift
(Signature)

Titel der Dissertation:
(Title of the thesis):

Morphological and intracellular response of the liver to bile acid-mediated

 toxicity in Cholestasis

_____

| Ich versichere hiermit an Eides statt, dass ich die vorliegende Dissertation mit dem Titel selbstständig und ohne unzulässige fremde Hilfe angefertigt habe. Ich habe keine anderen als die angegebenen Quellen und Hilfsmittel benutzt sowie wörtliche und sinngemäße Zitate kenntlich gemacht. Die Arbeit hat in gegenwärtiger oder in einer anderen Fassung weder der TU Dortmund noch einer anderen Hochschule im Zusammenhang mit einer staatlichen oder akademischen Prüfung vorgelegen. | I hereby swear that I have completed the present dissertation independently and without inadmissible external support. I have not used any sources or tools other than those indicated and have identified literal and analogous quotations. The thesis in its current version or another version has not been presented to the TU Dortmund University or another university in connection with a state or academic examination.* |

*Please be aware that solely the German version of the affidavit ("Eidesstattliche Versicherung") for the PhD thesis is the official and legally binding version.

_____
Ort, Datum
(Place, date)

_____
Unterschrift
(Signature)

7.5 Acknowledgement